



Product Model Creation and Simulation for Two-photon Polymerization Micro-manufacturing

Chao-Yaug Liao

► To cite this version:

Chao-Yaug Liao. Product Model Creation and Simulation for Two-photon Polymerization Micro-manufacturing. Mechanics [physics.med-ph]. Université Joseph-Fourier - Grenoble I; National Taiwan University, 2008. English. NNT: . tel-00417799

HAL Id: tel-00417799

<https://theses.hal.science/tel-00417799>

Submitted on 17 Sep 2009

HAL is a multi-disciplinary open access archive for the deposit and dissemination of scientific research documents, whether they are published or not. The documents may come from teaching and research institutions in France or abroad, or from public or private research centers.

L'archive ouverte pluridisciplinaire **HAL**, est destinée au dépôt et à la diffusion de documents scientifiques de niveau recherche, publiés ou non, émanant des établissements d'enseignement et de recherche français ou étrangers, des laboratoires publics ou privés.

Ph.D.

A dissertation submitted in partial satisfaction
of the requirements for the degree of

**Doctor of Philosophy of the
Joseph Fourier University / National Taiwan University**

Specialty: Mechanical Engineering

Chao-Yaug LIAO

**Product Model Creation and Simulation for Two-photon
Polymerization Micro-manufacturing**

Directors of thesis : J.-C. LEON and T.-T. CHUNG

Co-directors of thesis : P. L. BALDECK and C. MASCLET

Composition of the jury:

S. F. CHOU	President	Professor	NTU, Taipei, Taiwan
C. LARTIGUE	Reviewer	Professor	IUT Cachan/ENS Cachan, Cachan, France
J. Y. JENG	Reviewer	Professor	NTUST, Taipei, Taiwan
H. HANSEN	Examiner	Professor	DTU, Lyngby, Denmark

Thesis prepared within

Grenoble - Laboratoire des Sciences pour la Conception, l'Optimisation et la Production (G-SCOP, INPG, UJF, CNRS),
Laboratoire de Spectrométrie Physique (SPECTRO, UJF, CNRS)
and Computer-Aided Design Laboratory (CAD Lab, NTU)

Dedication

*To my parents,
may their souls rest in Heaven.*

Acknowledgments

First and foremost, I would like to express my gratitude to my both advisors Prof. Jean-Claude Léon and Prof. Tien-Tung Chung for their guidance and encouragements. This thesis is the outcome of their incomparable patience and constructive suggestions. Particularly, Jean-Claude gave me confidence in pursuing my Ph.D. degree and independent research. Prof. Chung being my advisor has been ten years since I was a graduate student. He not merely is my advisor, but rather my guiding light in life. Thanks for urging me to study in France.

One of my co-advisors, Dr. Patrice L. Baldeck receives my heartfelt gratitude for sharing his invaluable experiences of TPP technology with me. He is very humorous and I will remember his laughter forever.

I would like to extend my special thanks to another co-advisor, Prof. Cédric Masclet, for his tutelage in my research work and providing me with the facilities to complete my thesis.

I would also like sincerely thank my doctoral jury members: Prof. Shyan-Fu Chou, Prof. Claire Lartigue, Prof. Jeng-Ywan Jeng, and Prof. Hans Hansen. Their valuable suggestions make my work more complete.

I deeply thanks to Mr. Michel Bouriau for helping me a lot in experiments of TPP micro-manufacturing. Without his suggestions, I couldn't successfully fabricate those demonstrating microstructures.

I want to extend my appreciation to Institut Français de Taipei and Ministry of Education for providing me scholarship to study abroad in France. Except for an academic degree, they gave me an amazing opportunity to experience French-style life for two years. Thanks to Prof. Shyan-Fu Chou, Ms. Ching-Fang Ting, and Ms. Jean Lin for helping materialize this double degree program between UJF and NTU.

Thanks to all colleagues in G-SCOP and SPECTRO Laboratories (France), and in CAD Laboratory (Taiwan), especially Antoine who is an exceptional programmer and guided me in programming SIMPOLY, Nicoletta who always emboldened me when I encountered difficulties, Chen-Cheng who usually sent me a lot of specialties of Taiwan

when I was in France. I also want to extend my thanks to Chao-Yo, Chia-Fang, Yulin, and Chinwen for being around through all the happy and difficult time in the past two years.

Last but definitely not least, my sincerely appreciation goes to my dearest family for their consistent care, support, and endless love for more than thirty years. Not only do they supply me with unwavering faith toward my lifetime journey, but also help me to face various challenges at ease.

Table of contents

Abstract	xv
Résumé	xvii
摘 要	xix
Introduction	1
Chapter 1 State of art of micro-product fabrication and their integration in a design process	3
1.1 Two-photon polymerization micro-manufacturing technique	3
1.1.1 The principle of TPP	3
1.1.2 Spatial resolutions (Voxel) of the TPP process	6
1.1.3 Comparison between TPP and general silicon-based micromachining technologies	7
1.1.4 Main technological characteristics of the micro-product manufacturing process with TPP	9
1.1.5 Process flow of TPP micro-fabrication through the concept of product view	12
1.2 Analysis of existing approaches for TPP micro-fabrication	14
1.2.1 TPP applications for families of micro-products	14
1.2.2 Integrated manufacturing systems for the TPP process	16
1.3 Layered Manufacturing (LM)	17
1.3.1 Staircase effect and deposition inaccuracies in a LM process	18
1.3.2 Other micro-manufacturing processes using LM technique	20
1.4 Geometric representations for a product model	22
1.4.1 Boundary representation (B-Rep)	23

1.4.2 Non-manifold representation	24
1.4.3 Polyhedral representation	26
1.5 Major data exchange formats	28
1.5.1 Stereo Lithography (STL)	28
1.5.2 STandard for the Exchange of Product model data (STEP)	30
1.6 CAD model of components obtained through a reverse engineering process	33
1.7 Texture mapping a component	35
1.8 Simulation operations for TPP micro-fabrication	36
1.8.1 Basic intersection algorithms	36
1.8.2 Laser beam trajectory planning strategies	37
1.8.3 Critical issues for preventing microstructure collapses brought by CSM	38
1.8.4 Critical issues of a slicing process brought by CSM	39
1.8.5 Issues related to scanning path planning	41
1.9 Conclusion	42
Chapter 2 Product view interface for color models acquired through a reverse engineering process	45
2.1 Introduction	45
2.2 Laser scanning without destroying the color information of an object	46
2.3 Automation of texture map generation	49
2.4 Orientation between a polyhedral model and a texture space	52
2.4.1 Perspective mapping	53
2.4.2 Scale orientation mapping	54
2.4.3 Texture mapping criteria	56
2.4.4 Texture filtering	60
2.5 An integrated scanning system for reconstructing color models of objects	61
2.6 Application example	64

2.7 Conclusion	65
Chapter 3 Product view Interface for TPP micro-manufacturing of non-manifold models	67
3.1 Introduction.....	67
3.2 Combining micro-product shapes and functions within the TPP fabrication process	70
3.3 High level topology and mixed shape representation	73
3.3.1 The concept of High Level Topology (HLT)	74
3.3.2 The concept of mixed shape representation	78
3.4 The software environment for the model preparation process.....	80
3.5 The manufacturing model preparation process.....	82
3.5.1 Interactive Merger Specification (IMS) process	84
3.5.2 Overlap Boundary Curve Determination (OBCD) process.....	88
3.6 Tessellation of a non-manifold product model	90
3.7 Conclusion	95
Chapter 4 Product view simulation process for TPP micro-manufacturing.....	97
4.1 Introduction.....	97
4.2 Laser beam trajectory path obtained from slicing a polyhedral model.....	98
4.3 Voxel overlap ratio and layer thickness criterion	99
4.4 Two-dimensional slicing process for non-manifold model	103
4.4.1 Adaptive slicing process (primary slicing phase).....	106
4.4.2 Global 3D hatching process (secondary slicing phase)	108
4.4.3 Wire direct-writing process	110
4.5 Operators for enhancing the microstructure stiffness	111
4.5.1 Welding sub-domains	111
4.5.2 Double contours.....	113
4.6 Trajectory path planning	115

4.6.1 Focal distance criterion to characterize laser beam trajectories	115
4.6.2 Voxel exposure position	118
4.6.3 Fabrication Time	122
4.7 The slicing data structure	124
4.8 Conclusion	130
Chapter 5 Micro-products fabricated by TPP	133
5.1 The micro-fabrication set-up.....	133
5.2 The correction of voxel exposure time	135
5.3 The overall processing flow for the TPP micro-fabrication	137
5.4 Objects with simple shapes	139
5.5 Objects with complex shapes.....	142
5.6 Objects as non-manifold functional microstructures	146
5.7 Conclusion	148
Chapter 6 Conclusions and perspectives	151
6.1 Conclusions.....	151
6.2 Perspectives.....	152
Bibliography.....	155
Appendix A Basic intersection algorithms.....	165

List of figures

1-1	Energy diagram for TPA.....	4
1-2	Comparison of TPA with single-photon absorption generated by a tightly focused laser beam	5
1-3	Basic steps of the photopolymerization process.....	5
1-4	A voxel produced by TPP	7
1-5	Examples fabricated by bulk micromachining and surface micromachining technologies.....	8
1-6	A schematic view of the TPP micro-manufacturing process and its major components.....	10
1-7	The TPP micro-manufacturing process from the life cycle of the resin viewpoint	10
1-8	Overall process flow of the TPP 3D micro-fabrication	11
1-9	A typical case of TPP micro-fabrication	11
1-10	The product view of a generic preparation process for TPP 3D micro- fabrication.....	13
1-11	The TPP biomedical application: micro-needles with various tip sharpness	15
1-12	Assembly configurations of microstructures fabricated by TPP	15
1-13	Functional microstructures fabricated by TPP	16
1-14	The gray-level encoding applications in TPP	16
1-15	Staircase effect in a LM process.....	19
1-16	Deposition inaccuracies in a LM process.....	19
1-17	Other micro-manufacturing processes using LM technique	21
1-18	Graph representation of a face-based B-Rep data structure	23
1-19	Invalid B-rep models	24
1-20	Manifold and non-manifold configurations.....	26
1-21	Solid B-Rep NURBS model and its approximation (B-Rep triangulation)	27
1-22	Structure of the STL format.....	28
1-23	STEP application area within the product life-cycle framework	31
1-24	Different process flows for reverse engineering a component.....	33
1-25	Classification of data acquisition methods	34
1-26	The relationships between texture space, 3D model space, and screen space	36

1-27	Distortion of a texture at the boundaries of triangles when they are textured with different images	36
1-28	Two fabrication strategies.....	37
1-29	Schematic illustration of the difference between two approaches to increase contour thickness	39
1-30	Critical issues of the slicing process brought by the CSM path planning strategy	40
1-31	Over polymerization.....	40
1-32	The categories of scanning path planning of the laser beam during the TPP micro-fabrication process	42
1-33	The product view of the proposed preparation process for TPP 3D micro-fabrication	43
2-1	Laser scanner with a laser diode and two monochrome CCD cameras	46
2-2	Laser beam emitted on a color surface	47
2-3	Scan line data for using adaptive scan line capturing process.....	48
2-4	Object silhouette extraction process.....	50
2-5	The creation of a texture map using an image mask to cut the object background	52
2-6	Pinhole camera	53
2-7	The scale orientation from a polyhedral model to a texture space	55
2-8	Overlapping area between two adjacent texture maps	57
2-9	Schematic diagram of the triangular faces ignored because they are located around the rim of the object silhouette	58
2-10	An example for building belonged relationships between triangular faces and texture maps.....	59
2-11	The grouping process of triangular faces in overlapping areas between two adjacent texture maps	60
2-12	Point sampling between the texture map and the surface particle of a triangular face	60
2-13	The developed integrated scanning system	62
2-14	The configuration of the integrated scanning system.....	62
2-15	Position angle definition around the object.....	63
2-16	3D color model reconstruction procedure	63
2-17	Application example.....	65
3-1	Volume models of micro-products	68
3-2	Possible non-manifold models of micro-products.....	68
3-3	Various idealizations of 3D objects.	72

3-4	Surface decomposition required when an arbitrary surface point needs to be inserted.....	72
3-5	A common topology representation: HLT applied to an application of product behavior simulation.....	75
3-6	HLT data structure (UML representation).....	75
3-7	Example of HLT-Component with one non-manifold HLT-Body.....	77
3-8	Main constitutive elements of the mixed shape representation and corresponding relations	79
3-9	Interface between a CAD model and the HLT data structure.....	80
3-10	The links between the various software packages.....	81
3-11	The manufacturing model preparation process for TPP micro-fabrication	83
3-12	Possible shapes connected by a vertex	85
3-13	The merging configurations of vertices.....	86
3-14	Possible shapes connected by a boundary curve	86
3-15	The merging cases of boundary curves	87
3-16	An example of the merging operation of boundary curves	88
3-17	The overlap boundary curve determination algorithm	90
3-18	Comparison between a standard tessellation process and the proposed one.....	91
3-19	The exchange process of discretization results for OverlapEdges	92
3-20	Process flow of the tessellation process	94
4-1	Types of intersection path.....	98
4-2	The process flow of intersection paths obtained from a set of triangular faces of a polyhedral model.....	99
4-3	The concept of the voxel overlap ratio	100
4-4	Schematic diagram of voxel overlap ratio and layer thickness	102
4-5	Schematic diagram of wall thickness or wire section	102
4-6	Process flow of the two-dimensional slicing process.....	106
4-7	A schematic diagram of adaptive slicing process.....	107
4-8	Flowchart of the proposed adaptive slicing process.....	108
4-9	Comparison of slicing strategies devoted to the secondary slicing phase.....	109
4-10	Flowchart of the global 3D hatching process	110
4-11	The wire direct-writing process.....	111
4-12	Surface welding at a connection between adjacent surface sub-domains	112
4-13	Point welding at a wire connected to other sub-domains	113
4-14	A schematic diagram of offset path derived from a closed CCW path	115
4-15	A schematic diagram of focal distance.....	116
4-16	The sorting algorithm of laser beam trajectories in TPP micro-fabrication	118

4-17	Equidistant subdivision method of a laser beam path	119
4-18	The equidistant subdivision algorithm	119
4-19	The path comparison of possible subdivided trajectory results.....	120
4-20	The feature subdivision algorithm.....	122
4-21	The slicing data structure and its relationships with other data structures.....	125
4-22	A typical instance of SLICE entity	127
4-23	Two typical instances of SECTION entity	127
4-24	A typical instance of WIRE entity	128
4-25	Two typical instances of a WELD entity	129
4-26	Two typical instances of PATH entity	130
5-1	Schematic diagram of the TPP micro-fabrication system	134
5-2	Chemical structures of the photo-initiator: <i>RA 12</i>	135
5-3	Fabrication of reference models for finding the extended exposure time per voxel	137
5-4	The process flow of the proposed approach for the TPP micro-fabrication process	138
5-5	The micro-stair fabricated with SSM and TSM	140
5-6	Micro-hemispheres fabricated by TSM with different critical slicing angles	141
5-7	The processing efficiency comparisons for a simple shape (micro- hemisphere)	142
5-8	The micro-dragon fabricated by TSM	143
5-9	Processing efficiency comparisons for a complex shaped object (micro-dragon).....	144
5-10	The non-manifold microstructure incorporating a volume (arch), an open surface (plane), and two wires	146
5-11	A non-manifold microstructure incorporating two volumes (blocks) and an open surface (membrane).....	147
A-1	The parametric equation of a line.....	166
A-2	The intersection of projection lines	166
A-3	Intersection of a 3D segment and a plane.....	167
A-4	Intersection of a triangle and a plane.....	168
A-5	Distance of a point to a plane	168

List of tables

1-1	Comparison between TPP and silicon-based micromachining technologies	9
4-1	Previous reports about surface roughness induced by voxels	101
5-1	The major manufacturing equipments and their main characteristics.....	135
5-2	The actual fabrication times for the cube and its corresponding extended exposure time per voxel.....	136
5-3	Comparison between micro-bull and micro-dragon.....	145

Product Model Creation and Simulation for Two-photon Polymerization Micro-manufacturing

Abstract

Recently, the Two-Photon Polymerization (TPP) micro-manufacturing technology derived from two-photon absorption draws everyone's attention because of its fabrication capability of arbitrary-shaped and complex three dimensional (3D) microstructures. According to my observation of current researches, the trends have gradually changed from fabricating smallest possible features to expanding its application domains toward more effective topics such as increasing fabrication quality and/or efficiency. This thesis proposes a micro-product model creation and simulation scheme for TPP micro-manufacturing from Computer-Aided Design/Computer-Aided Manufacturing (CAD/CAM) points of view.

An analysis of TPP main features is performed to characterize its manufacturing capabilities. According to the analysis results and the incorporation of microstructure shape constraints and functional requirements, it is shown that the digital model of such objects should be able to describe non-manifold topological structure. Taking this requirement into account and pointing out the lacks of current practices, a non-manifold model preparation scheme is proposed for a product created at a design office. The CAD model imported from a STEP file is tessellated into several manifold polyhedral sub-domains forming a non-manifold polyhedron. Similarly, for an existing product, it can be reverse engineered to obtain its digital model. However, most of current approaches only reconstruct the object shape without its intrinsic colors. For this reason, an integrated scanning process is developed in this thesis in order to generate 3D colored models.

To avoid the destruction of the microstructure caused by over polymerization and the inconsistent voxel sizes originated by variations of light reflections, a two-dimensional slicing process and a dedicated trajectory path planning are developed with the aid of the 3D capabilities of the manufacturing equipment. Hence, the fabrication efficiency can be increased by applying the two processes above. In addition, to improve the microstructure stiffness, two methods developed through the concepts of welding and double contours are used to strengthen the connections between sub-domains and increase their wall thickness, respectively.

Finally, to demonstrate the efficiency of the proposed approach, several digital microstructures, including non-manifold ones, are fabricated according to the proposed model preparation and processing scheme.

Keywords: Micro-manufacturing, two-photon polymerization, non-manifold objects, two dimensional slicing, 3D color model reconstruction, layered manufacturing, reserve engineering.

Création et Simulation de Modèles de Produits pour leur Micro-fabrication par Polymérisation à Deux-photons

Résumé

Récemment, la technologie de micro-fabrication par polymérisation à Deux-Photons (TPP), dérivée de l'absorption à deux-photons, a attiré l'attention de chacun en raison de ses possibilités de fabrication de microstructures tridimensionnelles (3D) de formes très diverses et complexes. Selon mon analyse des recherches actuelles, les thématiques ont graduellement évoluées depuis la fabrication de dispositifs aussi petits que possible vers des thèmes relatifs à son opérationnalité tels que la qualité et/ou l'efficacité du procédé de fabrication. Cette thèse propose une démarche d'intégration pour la création et la simulation de fabrication de modèles de micro-produits pour leur micro-fabrication TPP, tant du point de vue de la Conception Assistée par Ordinateur que de la Fabrication Assistée par Ordinateur (CAO/FAO).

Une analyse des caractéristiques principales de la TPP est proposée pour mettre en évidence ses capacités de fabrication. Selon les résultats de cette analyse et l'incorporation des contraintes de forme des microstructures et de leurs contraintes fonctionnelles, on montre que le modèle numérique de tels objets doit pouvoir décrire des objets de type « non-variété ». Par la prise en considération de cette contrainte et en comblant les manques des approches en vigueur, on propose une démarche intégrée de préparation de modèles « non-variétés » pour un produit créé par un bureau d'études. Le modèle CAO importé à partir d'un fichier STEP est facettisé selon les variétés des sous-domaines polyédriques formant le polyèdre de type « non-variété ». De manière similaire, pour un produit existant, son modèle numérique peut être obtenu par une approche de type ingénierie inverse. Cependant, la plupart des approches existantes reconstruisent seulement les formes des objets sans tenir compte de leurs couleurs intrinsèques. Pour cette raison, un processus intégré de numérisation est développé dans cette thèse afin de produire des modèles 3D colorés.

Afin d'éviter la destruction de la microstructure causée par une « sur-polymérisation » et des tailles de voxels incohérentes provoqués par des différences de réflexion de la lumière, un processus de découpage en tranches bidimensionnelles et une planification adaptée des trajectoires sont développés en

utilisant les possibilités 3D de l'équipement de fabrication. Ainsi, l'efficacité du procédé de fabrication peut être augmentée par la mise en œuvre des deux processus ci-dessus. De plus, pour améliorer la rigidité de la microstructure, deux méthodes ont été développées à partir des concepts de soudure et de double épaisseur pour renforcer les raccords entre les domaines élémentaires de la microstructure et augmenter son épaisseur de paroi, respectivement.

En conclusion, pour démontrer l'efficacité de l'approche proposée, plusieurs modèles numériques de microstructures incluant des modèles « non-variétés » ont été fabriqués selon la démarche de préparation de modèles et le schéma d'intégration proposés.

Mots-clés : Micro-fabrication, polymérisation à deux-photons, objets non-variétés, découpage en tranches bidimensionnel, reconstruction de modèles 3D colorés, fabrication par tranches, ingénierie inverse

雙光子聚合微加工之產品模型建立與模擬

摘要

近幾年來，一種由雙光子吸收理論衍生出的雙光子聚合(TPP)微加工技術，因具有製造任意形狀且複雜之三維微結構的能力而逐漸受到矚目。觀察目前的研究，其趨勢已逐漸從製造最小可能特徵來擴展應用領域層面，轉變成針對提高其製造良率與/或效率等較實用方面上。本論文從電腦輔助設計/電腦輔助製造(CAD/CAM)的觀點，提出一個基於 TPP 微加工技術之微產品模型建立與模擬的完整解決方案。

在進行 TPP 的製造特性分析及考量微結構外型限制與功能需求之後，其結果顯示出此類物品的數位模型需要能表示出 non-manifold 拓模結構的特徵。考量上述需求及指出目前缺乏實用軟體的現實之下，對於那些創造於設計室的產品，本文提出一套 non-manifold 模型準備方案。將來自於 STEP 檔案的 CAD 模型予以網格化後，再用數個多面體次區域來構成一個 non-manifold 模型。至於若產品已存在的話，其數位模型可以使用逆向工程技術得到。然而目前絕大部分目前所使用的方法只重建了物品外型而未還原其本身顏色。因此，本文提出一套可重建三維彩色模型之整合掃描程序。

為避免因過度聚合導致產生的微結構毀壞及因反射率不同導致聚合體大小不一，在藉助三維製造設備的幫助下，本文分別發展出一套雙維切層方法及專屬的雷射掃描路徑之規劃程序。上述兩方法同時亦可以增加加工效率。此外為加強微結構的強度，本文以焊接與雙輪廓概念發展出兩種方法，用來強化各次區域之連接強度與增加結構壁厚。

最後，數個數位微結構(包含 non-manifold 結構)以本文所提出方法實際用 TPP 微加工技術製造出來，來展示本論文所提出的方法之效能。

關鍵字：微加工、雙光子吸收聚合、non-manifold 物品、二維切層、三維彩色模型重建、層加工、逆向工程

Introduction

Recently, the demand for fabrication of smaller and smaller components/products based on nano/micro technologies has significantly increased with the aim of developing a number of conceptually new and high-value-added products.

Although various micro-manufacturing processes have been proposed, few enable the fabrication of arbitrary-shaped and complex three dimensional (3D) microstructures. In the recent years, many studies of micro-scale fabrication technology using laser induced Two-Photon Polymerization (TPP) process have been carried out [Sun et al. 00, Kawata et al. 01, Sun et al. 03a]. Compared with other conventional miniaturization technologies, the superiority of TPP holds in that it can be used to fabricate not only one/two dimensional (1D/2D) simple patterns but complex 3D structures also.

Seeing that TPP or other micro-manufacturing processes still performs at the level of laboratories, useful Computer-Aided Design (CAD) /Computer-Aided Manufacturing (CAM) software specified for micro-product is still missing. Indeed, many previous researches [Divliansky et al. 05, Cunningham et al. 06] somehow use the so-called CAD/CAM systems to process their development process of the micro-products. However, most of them are suitable for mezzo or macro scale components rather than micro and nano scale ones. Sometimes, they cannot provide users with some particular properties specific to micro size during the development process of components. Therefore, to reach the batch-manufacture, CAD/CAM software suited for micro-manufacturing can be considered as a significant and necessary factor.

This article is a double degree thesis integrating the research results obtained at Université Joseph Fourier, France (UJF) and National Taiwan University, Taiwan (NTU). The objective of this thesis is to develop an integrated CAD/CAM scheme from micro-product model acquisition/preparation up to their fabrication using the TPP (Two Photon Polymerization) micro-manufacturing technology.

The whole methodology is split into two parts. The core study is the structure and development of a CAD/CAM system for TPP micro-fabrication (see chapters 3~5) performed at UJF (2005~2007), and the auxiliary one is a Reverse Engineering (RE)

research about reconstructing color models of objects (see chapter 2) developed at NTU (2000~2005).

Chapter 1 introduces the background knowledge related to this thesis such as the principle of TPP, geometric representations for components, RE techniques, ... It also points out the current research status of TPP micro-fabrication and its bottlenecks which are classified into three types: color product model acquisition, non-manifold model preparation, and TPP manufacturing simulation process. These bottlenecks are discussed deeply and are effectively solved with the proposals developed in chapters 2 to 4, respectively.

Chapter 2 presents an integrated scanning process for reconstructing three-dimensional (3D) object models with their intrinsic colors. The extracted color information from scanned objects can be utilized to fabricate color components in Rapid Prototyping (RP) processes [Z Corporation] or performed in gray-level encoding applications in TPP [Jia et al. 07].

From a micro-product point of view, the non-manifold representation is suited for describing its CAD model. Chapter 3 explains what non-manifold representation is needed and how to prepare and create a non-manifold model for a micro-product. A new slicing strategy to produce laser beam trajectories to fabricate micro-products with TPP is presented in chapter 4. In addition, an optimization process for the fabrication sequence of laser trajectories and operators for enhancing the microstructure stiffness are also taken into account in chapter 4. Several micro-products fabricated with the proposed approach are presented in chapter 5. Chapter 6 gives the conclusion and some perspectives are submitted to extend this work.

State of art of micro-product fabrication and their integration in a design process

In this chapter, the TPP micro-manufacturing technique and its state of art are introduced. After investigating cautiously, several critical issues related to the design and manufacture of micro-products are brought up, and this work aims at contributing to solve some of these issues through the proposal of a new effective and efficient fabrication preparation process for TPP integrated in a micro-product design framework.

1.1 Two-photon polymerization micro-manufacturing technique

The ‘micro-fabrication’ is the process of producing functional structures with arbitrary shapes having minimum dimensions currently defined to be $\leq 100 \mu\text{m}$. TPP provides a simple and straightforward way to produce 3D complex microstructures with a high resolution reaching minimum deposited material sizes down to sub-100 nm [Kawata et al. 01, Haske et al. 07, Xing et al. 07]. This section presents the principle and characteristics of a TPP process.

1.1.1 The principle of TPP

The Two-Photon Absorption (TPA), a popular multiple photon excitation approach to the initiation of photochemical changes, is a third order non-linear phenomenon during which two photons of same energy are simultaneously absorbed. The mechanism of TPA is shown in Figure 1-1. A virtual intermediate state is created by the interaction of the absorbing species with the first photon. Only if the second photon arrives within the virtual state lifetime, i.e. about 10^{-15} sec, can it be absorbed [Lee et al. 06]. Therefore, it is apparently requiring higher energy intensities. The energy of the incident photon is given by $h\nu$, where h and ν are the Planck’s constant divided by 2π and the angular frequency of the incident light, respectively. Thus, the absorbing species is raised to an excited state when it absorbs the energy of the single photon, which is equal to $h\nu = S_I -$

S_0 , where S_0 and S_1 are the energy levels ($S_0 < S_1$).

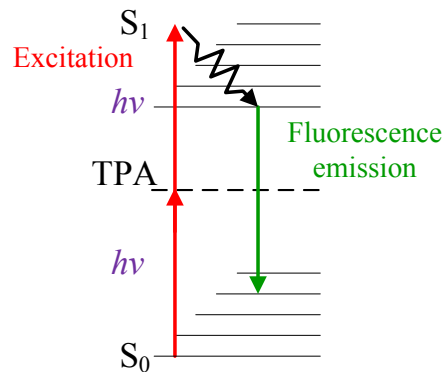


Figure 1-1 Energy diagram for TPA.

Ti:sapphire lasers are widely used for inducing TPA because they produce ultrahigh peak power with a very short pulse width of approximately 100 femto-seconds (fsec) or less. Furthermore, these lasers are very useful for TPP because of their central wavelength of approximately 800 nm, which is close to half of the wavelength of the polymerization [Lee et al. 06]. This enables an easy control of the polymerization energy threshold.

Photopolymerization is defined as the polymerization process requiring the absorption of a photon to occur. Two-photon polymerization is the case of two-photon induced polymerization. If a laser beam is focused at a point with a microscopic objective lens, as shown in Figure 1-2(a), a focused spot with high photon density is formed locally. Each cross section contains the same number of photons. Scanning the laser beam area in the 2D focused plane, the integrated intensity in each of its cross sections is constant, as shown in Figure 1-2(b). On the one hand, this means that the light intensity based on Single-Photon Absorption (SPA) does not have optical sectioning capability. On the other hand, if the material response is proportional to the square of the photon density, the time-integrated material response is enhanced at a focused position, as shown in Figure 1-2(c) for the TPP process. The two-photon transition rate is extremely small in general, so a very high spatial resolution can be obtained, i.e. beneath the limit of diffraction of the light used in the TPP process [Maruo et al. 98].

When a high intensity beam is closely focused into the volume of a liquid-state resin that is transparent to Near InfraRed (NIR) light, the photo-sensitizer chromophore generally used to enhance two-photon activation is excited by the simultaneous absorption of two photons, and then emits fluorescent light in the ultraviolet-visible regime. Photo-initiators with good photochemical reactivity absorb the fluorescent light and then generate radicals (initiation). The radicals react with monomers or oligomers,

producing monomer radicals, so the monomer radicals expand in a chain reaction (propagation) until two radicals meet (termination). The corresponding TPP procedure [Wang et al. 02] can be summarized in Figure 1-3.

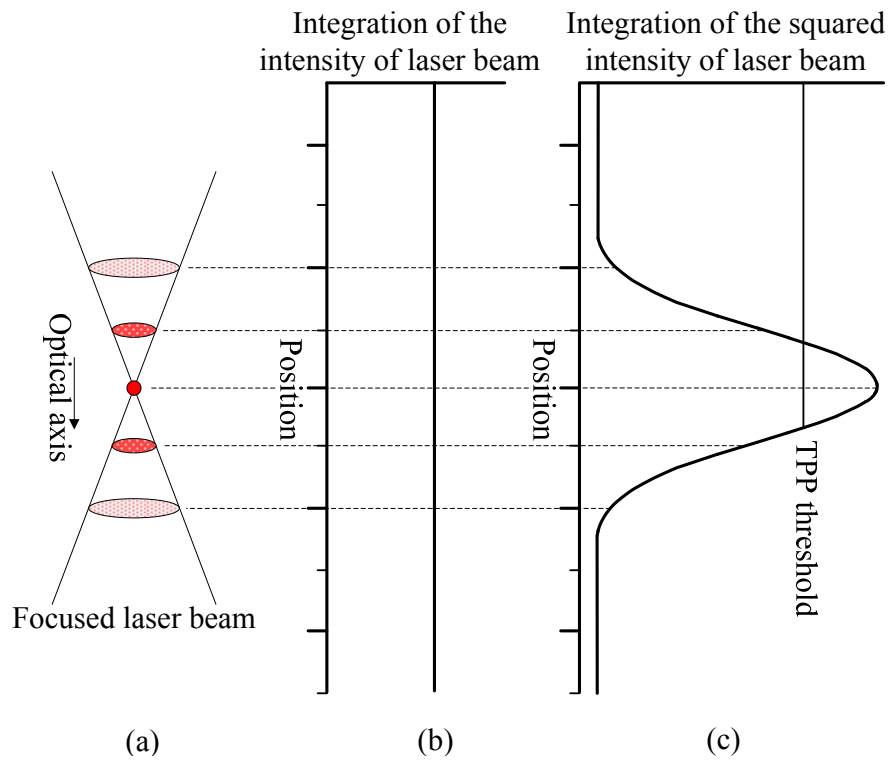


Figure 1-2 Comparison of TPA with single-photon absorption generated by a tightly focused laser beam.

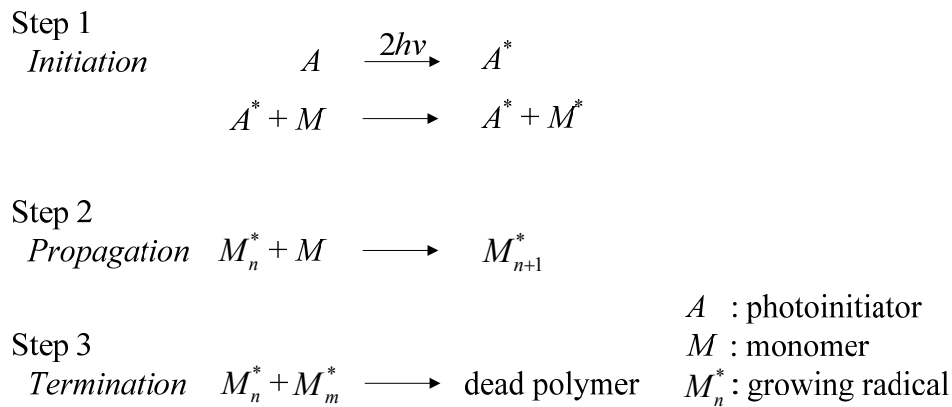


Figure 1-3 Basic steps of the photopolymerization process.

To focus the laser pulsed beam into the volume of the resin without any single-photon interaction, resins used for fabrication must be transparent in the visible and NIR regions. In addition, photosensitive resins usually exhibit shrinking behavior during the polymerization process. To avoid the shrinkage and distortion of the resulting structure, some complementary operations may be needed, such as exposing the

structure to ultraviolet light after the wash out of the micro-structure or calculating its shrinking ratio and then producing a new compensated digital model [Sun et al. 04].

A resin can be formulated with specific components to adjust its mechanical and surface properties and different initiators can be chosen to be adapted to the laser wavelength. In the recent years, several researches proposed the resin doped with metallic ion (Ti^{4+} , Au^{3+} , Ag^+ , Cu^{2+} , Ni^{2+} , etc.) and succeeded in using it to fabricate 2D and 3D metallic structures [Stellacci et al. 02, Kaneko et al. 03, Duan et al. 04, Bosson-Ehoomann et al. 06, Tosa et al. 06].

1.1.2 Spatial resolutions (Voxel) of the TPP process

Indeed, the TPP process is of type additive and can be reduced to a voxel-based approach. In fact, a single exposed voxel is the most fundamental element of the fabricated object. Moreover, the size and proportions of the voxel and the exposed position of each voxel also govern the surface roughness and the manufactured efficiency of a micro-structure, which are the two major and interdependent factors during its manufacturing process.

Indeed, a voxel has an ellipsoidal shape that is associated to the Numerical Aperture (NA) of the focusing lenses, so that it has two spatial resolutions in the lateral and vertical directions [Sun et al. 03c]. A high reproducibility of the pulse peak power is critical for high precision works. A fluctuation of the laser power of 1% was found satisfying since it has been observed from single spot exposure experiments that the voxel size varies within $\pm 8\%$ in that case [Sun et al. 03a]. In this work, the lateral and vertical sizes of a voxel are identified as v_a and v_b , respectively. These voxel sizes can be predicted by Eq. 1-1 and 1-2, and the laser power and the exposure time are among the major parameters to determine the dimensions of a voxel [Lim et al. 05]:

$$v_a = w_0 \left[\ln \left(\frac{4p^2 t}{\pi^2 w_0^4 E_{th}} \right) \right]^{\frac{1}{2}}, \quad (1-1)$$

$$v_b = \frac{2\pi w_0^2}{\lambda} \left[\left(\frac{4p^2 t}{\pi^2 w_0^4 E_{th}} \right)^{\frac{1}{2}} - 1 \right]^{\frac{1}{2}}, \quad (1-2)$$

where w_0 , λ , E_{th} , P , and t are the beam waist, the wavelength, the threshold energy for photopolymerization, the laser power and exposure time, respectively. In the recent

works performed at the laboratory, a lateral spatial resolution varying between 65 to 800 nm [Lim et al. 05, Xing et al. 07, Haske et al. 07] has been achieved, and the voxel aspect ratio, defined as the vertical over lateral lengths of a voxel, has ranged between 2.5 to 4.8 [Sun et al. 03a, Sun et al. 03b]. Based on the above voxel resolutions, the TPP falls into the category of micro-manufacturing processes.

Figure 1-4(a) shows the top- and side-view Scanning Electron Microscopy (SEM) images of a voxel [Sun et al. 03a]. It resembles a spinning ellipsoid with principal axis lengths of v_a and v_b . Figure 1-4(b) shows one of the configurations in which the geometrical center of the focal spot (x, y, z) falls exactly on the substrate surface at $z = 0$, where the potential voxel would need to be half cut. When the center of focal spot rises to a level $0 < z < v_b/2$ or descends to a level $-v_b/2 < z < 0$, a truncated or less than half of the voxel can be obtained, respectively. In other words, the size of the voxel can be controlled by adjusting the distance between the center of focal spot and the substrate surface. This characteristic of the TPP process can be used to monitor the layer thickness if a Layered Manufacturing (LM) procedure is used to manufacture a micro-structure or to locally tune its shape. Further details about LM techniques will be introduced later.

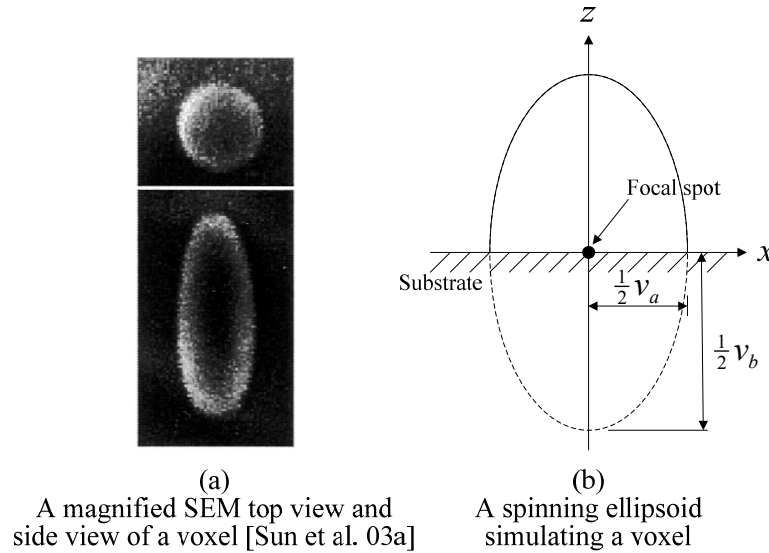


Figure 1-4 A voxel produced by TPP.

1.1.3 Comparison between TPP and general silicon-based micromachining technologies

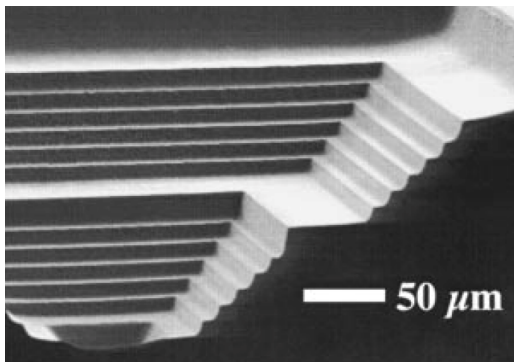
To address a more general scope of the micro-manufacturing processes, the differences of TPP micro-manufacturing and general silicon-based micromachining technologies are discussed in this section. This can let us more easily analyze the

advantage and drawback of the TTP micro-manufacturing.

The term micromachining refers to the fabrication of micromechanical structures with the aid of etching techniques to remove part of substrate or a thin film. Silicon has excellent mechanical properties making it an ideal material for machining. There has been activity in silicon-based micromachining since the early 1960's. Later, in the 1990's, fully integrated complex Micro-ElectroMechanical Systems (MEMS) where actuators, sensors, and control functions can be co-fabricated in silicon using micromachining and integrated circuit processing [Bustillo et al. 98]. In the development of silicon-based micromachining, two different technologies have emerged, those of bulk and surface micromachining.

Bulk micromachining usually refers to etching through the wafer from the back side to form the desired structures. However, surface micromachining represents a totally different process from bulk micromachining. Instead of forming mechanical structures in the silicon substrates, these devices are fabricated in thin films deposited on the surface. Figure 1-5 gives two microstructures fabricated by bulk micromachining and surface micromachining technologies, respectively. In Figure 1-5(a), the stair-like microstructure is made by laser-assisted chemical etching process, a kind of bulk micromachining technologies [Kovacs et al. 98]. As for Figure 1-5(b), it is a SEM cross-sectional image of the microstructure fabricated by the Sandia five-level process [Bustillo et al. 98].

(a) Bulk micromachining [Kovacs et al. 98]



(b) Surface micromachining [Bustillo et al. 98]



Figure 1-5 Examples fabricated by bulk micromachining and surface micromachining technologies.

Table 1-1 shows the comparison between TPP and general silicon-based micromachining technologies. Differing from bulk and surface micro-machining, usually using silicon-based materials, TPP has wide material choices: resin and metallic ions, even protein [Pitts et al. 00]. Besides, TPP process is relatively simple, low cost, and can fabricate arbitrary 3D objects. In addition, the spatial resolution of TPP has

reached sub-100 nm.

However, the control of the voxel size is non-linear, so that the dimensional accuracy is difficult to monitor. Furthermore, batch manufacturing is also difficult though there are some researches aimed at this issue [Kato et al. 05].

Synthesizing the above analyses, TPP is a novel micro-manufacturing technology and worth investigating more deeply.

Table 1-1 Comparison between TPP and silicon-based micromachining technologies.

	TPP micro-manufacturing	Bulk micromachining	Surface micromachining
Material	Resin, Ti^{4+} , Au^{3+} , Ag^+ , Cu^{2+} , protein	Silicon-based	Silicon-based
Process complexity	–	0	+
Lateral dim.	Sub-100 nm	3-5 μm	100-500 μm
Vertical dim.	0.25-3 μm	100-500 μm	0.5-2 μm
Complex 3D object	Easy	Difficult	Difficult
Equipment cost	--	+	0
Accuracy	–	+	+

1.1.4 Main technological characteristics of the micro-product manufacturing process with TPP

The TPP micro-manufacturing process is classified as 1D processing [Dimov et al. 06] due to its material structuring principle. It must be considered as a standalone manufacturing process, entitled to produce finished parts or microproducts with little or no post-processing because part or micro-structure repositioning after a first TPP processing step is currently not possible with the desired accuracy.

As mentioned above, the basis of a TPP process is the conversion of a liquid-state resin into a solid phase by photopolymerization initiated by exposure to a focused, high-intensity, laser light directed into the volume of resin where the microstructure is to be produced [Park et al. 05]. Using a precise mechanism control, it is possible to manufacture arbitrary shaped objects, assuming that the laser beam can move freely in 3D space. Furthermore, submitting resin at an appropriate degree of pre-exposure under a ultraviolet light (one photon absorption exposure process) can increase its viscosity, thus providing the necessary support to anchor each component at its right position when fabricating multi-components synchronously to form a micro-product [Sun et al. 00].

After the laser beam manufacturing phase, the resin will be immersed in a solvent to dissolve the unexposed material. Then, the polymerized microstructure is freed from its resin environment, thus obtaining the final micro-structure. Figure 1-6 shows a schematic view of the TPP micro-manufacturing process. Here, the manufactured microstructure contains a membrane type object as an external component and a free-moving ball as an internal component which are created by the laser trajectories in accordance to the desired shape of the microstructure in the resin. In addition, Figure 1-7 depicts the TPP micro-manufacturing process from another point of view, i.e. the life cycle of the resin.

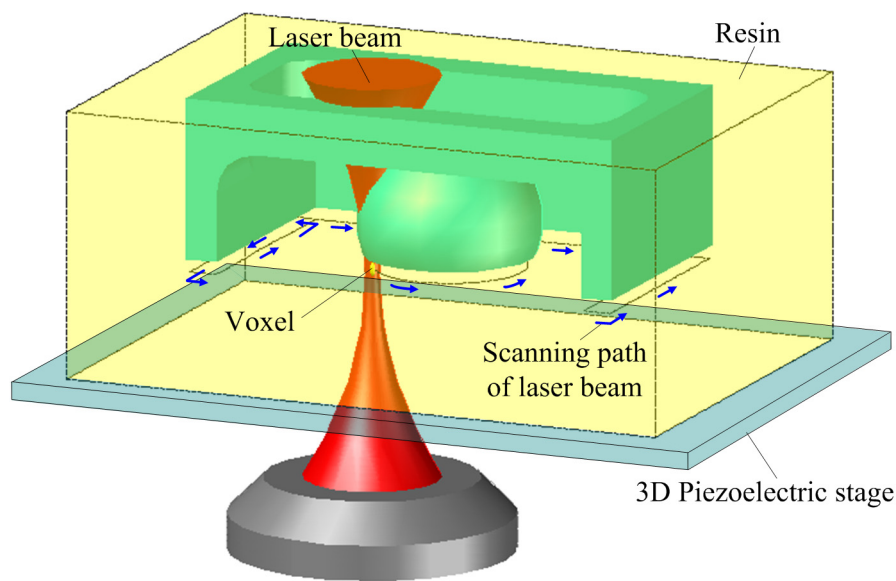


Figure 1-6 A schematic view of the TPP micro-manufacturing process and its major components.

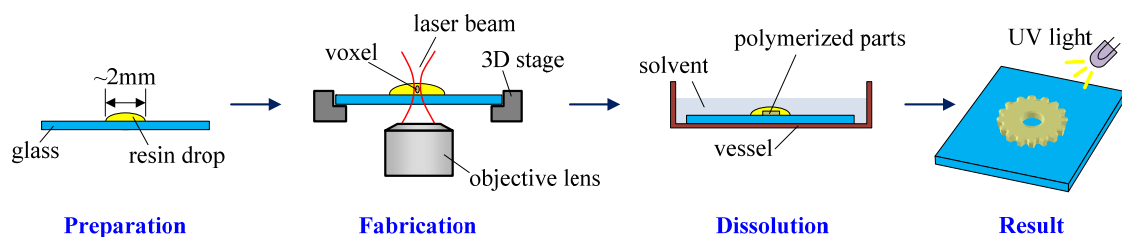


Figure 1-7 The TPP micro-manufacturing process from the life cycle of the resin viewpoint.

In most situations, to keep the polymerized microstructure after washing the resin, the microstructure needs to stick somewhere on the glass. However, for some micro-fluidic applications, the microstructures or their moveable parts are fabricated floating in the resin. After the dissolution process, they can be immersed in a solution and their positions and orientations can be controlled by optical tweezers (optical

trapping techniques) [Lin et al. 04, Maruo & Inoue 06, Lin et al. 06, Maruo & Inoue 07]. In a recent research [Park et al. 07], Park et al. proposed a contact print lithography technique which lets the microstructure fabricated by TPP be able to implant them as functional parts onto existing systems.

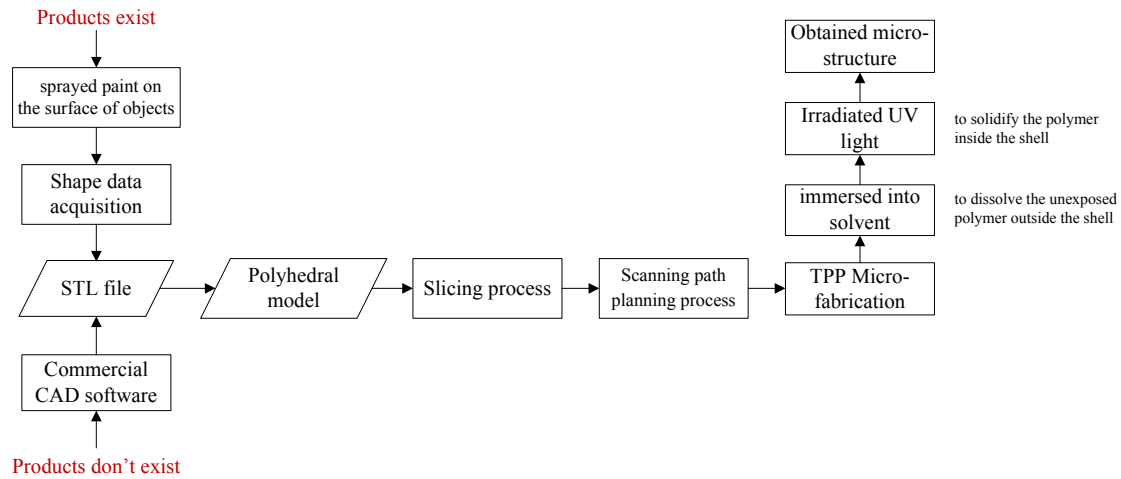


Figure 1-8 Overall process flow of the TPP 3D micro-fabrication.

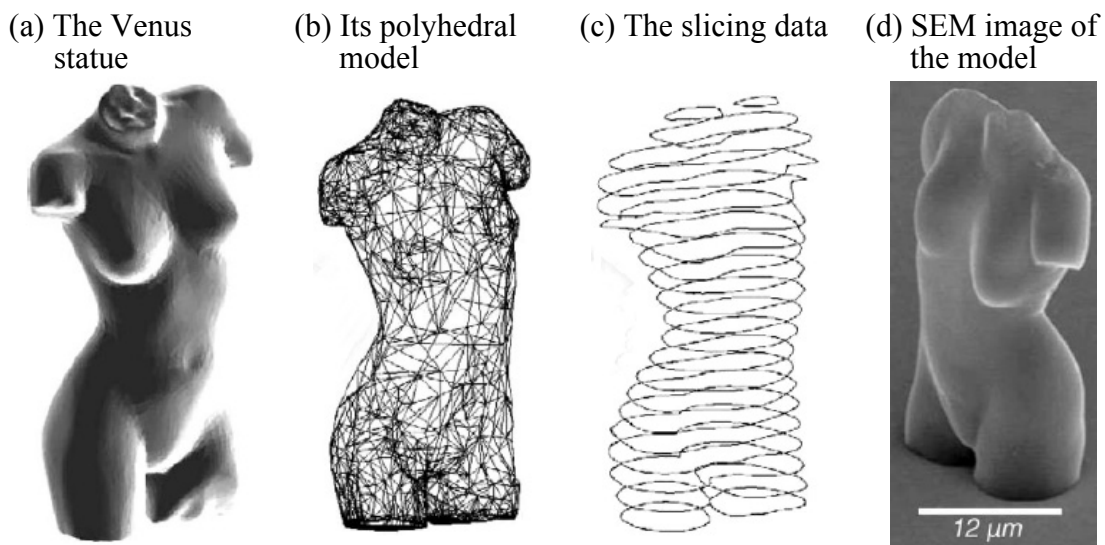


Figure 1-9 A typical case of TPP micro-fabrication [Wu et al. 06].

In general, when curves or simple 2D patterns parallel to the piezoelectric stage need to be fabricated with a TPP process, they can be produced by controlling this piezoelectric stage after all the control parameters have been set-up in the manufacturing environment [Wang et al. 02, Lim et al. 05]. To manufacture 3D micro-products, the concept of LM process introduced in section 1.3, also known as layer-by-layer method, is often used [Straub et al. 04]. Figure 1-8 depicts the overall process flow of a standard TPP 3D micro-fabrication process. Figure 1-9 shows a

typical TPP micro-manufacturing case found in the literature [Wu et al. 06]. The great benefit of a LM process is that the shape complexity of objects becomes relatively easy to handle. It is equally easy to fabricate a simple block or a complex object bounded by free-form surfaces.

Currently, the LM process used to produce standard mechanical components, at a macro scale, exhibits a high ratio regarding the acceptable minimum wall thickness over the minimum voxel size. Because of the effective manufacturability of the real component, LM, when used for RP, often produces a component made from an intermediate material applicable to the LM process to standardize this process and reduce the technological constraints set on it since the component functions don't need to be all materialized. When producing the effective object, both from the dimensional and material points of view, its structural behavior combined with the manufacturing techniques (machining, molding, ...) set minimum wall thickness constraints larger than the RP ones. Therefore, the described digital object is of type manifold and defines a solid object because the wall thickness of the model is effectively represented in its digital model.

1.1.5 Process flow of TPP micro-fabrication through the concept of product view

To more clearly comprehend the TPP development process of micro-products, the concept of product view is introduced hereunder. A Product View (PV) is attached to a task or a process, performed at least by one person, which is part of the overall product development process of a product [Hamri et al. 06]. The concept of PV is defined from a set of models needed to perform the given task or process of a product development process. A task is carried out in a product view called 'current PV' with input data/models coming from other product views designated as 'upstream PVs'. These upstream PVs deliver vehicular data which are not intrinsically linked to the 'current PV', and can be split into input shape and other product dependent data. In the present case, the addressed product view is the manufacturing preparation process of micro-products. Indeed in Figure 1-8, the polyhedral model, slicing process, and scanning path planning process belong to the current PV either as part of the input data or as more elementary tasks. An upstream PV could be a CAD modeller delivering a (Stereo Lithography) STL file or a process of shape acquisition delivering digital points.

The 'PV reference model' is a key input to the product development task performed in the current PV and is a core concept of the structure of a PV. The PV reference model of a product development task is generically designated as a 'PV simulation process'. The data only used in the current PV are called 'vernacular data'. The PV reference model is generated according to the vehicular data of the upstream PV

and the vernacular data of the current PV. Besides, the reference model generation activity contains all the shape changes needed to meet the requirements of the PV simulation process. These shape changes take place in the so-called PV Interface in during the PV reference model preparation. The PV simulation process is denominated that way to emphasize that these tasks are close to simulation processes in most stages of a product development process. For example, they can be product behaviour simulation, or manufacturing simulation processes, etc.

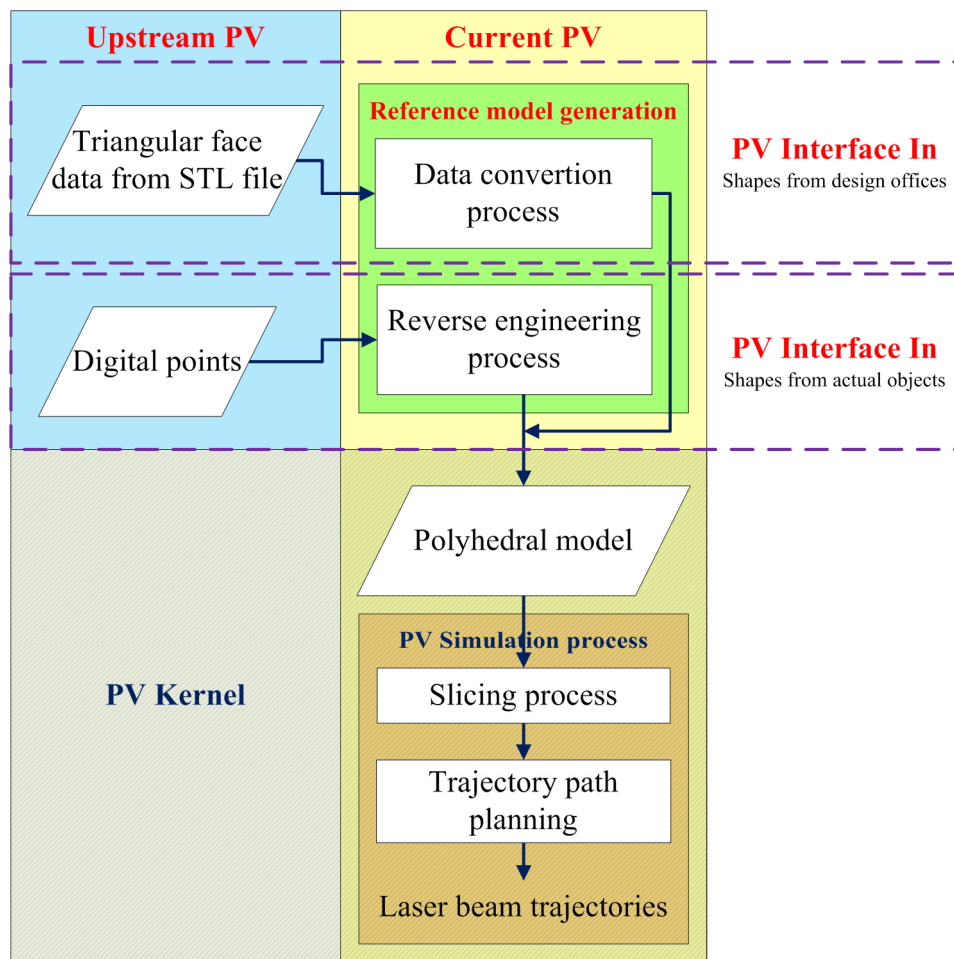


Figure 1-10 The product view of a generic preparation process for TPP 3D micro-fabrication.

In a generic product view structure of TPP micro-manufacturing preparation, the STL file conversion or model reconstruction can be considered as the reference model generation activities because both of them need to apply several shape changing operators to meet the requirements of the slicing process. Therefore, the PV simulation process is regarded as the laser trajectory simulation including the slicing and path planning processes.

Synthesizing the above explanations, the vehicular data of upstream PVs, the

vernacular data of the current PV and the processing for reference model generation are considered as the 'PV interface in' of the current PV since the tasks performed there use vehicular data and vernacular data only and are taken into account prior to the PV reference model. From the extent of the PV interface in, the functional structure of the current PV can highlight the PV kernel characterizing the objective of the current PV. The kernel elements can be globally reduced to the PV reference model and the PV simulation process where actors' know-how and knowledge are also critical to perform the desired simulation. Figure 1-10 depicts the product view of a generic TPP 3D micro-fabrication preparation process. With the concept of the product view, we can produce a generic model of the whole process of micro-manufacturing and further highlight its requirements in terms of models and model processing. It is also a mean to compare and synthesize the various approaches proposed to the manufacture of micro-products.

1.2 Analysis of existing approaches for TPP micro-fabrication

The aim of this section is to focus specifically on TPP micro-fabrication and to review the existing approaches as well as their ability to manufacture a wide range of micro-products.

1.2.1 TPP applications for families of micro-products

TPP has been used to fabricate 3D microstructures in numerous domains such as functional micro-machines, optical components, and biomedical micro-devices [Sun et al. 01, Cunningham et al. 06, Maruo & Inoue 06, Guo et al. 06].

For example, in biomedical applications, the main limitations of transdermal drug delivery systems arise from low permeability of the skin. Ovsianikov et al. fabricated arrays of hollow micro-needles by TPP to help overcome the barrier presented by the epidermis layer of the skin [Ovsianikov et al. 07], as shown in Figure 1-11.

Maruo and Inoue developed an optically driven lobed micro-pump using TPP micro-fabrication [Maruo & Inoue 06], as shown in Figure 1-12(a). Since the moveable micro-parts (no contact with the shafts) can be fabricated as floating in the resin because of the viscous force of the photopolymer, no supporting columns or layers, which are usually needed in general stereolithography process to fabricate the assembly components, are required during the TPP fabrication process. Figure 1-12(b) shows a micro gear-wheel affixed to a shaft [Sun et al. 00]. Other assembly configurations of microstructures can be found in [Maruo et al. 03a, Maruo et al. 03b, Maruo & Inoue 07].

- (a) Three cross-sections of original CAD models of micro-needles (b) SEM images of corresponding micro-needles fabricated by TPP

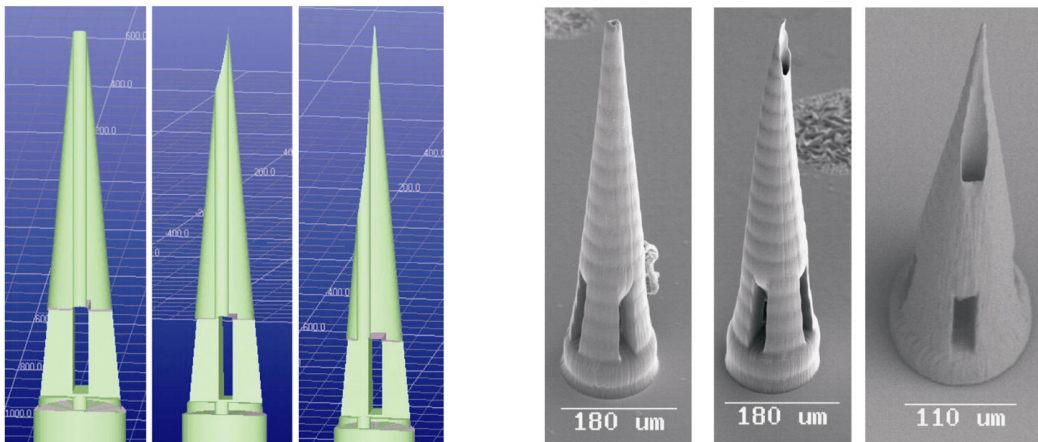


Figure 1-11 The TPP biomedical application: micro-needles with various tip sharpness [Ovsianikov et al. 07].

- (a) SEM image of a prototype of the lobed micro-pump [Maruo & Inoue 06]. The insets are the sequential SEM images which are taken while the laser drives the micro-pump. (b) A micro gear-wheel affixed to a shaft [Sun et al. 00].

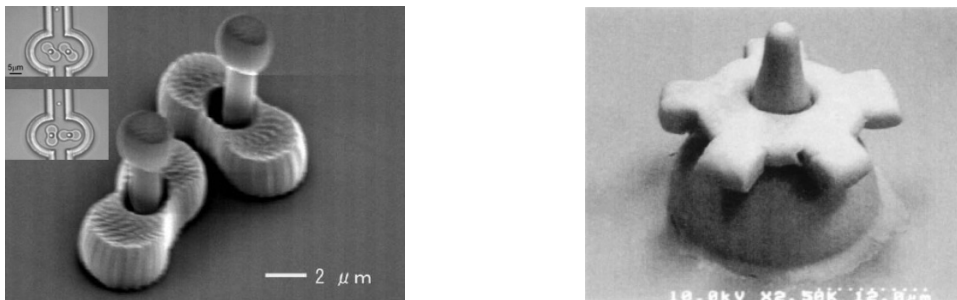


Figure 1-12 Assembly configurations of microstructures fabricated by TPP.

Knoll et al. reported a first concept of a mechanical micro-mixer [Knoll et al. 06], as shown in Figure 1-13(a). All the functional mechanical structures (two input oscillators, one output oscillator, the coupling, and the sensor) and the ‘T’-shape isolation wall were fabricated in one step.

Sun et al. made a micro-oscillator by TPP [Sun et al. 01], as shown in Figure 1-13(b). The diameter of the spring is 300 nm.

Jia et al. demonstrated the capability of the TPP method for fabricating high quality 3D Diffractive Optical Elements (DOEs) which refer to modulation devices for light field synthesis [Jia et al. 07], as shown in Figure 1-14. The 3D DOEs are encoded with gray-level information through the control of the voxel size and the thickness of each polymerized pixel, thus leading to the possibility of the intensity distribution synthesis.

- (a) Mechanical micro-mixer [Knoll et al. 06]. Two input oscillators: osc. 1 and osc. 2 are coupled to an output oscillator 'output'.
- (b) Micro-oscillator where the end bead was being trapped by a laser [Sun et al. 01]. The upper and lower insets show when the micro-spring is in its natural state and then pulled by a given length, respectively.

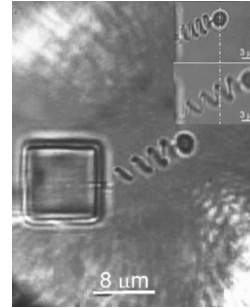
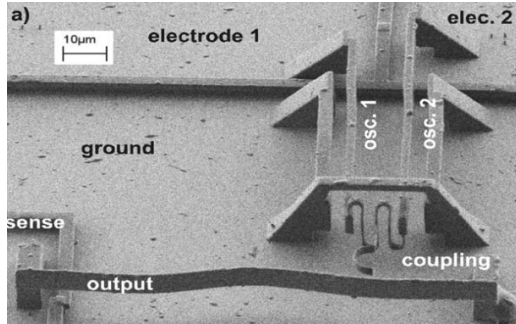
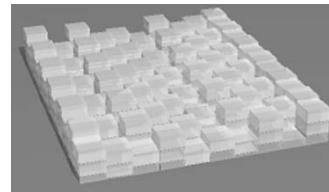


Figure 1-13 Functional microstructures fabricated by TPP.

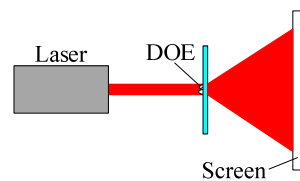
- (a) 2D intensity distribution of a Photo of the Sydney Opera House sampled by 128x128 points



- (b) Sketch showing an overall view of the designed DOE



- (c) Experimental setup for reconstructing the diffraction images from the DOEs fabricated by TPP



- (d) Reconstructed gray diffraction image of the Sydney Opera House

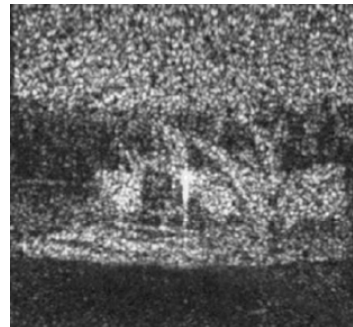


Figure 1-14 The gray-level encoding applications in TPP [Jia et al. 07].

1.2.2 Integrated manufacturing systems for the TPP process

Since the TPP micro-fabrication is an emerging technology, a CAD/CAM system completely suited for TPP process is still missing. As mentioned above, previous researches choose the layer-by-layer method to fabricate their 3D microstructures because this method is widely used for Rapid Prototyping (RP) macro products in the

industry and can be easily adapted to a TPP micro-manufacturing process. At present, few references related to the TPP manufacturing system exist. Two systems are introduced as follows.

Divliansky et al. developed an integrated software package for TPP micro-fabrication [Divliansky et al. 05]. This integrated system consists in a Micro-fabrication Path Planner (MPP) written in ANSI C++ and an Automated Control System (ACS) written in LabView 7.1. The targeted microstructure is first designed using industry standard CAD software, and then exported in the STL file format. The STL file is loaded and processed in the MPP, which uses a ray-triangle intersection algorithm to generate a set of raster lines that map the interior volume of the target structure. The set of sorted raster lines are exported to the manufacturing equipment as a control file that contains information about the starting and ending coordinates for each line, the shutter status during translocation of the sample, and the relative power at which voxels are to be written. The control file serves as the command input for the ACS.

The manufacturing system [Cunningham et al. 06] proposed by Cunningham et al. is similar to Divliansky et al.'s one. They used the RP software Materialise from Magics to slice the STL model and the CAD software AutoCAD to hatch 2D closed paths in each layer. The hatching density of the structure can be controlled by defining the fill pattern in AutoCAD, where choosing a tight fill pattern will directly correlate to denser polymerization.

Summarizing the above two systems, both use STL files as the source of the manufacturing model of a micro-product and use Raster Scanning Method (named RSM in this thesis and discussed in section 1.8.2) as a laser beam trajectory planning strategy. Using a STL file (discussed in section 1.5.1) format has the lowest system processing efficiency because topological information between faces is lacking. Besides, this file format can only represent volume objects, so that some complex treatments and interactive treatments would be needed to obtain a suitable model for fabricating objects combining volumes, open surfaces, or wires, and that kind of shape composition can satisfy a demand for fabricating smaller and smaller features in nano/micro technologies. As for RSM, it is not a good choice because the above limitations can greatly increase the fabricating time.

1.3 Layered Manufacturing (LM)

LM is a fabrication method whereby artifacts are generated by depositing material layer by layer under computer control. It complements existing (conventional)

manufacturing methods based on material removal and metal forming principles. In industry, LM is usually referred to as RP reflecting the most common use. It is used for the rapid fabrication of physical prototypes of functional parts (an important issues at the design stage), patterns for molds, medical prototypes (implants, bones), consumer products, and so on [Dutta et al. 01]. A unique feature of LM is its ‘direct’ fabrication capability—it does not involve tooling, fixture, and other peripheral activities associated with conventional manufacturing. The concept of LM process traditionally involves four steps:

- Creation of digital models of the desired products:

If the product already exists, then a shape acquisition system can be used to obtain digital data about its surface. Usually, to ensure the quality of the digital data obtained, some paint is sprayed over the surface of the product to generate uniform optical properties over the product surface. If the product does not exist, a CAD modeler can be used to create its digital representation,

- Transformation of the digital model of a product into facettted models:

The digital data obtained from scanning techniques or CAD models representing the product are transformed into facettted models through either a RE process or a tessellation procedure, respectively. In both cases, the product models are approximated by a polyhedral representation,

- Export of facettted models:

Most often, facettted models export under STL file format or other formats is necessary because the digital model of the product is generated in a software environment that cannot perform the manufacturing preparation phase. In addition, this export process is needed to get the digital model compatible with most of LM equipments,

- Fabrication preparation:

The facettted models are sliced with specific thicknesses to produce contour data of the product to define each layer. Then, the contour data can be used to compute the trajectories of material deposit and output these ones to manufacturing equipments.

1.3.1 Staircase effect and deposition inaccuracies in a LM process

In general, most of RP processes use LM method to fabricate an object by a sequential accumulation of layers with equal thickness. However, employing uniform

slicing can result in staircase effects and/or deposition inaccuracies [Luis Pérez et al. 01, Pandey et al. 03]. Figure 1-15(a) shows a staircase effect in an LM object with a uniform layer thickness. This inaccuracy reflects the deviation of the CAD model surface from the vertically built LM object. The error associated with the staircase effect can be quantified by considering the cusp height. The cusp height of a layer is the maximum distance measured along a surface normal between the shape of object and the layer. Uniform slicing typically results in an increase in the build time (if many thin layers are used) or a poor surface finish (when fewer thick layers are specified). In this article, we name the slicing process with uniform layer thickness as Single-dimensional Slicing Method (SSM).

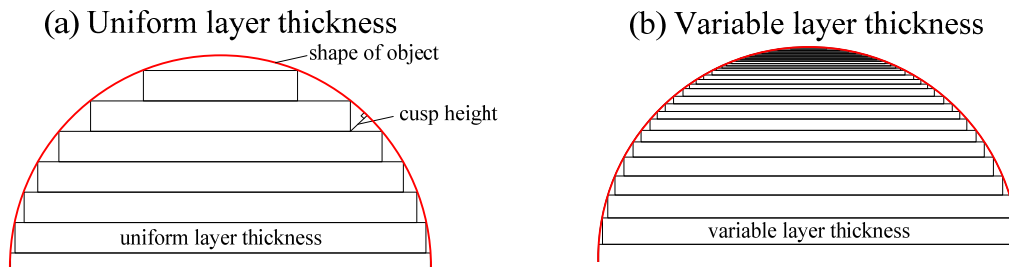


Figure 1-15 Staircase effect in a LM process.

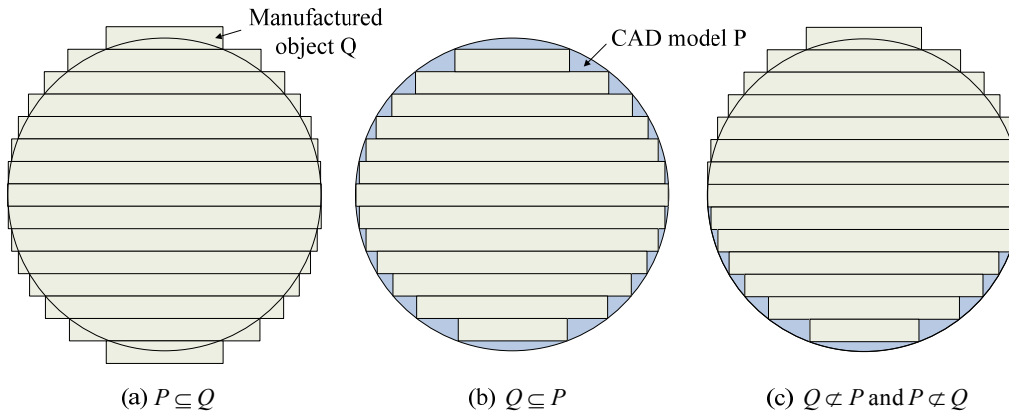


Figure 1-16 Deposition inaccuracies in a LM process.

An Adaptive Slicing Process (ASP) is desirable to decrease the fabrication time without drastically reducing the model accuracy in a LM process. The basic principle of adaptive slicing is to vary the layer thickness by evaluating locally the object shape characteristics. Figure 1-15(b) shows the concept of ASP. There are many references addressing the adaptive determination of the layer thickness [Kullarni & Dutta 96, Sabourin et al. 96, Luo & Tzou 04, Byun & Lee 06]. For example, Byun and Lee determine the layer thickness based on the facet that has the smallest angle between the facets to be sliced and the slicing plane [Byun & Lee 06]. Luo and Tzou compare the contour circumference or the center of gravity of the contour with those from the

adjacent layer to determine the layer thickness [Luo & Tzou 04].

Another inaccuracy is deposition inaccuracies, as shown in Figure 1-16. Between the CAD model P and the manufactured object Q , three situations can occur: (a) $P \subseteq Q$, (b) $Q \subseteq P$, (c) $Q \not\subseteq P$ and $P \not\subseteq Q$. Situation (a) implies extra volumes have been deposited by the LM process. This situation is referred to as excess of deposition. Situation (b) is referred to as deficient deposition and is useful if the LM object is to act, for example, as a master pattern for producing cores. Situation (c) is clearly undesirable. Depending on the micro-products, either the excess or deficient depositions could be used.

1.3.2 Other micro-manufacturing processes using LM technique

The 3D fabrication at micro size is more difficult than the one at macro/meso. Only few micro-manufacturing processes can operate at that scale, and most of them are additive processes and uses LM-like techniques with adaption to the micro-fabrication area.

In 1993, Ikuta and Hirowatari used the micro-StereoLithography (μ SL) technology to develop a first micro-RP system [Ikuta & Hirowatari 93]. Then, Zhang et al. improved its resolution from 5 μ m to 1.2 μ m [Zhang et al. 99]. The basic principle of μ SL is schematically shown in Figure 1-17(a). μ SL creates microstructures directly from a tank of UV curable solution by selectively solidifying the polymer by means of laser beam scans. Microstructures are built-up on an elevator platform which incrementally lowers the polymerized part into the vat by the distance of the layer thickness. To build each layer, a laser beam is guided across the surface to draw a cross-sectional pattern in the x-y plane to form a solid section.

In contrast to ‘drawing’ out each cross-section with laser photolithography, it is possible to image an entire cross-section in a single operation using photo-masks. Thian et al. presented a micro-fabrication technique using LM technique combined with mask-based micro-lithography, which is commonly used in the semiconductor industry [Thian et al. 06]. When the laser beam passes through a photo-mask, the laser beam is regulated into a special shape and the shape size can be reduced to a smaller scale with the use of an objective lens, as shown in Figure 1-17(b). This is more efficient than μ SL. The remaining procedure in mask-based micro-lithography is very similar to μ SL.

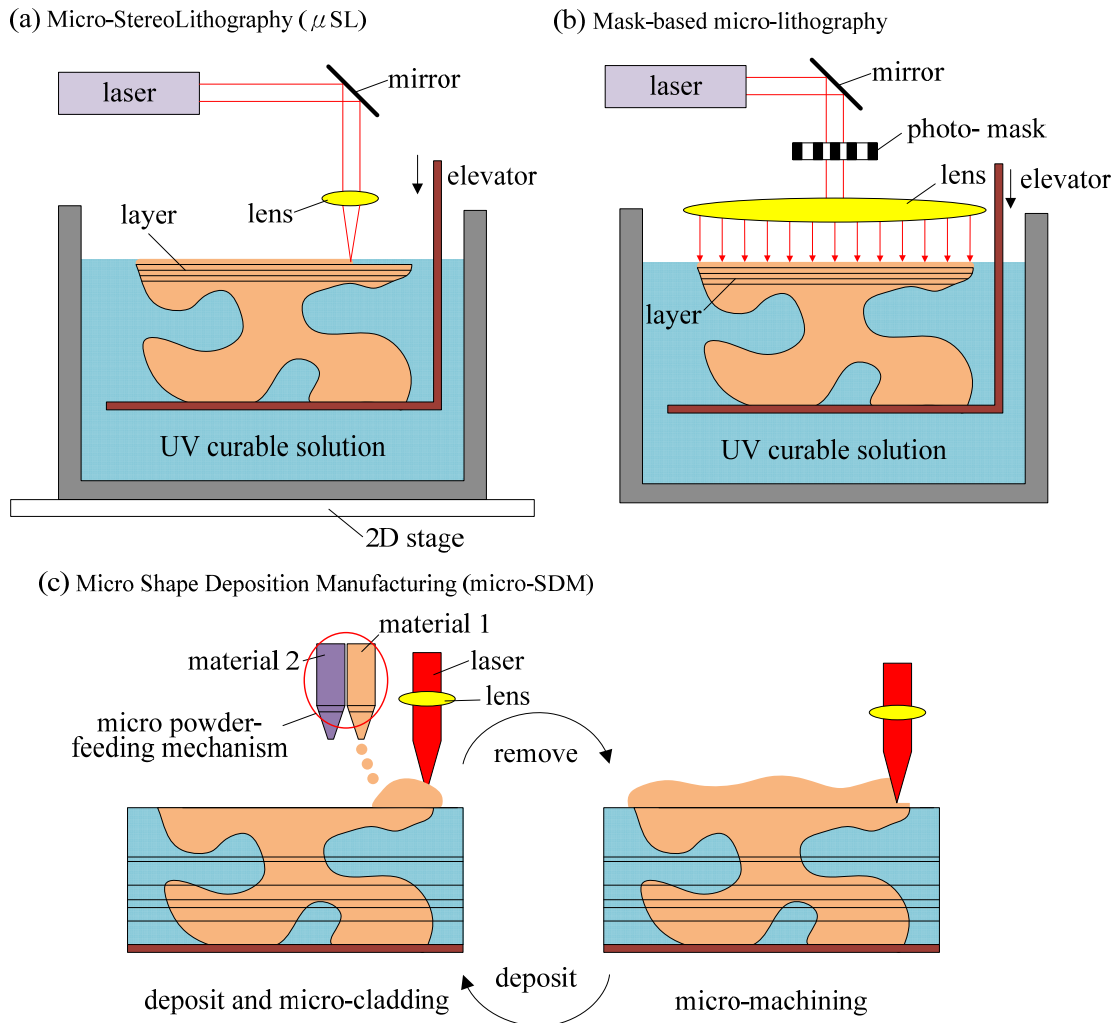


Figure 1-17 Other micro-manufacturing processes using LM technique.

Li et al. developed a micro rapid prototyping system that adapts Shape Deposition Manufacturing (SDM) methodology [Li et al. 02], one of the RP processes, to micro-fabrication. The manufacturing cycle for the micro-SDM process is depicted as shown in Figure 1-17(c). A pulsed laser is controlled spatially and temporally to obtain precise micro cladding and machining. In addition, a micro-powder feeding mechanism is used to lay down micro/nano powders. Since SDM can lay down multi-materials, the micro-SDM system derived from SDM could reproduce 3D heterogeneous micro-components from a wide selection of materials.

The μ SL and mask-based micro-lithography are the technologies based on SPA to induce polymerization. However, SPA doesn't have optical sectioning capability (see section 1.1.1) and it is difficult to control both the polymerized location and depth precisely. Therefore, the resolutions of μ SL and mask-based micro-lithographies (1~30 μ m [Ikuta & Hirowatari 93, Zhang et al. 99, Thian et al. 06]) are larger than TPP (less than 100 nm) and their working areas are localized on the surface of UV curable

solution. As for micro-SDM, the resolution is directly constrained by powder size (normally larger than $50\text{ }\mu\text{m}$), so its resolution (larger than $120\text{ }\mu\text{m}$ [Li et al. 02]) is much larger than the TPP one. Besides, the all three processes are mainly two-and-half-dimensional ($2\text{D}^{1/2}$) manufacturing techniques. Because TPP can induce polymerization at extremely small spots anywhere in the resin, its associated fabrication principle is not bound to the LM process, and can be a truly 3D manufacturing. Therefore, extending the capabilities of TPP micro-fabrication over the classical $2\text{D}^{1/2}$ approaches is a contribution addressed by this thesis.

1.4 Geometric representations for a product model

Throughout a product development process, different shapes of the product are required to support the various product views. The purpose of this section is to review the main categories of product shape descriptions that may be of interest in the context of a Product View devoted to a micro-manufacturing preparation process where input data or shape may vary significantly from existing objects to designed ones. Among the variety of shapes encountered, they can be categorized as:

- Geometric manifolds, i.e. lines, surfaces, volumes, of dimension d_m placed in a Euclidean space dimension d_E with $d_m \leq d_E$. As an example, a line ($d_m = 1$), can be placed in 3D space ($d_E = 3$). A d_m manifold is a topological space where every point has a neighborhood topologically equivalent to an open disk of the Euclidean space of dimension d_m ,
- Non-manifold objects when they are seen as a connection of manifold shapes glued together at key locations in such a way that they lose the topological equivalence of the point neighborhoods. Point neighborhoods can be formed either of half disks of different dimensions d_m or with a number of half disks strictly larger than two, which is the requirement to define manifolds with $d_m = 1$ (lines) or $d_m = 2$ (surfaces).

Mostly, during a product development process, solid shapes, i.e. closed volume representations $d_m = 3$ in 3D space ($d_E = 3$), are common for manufacturing purposes. Non-manifold shapes are less frequent with B-Rep NURBS (Non-Uniform Rational B-Spline) models due to the modeling capabilities of the commercial CAD software and the objectives of the modeling task, which are generally centered on defining a component shape for conventional manufacturing at macro-scale. Non-manifold shapes are much more common for Finite Elements (FE) models or other component behavior simulation models or at early design stages where the overall component/product shape cannot be entirely specified.

1.4.1 Boundary representation (B-Rep)

In the Boundary representation scheme, the solid objects are represented by the surfaces representing their boundary. The object surface is then divided into a collection of faces, which are bounded by edges and vertices. The division in faces is performed so that the shape of each face has a compact mathematical representation, e.g., that the face lies on a single planar, quadratic, toroidal, parametric surface [Mäntylä 88]. This division reflects the shape construction process as conducted by a designer rather than a functional decomposition in accordance to product function or manufacturing operations.

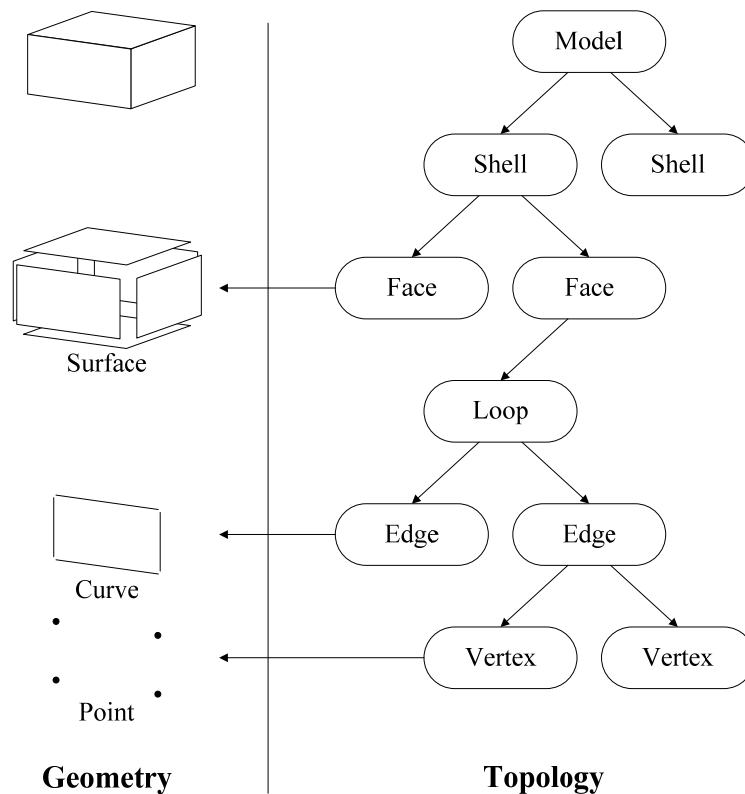


Figure 1-18 Graph representation of a face-based B-Rep data structure.

B-Rep uses a collection of 2D topological entities, called faces, properly connected and consistently oriented, to define volume boundaries. Each face is bounded by loops and is embedded on one 3D surface. Each loop is a sequence of edges, properly connected to form a simple oriented closed 3D contour. Each edge is the topological representation of an open or closed curve, embedded in one curve and bounded by two vertices, possibly coincident depending on the variants of B-Rep scheme set up in a modeler. In addition, a shell is defined as a collection of faces whose union is a connected 2-manifold with boundary. Figure 1-18 shows the diagram of such a

hierarchical structure to describe the topological relations between faces, edges, vertices to form shells and a volume.

The main drawback of such a representation is the difficulty of obtaining a meaningful decomposition of an object surface containing a set of functional elements, manufacturing entities, ... and most B-Rep modelers use a starting point based on primitive volumes only, which don't help much when objects are partially defined. The most important advantage of such a representation is the flexibility of shape modeling and the possibilities of local modification to refine the component shape.

Connection relationships among these topological entities are referred to as topology or topological structure of an object and their underlying geometries is referred to as geometric representation. A B-Rep model is valid if its faces form a 2-manifold, that is, a surface where every point has a full 2D neighborhood, i.e. a disk of the surface. The validity criteria of a B-Rep model include the following conditions [Mäntylä 88]:

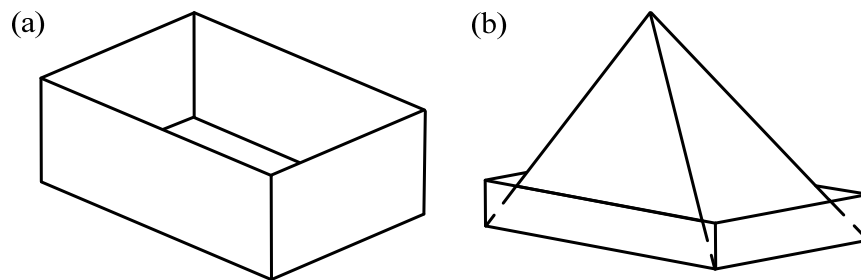


Figure 1-19 Invalid B-rep models.

- The set of faces 'closes', i.e., forms the complete skin of the solid with no missing parts,
- Faces do not intersect each other except at common vertices or edges.
- The boundaries of faces are simple polygons that do not intersect themselves.

The first condition disallows 'open' objects such as the 'open box' in Figure 1-19(a). The second and third conditions exclude self-intersecting objects such as the object of Figure 1-19(b). The bottom surface of the pyramid-shaped object intersects its top surface.

1.4.2 Non-manifold representation

A non-manifold representation removes the constraints associated with manifold solid modeling systems by permitting the coexistence of wireframe, surface and solids

in the same object and hence provides the ability to represent models of mixed dimensionality.

As a simple approach to non-manifold shapes, connections between volumes, surfaces, lines, generating non-manifold shapes can be characterized locally through point neighborhoods. The classical local characterization can be reduced to the notion of topological half disks around a point. This concept is also combined with the notion of dimension of geometric manifold describing the corresponding shape. If the concept of topological half-disk is applied at a surface point, the manifold dimension equals 2, $d_m = 2$, and there is effectively at least one half-disk around that point. If the concept of topological half-disk is applied at a line point, the manifold dimension equals 1, $d_m = 1$, and the topological half-disk becomes a half-segment. Based on these concepts, manifold configurations describing volumes or open surfaces can be listed as follows:

- if every surface point of a shape possesses a neighborhood defined by two half-disks, then the object surface is closed and may define a volume. The object is a geometric manifold with $d_m = 2$,
- if there exists some surface point of a shape where its neighborhood is defined by one half-disk only. The object is an open surface.

Shapes become non-manifold when there exists at least one point, and its neighborhood equivalent to more than two half-disks or two half-segments or any combination incorporating at least one half-disk and one half-segment.

The term ‘non-manifold’ is used because non-manifold models relax some of the topological correctness criteria for 2-manifold B-Rep models, in particular those requiring that:

- All the edges separate exactly two faces,
- All the vertices are surrounded by a single circuit of faces.

This latter condition holds for the model in Figure 1-20(a), where three types of vertices can be distinguished:

- Vertex (\mathbf{p}_1) lies in the interior of a face and its neighborhood consists in a disk,
- Vertex (\mathbf{p}_2) is an extremity of some edges, and its neighborhood is equivalent to a disk,
- Vertex (\mathbf{p}_3) is interior to an edge and its neighborhood consists in two half disks.

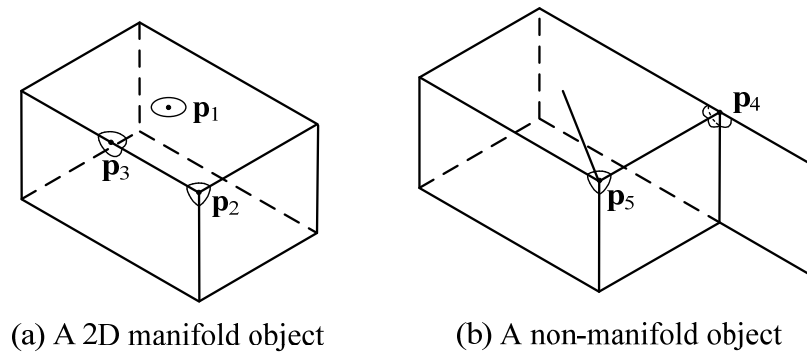


Figure 1-20 Manifold and non-manifold configurations.

In a non-manifold model such as the one shown in Figure 1-20(b), other types of point neighborhoods exist such as:

- Vertex (p_4) is an extremity of some edges, and its neighborhood is topologically equivalent to three half disks. Therefore, this configuration is non-manifold,
- Vertex (p_5) is also an extremity of some edges. In this case, its neighborhood is equivalent to a disk and a half segment, so this configuration is non-manifold too.

The non-manifold representation can be of B-Rep type and allows the designer to describe a wider range of shapes but the modeling operators available and their corresponding properties or not comparable to that of volumes with the generalized Euler theorem and the Euler operators.

1.4.3 Polyhedral representation

Solid models are often approximated by polyhedrons (or sometimes convex polyhedrons) for simulation or visualization purposes (see Figure 1-21). Polyhedrons can be regarded as piecewise linear surfaces and, as such, can be also considered as a particular category of B-Rep models. This is because graphics libraries and hardware graphics accelerators can render such simple shape primitives very fast. When the polygons are all of the same type, for example, all quadrangles, or all triangles, the B-Rep is called a tessellation. Tessellations with triangular faces are called triangulations. Arbitrary polygonal faces are decomposed into triangles and curved surfaces are approximated by triangulations, which may automatically adapt their resolution so as to guarantee the desired accuracy. A triangulation is also a B-Rep model where the faces are triangles and the edges are line segments.

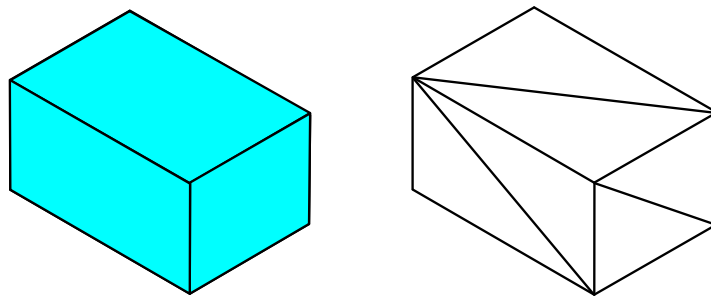


Figure 1-21 Solid B-Rep NURBS model and its approximation (B-Rep triangulation).

Triangulating trimmed surfaces requires combining the 3D surface tessellation with the triangulation of the face representation into the 2D parameter space of the surface. The implementation of such triangulations must ensure that the triangulations of any two adjacent faces do not generate gaps, which would occur if the two triangulations were used to produce different piecewise linear approximation of the common edge of the two faces [Rossignac & Requicha 99].

Most of the time, the common edge of two adjacent faces is parameterized in different ways according to the (u, v) parametric space of each face, and their approximations, for example by splines, are often used. This can cause delicate numerical problems, because points on this curve do not necessarily lie on the surfaces whose intersection creates the edge. Approximate representations in the parametric spaces of the involved surfaces are even more pernicious, because each edge is represented twice, one for each face the edge is attached to and these two representations do not coincide exactly. However, conform triangulations can be generated both for B-Rep NURBS models when their topological data structure is available and from scanned data with RE applications as a first digital model of an existing object.

The validity conditions for a triangulation (polyhedral representation) scheme are as follows [Requicha 99, Agoston 05]:

- Each face must have three edges,
- Each edge must have two vertices,
- Each edge must belong to an even number of faces. If we restrict the domain to manifold polyhedrons, an edge has to belong exactly to two faces,
- Each vertex of a face must belong to precisely two edges of the face,
- All points must be distinct,

- Edges must be either disjoint or intersect at a vertex,
- Faces must be either disjoint or intersect at an edge or a vertex.

These conditions are easy to establish intuitively, and can be derived mathematically. Conditions 1-4 are combinatorial or topological. They are easy to check algorithmically by counting nodes or links in the graph structure representing the object boundary. In contrast, conditions 5-7 are metric, i.e. they involve coordinates of vertices and equations of lines and planes. They are computationally expensive to check and, for this reason, are often left apart by modelers because they require numerous intersection tests.

1.5 Major data exchange formats

During a product development process, it is often necessary to extract shape models from one product view software environment to insert this shape into another product view. There, the shape or model exchange formats are the critical issue that needs to be addressed to obtain an efficient process flow where shapes can be seamlessly transferred between product views. This is the reason why this section is devoted to the analysis of the major exchange formats encountered in RP, RE, CAD, ..., that can be of interest in the context of micro-manufacturing.

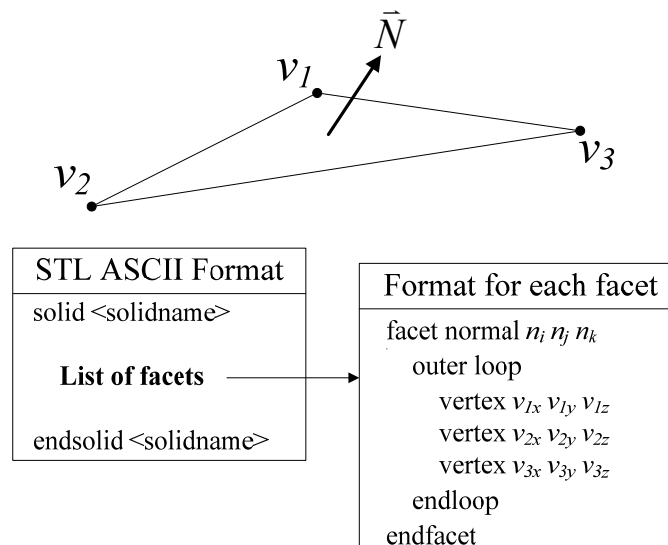


Figure 1-22 Structure of the STL format.

1.5.1 Stereo Lithography (STL)

The STereoLithography (STL) format, developed by the Albert Consulting Group, was put forth by 3D Systems in 1987 and has since become the *de facto* industry

standard, especially in RP [Dutta et al. 01]. The STL format describes the boundary of a 3D object by a list of triangles, i.e., a faceted representation, and each triangle is described by its three vertices and outward pointing normal. The STL format is illustrated in Figure 1-22. As the STL format stores the vertex list for each triangle explicitly, the edges of the triangle are defined implicitly. In any case, the data are ordered, traversing along the boundary according to the listed vertices.

With respect to the LM process, the STL format has the following advantages [Kumar & Dutta 97]:

- Easy conversion and wide range of input software:

Arbitrary shapes of 3D geometry can be simply converted to STL models due to the standard triangulation algorithms which are very robust and used frequently in computer graphics, RE or Finite Element Analyses (FEAs). Also, the accuracy of the output model can be easily controlled by triangulation algorithms and the degeneracy that could occur is minimal.

- Simple slicing algorithm:

The algorithm for slicing a STL model is usually simple (but not necessarily efficient and robust) as it only involves processing a list of triangles compared to parametric surfaces processing. All operations on a triangle are simple and accurate.

Despite the above-mentioned advantages, the STL format also has the following drawbacks [Kumar & Dutta 97]:

- Verbose:

A STL file is verbose and has redundant data. The storage of facet normal is redundant as this can be obtained by accessing the vertex list of each triangle in a specific order. Also, specifying the vertices of each triangle is not required as each vertex appears in more than one triangle.

- Approximation:

A major problem with STL is in its representation of curved surfaces, which can only be approximated by the triangular facets. This may be of particular interest when a shape, represented with a NURBS model, transferred among product views doesn't need to be converted into another representation. There, the need to convert a NURBS model into a faceted representation produces an unnecessary approximation. In addition, a large number of triangles can yield a high accuracy in approximation, but would result in an

extremely large file. A smaller number of triangles would create an efficient file but would lack accuracy.

- Truncation:

An original CAD model is often represented with double precision numbers and will be converted to single precision while generating the STL data. Hence, with the absence of topological information in the STL model, truncation errors may become significant and lead to models that don't conform to the input one.

- Lack of topological information:

The original 3D models created by commercial CAD softwares, in general, contain the complete information regarding geometry, topology and eventually, some information about their constitutive material. When converting such models to STL format, only the basic geometrical information is stored, neglecting the topological information. Indeed, this information could be used in downstream processing such as selecting the orientation of the matter or analyzing the model for support creation when a model is processed for RP. Even though the STL file format can contain a non-manifold object, processing such models based on their geometric description only becomes ambiguous. Whether for manifold or non-manifold models, the lack of topological information severely reduces the efficiency and robustness of the STL format.

Since there is widespread limitations with the STL format, efforts are needed in the receiving applications either to develop additional operations performed on the STL model to guarantee the correctness of the model [Zhang et al. 02] or to leave the STL shape description and directly develop new representation schemes and data formats [Qian & Dutta 98, Patil et al. 00].

1.5.2 STandard for the Exchange of Product model data (STEP)

In 1993, STEP (STandard for the Exchange of Product Data) became an international standard for the description of physical and functional characteristics of product data. The standard is formally known as “ISO 10303 Industrial automation systems and integration - Product data representation and exchange”. STEP is designed to support a product through its entire life cycle, as shown in Figure 1-23. Therefore, STEP standard is published in a series of parts which include the following ones: Description Methods, Integrated Resources (IRs), Application Protocols (APs), Abstract Test Suites, Implementation Methods and Conformance Testing [SCRA 06]. Among

which, STEP uses APs to specify the representation of product information for one or more applications associated to a particular engineering domain or a particular product view or set of product views. For example, the AP that defines the information model for the exchange of parts and assemblies as well as for design configurations, optionally with associated 3D geometry is called Configuration Controlled Design, AP203. It covers the generic framework of product design in a mechanical engineering context. Since STEP does not have an AP for LM at present, Patil et al. used the EXPRESS language, a part of the STEP standard, to develop an information model for heterogeneous objects which is one of blazing subjects in LM [Patil et al. 00].

The ability to support many application protocols, i.e. to cover different and partly overlapping areas, within the same framework is one of the key strengths of STEP. All the APs are built on the same set of IRs so they all use the same definitions for the same information. For example, AP-203 and AP-214 (Core Data for Automotive Mechanical Design Processes) use the same definitions for 3D geometry, assembly data and basic product information. Therefore, CAD vendors can support both with one piece of code for their common data.

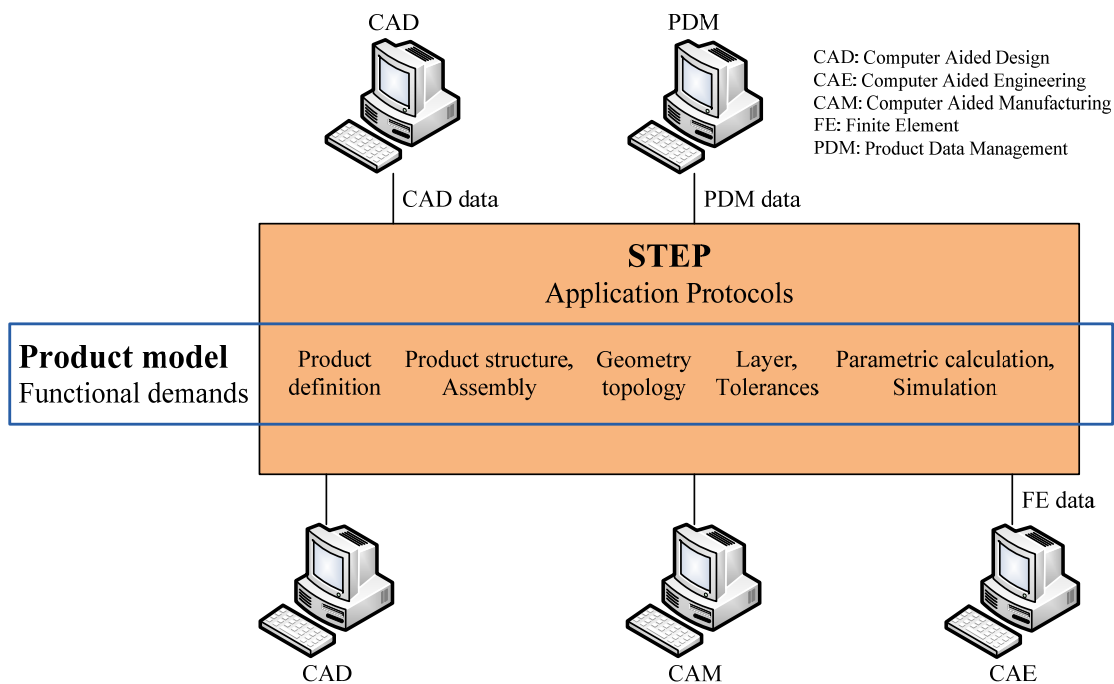


Figure 1-23 STEP application area within the product life-cycle framework.

Another key strength of STEP is its extensibility. This extensibility is the result of the decision to base STEP on an information modeling language called EXPRESS. STEP uses EXPRESS to represent the information and its structure. The STEP APs standards and EXPRESS are important to the design and manufacturing communities

for several reasons [Loffredo]:

- The standard contains a large body of definitions for engineering data. The scope of the definitions includes mechanical and electrical CAD, manufacturing processes, and specialty domains such as composite materials and shipbuilding,
- The EXPRESS language defines constraints as well as data structures. These constraints contribute to a correctness standard that must be met before an engineering data set is sent to any other application,
- The standard defines a logical description that is technology independent of any software and any operating system,
- The standard allows engineering applications to exchange information about products and process designs.

Nearly every major CAD/CAM system now contains a module to read and write data defined by one of the APs. So, data exchanges can be performed among different computer softwares and environments associated with the complete product life cycle including design, manufacturing, utilization, maintenance and disposal. In CAD softwares, the major AP of STEP used to transform the shape information of products is AP 203. AP 203 defines the data structures for representing product shapes as well as assembly information. For example, AP 203 covers five types of geometric shape representations [SCRA 06]:

- Wireframe and surface representation without topology,
- Wireframe representation with topology,
- Manifold surface representation with topology,
- Faceted boundary representation,
- Boundary representation.

Compared to STL, AP 203 has the advantage of providing various geometric shape representation as well as topology information. In addition, it has been experimentally observed that most of the CAD software providers are able to exploit STEP such that a B-Rep NURBS model of a shape is produced simultaneously with the description of the analytic surfaces (planes, cylinders, spheres, ...) that may be contained in that shape.

However, STEP still suffers of limitations regarding shapes represented as non-manifold models as it is often needed for FEAs since such models are not part of the standard. Similarly, experiments of shape exchange has revealed that the model accuracy which is attached to a STEP model during the file generation phase is hardly

used by the receiving software, hence reducing the robustness of the shape exchange process.

1.6 CAD model of components obtained through a reverse engineering process

Reverse Engineering (RE) is a technology that enables us to generate a computerized representation of an existing object based on point-based data acquired from the object's surface. Such an approach can be useful in many configurations [Huang & Tai 00, Woo et al. 02]:

- When the clay model of a product is created by an artist and a CAD model of this object is needed, capturing the digital shape of this object is of prime interest;
- When a sample component exists without its original drawing or documentation definition;
- When the CAD model representing the part has to be revised because of design changes during manufacture that was not inserted in its digital representation.

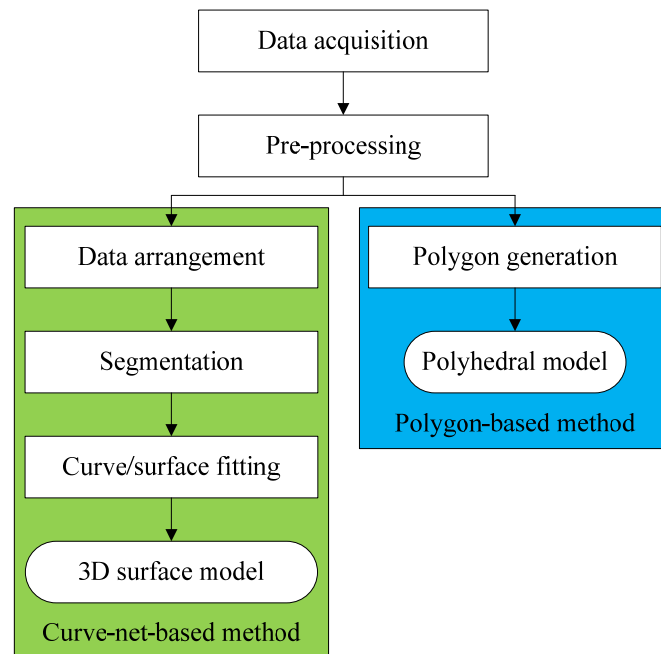


Figure 1-24 Different process flows for reverse engineering a component.

In the framework of the present contribution, RE acts as one mean for acquiring the shape of possibly complex micro-products, thus justifying its review in the present section. The typical RE process begins with collecting point data from the surfaces of a

physical object. The initial digital data acquired by a shape measurement system generally require pre-processing operations such as noise filtering, smoothing, merging and data ordering in order to be useable in subsequent operations. Using the pre-processed point data, a surface model or polyhedral model can be generated either by curve-net-based methods or polygon-based ones, as it is depicted in Figure 1-24.

The curve-net-based method is more commonly used in industry because it is able to produce a NURBS-based model, which can be straightforwardly input into a CAD software. After a part is scanned, the acquired point cloud should be divided into several smooth regions for surface-fitting purposes [Huang & Menq 01, Woo et al. 02]. Then, a surface model, usually a NURBS model, is created. The polygon-based method is fast and efficient in fitting surfaces; however, it generates less smooth and less accurate surface models than those of the curve-net-based method and it may be also difficult to modify the final model because transformations can be applied to vertices only with very basic operators [Várady & Benkő 00], which requires numerous low level operations. The polygon-based method is usually used in applications of animation and arts.

In RE, traditional methods for capturing object shapes can be generally classified into two broad categories: contact and non-contact measuring methods [Várady et al. 97], as shown in Figure 1-25. With contact measuring methods, the measuring sensor is usually a probe or a stylus, and there is a direct contact between the sensor tip and the object surface. Non-contact measuring methods use light as the main mean in acquiring object shapes.

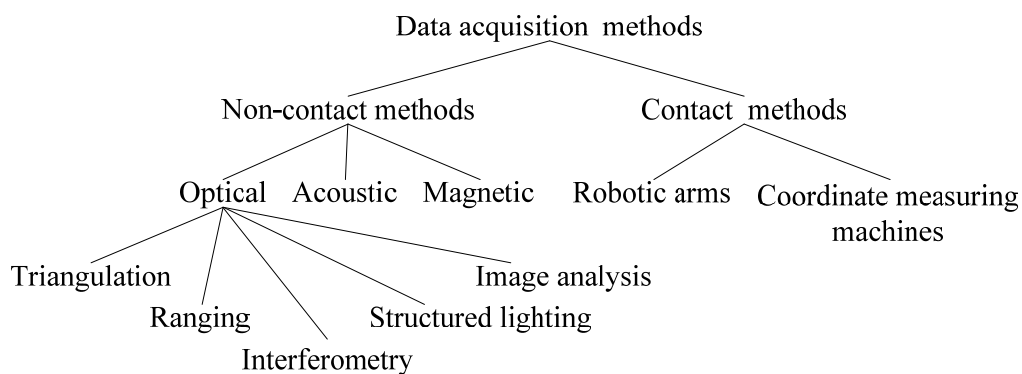


Figure 1-25 Classification of data acquisition methods.

Optical methods for shape capture are probably the broadest and the most popular ones with relatively fast acquisition rates. As with a laser digitizer, structured light is used for capturing the shape data of objects. Since the laser light is very sensitive regarding the reflection characteristics of object surfaces, in order to obtain consistent reflection rates of object surfaces, either red or white paint can be sprayed over the

surface of colored objects, but it causes the perpetual destruction of object's brilliance. Such a technique is unacceptable if the object is invaluable and unique.

In addition, current contact or non-contact measuring methods can only acquire object's 3D shapes. No intrinsic color information of objects can be included during the acquisition phase. There is few literature discussed about how to reconstruct the color model of physical objects [Niem 94, Niem & Broszio 95, Niem 99, Xu et al. 02, Albamont & Goshtasby 03]. However, 3D models without color information don't satisfy the requirements of demonstration in terms of realism. In modern visual applications, such as computer animation, online shopping, digitization of antiques, advertisements, etc., 3D models with color information are required. Furthermore, through some imaging techniques, such as texture mapping, the color information can be incorporated into a 3D shape model to produce a set of 4D data, i.e. x , y , z , and *color*. These 4D data can provide the appropriate input data for RP or TPP micro-manufacturing to fabricate the object with its color, in the future. In the scope of TPP, manufacturing components with different colors has been already addressed [Jia et al. 07], which justifies the interest of this RE approach in the present context.

1.7 Texture mapping a component

Texture mapping, in its simplest form, consists of applying a graphics image, a picture, or a pattern to a surface. For example, a texture map can map an actual picture to a surface such as a label on a can or apply semi-repetitive patterns such as wood grain or stone surfaces. Except color information, texture mapping also uses other surface parameters to define the mapping function between a polyhedral surface and a texture. These include the perturbation of surface normal vectors to simulate bumpy surfaces (bump mapping), transparency mapping to modulate the opacity of a translucent surface, specular mapping to vary the glossiness of a surface, and illumination mapping to model the distribution of incoming light in all directions [Carey & Greenberg 85, Buss 03].

Although texture mapping has versatile applications, this thesis focuses on texture maps that are mapped onto surfaces of 3D models. The process of texture mapping can be subdivided into two steps [Niem & Broszio 95, Niem 99], as shown in Figure 1-26. The first step is called parameterization, where a 2D texture space is mapped onto the 3D model space, i.e. a mapping function is established to map a specific area of a texture map onto each triangular mesh of the object's surface. The second step is called the viewing projection, where a 3D model space is mapped onto the screen space. By varying the viewing directions, arbitrary views of the parameterized model can be obtained. The detail process of the viewing projection is not investigated in the present

work.

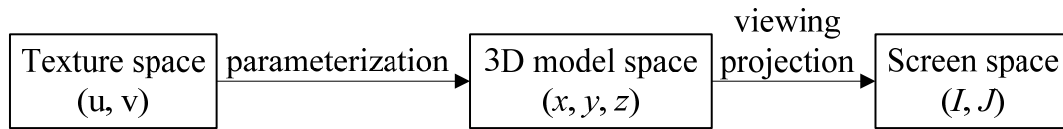


Figure 1-26 The relationships between texture space, 3D model space, and screen space.

A CCD camera is frequently used to capture color texture maps of an object surface. The texture mapping from multiple camera images leads to the following problems:

- Distortion of textures at the boundaries of triangles which are textured with different images, as shown in Figure 1-27. This can occur in case of errors in the model shape or the camera parameters or not good enough illumination conditions,
- Surface parts of the real object that are not visible, i.e. areas which cannot be observed from any of the camera views.

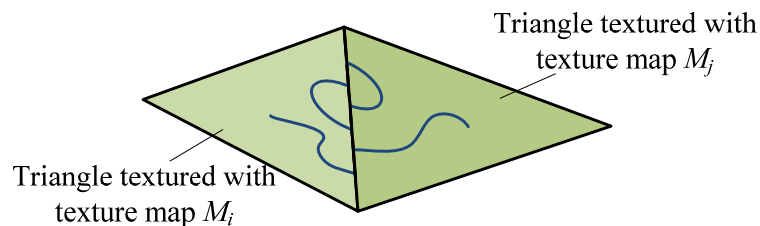


Figure 1-27 Distortion of a texture at the boundaries of triangles when they are textured with different images.

1.8 Simulation operations for TPP micro-fabrication

Here, the objective is to review the basic concepts from low level to high level operators that take part to the preparation process of a micro-product fabrication.

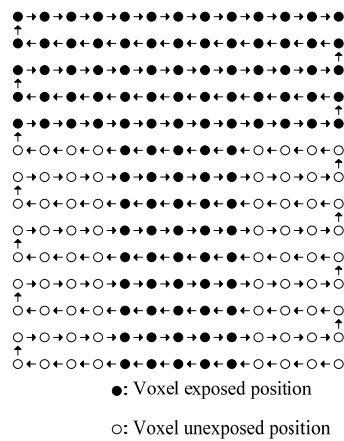
First of all, the basic operators contributing to the elementary treatments needed during the TPP micro-fabrication preparation process are described since they form the core operations needed for laser path planning. Then, current laser path planning strategies are reviewed to evaluate their current advantages and limitations.

1.8.1 Basic intersection algorithms

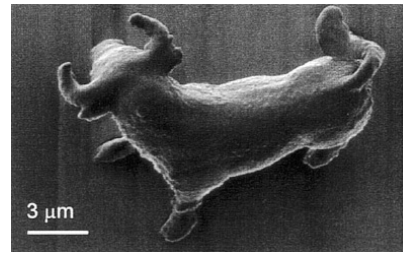
Generally, an intersection operator is applied to obtain the needed contour data of a

product model as one step of a micro-fabrication preparation process when it is based on a LM principle. The contour data is composed of a sequence of intersection points obtained when intersecting a micro-product model with a series of virtual planes. This procedure is also called the slicing process, and the virtual planes are named the slicing planes. The appendix A introduces the basic principles of intersection algorithms such as the intersection between 3D lines/segments [Sunday b], the intersection of a plane and a 3D segment [Sunday b], and the intersection of a triangle and a plane. These principles will be used in section 4.2, 4.4 and 4.5 to obtain the contours of micro-products for the laser beam, weld lines, and the offset paths of contours.

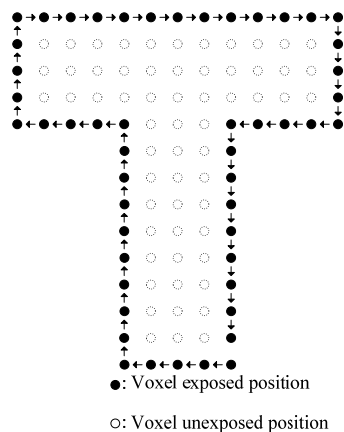
(a) Raster scanning method



(b) SEM image of a micro-bull structure using RSM [Sun et al. 03a]



(b) Contour scanning method



(d) SEM image of a micro-bull structure using CSM [Sun et al. 03a]

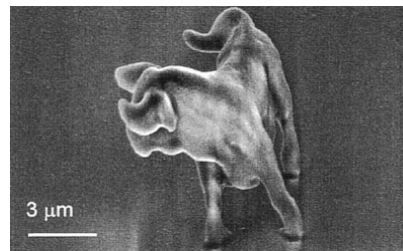


Figure 1-28 Two fabrication strategies.

1.8.2 Laser beam trajectory planning strategies

There are two fabrication modes: the Raster Scanning Method (RSM) and Contour Scanning Method (CSM).

In RSM, all voxels in the parallelepiped volume that contains the micro-object are scanned in accordance to the voxel exposed/unexposed positions, with the appropriate shutter ON/OFF (exposed /unexposed) state. In CSM, the laser focus will only trace the voxels located on the contour of the micro-object. Figure 1-28(a) and (c) illustrates how a character 'T' could be scanned with these two modes. Apparently, CSM requires the access to a smaller number of voxels than RSM, but the kinematics of the stage movements is slightly more complicated than those of RSM because the movements are not reduced to simple increments along the x and y axes of the machine. The distribution of voxel exposed positions is the critical point of CSM to improve the fabrication efficiency. Depending on the shape of a microstructure, alternations and combinations of these two basic manufacturing modes could be utilized to reduce the manufacturing time.

Experiments have been carried out [Sun et al. 03a] to determine that the contour scanning method is the most efficient scanning technique for producing a given structure. In Figure 1-28(b) and (d), the fabrication time of micro-bulls made by RSM and CSM are 3 hours and 13 minutes, respectively. The fabrication time in CSM is reduced by more than 90%. This demonstrates the impact of the laser beam trajectory over the manufacturing time and enforces the attention that must be paid to the path planning strategies to obtain an efficient micro-manufacturing process.

1.8.3 Critical issues for preventing microstructure collapses brought by CSM

CSM differing from the RSM (because only outer contours are scanned for polymerization), it leaves the inside of the contours in an un-polymerized state. For this reason, CSM requires a relatively small number of voxels for 3D fabrication, and it is considered as more efficient for 3D micro-fabrication based on TPP than RSM. Furthermore, shorter fabrication time means that the probability of facing external interferences, such as vibrations or the fluctuation of the pulse peak power, during the laser beam scanning process is effectively reduced. However, with CSM, the shell thickness of the solidified contours is generally very thin, hence the fabricated microstructures by CSM can be deformed easily due to the surface tension after washing out the resin, i.e. dissolution process of the resin. A research [Takada et al. 06] reported if the shell thickness is less than 350 nm, then its shrinkage rate would be greater than 10% after the dissolution process.

Roughly, the mechanical strength of a structure increases in accordance to the cube of its thickness, so the thickness of a 3D microstructure is an important factor to fabricate successfully microstructures via CSM. A simple method to thicken the contours of 3D microstructures in TPP is to increase the laser power and exposure time

in the fabrication process. When the laser power is high, the threshold region for polymerization at a focal spot is rapidly increased, which leads to an enlargement of the voxel size. Moreover, when the exposure time gets longer, the voxel size gradually grows depending on the exposure time, based on the radical expansion toward the outside of an initially formed voxel. Although these approaches permit the improvement of strength by enlarging the contour thickness, they are not suited for an ultra-precise fabrication of complicated 3D microstructures due to the large voxel sizes. Essentially, the height of a voxel is enlarged depending on the increase of the laser dose from v_a to v_{na} , see Figure 1-29(a), and also, an extra shape appears due to the growth of lateral size of a voxel, which becomes obstacles to monitor accurately the fabrication process.

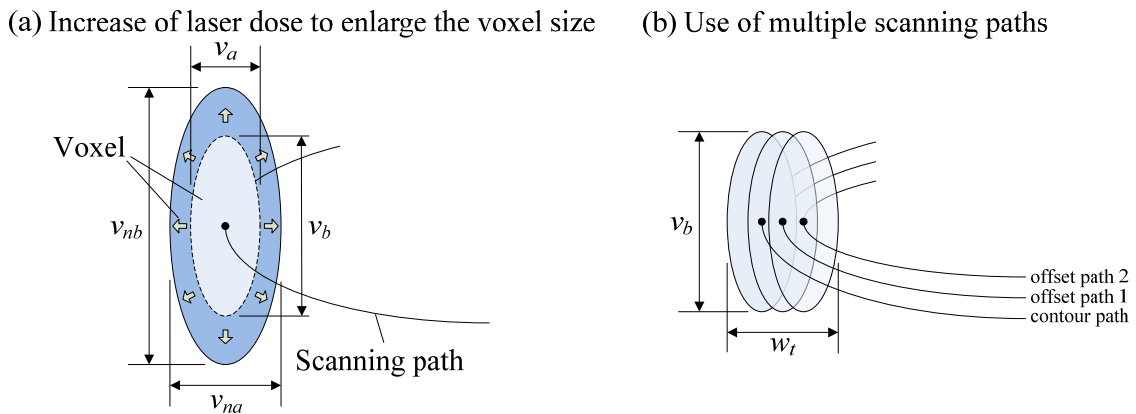


Figure 1-29 Schematic illustration of the difference between two approaches to increase contour thickness.

The multipath scanning method [Yang et al. 07] is an alternative for an effective and precise stiffening of 3D microstructures without the reduction of a resolution, as illustrated in Figure 1-29(b). After obtaining the outer contour from the slicing process, an offsetting process is carried out to generate a new interior contour by connecting intersection points obtained when offsetting the elementary paths of the initial contour. The target thickness of a contour can be obtained readily by controlling the offset distance between contours and the number of inner contours of the multi-path scanning method. However, the consequence of this strategy is the significant increase of manufacturing time since contours need to be scanned several times.

1.8.4 Critical issues of a slicing process brought by CSM

As addressed previously, processing time is one aspect of the micro-product manufacturing process but the integrity of the micro-product is also an issue. To this end and to increase the stiffness of the microstructure fabricated by CSM, a fully sealed shell of microstructure must be built to keep the un-polymerized molecules inside this

shell, thus avoid deformations during the resin wash out phase. This constraint brings two issues (see Figure 1-30):

- Ultra-thin layers needed to represent the approximately planar areas,
- Un-sliced areas create cavities in the micro-structure.

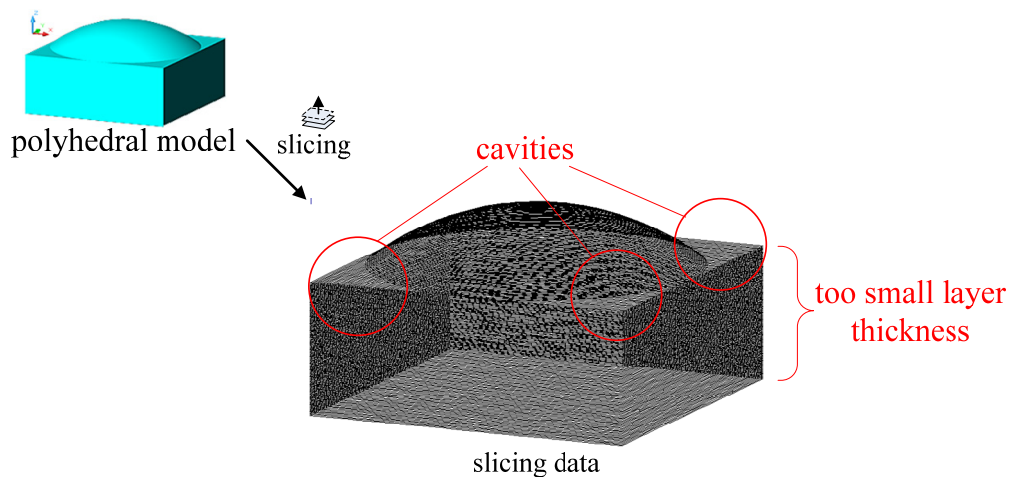


Figure 1-30 Critical issues of the slicing process brought by the CSM path planning strategy.

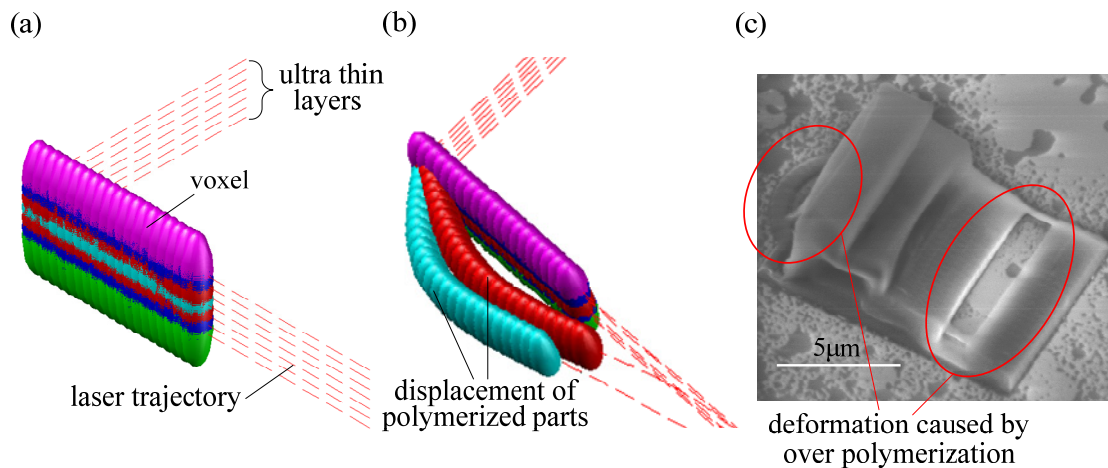


Figure 1-31 Over polymerization.

Except for fabrication efficiency, the ultra thin layer (probably less than 10 nm) is really a serious problem in TPP micro-fabrication with the equipment available in the scope of the current project. From the manufacturing machine kinematics point of view, it is difficult to monitor the machine movements within sub-10 nm for the moment. However, comparing the problem of the over polymerization to that of the resolution of the machine movements, the monitoring the machine movements is the minor issue. Indeed, the TPP being a laser induced photopolymerization technology, if there is too much energy accumulation either in extreme neighboring regions or due to the

definition of ultra thin layers, then over polymerization will occur in the resin. In both cases, the over polymerization originates because several laser beam locations become too close to each other and an energy threshold is reached that lead to the local destruction of the micro-structure, an consequence opposite to the material buildup principle that is at the heart of the TPP manufacturing technique. The laser beam just acts as a cutting tool and the energy destroys the polymerized part in the resin. Figure 1-31 depicts a case of over polymerization. Based on the observation of the voxel distribution, a tight voxel aggregation due to ultra thin layers is shown in Figure 1-31(a). Different colors represent voxels in different layers. Voxels produced too close to each other may let their neighborhood gather too much energy and can generate bubbles (like explosions) to push the polymerized parts far away from their predetermined positions, as shown in Figure 1-31(b). Figure 1-31(c) is a SEM image of a micro-stair fabricated by TPP, and it shows two deformation places caused by over polymerization.

As stated above, several phenomena interact with each other that necessitate an analysis and evolution of the laser beam path planning strategy to produce efficiently and with a good integrity the desired micro-products.

1.8.5 Issues related to scanning path planning

The two-photon transition rate is extremely small in general, so that a high intensity laser beam is needed to induce the polymerization. The polymerized parts of the resin have different optical properties from the original ones. For example, due to the light reflection, if the focus spot of the laser beam goes through the polymerized region, it may reduce the beam intensity and influence its ability to initiate the polymerization at its focal point. Inconsistent sizes of voxels in polymerized and un-polymerized regions are a consequence of these configurations, which reduces the reliability of the manufacturing process and should be avoided.

For example, in Figure 1-32(a), the laser beam comes from bottom up. If the fabrication is also made from bottom upward, the focused spot always goes through the polymerized region of the resin during the manufacturing process, and it is an unsuitable way to fabricate micro-products with the TPP process. Figure 1-32(b) shows another fabrication direction where the micro-product is manufactured from top to bottom. This time, the focused spot is under the polymerized region of the resin during the whole process, and this is considered as the best way for fabrication. Similarly, if the beam comes from top down, the best fabricating direction is from bottom up. So, we can make a simple conclusion that the fabricating direction must be opposite to the laser beam emitting one. To make sure the fabricating order of laser trajectories is satisfied as frequently as possible, a scanning path planning process need to be carried out.

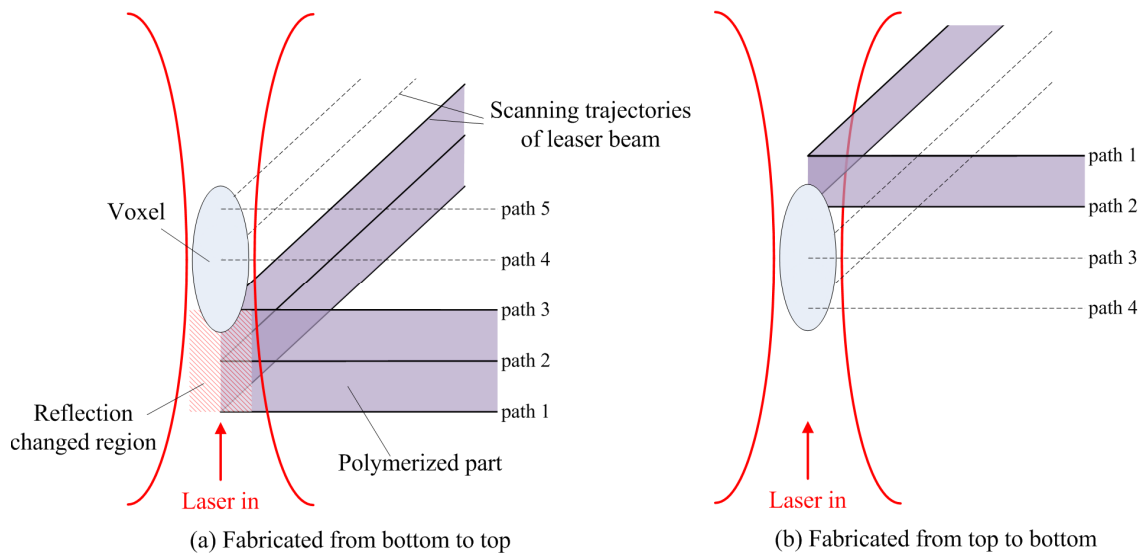


Figure 1-32 The categories of scanning path planning of the laser beam during the TPP micro-fabrication process.

The bottom-up layered fabrication is easier to implement than the top-down one because the polymerized parts can be fixed on the carrier plate. At the opposite, the top-down layered fabrication means that the polymerized parts should ‘fly’ in the resin during the manufacturing process. To ensure the success of 3D micro-product fabrication, a sufficient viscosity of the resin and anti-vibration treatments are mandatory. Furthermore, the probability of obtaining an unfinished object increases with larger fabrication times because vibrations and other perturbations may take place. For this reason too, using an efficient slicing process and optimizing the order of laser beam trajectories can effectively decrease the processing time and increase the quality of TPP micro-fabrication process.

1.9 Conclusion

After synthesizing the background of TPP micro-fabrication and other relative topics, there are several significant requirements which are not taken into account among previous works and some of these requirements, as highlighted previously, form the targets of this research. The requirements are described as follows:

- Requirements of the PV interface for color product models acquired through a RE process (see chapter 2):
 - A suitable shape capturing method without destroying the inherent color of object is needed when a laser scanner is used to obtain the digital points of colorful objects,

- Preserving the inherent color information of a scanned object is important for some commercial applications; and would be useful for TPP micro-manufacturing in the future. Therefore, a more efficient reconstructing process of color product model is necessary,

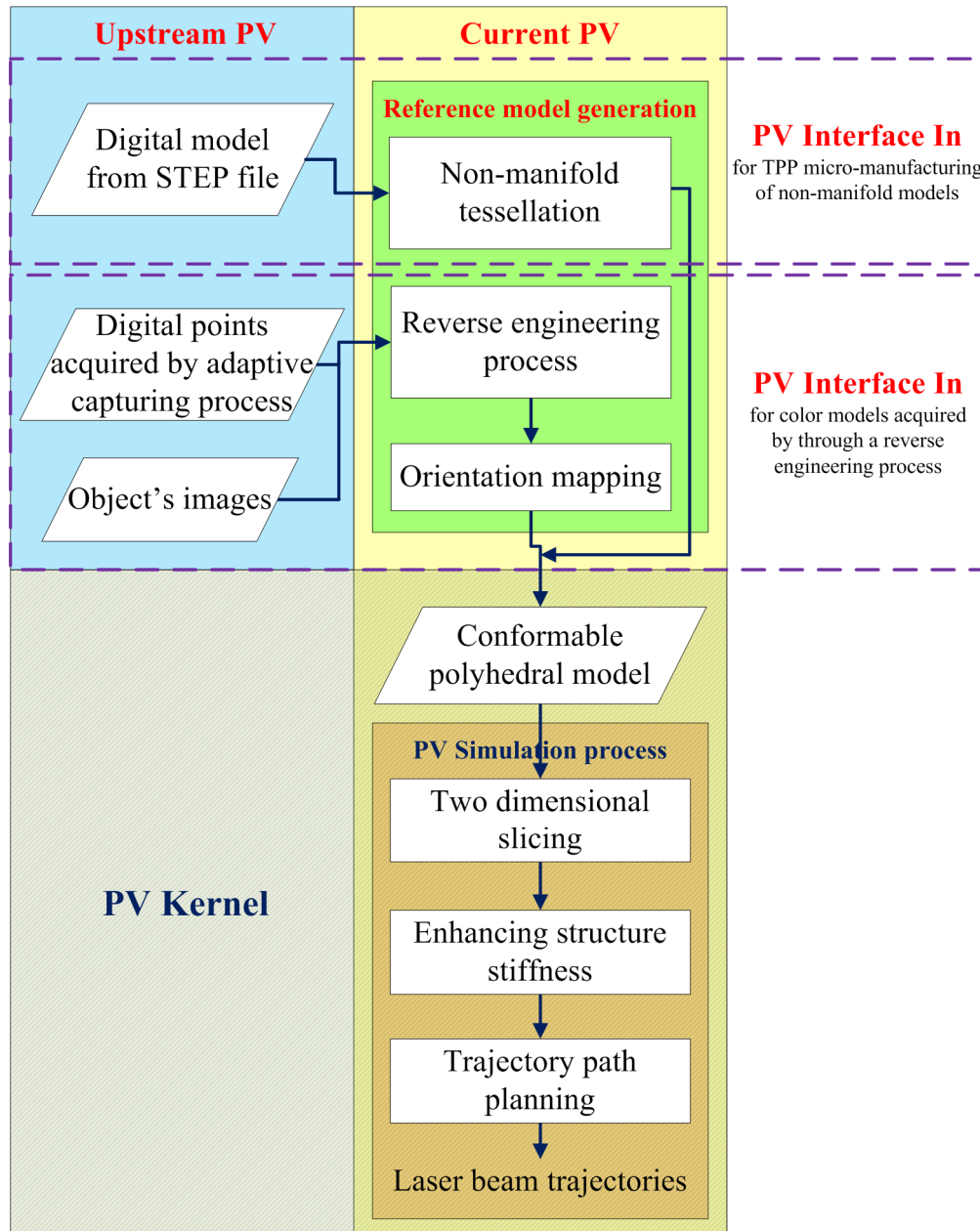


Figure 1-33 The product view of the proposed preparation process for TPP 3D micro-fabrication.

- Requirements of the PV interface for TPP micro-manufacturing of non-manifold models (see chapter 3):
 - Product models need to be described by a non-manifold representation to

produce a wide diversity of micro-products,

- Since commercial CAD modellers don't incorporate efficient modelling capabilities to describe non-manifold objects, some strategies need to be implemented to reduce the effect of these limitations when the designer wants to fabricate a non-manifold micro-product,
- Requirements of the PV simulation process for TPP micro-manufacturing (see chapter 4):
 - An effective manufacturing process having a good balance between surface roughness and processing efficiency is necessary,
 - Effective strategies for enhancing the microstructure stiffness in order to decrease the influence of a cohesive force and prevent the structure collapse are also needed,
 - An optimal planning process of laser beam trajectories is needed to arrange the slicing data of a microstructure,
 - A suitable data structure to represent all the necessary slicing data and its derivatives efficiently is also important.

After identifying the requirements of the TPP micro-fabrication in this study, a comparison can be made with the product view of a generic simulation preparation process. Figure 1-33 depicts our proposed simulation preparation process.

Product view interface for color models acquired through a reverse engineering process

During TPP micro-manufacturing preparation process, the source of the manufacturing reference model can be obtained from digitized points acquired through RE of physical objects. Then, the color information of the fabricated object can be a requirement for the DOEs of the TPP manufacturing equipment. To meet our research objectives, this chapter introduces the critical issues and treatments for automatically reconstructing an object model with color information. Subsequently, this model can be the model processed during the TPP manufacturing preparation phase and, as such, part of the product view interface for TPP manufacturing. These issues include how to acquire the object's shape information without destroying its intrinsic color, how to obtain a color texture map automatically, and how to correctly map the texture onto the surface of the object model.

2.1 Introduction

This chapter describes the contribution carried out at NTU during the first half of the PhD studies devoted to the shape acquisition for the TPP manufacturing process.

As mentioned in chapter 1, to obtain the best quality of digitized points with a non-contact optical technology in RE, most of the time it is necessary to spray some paint over the object's surface. However, it is also mandatory to construct a color model of the physical object to generate a more complete object model which can be propagated to other product views for improving their efficiency. In addition, this model must favor an undamaging-color measurement because sometimes this object is invaluable and unique.

At present, the laser scanning technology plays a key role in RE since it can capture the object's shape information quickly and for a wide range of object shapes and materials. However, most of the applications devoted to the generation of a numerical

shape from digitized points can only reconstruct an object's shape but don't include color. We can say that such a process is only a part of a RE process whose aim would be to produce a more complete digital model of an object. In most practical applications, a texture mapping process is applied to support further the color data wrapping on object's shape and must become part of the RE process if a color model is part of the desired digital model.

Generally, during a texture mapping process, a texture map needs to be prepared first and the corresponding relationship between the object's surface and the map has to be adjusted manually. Such a process is time consuming. This chapter proposes an automated process for creating a color model of an object after scanning it.

2.2 Laser scanning without destroying the color information of an object

A typical laser scanner, as shown in Figure 2-1, uses a laser diode to emit a laser beam on the object surface and captures the reflected light by two monochrome CCD cameras. Given the positions of the laser head and CCD cameras, coordinates of the object surface can be computed using the triangulation principle or a coordinate mapping method [Yau et al. 00].

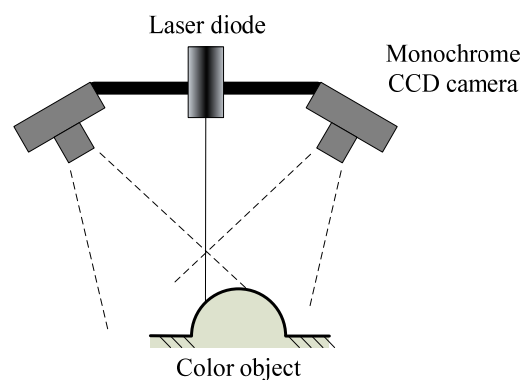


Figure 2-1 Laser scanner with a laser diode and two monochrome CCD cameras.

One of the key points for applying laser scanning technology to obtain accurate measurement data is the surface reflection of scanned objects which is needed as uniform and mat as possible. Therefore, objects owing metal brilliance or various colors are not suitable due to differences about their local reflection. Except for using the traditional object preparation, i.e. spraying some paint over the object surface, some researchers have proposed strategies to solve the issue of differences in surface reflection. For example, Clack et al. used polarization analysis in triangulation-based

laser scanning to disambiguate the true measuring data from spurious inter-reflections caused by holes and concavities on metal surfaces [Clark et al. 97]. As for colorful objects, in order to scan them with detailed color and under bright lighting, Albamont and Goshtasby developed a scanner using an imaginary (virtual) laser rather than a real one for scanning [Albamont & Goshtasby 03]. However, this method is only suitable for those objects owing rich textures or diffuse surfaces. In addition, the measurement error of using this virtual laser is also larger than using a real one.

In what follows, this research concentrates on the laser measurement issues for colorful objects. Some observations are described and analyzed and provide us an idea to develop a new shape capturing method.

When the laser diode emits a laser beam on the color surface of an object, the darker color having a lower reflection rate will absorb the laser light and affect the quality of scan data. In order to obtain a consistent reflection rate of object surfaces, red or white paint is sprayed over the surface of colored objects. However, such a process destroys the inherent object color itself and in some cases, it is even not permitted because the object is unique and invaluable.



Figure 2-2 Laser beam emitted on a color surface.

In general, dark surfaces need larger laser diode power than bright ones. When object surfaces have a specific reflection rate, the power of the laser diode should be adjusted to a suitable value for obtaining the best quality of scan line data. As shown in Figure 2-3, to measure the same scan line with laser beams having different laser diode power (see Figure 2-2), images captured from the CCD cameras are different and the number of digitized points for each laser beam configuration differs also.

The above observations justify the need for an adaptive scan line capturing process to take into account the effect of these dark areas.

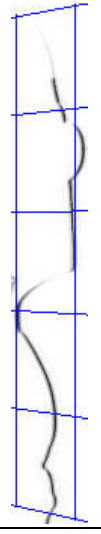


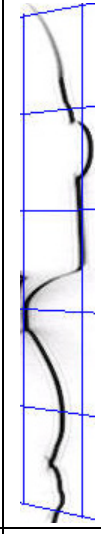
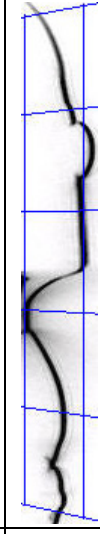
Images captured from CCD camera					
Laser power/ P_{min}	1.00	1.13	1.25	1.38	1.50
No. of data points	157	160	175	189	190
\bar{d} (mm)	0.364	0.362	0.351	0.352	0.361

Figure 2-3 Scan line data for using adaptive scan line capturing process.

This adaptive scan line capturing process is developed with the help of a specific feature of equipment, i.e. the variable power of the laser diode. Assuming that the power of the laser diode can be adjusted between P_{min} and P_{max} , where P_{min} is the minimum power and P_{max} is the maximum one. Let P_{min} be the initial laser diode power for each scan line. If the number of digitized points in a scan line is less than a given threshold value, a power adjustment process is executed. t sets of scan lines are acquired with t different power values which span the interval between P_{min} and P_{max} . However, a large power also induces noise in the scan line data. The noise can be indicated by the average distance between each scan line point. The definition of the average distance \bar{d}_i for all the points in the i -th scan line can be written as:

$$\bar{d}_i = \frac{\sum_{j=1}^{N_i-1} \|\mathbf{p}_{j+1}^i - \mathbf{p}_j^i\|}{N_i - 1}, \quad i = 1, \dots, t \quad (2-1)$$

where \mathbf{p}_j^i is the j -th point vector of the i -th scan line, and N_i is the number of digitized points in the i -th scan line. Given the behavior of the laser scanner, it is possible to observe, on the one hand, that the number of fitted digitized points will be increased with the increased power of the laser diode, and \bar{d}_i will become smaller. On the other hand, the noise will also increase with the increased power of the laser diode, and \bar{d}_i will become larger because noisy points get farther from the real points. So, the average

distance of points for a given scan line has a relative minimum value when the laser diode power is increased, and the power with the relative minimum average distance is considered as the optimum laser diode power for the object surface. As shown in Figure 2-3, when the laser power is increased to 125% of P_{min} , the \bar{d} has the local minimum value. At the optimum laser diode power, the number of data points is increased to 111.4% of points compared to the number obtained with the P_{min} laser power.

Certainly, applying the adaptive scan line capturing process would let the processing time slow down. For example, let us assume a digitizing process scanning 100 lines is set for a target object. If each line has 5 laser beam power adjustments, then the processing time would be increased by around 80%.

2.3 Automation of texture map generation

In sections 2.3 and 2.4, the automatic process of mapping textures onto the polyhedral model of an object is introduced. Before, the hypotheses about this process are defined as follows:

- The processed objects own spherical shapes, i.e. every surface point is visible from the laser scanner,
- The object shapes are circularly digitized by the adaptive scan line capturing process mentioned in section 2.2, and reconstructed with polyhedral models,
- Because the processed object owns a spherical shape, the texture maps generated from images which are captured horizontally around the object by a CCD camera are enough to cover the entire object surface.
- The planar texture mapping technique is used to warp the color texture maps onto the surfaces of processed objects.

To process texture mapping automatically, the first step is to produce the accurate texture maps needed. A CCD camera is used to capture color texture maps of the object surface in this study. However, the object and the background behind it are blend together in this kind of images. It is needed to isolate or highlight the object from its background to help define its orientation easily. In this work, the object silhouette is used as a mask to filter the background. This segmentation technique like the one used in TV studios ('blue screen technique') is used to increase the accuracy of the coordinate mapping in the subsequent texture mapping process.

In a photography, if a bright background light is applied behind objects, part of this background light will be occluded by the object and a shadow of the object silhouette

will be produced, as shown in Figure 2-4(a). A histogram illustrates how pixels in an image are distributed by graphing the number of pixels at each gray intensity level. The histogram shows whether the image contains enough detail in the shadows (shown in the left part of the histogram), midtones (shown in the middle), and highlights (shown in the right part) to make a good correction. Generally, in an image with a high contrast like Figure 2-4(a), its histogram contains over detailed areas in the shadows and highlights, and under detailed areas in the midtones, as shown in Figure 2-4(b). Furthermore, an image contrast stretching process [Gonzalez & Woods 92] can be applied to a high-contrast image to strengthen its contrast.

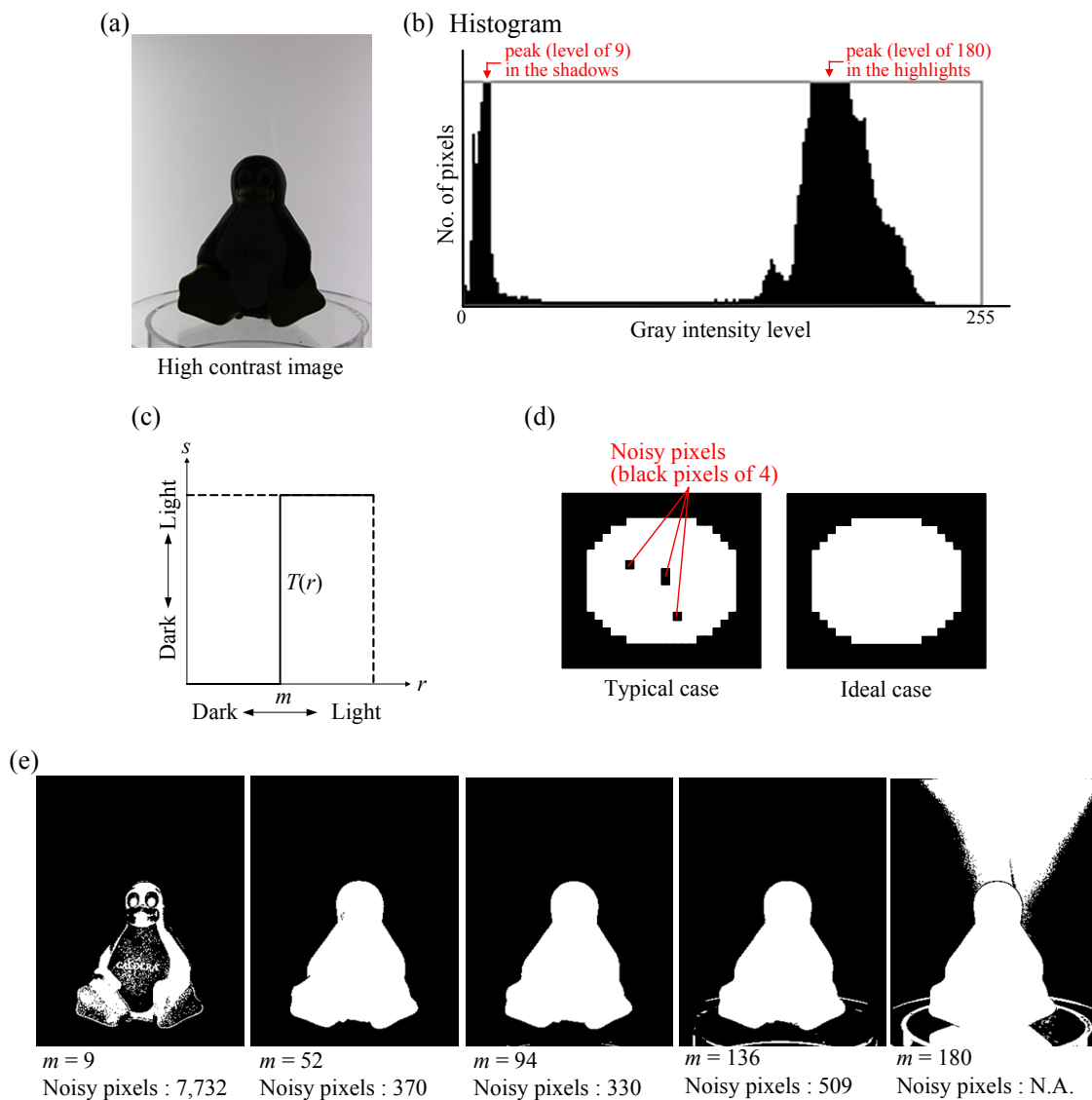


Figure 2-4 Object silhouette extraction process.

Assuming that r is the gray level of the original image, and s is the enhanced gray level after the contrast stretching process. The gray-level transformation function T has

the following form:

$$s = T(r). \quad (2-2)$$

The effect of this transformation is to produce an image with a higher contrast than the original one by darkening the levels below a given threshold value and brightening the levels above the threshold value of the original image. For example, if $T(r)$ is a step function where m is the threshold value, as shown in Figure 2-4(c), $T(r)$ will produce a two-level (binary) image. From the histogram point of view, two broad bands at the right and left parts of the histogram are reduced to two single peaks. Then, the object silhouette can be obtained at the transition between black and white pixels. As a consequence, when varying the threshold values (m) applied to images, different two-level images are produced, as shown in Figure 2-4(d). To demonstrate clearly this influence, all the images where the contrast stretching process has been applied are shown with their reverse images, i.e. the white and black areas are represented as the object and its background, respectively. However, the quality of an object silhouette and the quality of a texture map depend upon the choice of the threshold value applied to the contrast stretching process. The left of Figure 2-4(d) shows a typical binary image where the contrast stretching process has been applied. There are always either many or few black pixels remaining inside the object silhouette. These black pixels can be called noise pixels because their existence may cause either a failure when detecting the object silhouette or an unreal creation of texture map in the procedure described in the following paragraphs. At the right of Figure 2-4(d), an ideal case is shown: there is no black pixel inside. To produce a binary image conforming with a situation as ideal as possible, an image quality estimation method for the object silhouette has been developed. This estimation method is considered as an object-dependent function and is carried out through a simple optimization process to find out the best threshold value for a given object. Some constraints of this estimation method need to be carefully addressed:

- The file format of the target images is BMP (Bitmap) which is a common and simple bitmapped graphics format. The image is described directly as a block of bytes, pixel per pixel. Pixels are stored starting from the bottom left hand corner ranging from left to right and then row by row from the bottom to the top. Each pixel is described using one or more bytes. In other words, if we know the number of pixels along the width and length of an image, and the number of bytes per pixel, we can easily obtain the gray level of any pixel in an image,
- The object needs to be placed at the centre of the image, so that its silhouette

doesn't intersect the image boundary. Regarding the distribution of pixels in each row of the binary image, its extremities must be black in ideal situation. If there are many rows where one of their extremities at least is white, we can say that this binary image contains too much noisy pixels due to the selection of a too large threshold value, as shown at the right of Figure 2-4(e),

- The image quality estimation method based on the object-dependent function minimizes the noisy pixels inside the silhouette area, i.e. the number of black pixels inside the white area. The search space for threshold values can be set up between the two highest peaks in the histogram of a target image. For example, in Figure 2-4(b), the peaks in the shadows and highlights reach gray intensity levels of 9 and 180, respectively. Therefore, the search space lies between levels 9 to 180.

Figure 2-4(e) shows the results after applying the contrast stretching process on Figure 2-4(a) with threshold values of 9, 52, 94, 136, and 180, respectively. Checking the number of noisy pixels, the binary image with a threshold value of 94 is identified as the best one. Hence, it can be used as an image mask to remove the background environment of an object. Figure 2-5 shows the creation of a texture map using this binary image (middle of Figure 2-4(e), i.e. the binary image with a threshold value of 94) as the image mask.

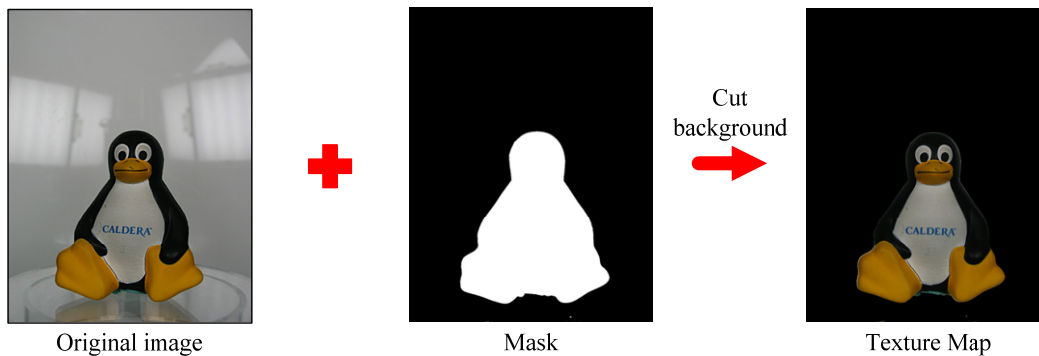


Figure 2-5 The creation of a texture map using an image mask to cut the object background.

2.4 Orientation between a polyhedral model and a texture space

Texture mapping is an image synthesis technique in which 2D texture images are mapped onto surfaces of a 3D model. Then, the colored 3D surfaces are either projected onto a 2D screen for display or filtered with a color gray level for other applications. To process texture mapping automatically, another critical issue is to systematically build

up the mapping between the 3Dtexture and 3D model spaces respectively in order to locate the texture at the right place on the 3D object model.

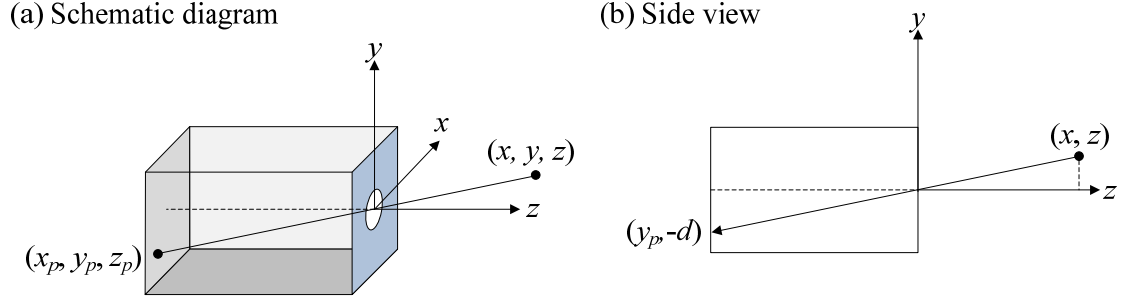


Figure 2-6 Pinhole camera.

2.4.1 Perspective mapping

The perspective formation of the image by a CCD camera can be generally described as an aperture image formation [Xu et al. 02]. The pinhole camera in Figure 2-6(a) provides an example of image formation with a simple geometric model. A pinhole camera is a box with a small hole at the centre of one of the sides of this box; the film is placed inside this box on the side opposite to the aperture at the origin of our coordinate system. Assuming that the hole is small enough, only a single ray of light originating from a point can enter it. The film plane is located at a focal distance d from the pinhole. A side view of this configuration (see Figure 2-6(b)) allows us to calculate where the image of the point (x, y, z) lies on the film plane $z = -d$. Using the elementary properties of two similar triangles, the projection point (x_p, y_p, z_p) can be defined as:

$$\begin{bmatrix} x_p \\ y_p \\ z_p \\ 1 \end{bmatrix} = \frac{d}{z} \mathbf{M}_p \begin{bmatrix} x \\ y \\ z \\ 1 \end{bmatrix} = \begin{bmatrix} \frac{x}{z/d} \\ \frac{y}{z/d} \\ -d \\ 1 \end{bmatrix}, \quad (2-3)$$

$$\mathbf{M}_p = \begin{bmatrix} 1 & 0 & 0 & 0 \\ 0 & 1 & 0 & 0 \\ 0 & 0 & -1 & 0 \\ 0 & 0 & 1/d & 0 \end{bmatrix}, \quad (2-4)$$

where \mathbf{M}_p is a homogeneous projection matrix of one perspective point used to map a point from 3D space to the 2D projection space of the camera. This is the so-called perspective projection of one point, and it means that all the points lying on the same projection line are projected into a single point, i.e. projection centre.

To solve Eq. 2-3, the geometric relation between the CCD camera and the reference object must be computed, i.e. the image acquisition system needs to be calibrated. The calibration of such a system produces the extrinsic parameters of the camera, which are the position and orientation of the camera with respect to the real world, and its intrinsic parameters, which are the focal distance and the shift of the optical center [Niem 94]. Undoubtedly, this calibration process is time consuming.

2.4.2 Scale orientation mapping

Assuming that a polyhedral model is reconstructed first from the physical object through a RE process. Then, a CCD camera is taking pictures from this physical object at view angles identical to those used for acquiring its polyhedral model. The image of the polyhedral model can be thought as a result such that the model is projected in perspective onto the CCD plane. From an abstract point of view, when the image of the projected polyhedral model is superimposed onto the image of physical object, i.e. a texture map representing the object, the geometric relation between them can be built with translation and scaling operations.

There is one thing needed to emphasize that these two images are captured by a pinhole camera at identical view angle. Based on the principle of a one-point perspective projection, only simple geometric operations (like translation, scale, but no rotation) are needed to build the relation between the model and texture spaces during the texture mapping process. When associated to the camera calibration process introduced in section 2.4.1, the texture mapping process becomes simple to implement.

In this work, a simple scale orientation method is proposed to define this geometric relationship between the digital object and the texture map.

Figure 2-7(a) shows the perspective projection of the polyhedral model onto an $x' - y'$ plane. A projected domain, a rectangle containing all the projected triangular faces on the projection plane, can be found. The width and height of the projected domain are denoted as w_c and h_c , as shown in Figure 2-7(b). This domain can be regarded as the maximum visible region from the given angle of view. If there is a texture map created from the same visual angle (see section 2.3) and its texture plane is exactly parallel to the projection plane of the polyhedral model, a texture domain, i.e. a rectangle

containing the silhouette, can be found simultaneously. The width and height of the texture domain located on a u - v plane are denoted as w_t and h_t , as shown on Figure 2-7 (c).

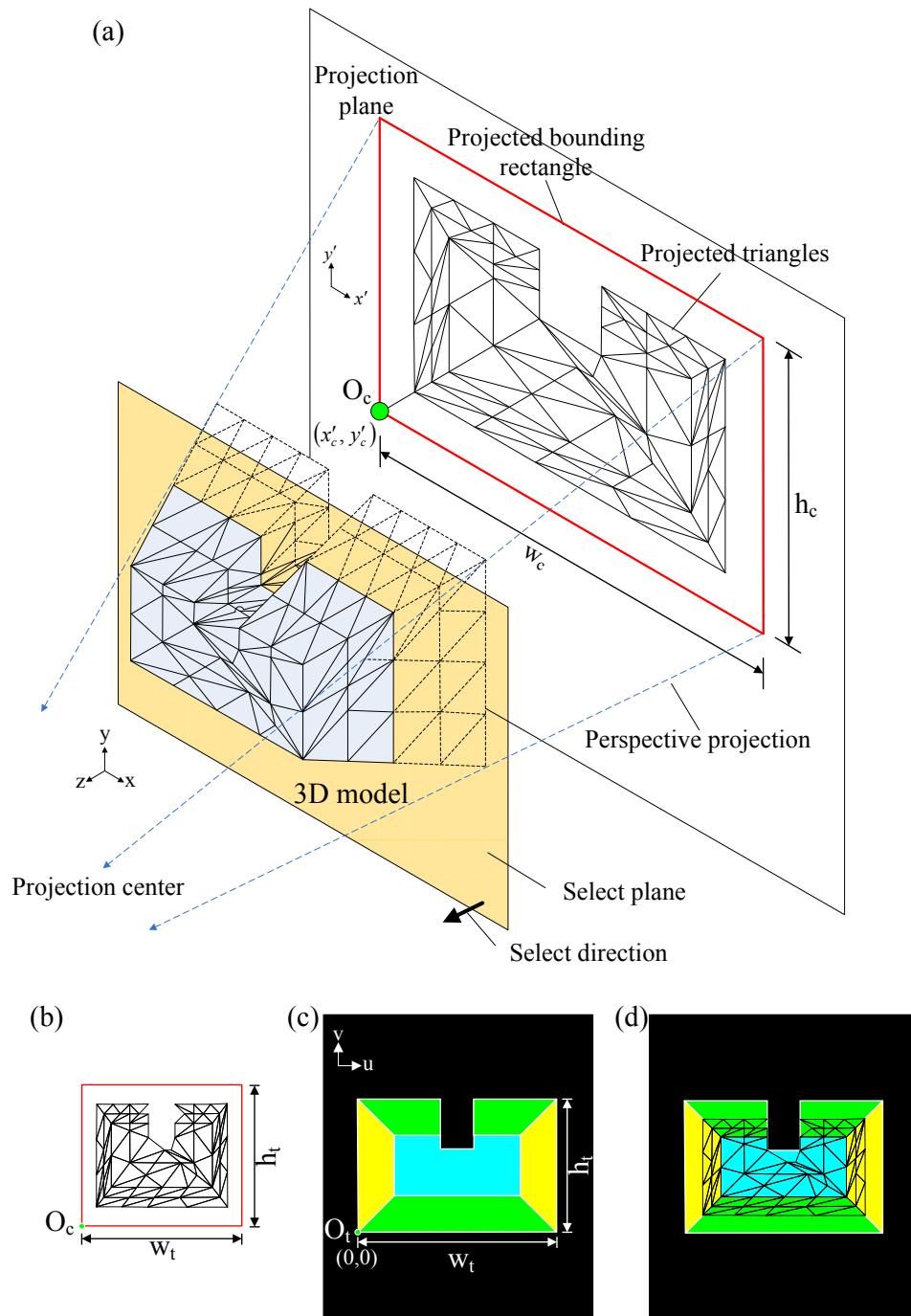


Figure 2-7 The scale orientation from a polyhedral model to a texture space.

Based on the concept of pinhole camera, in the ideal configuration, the projected and texture domains must only differ from each other through a scale factor. Therefore, two ratios λ_u and λ_v are defined as:

$$\lambda_u = \frac{w_t}{w_c}, \quad (2-5)$$

$$\lambda_v = \frac{h_t}{h_c}. \quad (2-6)$$

Assuming that the reference point of the projected domain is $O_c (x'_c, y'_c)$ and the reference point of the texture domain is $O_t (0, 0)$. The coordinate transformation equation can be written in a 2D homogeneous space as:

$$\begin{bmatrix} u & v & 1 \end{bmatrix}^T = \mathbf{M}_c \begin{bmatrix} x' & y' & 1 \end{bmatrix}^T, \quad (2-7)$$

$$\mathbf{M}_c = \begin{bmatrix} \lambda_u & 0 & 0 \\ 0 & \lambda_v & 0 \\ -\lambda_u x'_c & -\lambda_v y'_c & 1 \end{bmatrix}, \quad (2-8)$$

where \mathbf{M}_c is the transformation matrix, and (x', y') and (u, v) are the projected and transferred coordinates, respectively. When using this coordinate transformation, the 2D texture map and the 2D projected triangular faces lying into two different coordinate systems are transformed into a unified coordinate system.

In addition, a virtual selection plane is used to pick up the correct triangular faces for mapping, i.e. the faces not covered by other faces as seen from the selected angle of view. This selection plane is parallel to an $x' - y'$ plane, and its position is located at the geometric centre of reference of the object. The triangular faces lying in front of the selection plane are picked up. Following the texture mapping criteria (see section 2.4.3), some faces are either ignored or moved to other texture maps. The final result of the scale orientation process is shown in Figure 2-7(d).

2.4.3 Texture mapping criteria

Since one texture map cannot cover more than 180 degrees of view angle around an object, at least two or more texture maps are needed to cover the whole surface of this object. However, it raises another issue about overlapping areas between two adjacent texture maps, which needs to be taken into account. These overlapping areas usually appear around the rim of the object silhouette in a texture map, as shown in Figure 2-8. Therefore, before defining the texture mapping criteria, some hypotheses are

set up as follows to clarify the suitable applications of our proposed method:

- Only the texture maps generated around the object are mapped onto the polyhedron representing the spherical object. It means that there is no other specific views of texture maps (such as top or bottom views) mapped onto object surfaces. This hypothesis simplifies the development of an automatic mapping process,
- Each triangular face of the polyhedron participates to the mapping with only one of the texture maps to avoid mapping errors that would not produce a satisfactory representation of the object.

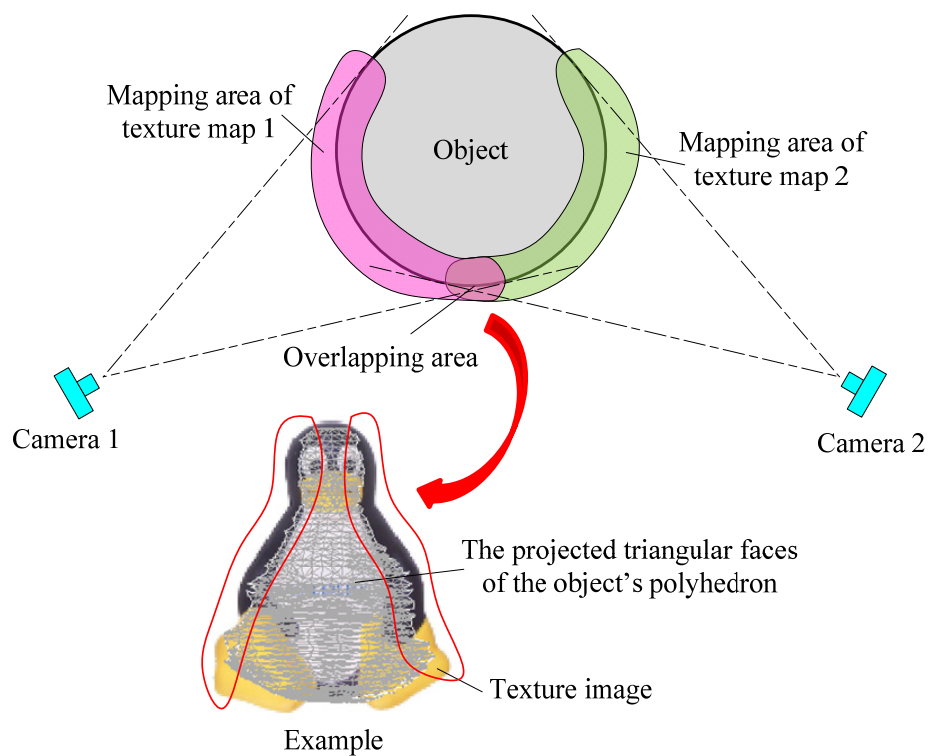


Figure 2-8 Overlapping area between two adjacent texture maps.

In addition, to avoid inconsistencies of texture luminances between texture maps captured from different visual angles because the lightning conditions may vary, the photographic environment, diaphragm, shutter, and even white balance need to be kept consistent between the adjacent texture maps.

Since two adjacent texture maps have some overlapping visual angle, some mapping criteria are needed to improve the global mapping result. These mapping criteria are described as follows:

1. Select the triangular faces located in the front camera view, i.e. the visible ones,

and ignore the triangular faces located around the rim of the object silhouette, i.e. the triangles partially visible or parallel to the projection lines:

Usually, the mapping result is distorted for triangular faces around the rim of the object silhouette. So, the mapping operation is only applied to faces corresponding to the central region of the texture map. An inward offset silhouette is used as the selecting mask to eliminate triangular faces around the rim of the object, as shown in Figure 2-9,

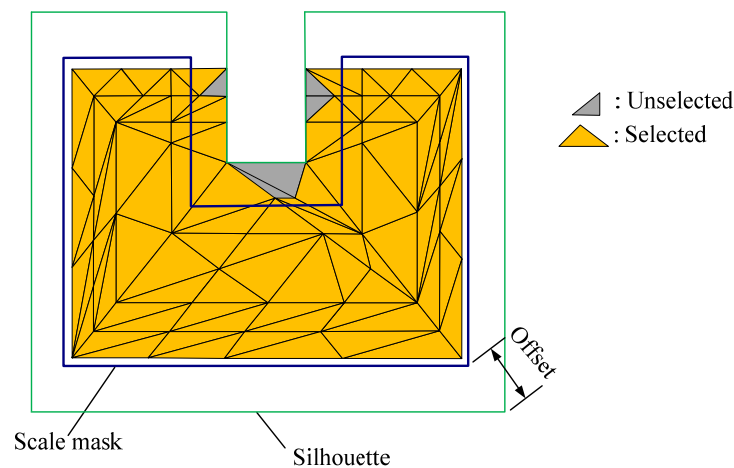


Figure 2-9 Schematic diagram of the triangular faces ignored because they are located around the rim of the object silhouette.

2. Apply the criterion of maximum projected area in the overlapping area:

If a triangular face can be assigned to different texture maps with different camera viewing angles, choose the one which has the maximum projected area, i.e. the normal of the triangular face having the smallest angle relative to a camera viewing angle, to reduce the distortions,

3. Assign remaining triangular faces to a texture map directly:

After applying the first two mapping criteria, the triangular faces having zero projected area would be left. We assign them directly according to the geometric relationships between the triangular faces and the texture maps. This criterion is compulsory to ensure each triangular face being mapped to a texture map.

Figure 2-10 gives an example for building relationships between triangular faces and texture maps. In a first step, the inward offset silhouettes are used as selecting masks to select the central projected triangles mapping on the corresponding texture maps. In a second step, the projected areas of each

remaining triangle are compared between two adjacent view angles, and the triangle is mapped on the one which has a maximum area. After two steps, the triangles having zero projected area are left. They are assigned directly in a third step.

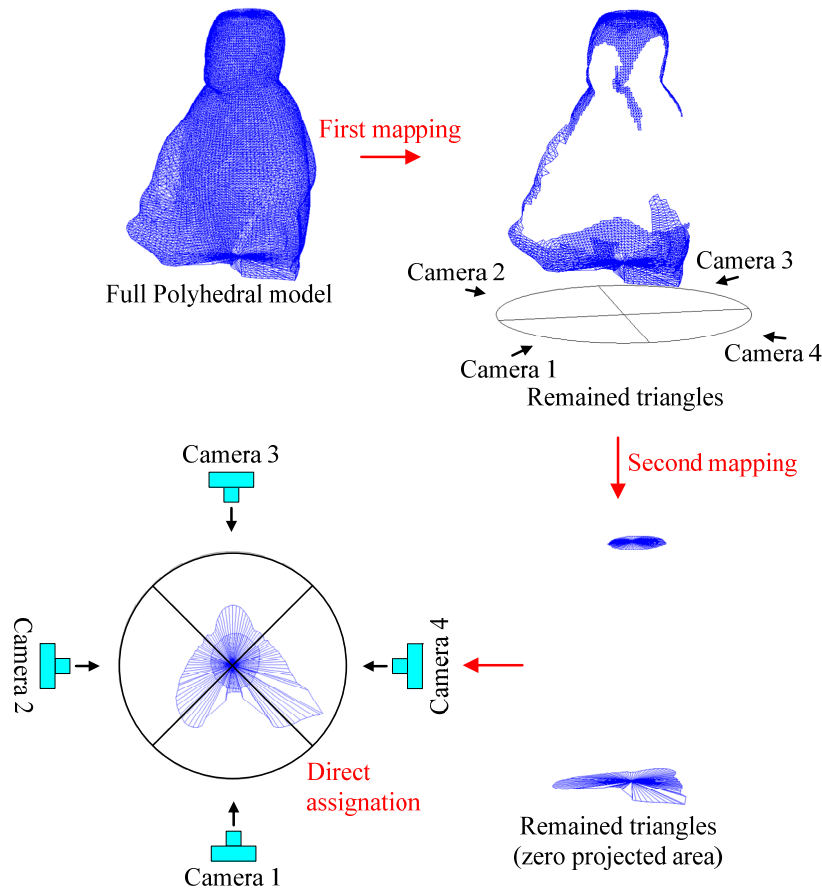


Figure 2-10 . An example for building belonged relationships between triangular faces and texture maps.

4. Apply the grouping process of triangular faces in overlapping area:

This process is a fine-tuning criterion. Triangular faces mapped to the same texture map are referred to as surface regions here. In fact, the distribution of surface regions may be quite inhomogeneous, as shown in Figure 2-11(a). This distribution may results in a large number of disconnected domains for each surface region. In order to obtain connected domains (see Figure 2-11(b)), a grouping process is applied [Niem 99], which contains the following steps:

- (1) Detect a triangle T assigned to a texture map M_i such that T is adjacent, on at least two sides, to triangles assigned to a different texture map M_j .

- (2) Calculate the projected area of the detected triangles by applying the texture from texture map M_j .
- (3) Assign the triangle T to the texture map M_j if the reduction of the projected area is within a predefined tolerance.

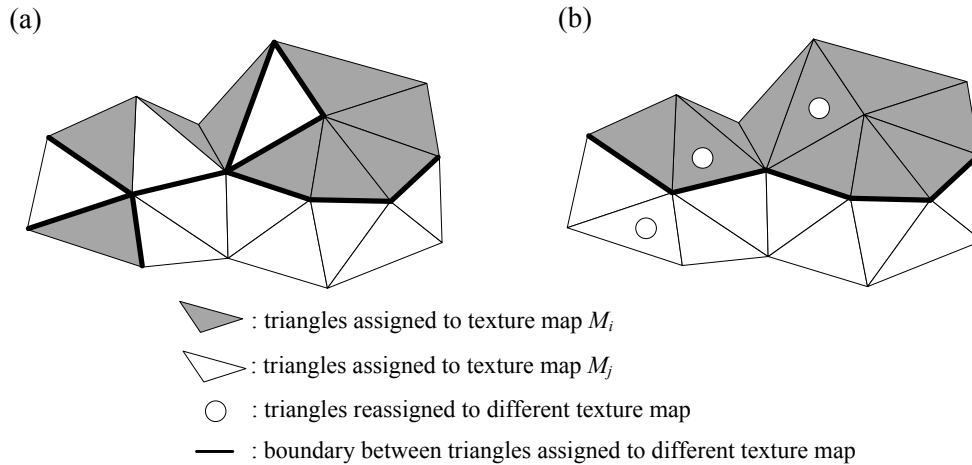


Figure 2-11 The grouping process of triangular faces in overlapping areas between two adjacent texture maps.

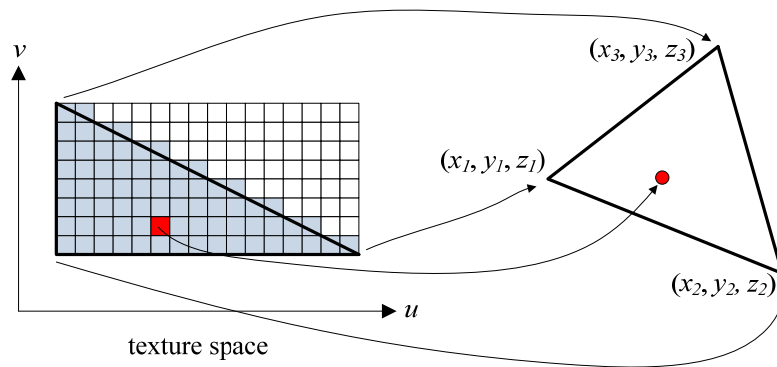


Figure 2-12 Point sampling between the texture map and the surface particle of a triangular face.

2.4.4 Texture filtering

After the mapping is computed and the texture is warped around the 3D digital model of the object, the image must be re-sampled in accordance to the screen grid while the result is displayed on screen. Based on the same process, the image can also be extracted as a color gray level to act as a kind of manufacturing data. Transforming the image to meet the screen resolution can be regarded as similar to transforming it to a fabrication system because both of them need to match the resolutions of their

corresponding equipments, i.e. the screen resolution for the visualization system and the machine axis resolution for the machining equipment. This process is called filtering [Heckbert 86].

The cheapest texture filtering method is the point sampling one (see Figure 2-12), wherein the pixel nearest to the desired sample point is used. It works relatively well on un-scaled images, but for stretched images, the texture pixels may become visible as large blocks, and for shrunken images aliasing can cause distracting moiré patterns.

After texture filtering, the triangular faces of a polyhedral model contain the relations with the intrinsic colors of the object and this information may be useful for several categories of applications. In the current state of this work, this operator has not been implemented, and will be set up in the future.

2.5 An integrated scanning system for reconstructing color models of objects

Based on the proposed approach, an integrated scanning system has been developed. This system is composed of a laser head, a digital camera, a light control system, and a moving table with 4 degrees (X, Y, Z, R) of freedom. The control software is developed in Visual C++ .NET and AutoCAD ObjectARX Library. The AutoCAD software is used as the graphic engine to manipulate scan data and triangular meshes, while the 3D animation software 3ds max is used to reconstruct the 3D color model and display the results of rendered color images. The integrated scanning system developed is shown in Figure 2-13, and the configuration of the system is shown in Figure 2-14.

The process for reconstructing a 3D color model using this integrated scanning system is described briefly now. Firstly, the object is placed on the rotary stage for the scanning operation. The shape is digitized by the laser head at each predefined angular position. When digitizing the darker surface, the adaptive scan line capturing process is applied to reduce the noise and improve the quality of the scan data. After the scanning operation, some data pre-processing operations, such as data reduction, data redistribution and data smoothing [Volino & Magnenat Thalmann 98], will be also applied on the scanned data points. Then, 3D triangular faces are constructed from the digitized points and a polyhedral model of the object can be obtained.

As for digital images, both general color images and high-contrast ones are needed to reconstruct a 3D color model of the object. When capturing general color images, foreground lights are turned on and background lights are turned off. When capturing high-contrast images, foreground lights are turned off and background lights are turned

on. To create the texture maps needed, the image contrast stretching process is applied on high-contrast images to obtain the object silhouettes. Then, the object silhouette is used as a mask to remove its complex background such that the image texture inside the object silhouette is simplified.

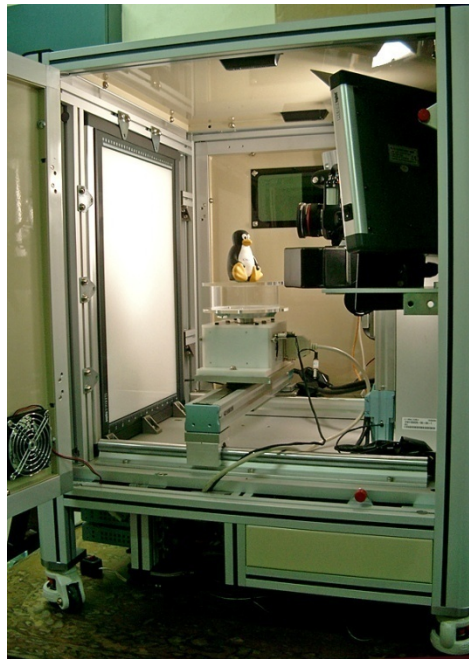


Figure 2-13 The developed integrated scanning system.

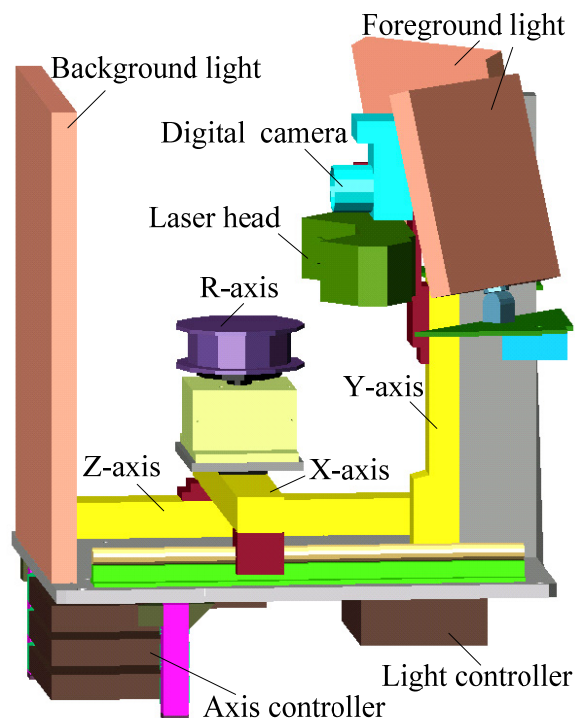


Figure 2-14 The configuration of the integrated scanning system.

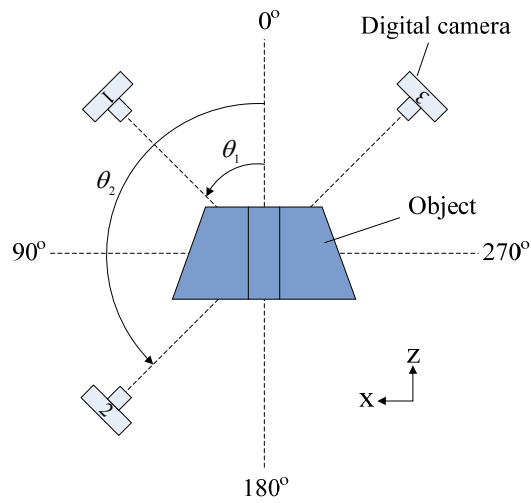


Figure 2-15 Position angle definition around the object.

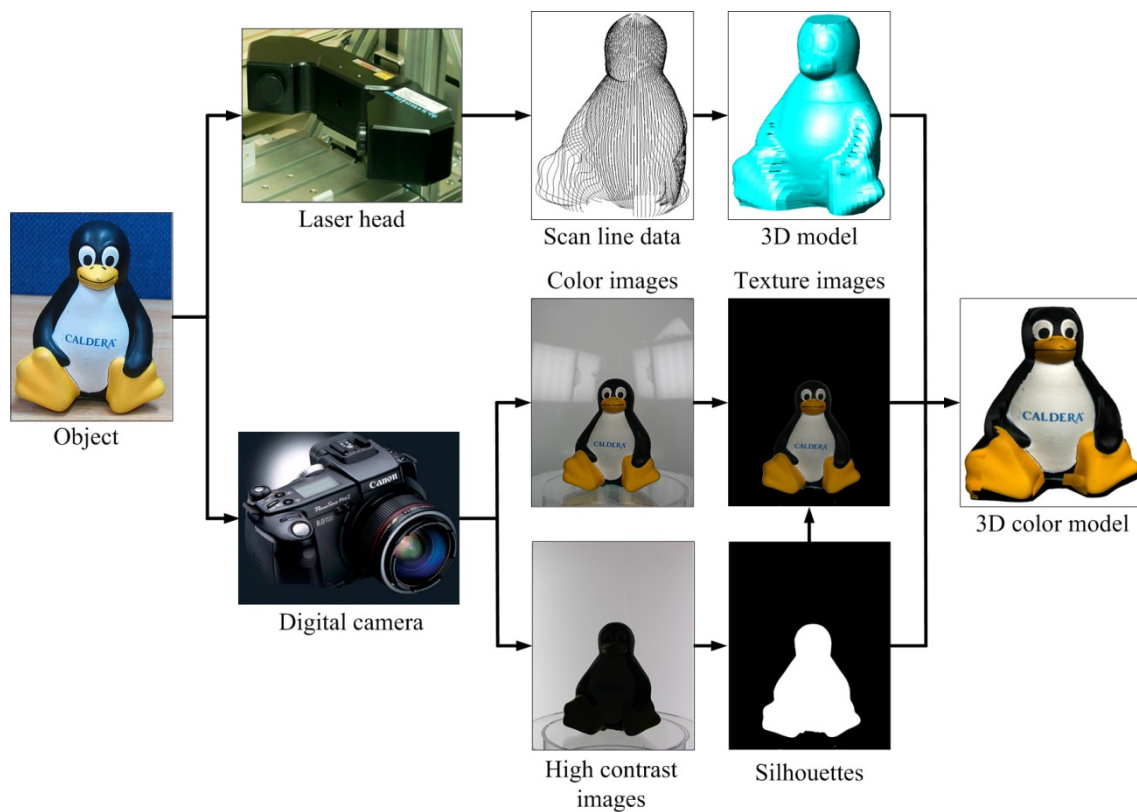


Figure 2-16 3D color model reconstruction procedure.

In the integrated system, the mapping relationship between the texture maps and the 3D space is connected with the rotary stage. Assuming that a digital camera located at an angle θ_i ($i = 1, \dots, k$) relative to the target object, a color texture image is captured at each angle position around the object, as shown in Figure 2-15. Because the maximum view angle of a digital camera is less than 180 degree, more than two texture maps are

needed to cover the whole object surface.

Then, the projection transformation between the 3D model space and the texture space can be built up. At each angular position θ_i ($i = 1, \dots, k$), a point $p(x, y, z)$ in the 3D model space is mapped into a point $p(x', y')$ after applying a parallel projection to the plane of the corresponding texture image. The projection transformation equation is written in homogeneous form as:

$$\begin{bmatrix} x' & y' & 1 \end{bmatrix}^T = \mathbf{M}_t \begin{bmatrix} x & y & z & 1 \end{bmatrix}^T, \quad (2-9)$$

$$\mathbf{M}_t = \begin{bmatrix} \cos \theta & 0 & \sin \theta & 0 \\ 0 & 1 & 0 & 0 \\ 0 & 0 & 0 & 1 \end{bmatrix}, \quad (2-10)$$

where \mathbf{M}_t is the homogeneous transformation matrix. After transformation, the orientation between each texture map and 3D model is implemented in accordance to the process described in section 2.4.

Finally, these texture maps are warped onto the 3D triangular faces of the polyhedral model to form the 3D color model associated with the digital model of the object. The whole 3D color model reconstruction procedure is shown in Figure 2-16.

2.6 Application example

A doll product is used to test and verify the proposed procedure for 3D color model reconstruction. The doll photo is shown in Figure 2-17(a). First of all, the laser scanner emits a laser beam on the object surface and digitizes the shape of the doll at 100 angular positions with a 3.6 degree step. When digitizing the darker object surfaces, the adaptive scan line capturing process is executed. The processing time is 3.5 minutes in this case.

After digitization, 27,656 points are obtained, and the scan lines are shown in Figure 2-17(b). Data pre-processing operations are applied to the digitized points, and then 3D triangular meshes are generated. The polyhedral model which contains 29,998 triangular faces is shown in Figure 2-17(c). Next, the digital camera and the light system are used to capture 4 color texture images at 4 angular positions with 90 degree increments. Then, it takes 10.75 minutes (CPU: Intel Pentium 4 2.4GHz, PC266 512Mb) to compute the relationships between the triangular faces and the texture maps. Finally,

color texture maps are wrapped onto 3D triangular faces, as shown in Figure 2-17(d). The final the 3D color model of the doll is shown in Figure 2-17(e). Another example, the penguin doll, has been also tested with the same procedure and the result is shown in Figure 2-16.

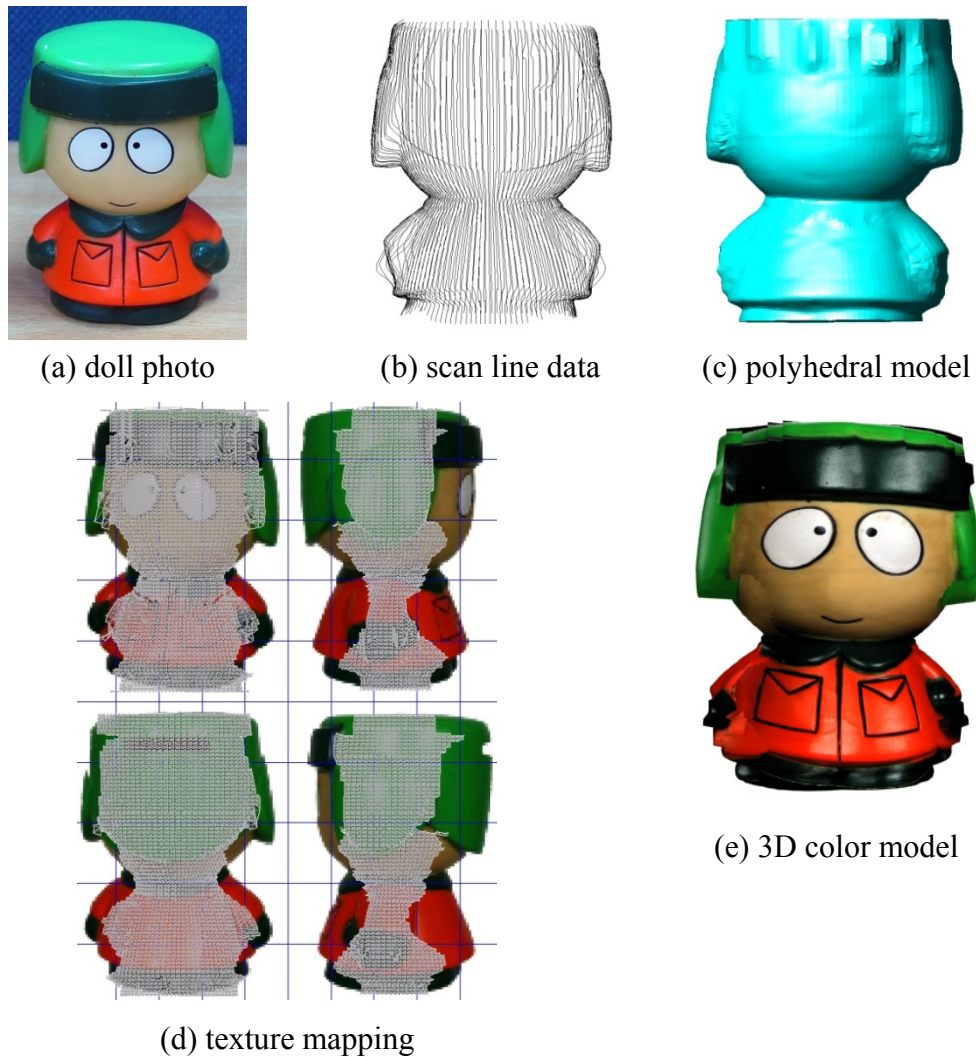


Figure 2-17 Application example.

2.7 Conclusion

An adaptive capturing process of color objects has been developed to acquire the digital data of color objects with a laser scanner and a digital camera without destroying their original colors. Furthermore, after scanning this kind of color object, an automated process, including a texture map generation and an orientation process between a polyhedron and a texture space, has been proposed to create its color model. Finally, an integrated scanning system has been developed based on the proposed approaches.

When applying a texture filtering technique on this color model, the extracted color

information can be used during the TPP manufacturing preparation phase. A preliminary test [Jia et al. 07] carried out by Jia et al. is introduced in section 1.2.1.

Chapter 3

Product view Interface for TPP micro-manufacturing of non-manifold models

As mentioned in section 1.1.5, the PV reference model is one of the kernel elements in the product view of the preparation process for TPP micro-fabrication. In order to produce the result reliably and efficiently in the following simulation processes, it is necessary to develop specific model processing techniques for preparing the product models. In this chapter, some applications of micro-products are investigated for finding major requirements of reference models to drive the TPP micro-fabrication preparation process. After surveying previous literatures, it has been considered that using non-manifold models to represent the product manufacturing model is very suitable for meeting our purposes in TPP micro-fabrication preparation process. However, until today, commercial CAD modelers don't incorporate efficient modeling capabilities to describe non-manifold objects. In addition, these shapes cannot be exchanged between product views through standards like IGES or STEP. To overcome these critical issues, some specific treatments like a method for determining boundary overlaps and a tessellation algorithm, etc. are developed within the framework based on our previous researches.

3.1 Introduction

The demand for fabricating smaller and smaller features is increasing to meet the functionalities of micro-products and to reach a higher level of function integration enabled by the micro-system technology. Elementary shapes of a micro-manufacturing process usually form a basis of the needed features to produce such micro-products.

From the 'real world' point of view, these features all have volumes and these micro-products can be regarded as volumes. However, from the digital point of view, they could just be modeled by curves or surfaces. In other words, the digital model of a micro-product manufacturing model, i.e. the PV reference model for TPP micro-manufacturing used as basis to generate laser beam trajectories, could be based on curves, surfaces, and volumes depending on the main parameters of the manufacturing process. These kinds of manufacturing models fall into the category of

non-manifold models and are greatly different from digital models of classical mechanical components manufactured with machine tools where volume models form the input of tool path trajectory calculations. Figure 3-1 shows four different volume models of micro-products. As for contrast, Figure 3-2 shows the possible non-manifold models of the same micro-products as in Figure 3-1.

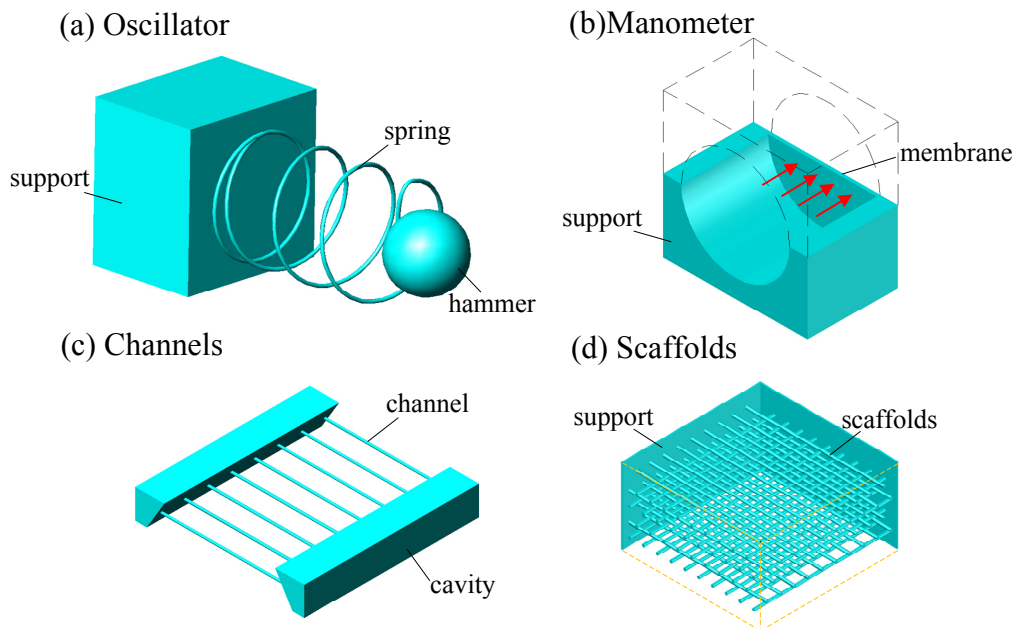


Figure 3-1 Volume models of micro-products.

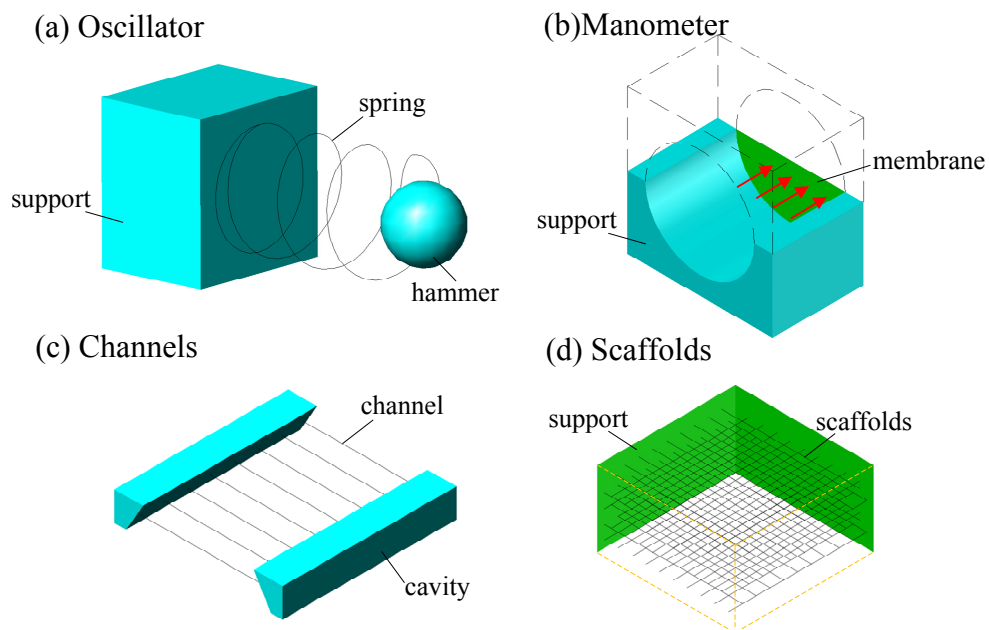


Figure 3-2 Possible non-manifold models of micro-products.

Figure 3-1(a) illustrates a digital model of the sub-micro oscillator fabricated by Sun et al. [Sun et al. 01]. This oscillator includes three elements: a support, a spring, and a hammer. Since the spring constant (k) and spring radius (r) have the relation of $k \propto r^4$, we can say that the size of the spring radius is the main parameter and it controls the mechanical behavior of the whole oscillator system. Being restricted by current commercial CAD models, the digital model of the spring probably uses a tubular volume or some other volume entities to represent this element. As a result, only large spring constants can be obtained. Figure 3-2(a) shows another possible digital model of the oscillator. If the spring model uses a wire (a non-volume entity) to represent it in the digital model for manufacture and fabricated directly along this wire direction, then the size of spring radius can be adjusted by controlling the section of the wire through the voxel size. As introduced in section 1.1.2, where the width of the voxel size can vary from sub-100 nm to 1 μm (depending on the laser beam power and the exposure duration), the possible manufactured region of the spring section can be greatly enlarged.

A membrane, i.e. a very thin wall, can be used to measure the fluid pressure when detecting the membrane deformation. When a membrane is subjected to a fluid pressure, its thickness influences the sensitivity of pressure detection. At the condition of identical fluid pressure, less thickness causes more deformation and an improved resolution if it is used in a sensor. As a result, the suitable way for creating its digital manufacturing model is to use a surface as a geometric entity containing the laser beam trajectories (see Figure 3-2(b)) instead of thin rectangular volume (see Figure 3-1(b)). The range of voxel sizes enables the generation of thicknesses covering the proportion of membranes at the scale of micro-products.

Divliansky et al. use the ‘positive-tone’ media to fabricate a micro-channel device [Divliansky et al. 05]. Figure 3-1(c) shows its volume model. The volumes and tubes represent cavities and channels, respectively. After the fabrication process is finished, the un-polymerized resin will remain and these elements will dissolve. Again, to generate the smallest diameter of channels possible, a suitable way is the use of wires to represent them in the digital manufacturing model, as shown in Figure 3-2(c).

Cunningham et al. built 3D scaffolds for tissue engineering [Cunningham et al. 06], and their volume model is shown in Figure 3-1(d). The scaffolds are composed of a set of tubes organized as woodpiles and the thin rectangular volumes are modeled as supports defining the positions of woodpiles. If we use wires instead of tubes (see Figure 3-2(d)) in the digital manufacturing model, then it becomes possible to raise substantially the density of woodpiles. In tissue engineering, it can provide more areas to speed up the growth rate of cells.

Referring to the above application examples of micro-products, one fact is observed that using volume models for the digital manufacturing models of micro-products doesn't meet the requirements of micro-manufacturing. Besides, a volume model can be undoubtedly generated through a slicing algorithm to produce contour lines defining the laser beam trajectories to form the volume boundary. However, too tight contour lines will be obtained if the model has extremely thin features. In TPP micro-fabrication, over polymerization may occur in such areas and causes the collapse (as mentioned in section 1.8.4).

Below the content, the requirements and arguments about the reference model preparation for TPP micro-manufacturing are emphasized and discussed further. Then, corresponding treatments and strategies have been developed to solve the above issues.

3.2 Combining micro-product shapes and functions within the TPP fabrication process

Prior to address the functions of a micro-product, two complementary configurations should be distinguished:

- a micro-product represents a single component quite similarly to a classical mechanical component,
- a micro-product describes an assembly of components.

In both configurations, one characteristic of the current TPP process is that it should deliver an object that must be usable directly after the TPP process stage, i.e. there is no assembly process taking place after the manufacturing stage. As a result, the micro-product produced should incorporate all the product functions available in an assembly, e.g. the relative movements between the components of an assembly. However, this thesis only addresses micro-products made up from a single piece of material (handling multi-component micro-products is future work). Even with single parts, relative movements between functional surfaces of the micro-product are obtained through mechanisms such as deformable linkages used to obtain small amplitudes of relative movements in classical mechanical components. In chapter 5, Figure 5-10 depicts an example of such a microstructure where the plate lying in the middle of the microstructure aims at rotating around the vertical wires attached to it. The torsion of these wires is equivalent to a vertical rotating joint between the plate and the gantry surrounding it.

Besides, based on the fact that:

- a strong objective of the ongoing research work is to downscale as much as

possible the size of the products,

- the voxel size and aspect ratio can vary enough within a significant range to adapt the thickness of membranes or wires,
- the laser beam power dissipated per voxel may have an important impact over the resulting shape, so there is an interest in avoiding, as much as possible, laser beam paths that are too close to each other.

Toward this goal, manufacturing a wire can be reduced to a single laser beam trajectory using the voxel size to monitor its section. Similarly, manufacturing a membrane reduces to a trajectory path lying on an open surface with a thickness monitored through the voxel size. Manufacturing a solid object is addressed here as the manufacture of a closed shell whose interior will be polymerized at a later stage to speed up the overall process (this method is called CSM and mentioned at section 1.8.2).

Such a single micro-product brings new concepts related to the manufacturing capability of the TPP: it can be seen as a connected set of blocks, plates or membranes and wires welded altogether. In a way, this concept is similar to sheets of metal welded or bolted together to produce a global structure. Since the voxel size parameters can be set within the range specified at section 1.1.2, the minimum wall thickness and wire section possible can be achieved with the smallest voxel size on the premise that the structure is strong enough. Thus, the laser beam paths producing such minimum thickness configurations are reduced to a polyline for a wire and a tessellated surface for a membrane or a plate.

Anyhow, the envelope of the voxel positions define solids but its shape may not be trivial in general compared to that of the laser beam paths needed for wires or thin shells. In addition, the laser beam path trajectories computed from the volume model of a micro-product, assuming it contains wires and thin shells through offset surfaces, could lead to nearly superimposed trajectories. That would be difficult to clean up to avoid densification of laser beam energy in such shape features.

The voxel size parameters can be regarded as strict manufacturing parameters like the pitch of a thread whereas the digital representation of a wire will be reduced to a line (in a similar way to a threaded hole whose digital CAD model is often a cylindrical hole). Similarly, a membrane or a plate can be represented digitally by surfaces only, their thickness becoming a strict manufacturing parameter. Figure 3-2 illustrates such configurations where the digital models of the micro-products are defined by a set of connected lines, open and closed surfaces. Namely, these models are non-manifold ones that define the laser beam paths. Here, they designated as manufacturing models. The solid model defining the material domain of a micro-product can be called the design

model of the micro-product and is not explicitly specified in the proposed approach.

Starting from a 3D solid model defined in a CAD environment and computing laser beam paths based on offset trajectories would be a possibility close to classical CAM processes. However, paths close to each other would need to be detected and processed in a way equivalent to idealization operations performed on structural models which are complex treatments. The idealization operation (or dimensional reduction) of a CAD model involves reducing locally the degree of spatial analysis [Hamri 06]. From a geometrical point of view it produces a reduction of the manifold dimension of the model. This may involve reducing a 3D model to a 2D model or a 1D geometric model with many complicated topological modifications. In Figure 3-3, 3D solid models have been idealized to 2D or 1D structural models, i.e. solid models have been transformed to beam or to shell structural models [Armstrong 94].

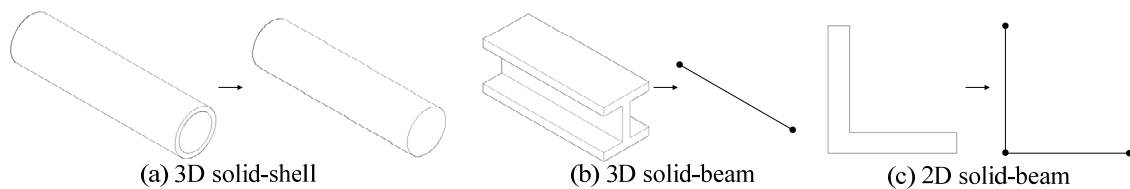


Figure 3-3 Various idealizations of 3D objects.

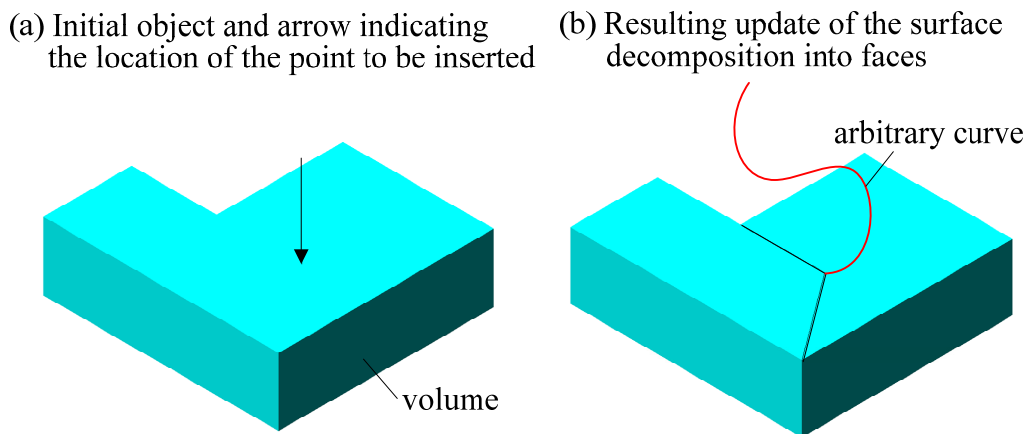


Figure 3-4 Surface decomposition required when an arbitrary surface point needs to be inserted.

To avoid addressing this complexity at the moment, non-manifold shapes appears as a necessary model type to reach a compromise between the TPP capabilities, the micro-product description and its usage functions. However, modeling such shapes incorporates CAD modeller constraints about the model boundary decomposition [Hamri et al. 06] that have neither functional nor manufacturing meanings because some

boundary decompositions take place to create connections between surfaces or lines, generating extraneous geometric elements. For example, when a user needs to link an arbitrary curve to a volume at a point that is not part of its shape, he/she needs to subdivide the surface to insert new arbitrary curves, edges meeting at the point of interest so that this point is effectively part of the shape model (see Figure 3-4). As a result, the new surface decomposition (Figure 3-4(b)) incorporates edges and faces that bear the same meaning as the ones produced during the initial shape generation (Figure 3-4(a)) whereas they are semantically different. Indeed, this prescriptive behavior of the surface description can be regarded as a ‘noise’ generator in a component shape that requires further downstream treatments to get rid of these unnecessary prescriptions.

In addition, non-manifold shapes cannot be exchanged between product views through standards like IGES or STEP, i.e. the connections between line, surface and volume sub-domains does not exist as basic entities in these standards. Therefore, the connections between wires, open surfaces and volume areas cannot be expressed through these standards and transferred between software applications.

Finally, the micro-manufacture of a unique non-manifold component with a complex shape can be also addressed through specific capabilities requiring true 3D paths rather than 2D $\frac{1}{2}$ paths as it is the case for standard LM techniques. Based on the capabilities of the TPP manufacturing equipment available, the elementary path between two arbitrary reference points is in fact a 3D vector, thus enabling arbitrary 3D trajectories and hence, complex shaped objects. Such a capability is also mandatory to be able to manufacture arbitrary-shaped wires in 3D space.

The above configurations of assemblies and components represented by non-manifold models show that the functions of the obtained micro-product should be embedded in it. Membranes and wires are regarded as particular structural functions of an object. Whether micro-products behave like assemblies or standalone components, wires and plates are linked together. Due to the principle of the TPP process they can be considered as welded together and, as such, they may need specific manufacturing features to reinforce their links along their non-manifold connections to stiffen the structure and meet in-usage structural requirements of the micro-product. This is discussed further at section 4.5.1.

3.3 High level topology and mixed shape representation

As mentioned before, B-Rep NURBS stays the most widely used model representation for CAD applications in the industrial context. Then, based on different product views purposes, this B-Rep will be transformed into other shape representations

to proceed with simulation or manufacturing processes. Often, it would lead to a tessellation and a category of polyhedral model approximating the B-Rep NURBS one. The resulting model is generally based on triangular facets. Indeed, polyhedral models for describing shapes are widespread and compatible with many product views objectives. In this thesis, the same concept is adopted because during the TPP preparation process, i.e. the slicing process, the targets are laser beam trajectories defined by polygons. Instead of processing complex B-Rep NURBS models, polyhedrons can greatly simplify slicing algorithms and trajectory generation much in the same way it is set up for rapid prototyping.

To tessellate a non-manifold model, as it is needed here, surfaces or volume sub-domains must be processed differently compared to wires. Therefore, most of the present tessellation algorithms must be adapted for the tessellation of non-manifold models.

In addition, the polyhedral representation is not sufficient to address high level operations. It requires a higher level topology and geometry support to reflect the initial geometry of the B-Rep model and establish link with it to improve the efficiency of the model processing operators.

To address the above issues, previous research work performed at the G-SCOP laboratory [Hamri 06] led to the concept of High Level Topology (HLT) representation and mixed shape representation, which are introduced below as basis of the present work. The HLT representation is used to store and process the topology of non-manifold objects. Besides, the tessellated polyhedral model is linked to the HLT data structure through partitions and polyedges entities and these links, with the addition of the B-Rep NURBS model compose the proposed mixed shape representation.

3.3.1 The concept of High Level Topology (HLT)

As mentioned before, there are various shapes involved in the reference (or manufacturing) model preparation for TPP micro-manufacturing. For example, a shape may be represented as a B-Rep surface or wire-frame representation as input, and may be approximated by a polyhedron representation during the manufacturing simulation process. To achieve consistency between all the shapes involved, a common topology representation is necessary.

The HLT representation is a common topology representation and can be applied to handle not only manifold objects but also non-manifold ones (see Figure 3-5). Therefore, it can be used to represent all the required shapes during the preparation process for TPP micro-manufacturing.

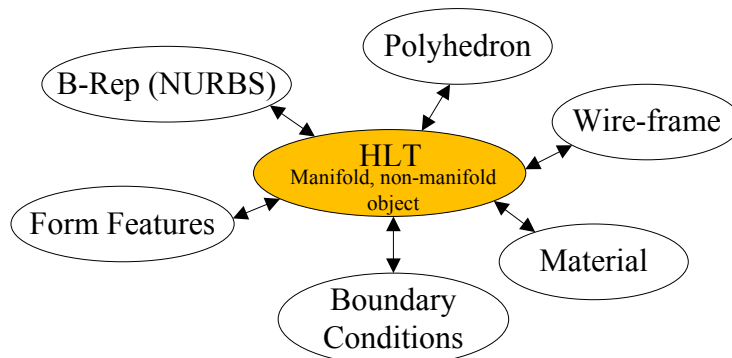


Figure 3-5 A common topology representation: HLT applied to an application of product behavior simulation.

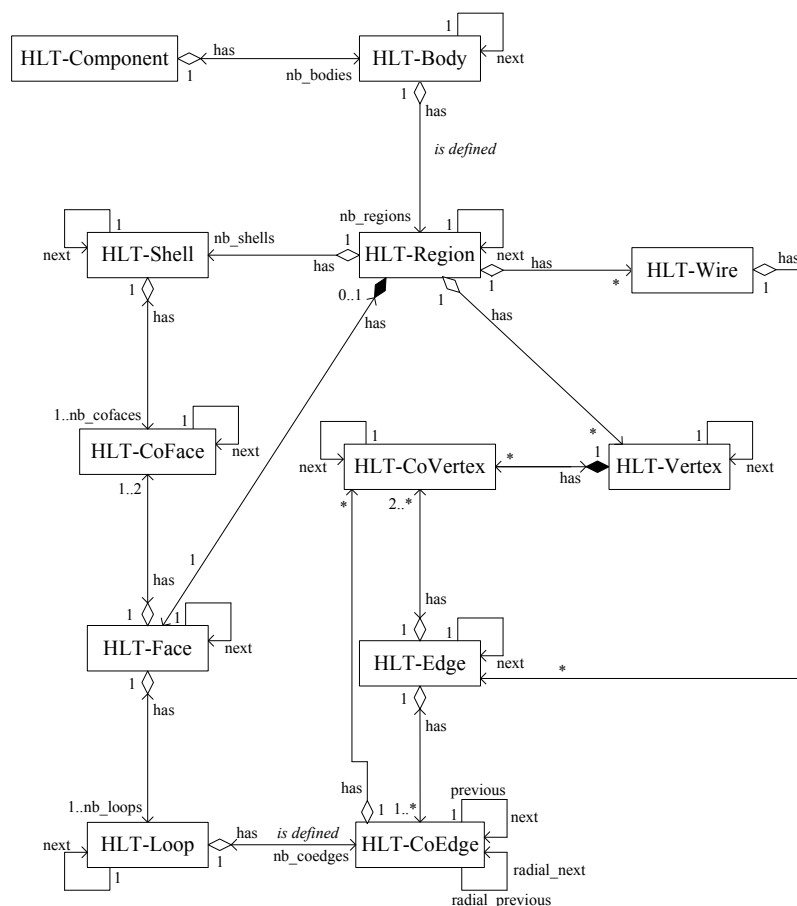


Figure 3-6 HLT data structure (UML representation).

The relationships between HLT entities are depicted in Figure 3-6 and expressed through the Unified Modeling Language (UML) graphical representation. In the HLT representation, a face, an edge and a vertex are called HLT-Face, HLT-Edge, HLT-Vertex, respectively, to distinguish them from faces, edges and vertices entities related either to polyhedron or B-Rep NURBS models. Moreover, additional

topological entities have been included to logically group HLT-Face, HLT-Edge, HLT-Vertex into HLT-Loops, HLT-Regions, HLT-Shells to express higher level concepts or to define specific element occurrences needed in the non-manifold configurations, i.e. HLT-CoFace, HLT-CoEdge, HLT-CoVertex. HLT-Regions, HLT-Shells are used to describe volumes and shells sub-domains in general non-manifold configurations. A specific entity, HLT-Wire, describes line sub-domains of non-manifold model. The concept of HLT-Region is used to describe a connected set of areas of type line, surface or volume generating non-manifold configurations. Lastly, a HLT-Component, the highest level of topological entity, is used to logically group all entities to be able to describe objects composed of disconnected pieces. Here, each such piece will be assigned a HLT-Region as topological entities. In addition, the links and interactions between the HLT data structure and others used in this thesis are also introduced in section 3.4.

The original purpose of HLT aims at supporting efficiently all the processes in the FE reference model preparation where non-manifold objects are very common. Here, this thesis does not intend to introduce all HLT entities completely. Only the first three levels of topological entities, i.e. HLT-Component, HLT-Body and HLT-Region, are discussed. Through them, the differences of topological configurations between manifold and non-manifold objects described through a HLT representation can be expressed. Further, these explicit definitions act as a complement to develop the mixed representation scheme and help produce a robust tessellation algorithm for non-manifold models described in the following tessellation process (see section 3.6). The topological entities: HLT-Component, HLT-Body and HLT-Region are characterized as follows:

- HLT-Component:

A HLT-Component entity must be composed of at least one HLT-Body. In this case, the constituting bodies must be disconnected, this means that two distinct bodies cannot share faces, edges or vertices otherwise they would form a unique non-manifold HLT-Body. In this configuration, a HLT-Component can be interpreted as an element of an assembly where each HLT-Body represents an entity of this assembly. Under this type of information, this concept can be extracted from the STEP AP 203 standard.

- HLT-Body:

A HLT-Body is composed of one or more HLT-Regions. For example, two boxes sharing one face can be seen as a non-manifold component with three regions: an infinite external region and two bounded internal regions.

- HLT-Region:

To express the space dimension where the topological entities are immersed, the concept of HLT-Region is introduced. A HLT-Region must contain manifold entities. Based on different space dimension characterizing a manifold sub-domain (it can be either 1, 2, or 3), different HLT entities can be classified. For example, if the Euclidean space dimension equals 3, the HLT-Region can be:

- A volume described by its boundary, which is a HLT-Shell, with a manifold dimension equal to 3. In this case, the HLT-Shell must be closed. It should be also noticed that the associated HLT-Shell must be a sub-domain with a manifold dimension equal to 2,
- An open surface described by its boundary which is represented by HLT-Loop entities and has a manifold dimension equal to 2; in this case, the HLT-Shell describing the HLT-Region must be an open HLT-Shell and its boundary is immersed into HLT-Faces,
- A line described by its boundary which is represented by HLT-Vertex entities and has a manifold dimension equal to 1. In this case, the HLT-Wire describing the HLT-Region can be either open or closed and its boundary is immersed into HLT-Edges,
- A point described by its boundary which reduces to a HLT-Vertex with a manifold dimension equal to 0.

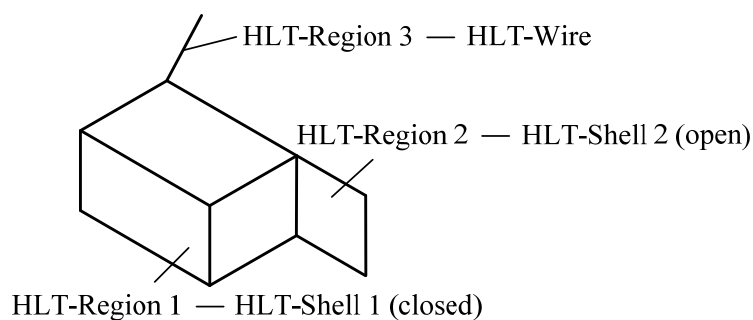


Figure 3-7 Example of HLT-Component with one non-manifold HLT-Body.

Figure 3-7 is a typical non-manifold shape example. A main sub-domain is a rectangular volume, and some of its edges and vertices are shared with an open surface and a line, respectively. Using the HLT representation to describe this non-manifold shape, the first two levels of the topological structure would be a HLT-Component with a unique non-manifold HLT-Body. It indicates that this shape is a single non-manifold

part and cannot be perceived as an assembly. The HLT-Body contains three HLT-Regions whose lower levels are HLT-Shell 1(closed), HLT-Shell 2(open) and HLT-Wire, and store the topological information of the rectangular volume, open surface and line, respectively. Then, geometrical information can be associated to these topological entities.

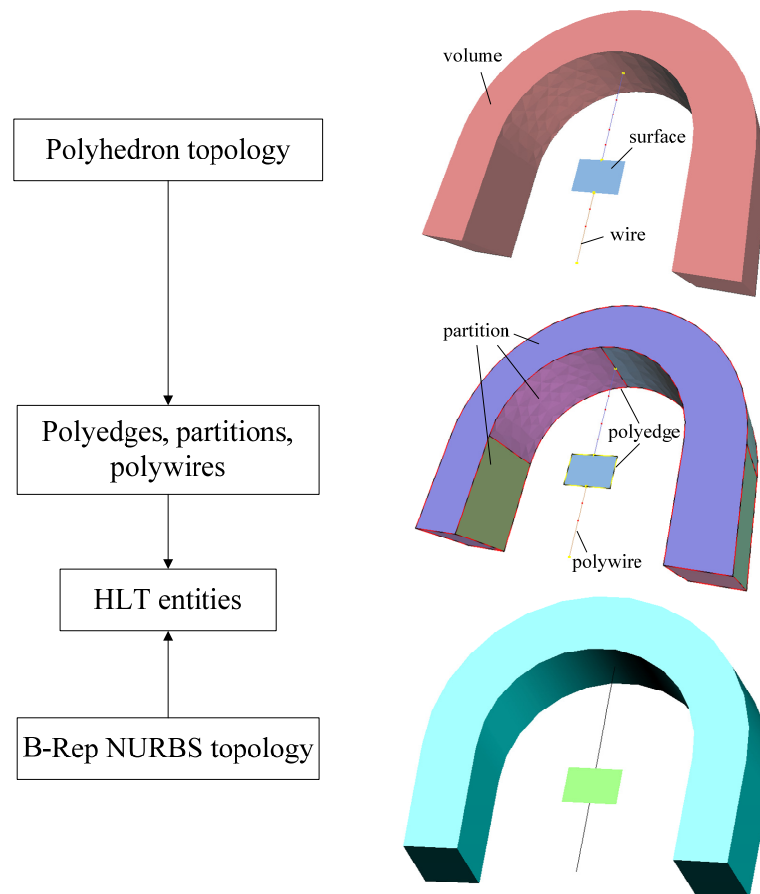
3.3.2 The concept of mixed shape representation

In many previous researches, the STL file format plays a key role about data exchange between CAD modellers and CAM systems [Park et al. 05, Divliansky et al. 05, Cunningham et al. 06]. However, the STL file format lacks of model topology description, i.e. in a STL file, there is no topological relation between the triangles forming the surface of the model. It has also to be considered that model processing efficiency can be significantly reduced if the triangle size in a STL file is uniformly decreased in order to keep some critical small features. Besides, computing TPP paths cannot be robust when handling non-manifold models because the connections between triangles cannot be always correct since there is no information able to distinguish non-manifold configurations from manifold ones when triangles are close to each other, hence triangle adjacency relations cannot be decided if non-manifold models are described with a set of disconnected triangles only.

As mentioned in previous sections, this research work uses a STEP file format as input. Indeed, a STEP file contains topological information as well as geometric information about B-Rep NURBS models, so it can process efficiently these models during the tessellation process. However, the resulting polyhedral model is a linear approximation of the initial NURBS model that uses polygons to describe the original shape. Therefore, there are shape deviations between the original B-Rep NURBS model and its derived polyhedron. Generally, the topological relations between these two models are ignored. As a result, some high level operations (for example, the ‘welding-like’ function mentioned at section 4.5.1) which needs higher level topology and geometry support to process robustly the initial geometry of the B-Rep model cannot be applied on a polyhedral model because the adjacency relations contain only low level information.

The concept of mixed shape representation is developed to let the B-Rep model and its derived polyhedral model have tighter topological links and coexist simultaneously. Figure 3-8 shows the main constitutive elements of the mixed shape representation and their corresponding relations. If a B-Rep NURBS model is input, a polyhedral representation is effectively generated. In the meantime, the B-Rep model is kept also and connected to this polyhedral representation. It is not a model conversion,

and both representations are linked with each other during the whole ‘PV Reference model’ preparation, hence the term ‘mixed shape representation’ designates this configuration. Linking directly the topological entities of a polyhedral model to HLT entities is not possible because they don’t match generally. To achieve the desired link, ‘polyedges’, ‘polywires’ and ‘partitions’ are introduced:



In the middle right of the figure, the dotted red/black and yellow/black polylines are the polyedges of the closed surfaces and open surfaces, respectively. The dotted red polylines are the polywires. Each partition is represented with a different color to outline each of them.

Figure 3-8 Main constitutive elements of the mixed shape representation and corresponding relations.

- **Polyedge:**

Polyedges are defined as a set of connected edges of a polyhedron such that it forms a manifold of dimension 1, i.e. the geometric description of a polyedge is a polygon discretizing a curve. A polyedge is connected to the 3D mesh of a HLT-Edge,

- **Polywire:**

A HLT-Wire may be composed of several HLT-Edges. A polywire is connected to the 3D mesh of a HLT-Wire, i.e. a collection of polyedges,

- Partition:

Partitions are defined as a set of connected faces of a polyhedron such that it forms a manifold of dimension 2, i.e. the geometric description of a partition is a polyhedron, either closed or open, discretizing a surface. A partition is connected to the 3D mesh of a HLT-Face.

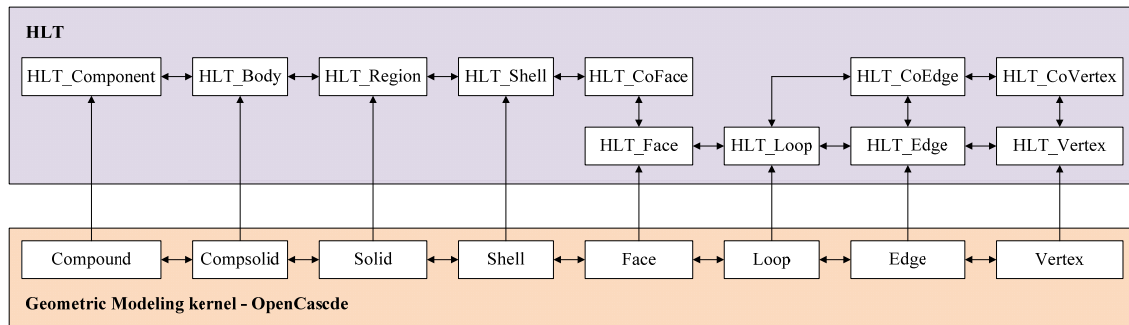


Figure 3-9 Interface between a CAD model and the HLT data structure.

3.4 The software environment for the model preparation process

Hence, we allow designers to work in a well known context of a 3D CAD modeler of their choice where the shape needed for the manufacturing process can be generated. This approach is a natural process in the current context of the TPP emerging technology and should evolve as soon as it will be possible to include well formalized process constraints during the micro-product design phase. To reflect the topology and geometry of the initial object to be analyzed, the HLT is created directly from this B-Rep NURBS object and linked to the partitions, polyedges and poly-wires built on top of the polyhedron model. As a result, to be able to accept a wide range of input data, like the STL, VRML... file formats, but to keep the necessary geometrical and topological information in a polyhedral model after the tessellation process and attach it to a NURBS model, the STEP file format must be used as input source. The STEP entities are loaded into the B-Rep CAD data structure of a hosting CAD modeler. In the implementation described in this thesis, we used Open Cascade as the host geometric modeling system. At this level, non-manifold solid models have been considered as they can be available in CAD systems through STEP files. The interface between a CAD model and the HLT data structure is shown in Figure 3-9.

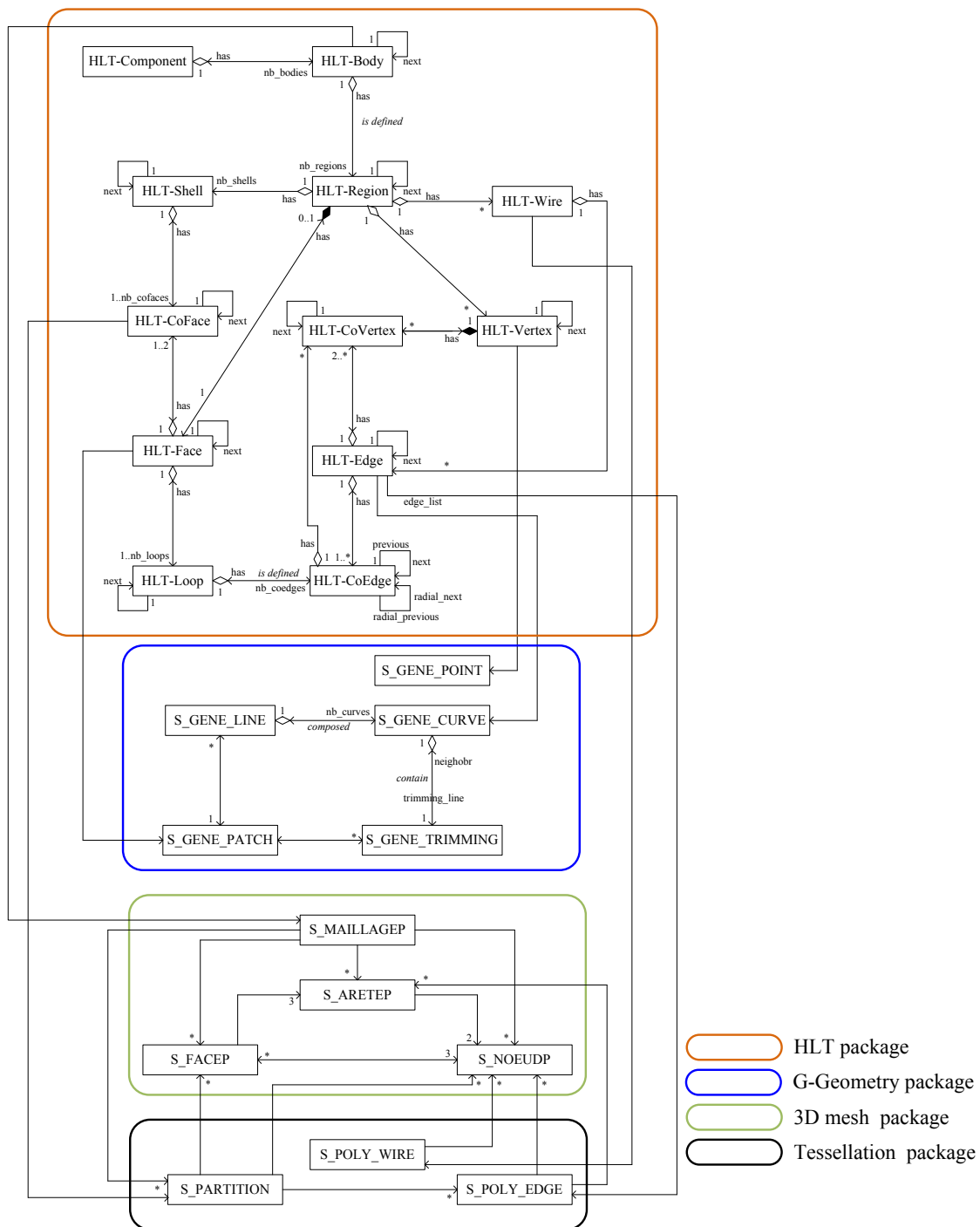


Figure 3-10 The links between the various software packages.

The Figure 3-10 illustrates the main software packages used in this research and the links between them. The main features of these four packages are:

- HLT package: to store and process the topological data suited for non-manifold models,
- Generic-geometry (G-Geometry) package: to store and process the geometrical data defining the NURBS model,

- 3D mesh package: to store and process the polyhedron data,
- Tessellation package: to generate a polyhedron model and link it with the HLT data.

The HLT package is connected to the G-Geometry and the 3D mesh packages. The HLT-Geometry establishes a link between the HLT-Face, HLT-Edge, HLT-Vertex, and their corresponding geometry description i.e. GENE-PATCH, GENE-CURVE, GENE-POINT, respectively.

The Tessellation package i.e. concepts of the polyedge, polywire and partition, maintains a geometric semantic over the polyhedron using a specific attribute attachment mechanism, i.e. P-DATA-LISTE, that stores the semantic of a particular application, e.g. the TPP preparation process, attached to the geometry of HLT-Edges, HLT-Wires, and HLT-Faces, respectively.

Similarly, for each HLT-Body entity attached to a HLT-Component, one polyhedron, i.e. a S-MAILLAGEP on Figure 3-10, is associated to it.

The above elements also justify the need for an autonomous topological description at the polyhedron level as depicted in Figure 3-10 in the green frame. The structure also justifies the term HLT since the polyhedral model, including its topological description, is the reference one for the shape transformation operators and the HLT data structure is effectively acting at a higher level to semantically annotate the polyhedron model at which it can be attached while enabling the development of high level operators.

3.5 The manufacturing model preparation process

The previous sections have shown that micro-manufacturing capabilities combined with the functional requirements of a micro-product have led to digital models for micro-product manufacturing that can be represented as non-manifold objects. The purpose is now to describe how these non-manifold models can be processed. Based on the LM principle, it is shown how this concept needs to be adapted to get a compromise between the manufacturing parameters and the shape complexity to produce a microstructure.

As depicted by Figure 3-11, the process flow of the manufacturing model preparation for TPP micro-fabrication starts from the 3D model generation using a standard CAD modeler. Indeed, using commercial CAD modellers is restrictive because they don't incorporate efficient modelling capabilities to describe non-manifold objects. However, the subsequent steps of the model processing scheme reduce the effect of this

limitation.

Non-manifold models can be generated through wireframe-based modules where lines, surfaces, volumes can be either stitched together or only positioned with respect to each other to produce the desired configuration. Then, they are exported to our specific software environment for TPP pre-processing and micro-manufacture and converted to a mixed representation.

The model exchange file format between these two environments is the STEP standard. In the present context, using this file format has the following characteristics for TPP pre-processing:

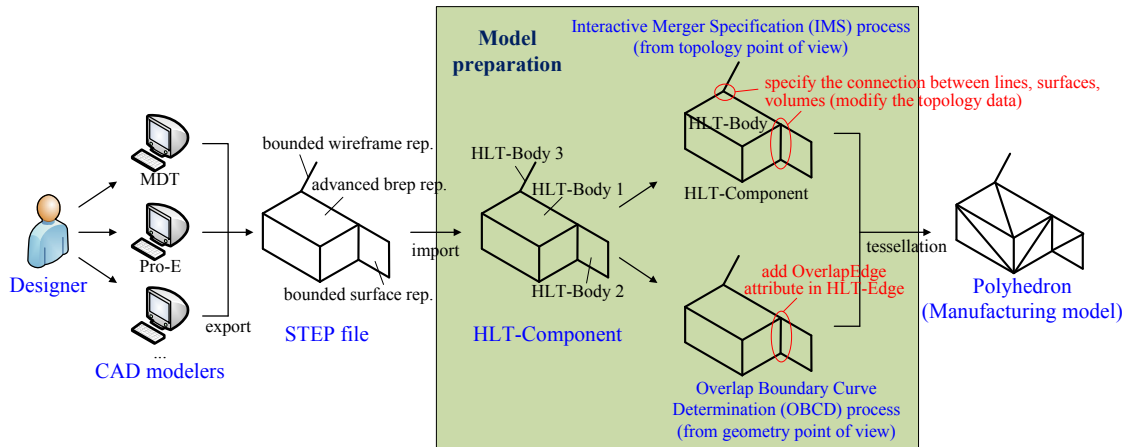


Figure 3-11 The manufacturing model preparation process for TPP micro-fabrication.

- it is possible transfer a subset of the microstructure topology, i.e. volumes defining a standalone cell, open surfaces made up from a collection of patches, connected lines,
- the overall non-manifold topology of a microstructure cannot be transferred since STEP standard does not incorporate such a feature but no other file format is able to transfer this information,
- the 3D trimming lines characterizing the connection between adjacent patches are available in the STEP file.

In addition, the stakeholders of this process need adapting the following rules to create digital models of micro-products:

- based on the stakeholders' domain of knowledge, they need to use the minimum numbers of steps to create digital models of micro-products in CAD modelers to avoid producing too complex topological data structures to express the connections between different sub-domains. Indeed, such connections are

useless since they cannot be exported using the STEP standard,

- whatever CAD module the stakeholders use to create shape sub-domains of micro-product models, these models must to the export through the STEP standard AP203. After STEP models are transformed into a mixed representation and because non-manifold connections among shape sub-domains cannot be represented through STEP, an ‘assembly’ configuration (each disconnected shape sub-domain is described to as a HLT-Body) is represented within a single HLT-Component.

After a STEP file is input into the TPP product view and the non-manifold shape of the micro-product is obtained as a collection of disconnected sub-domains, two methods are proposed in this thesis to produce a manufacturing model corresponding to the shape requirements of TPP micro-manufacturing preparation process, i.e. the shape sub-domains must be properly connected to obtain a consistent representation of the non-manifold shape of the micro-product so that the slicing process can be successfully applied to produce continuous laser beam paths. One is called the Interactive Merger Specification (IMS) process which uses user input to specify the connections between lines, surfaces and volumes and to apply the merging operations on their topological structures. The IMS process is discussed in section 3.5.1. However, if the configuration of merging boundary curves is not the one-to-one case, the Overlap Boundary Curve Determination (OBCD) process can be applied to find the connections automatically. The OBCD process is discussed in section 3.5.2.

3.5.1 Interactive Merger Specification (IMS) process

Based on the STEP file containing the description of the micro-product, the pre-processing environment for the TPP can start with the IMS process between lines, surfaces, and volumes. This process aims at creating a non-manifold model of the micro-product based on the disconnected sub-domains input because it is dedicated to the description and transformation of non-manifold objects. The connections between the elements of the micro-product are specified interactively since multiple solutions may exist to generate these connections, hence this process is not decidable and the present approach is to rely on the user’s understanding of the microstructure’s shape to monitor it.

The concept of IMS is to process a model from its topology point of view, and it has two types of merging operations:

- Merging vertices (HLT-Vertices): one vertex of a line, surface or volume is connected another sub-domain. Figure 3-12 depicts the possible combination of

sub-domains. Based on the connection configurations, two categories are distinguished (see Figure 3-13):

- there are corresponding vertices in the sub-domains being connected, and they can be merged in the topological data structure directly and easily,
- there is no corresponding vertex in the sub-domains being connected, hence there is a need for preliminary operations before merging the sub-domains.

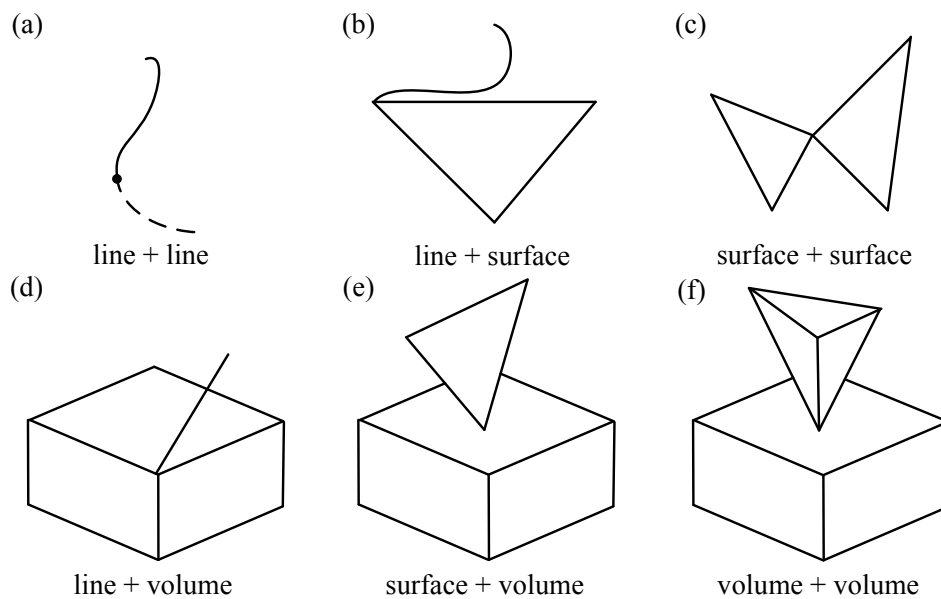


Figure 3-12 Possible shapes connected by a vertex.

- Merging boundary curves (HLT-Edges): at least one of the boundary curves of a surface or a volume is entirely or partially overlapping at least one of the boundary curves of another surface or volume. Figure 3-14 depicts some of these possible configurations. Based on the relation between overlapping boundary curves, three categories are distinguished (see Figure 3-15):
 - one-to-one case: one boundary curve is exactly overlapping another boundary curve,
 - one-to-multiple case: one boundary curve is completely overlapping at least two other boundary curves,
 - one-to-partial case: one boundary curve is partially overlapping at least another boundary curve.

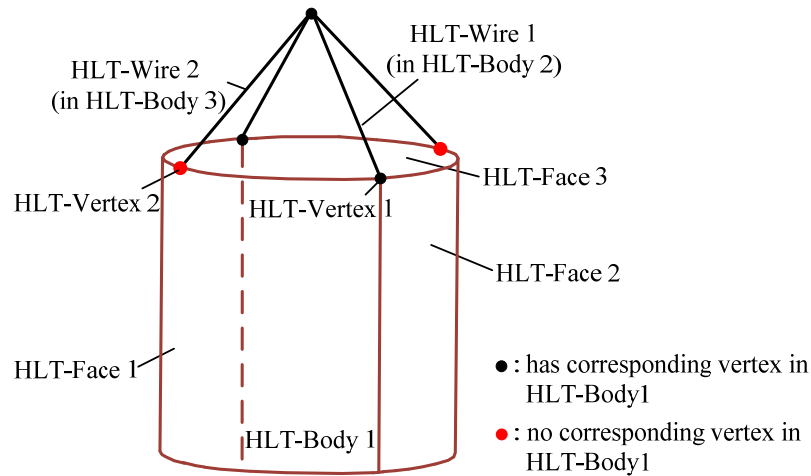


Figure 3-13 The merging configurations of vertices.

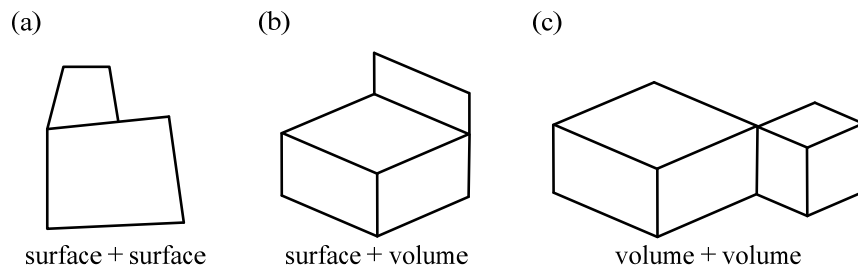


Figure 3-14 Possible shapes connected by a boundary curve.

To confirm whether two boundary curves in the one-to-one case are overlapping completely or not, the following constraints must be true:

- their two extremity points must be identical,
- the type comparison of the two boundary curves (the curve type is extracted from the STEP file and can be for example: a line, a circle, an ellipse, a Bézier curve, B-spline curve, ...) fits into one of the following configurations:
 - the types of two boundary curves are identical,
 - or the type of one boundary curve is a circle and the other one is an ellipse and its minor radius is equal to its major radius, i.e. it is degenerated into a circle,
 - or the type of one boundary curve is a line, and the other one is a Bézier or B-spline curve and its degree equals 2, i.e. it is degenerated into a line,
- the analytical data comparison of the two boundary curves are equivalent (for circle example it means same centre and radius).

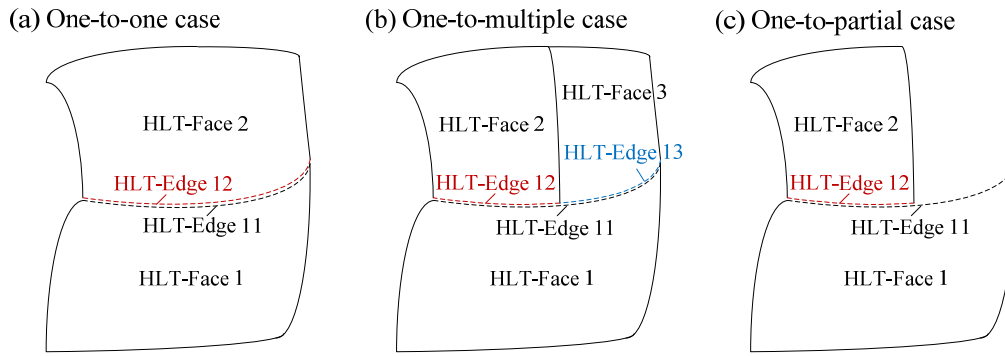


Figure 3-15 The merging cases of boundary curves.

In ideal situations, after the user has specified the connections and performed merging and other associated operations, the HLT topological structure of a micro-product could be updated and changed from the initial ‘assembly’ configuration (one HLT-Component contains several HLT-Bodies) to a non-manifold configuration (one HLT-Component contains one non-manifold HLT-Body with several HLT-Regions). Thus, a non-manifold model will be created.

Indeed, it is a good compromise and an easy way to let our TPP product view software having non-manifold capabilities based on current CAD models if the connections of vertices and boundary curves are simple. Indeed, this is not so straightforward. Due to the principles of model creation or the principles of STEP translations between different CAD modelers, there are cases where the topological merging processes are complex.

For example, Figure 3-16(a) shows a B-Rep NURBS CAD model created with the CAD software Autodesk Mechanical Desktop (MDT). It has two disconnected shape elements: a volume with a U-slot and a semicircle plane. After transforming this model to a HLT representation without any topological modification, we discover that the U-slot is described by two faces (HLT-Face 1 and HLT-Face 2 of HLT-Body 1), and the semicircle boundary curve of the semicircle plane (HLT-Face 1 of HLT-Body 2) is entirely covering one of the boundary curves of the U-slot. Now, it becomes a boundary curve merging issue corresponding to a one-to-multiple case (HLT-Edge 12 of HLT-Body 2 needs to be merged with HLT-Edge 11 and HLT-Edge 21 of HLT-Body 1).

Consequently, it is more complex than one-to-one case. To create such a non-manifold model correctly, users need to understand this situation and halve the semicircle plane to two quarter-circle planes, as shown in Figure 3-16(b). Thus, it reduces to a one-to-one case. HLT-Edge 11 and HLT-Edge 21 of HLT-Body 1, and HLT-Edge 22 of HLT-Body 2 will be merged with HLT-Edge 12 of HLT-Body 2, and HLT-Edge 13 and HLT-Edge 23 of HLT-Body 3. After finishing the above merging

operations, a non-manifold model (one HLT-Component containing one HLT-Body with three HLT-Regions) can be created.

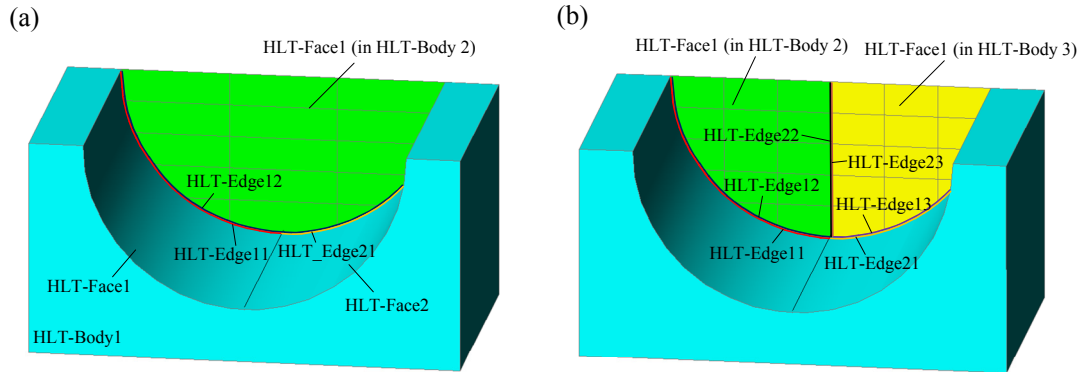


Figure 3-16 An example of the merging operation of boundary curves.

3.5.2 Overlap Boundary Curve Determination (OBCD) process

Performing the IMS process strongly depends on the modeling knowledge of the user and can be time consuming, especially when there no vertex matching configuration of vertices and no one-to-one case of boundary curves. From the geometric point of view, producing a non-manifold polyhedral model obtained from overlapping boundary curves is more complicated than the vertex connection issues. For this reason, the vertex connection issues are ignored here. Taking advantage of one HLT characteristics: the assembly configuration, an OBCD process is developed to solve the boundary curve overlapping issues.

In the transformation of a STEP file into a HLT representation, each disconnected manifold shape element is described as a HLT-Body with one HLT-Region and all HLT-Bodies are collected to form an assembly configuration (HLT-Component). If overlapping boundary curves between these disconnected elements are found, then these boundary curves use the same tessellation parameters in the tessellation process. such a process would solve easily the boundary curve merging issues and produces a conformable polyhedral model of the micro-product as it is required. Hence, how to find the overlapping boundary curves quickly and automatically would be the first topic. To this end, a simple OBCD process (see Figure 3-17) has been developed to increase the efficiency of the model preparation process.

The main concept of the OBCD process is based on the HLT representation and the identification of all overlapping relations of HLT-Edges between different HLT-Bodies. All HLT-Edges are pre-tessellated and converted into 3D mesh data. Then, it uses a least squares method to qualify the overlapping level (no, partial, or complete overlap) of two

HLT-Edges. In this research, an OverEdge entity is defined for store the overlap relationships of HLT-Edges, and it has two attributes:

- Master edge: it is the longest HLT-Edge among all involved in these overlapping HLT-Edges. During the proposed tessellation process (see section 3.6), if the master edge is processed, then the slave edges will be tessellated instead of it. It should be noticed that when each slave edge is processed as follows, the tessellation parameters must be identical to the ones used in master edge,
- Slave edges: a collection of at least one HLT-Edge which have some overlap with the master edge.

Data: *HLT-Component*

Result: *Lst-OverlapEdges*

foreach *HLT-Body* B_i **in** *HLT-Component* **do**

foreach *HLT-Body* B_j **in** *HLT-Component* **do**

if $B_j \neq B_i$ **then**

forall *HLT-Edges* **in** B_i **do**

 tessellate the current HLT-Edge E_m to Polyedge P_m

forall *HLT-Edges* **in** B_j **do**

 tessellate the current HLT-Edge E_n to Polyedge P_n

if P_m & P_n *are overlapping after comparing them by least square method* **then**

if *the length of* $E_n \geq E_m$ **then**

 set *MasterEdge* = E_n and *SlaveEdge* = E_m

else

 set *MasterEdge* = E_m and *SlaveEdge* = E_n

end

if *MasterEdge is not exist in* *Lst-OverlapEdges.master* **then**

 set new *OverlapEdge* O

 let $O.master$ = *MasterEdge* and add *SlaveEdge* in $O.slaves$

 set O in *Lst-OverlapEdges*

else

 add *SlaveEdge* in *FoundOverlapEdge.slaves*

end

end

end

```

        end
    end
end
end
if Lst-OverlapEdges not empty then
    sort all slaves in each OverlapEdge and place them in sequentially
end

```

Figure 3-17 The overlap boundary curve determination algorithm.

3.6 Tessellation of a non-manifold product model

In many previous researches on TPP micro-fabrication, a B-Rep NURBS CAD model of a micro-product is tessellated to generate an approximated polyhedral model described in a STL file format supported by most commercial CAD software [Divliansky et al. 05, Park et al. 05]. Since this polyhedral model is only composed of triangular facets, the contours of the micro-product can be easily obtained by a simple slicing algorithm. Unfortunately, only single surfaces or solid models can be tessellated into triangular facets because they are described by surface areas. Moreover, the STL file format is sufficient to describe volumes or open surfaces. A wire-frame model consists in wires, hence it cannot produce any triangular facets and it is not compatible with the STL format. Here, we concentrate on developing an extended-LM process which is suitable for non-manifold models. Therefore, a wire tessellation process tessellating arbitrary wires into a set of lines is needed.

Not only for wires, but it also exists other problems when tessellating an arbitrary non-manifold object. Figure 3-18(a) shows a typical non-manifold model which is formed by an L-shaped solid, a planar surface, and an arched wire. If the planar surface is not topologically connected to the volume sub-domain, the tessellation process will result into a non conformable polyhedral model. Although the L-shaped solid and planar surface are visually connected through two edges, they are considered as two disconnected entities and tessellated independently of each other even though they are represented as only one polyhedron after a general tessellation process, as shown at Figure 3-18(b). The inconsistent tessellation occurs at the edges connecting the sub-domains and result in cracks that are not correctly representing the connection between the sub-domains of the object. A logical crack is characterized by the vertex of a triangular facet lying on the boundary of another one. On the other hand, a non-manifold connection is characterized by one edge of a triangular face shared by more than two adjacent faces [Zhang et al. 02]. If a logical crack is a simple defect and doesn't affect directly the slicing result, a non-manifold connection does. It will confuse

the slicing process when determining which face follows the current one if the topological information attached to an edge cannot uniquely determine a laser beam path. Figure 3-18(c) shows that there are three choices of paths while slicing the polyhedron in Figure 3-18(b).

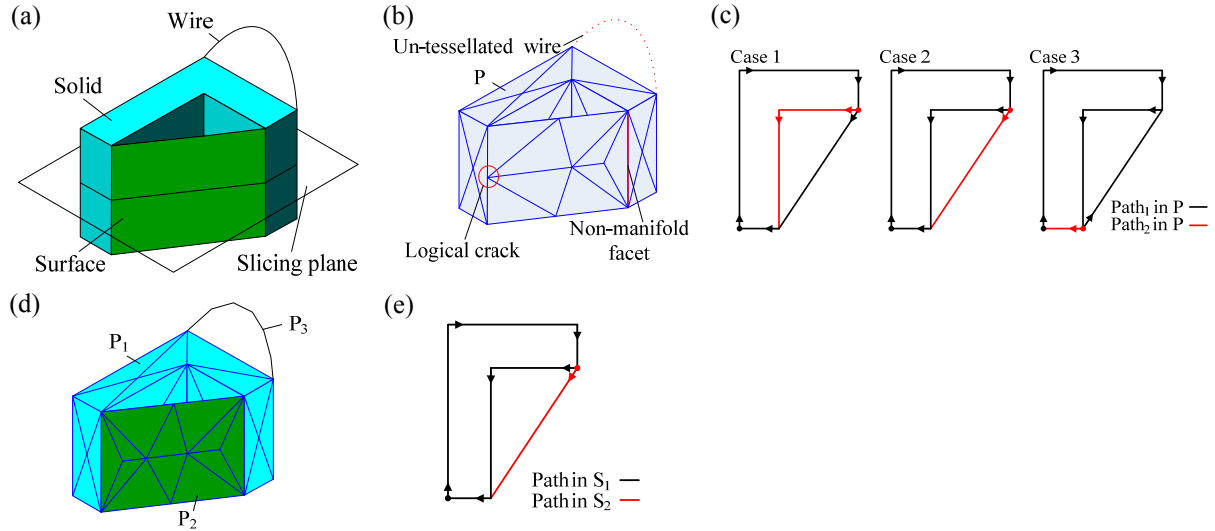


Figure 3-18 Comparison between a standard tessellation process and the proposed one.

The tessellation process used in this research is based on the mixed representation and the HLT data structures, and derived from Hamri's one [Hamri 06] plus the conformable discretization for OverlapEdges (this process will be introduced later). Before the HLT models are subjected to this tessellation process, IMS or OBD processes are implemented to produce a non-manifold HLT-Body including the detection of the overlapping boundary curves between HLT-Bodies. Figure 3-20 depicts the process flow of the proposed tessellation process. The significant steps of this tessellation algorithm for non-manifold objects are:

1. Input data:

- A HLT-Component which can be composed by a single HLT-Body or a set of HLT-Bodies, i.e. an 'assembly' configuration,
- A set of tessellation parameters, which are the max edge length and deflection between the input B-Rep NURBS model and the polyhedral one,
- An option parameter (only needed if the HLT-Component is an assembly configuration), which is a collection of OverlapEdges.

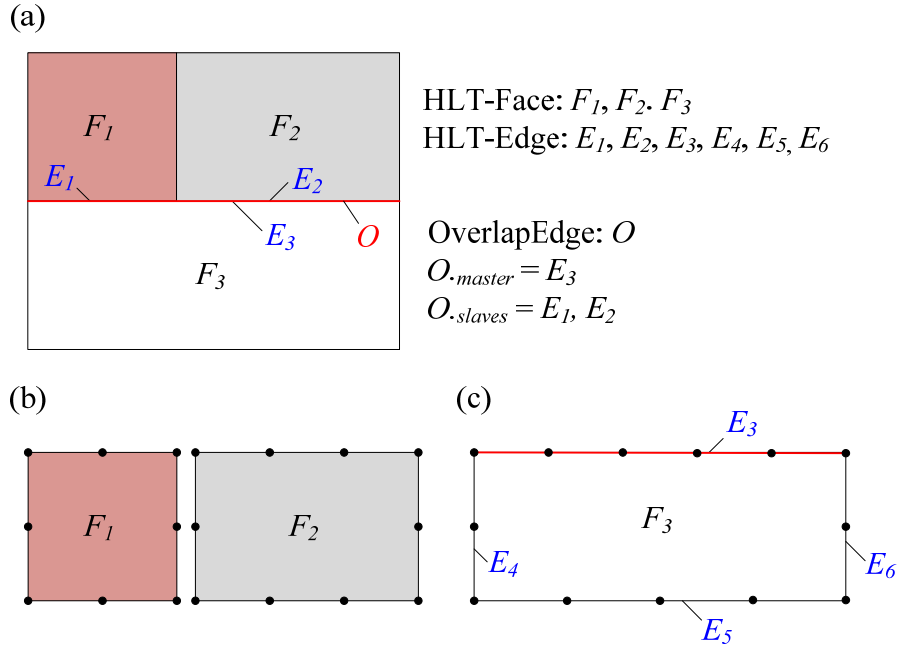


Figure 3-19 The exchange process of discretization results for OverlapEdges.

2. Scanning the object structure:

- A HLT-Component composed of several HLT-Bodies: during the HLT-Face tessellation, if the current HLT-Edge is a master edge in one of the OverlapEdges, then the conformable process for overlapping edges is applied (see block D in Figure 3-20). Figure 3-19 depicts how this process operates. Figure 3-19(a) shows a one-to-multiple merging case of boundary curves. There, an OverlapEdge O ($O_{\text{master}} = E_3$ and $O_{\text{slaves}} = E_1, E_2$) is created. Since all HLT-Edges of the HLT-Face F_1 and F_2 are not the master edge of the OverlapEdge O , all HLT-Edges are subjected to the standard discretization process of the face boundary curves (see the step1 of face tessellation), as shown in Figure 3-19(b). However, the HLT-Edge E_3 of the HLT-Face F_3 is the master edge, so that the discretization result of E_3 is replaced by the results of HLT-Edge E_1 and E_2 , to create a conformable tessellation. As for other HLT-Edges (E_4, E_5 and E_6) of HLT-Face F_3 , the standard discretization process is applied to the face boundary curves (see Figure 3-19(c)). After this process, the discretization result is conformable in the neighbourhood of OverlapEdge O .
- For each HLT-Region of a HLT-Body, the tessellation is performed in accordance to the type of the HLT-Region (see block A in Figure 3-20):
 - Case of a HLT-Shell: the tessellation process is performed on a patch by patch basis, each of them being associated with a HLT-Face. The boundary

curves of each HLT-Face are discretized with the same parameters, i.e. max edge length and deflection, according to their geometry types (line, circle, B-spline curve, ...),

- Case of a HLT-Face: the tessellation process is based on the discretization of the boundary curves of a HLT-Face (see block C in Figure 3-20 and face tessellation in the paragraph hereunder),
- Case of a HLT-Wire: the tessellation process is performed on a curve by curve basis (see block B in Figure 3-20). The curve geometry of each HLT-Edge is discretized with the same parameters (max edge length and deflection) according to their geometry types (line, circle, B-spline curve, ...),
- Case of a HLT-Vertex: no corresponding tessellation process. Therefore, the HLT-Vertex is straightforwardly associated to a polyhedron vertex corresponding to the geometric location of the HLT-Vertex,
- The tessellation of the whole object is performed on a HLT-Body by HLT-Body basis, i.e. each HLT-Body generates a corresponding tessellated polyhedron,
- A polyhedron is composed of several sub-domains and the number of sub-domains is equal to number of HLT-Regions in a HLT-Body,

3. Face tessellation:

The HLT-Face tessellation is the main part of the whole tessellation process and includes three steps:

- Step 1: discretization of the face boundary curves

The 3D boundary curves of the faces, i.e. HLT-Edges or slaves of OverlapEdges, are discretized according to the maximum edge length and deflection. Indeed, this operation ensures that the curves shared by several faces are meshed similarly in 3D space. Therefore, the tolerance used for the approximation of the trimming curves is exactly the same for the face triangulation and their vertices and edges are matching,

- Step2: 2D triangulation generation

The 3D points obtained at step 1 are projected into the parametric space of the face. Then, a first triangulation takes place using a constrained Delaunay triangulation,

- Step3: refine and transform a 2D triangulation into a 3D triangulation

can be developed. Now, the slicing targets change from a polyhedron to the sub-domains of a polyhedron, and these sub-domains are obtained from the different HLT-Regions forming the non-manifold object. The benefit is that a simpler sub-domain-based slicing algorithm can be developed, since it only concentrates on tracing open or closed paths in each sub-domain. Therefore, the slicing issue of multiple paths around non-manifold connections can be easily solved (see details in section 4.2).

In addition, the faces of the output polyhedron are constrained by form criteria (no very small angles to avoid numerical instabilities) and size (edge length lower than a given size) requirements in order to produce a satisfactory shape processing.

Figure 3-18(d) shows the result after applying the proposed tessellation process. There is now one polyhedron composed of three sub-domains, and meshes at the connected boundaries are identical, i.e. the tessellated polyhedron is conformable. Based on the non-manifold description of the polyhedron, the laser beam trajectory computation is able to distinguish the non-manifold vertices along the trajectory and produces only one result while slicing the non-manifold microstructure, as shown in Figure 3-18(e). One of the benefits is that each intersection path will not create a self-intersecting configuration, so that the double contour process, one of strategies for improving structure stiffness in this research (see section 4.5.2), can be applied to produce its offset path. In addition, the algorithm for laser trajectory planning also can be simplified. This is because in the TPP process, we need to avoid, as much as possible, the polymerization induced by laser light through already polymerized areas. If a laser trajectory contained self-intersections in a 3D path, i.e. this path does not lie on a slicing plane during the primary slicing phase (see details at section 4.4.1), avoiding the above situation would become more difficult.

3.7 Conclusion

This chapter has presented the specific model processing techniques for preparing a product model for its TPP micro-fabrication. Firstly, according to previous researches about micro-products manufacturing and the TPP specific properties, a non-manifold manufacturing model, i.e. a conformable non-manifold polyhedral model in this thesis, is proposed.

Then, with previous researches, HLT data structure and mixed shape representation are introduced in order to build the connections between the original B-Rep NURBS model and its polyhedral one. The software environment for the model preparation process has been presented here also.

Moreover, considering the present configurations of CAD software environments,

two auxiliary methods, IMS and OBCD processes, have been developed to help stakeholders creating a suitable non-manifold model of a micro-product.

Lastly, a tessellation process for non-manifold model, including specific features to handle OverlapEdges, is introduced to produce a conformable polyhedral model of a micro-product.

Product view simulation process for TPP micro-manufacturing

In chapter 2 and 3, the model processing techniques for preparing the micro-product model have been introduced. This chapter proceeds with representing simulation processing techniques to produce the key data defining the laser beam trajectories for these product models. Among these techniques, the proposed slicing algorithm is the principal phase to produce the laser beam trajectories used to generate a product shape. The others are developed to produce some auxiliary trajectories according to the TPP specific features such as structure stiffness, over polymerization, etc.

4.1 Introduction

After completing the preparation of micro-product model, a polyhedral model can be obtained from reverse engineering or from a CAD modeler. In any case, the polyhedral model needs the implementation of the follow-up simulation process to produce the voxel exposed positions contained in all laser beam trajectories. Since the CSM is the most efficient way to fabricate 3D products in TPP micro-fabrication, all the treatments of the simulation process described in this section complement the CSM.

However, there are some critical issues, such as ultra-thin layers and un-sliced areas, brought by CSM. In this section, they are discussed and solved by our proposed strategies. Regarding issues about the structure strength, there are two auxiliary techniques provided to stiffen the volume sub-domain and the connections between sub-domains of a micro-product. As for the laser focusing problem mentioned in section 1.8.5, a scanning path planning strategy is also taken into account to better schedule the laser beam trajectories of a micro-product model.

4.2 Laser beam trajectory path obtained from slicing a polyhedral model

Some basic intersection algorithms have been mentioned at section 1.8.1. This section describes further how to obtain the intersection paths from a polyhedral model. A polyhedral model is represented by a set of triangular faces, such as the polyhedral model created by reverse engineering in chapter 2. In addition, this polyhedral model can be closed to define a volume. Therefore, this chapter also discusses the necessity of non-manifold polyhedral model in micro-manufacturing. Such models can be formed of three types of sub-domains: volume, surface, and wire connected into a non-manifold polyhedral model. As shown in Figure 4-1 when slicing a volume sub-domain, the intersection paths must be closed, and when slicing an open surface, open paths are obtained. Although a set of points can be obtained when slicing a wire sub-domain and in turn, a wire can produce at least a dot per layer during the TPP slicing process. Taking the TPP manufacturing efficiency into account, the wire domains will be treated by another way and will be discussed in section 4.4.3.

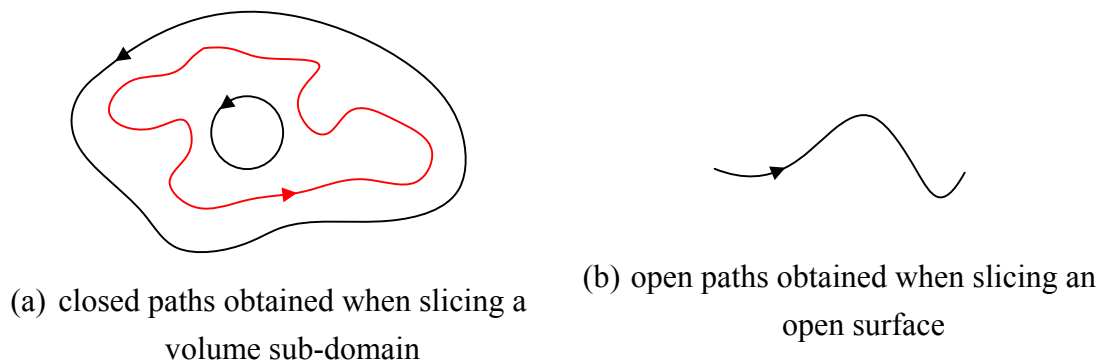


Figure 4-1 Types of intersection path.

Figure 4-2 shows the process flow of trajectory generation obtained from a set of triangular faces in a polyhedral model. The O and N are a reference point and the normal of the slicing plane, respectively. Triangular faces of the input polyhedral model are separated into two flow processes in accordance to their angle with respect to the slicing plane. When the triangular faces and slicing plane are coplanar (see block A in Figure 4-2), it is difficult to find the exact outer contour with an intersection algorithm because all the edges of these triangular faces intersect with the slicing plane. Therefore, these coplanar faces are treated independently, and their outer boundary edges are traced to become the corresponding intersection path. At this stage, the intersection path must be a closed path. Regarding the remaining triangular faces, all of them are treated in block B of Figure 4-2 and subjected, in a first place, to intersection operations with slicing planes (see block C in Figure 4-2). Then, intersection segments lying in the same

slicing plane are sorted (see block D in Figure 4-2) to generate at least one closed or open path.

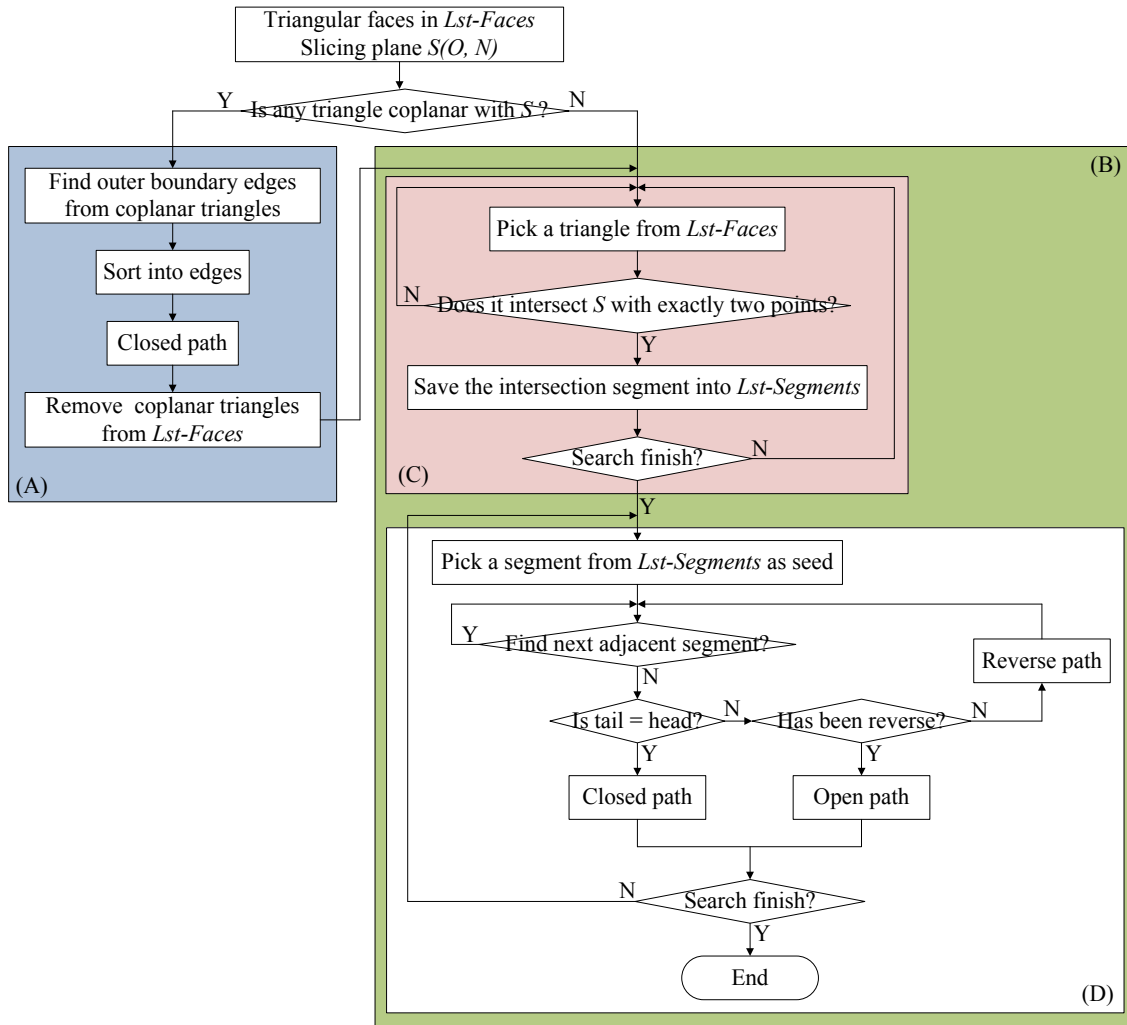


Figure 4-2 The process flow of intersection paths obtained from a set of triangular faces of a polyhedral model.

4.3 Voxel overlap ratio and layer thickness criterion

Using the CSM principle to fabricate a fully closed shell (volume sub-domain) of a 3D microstructure, it is mandatory to have all the voxels overlapping each other in two adjacent layers. A voxel has an ellipsoidal shape, due to the laser beam focalization, with two spatial resolutions corresponding to the lateral and longitudinal directions. Furthermore, the longitudinal size of a voxel is far larger than the lateral one (around 2.5 to 4.8 times [Takada et al. 05, Wu et al. 06], see details in section 1.1.2). In order to handle and use this TPP property, this thesis assumes that TPP users are aware of this fact and use it to determine the slicing direction of a micro-product during the slicing process. The complex shaped areas of a micro-product need be as much possible as

perpendicular to the slicing direction, so that they can be fabricated by the lateral resolution of a voxel to ensure a better generation of the details. As for the body of a micro-product, the corresponding areas can be fabricated while taking advantage of the longitudinal resolution of a voxel to reduce some extra manufacturing time.

Back to the issue about creating a fully closed shell of a 3D microstructure, we consider that the lateral overlap ratio of voxels determines whether a sealed shell of a microstructure can be fabricated or not. In this thesis, we introduce the voxel overlap ratio (α), which indicates the relationship between adjacent locations of exposed voxels defined as:

$$\alpha = 1 - d_l / v_a, \quad (4-1)$$

where the d_l is the lateral voxel distance and v_a is the lateral size of a voxel. Figure 4-3 shows the concept of voxel overlap ratio. This figure depicts a side view of a planar surface fabricated by TPP. When $\alpha > 0$, it means that voxels are overlapping. If $\alpha < 0$, voxels are isolated and it means that it is a path containing intermittent points.

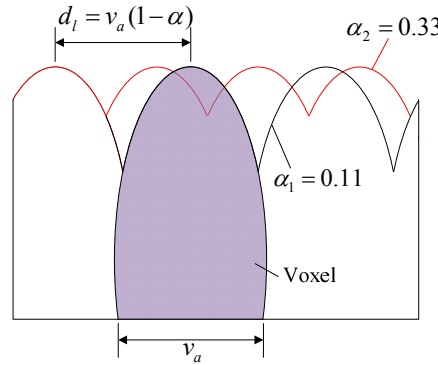


Figure 4-3 The concept of the voxel overlap ratio.

A larger α means a higher resolution surface can be produced. In other words, the magnitude of α is related to the degree of the object's surface roughness. Surface roughness is one of the important issues to address since it significantly affects the surface forces that dominate in micro-machines, and as for photonic elements, coarseness-induced scattering is the principal source of power dissipation [Takada et al. 05]. Here, we used the definition of the surface roughness, R , as follows:

$$\frac{1}{S_0} \iint |f(x, y) - z_0| dx dy \quad (4-2)$$

where S_0 is the scanned area, $f(x, y)$ is the height at each point, and z_0 is the average

height. Table 4-1 shows two previous reports [Takada et al. 05, Guo et al. 06] using an Atomic Force Microscope (AFM) and Eq. 4-2 to analyze a planar surface fabricated by TPP.

Table 4-1 Previous reports about surface roughness induced by voxels.

Takada et al.'s report [Takada et al. 05]					Guo et al.'s report [Guo et al. 06]			
v_a	243 nm				v_a	200 nm		
d_l	50 nm	100 nm	200 nm	300 nm	d_l	100 nm	200 nm	300 nm
α	0.79	0.59	0.18	-0.23	α	0.5	0.0	-0.5
R	8 nm	9 nm	16 nm	38 nm	R	15 nm	22 nm	32 nm

Synthesizing these two research works, the roughness propagated to the polymerized surface tends to saturate when the lateral overlap ratio is high enough, i.e. $\alpha > 0.5$, but it must be counterbalanced with the manufacturing time which increases proportionally.

As a synthesis of the TPP process, manufactured voxels need some overlapping to effectively form and give stiffness to a micro-structure. Given α , starting and ending points, manufacturing a straight line path in 3D space between these points is equivalent to rasterizing a vector for display on a video screen. However, the difference is that an elementary straight line path is a 3D trajectory with a really identical resolution along each axis.

At each position subdividing this path, a voxel is created by exposing the resin from one up to tens of milliseconds (depending on the laser power and the desired voxel size) under the laser light. Then, it polymerizes with its neighbors into a continuous line. From the micro-machining process point of view, this straight line path acts as the elementary movement acceptable by the current equipment. Thus, the laser beam elementary trajectory, as seen from the user point of view, can be regarded as a vector.

To avoid the layer separation because of a too large layer thickness compared to the voxel size, a suitable layer thickness is deduced from the geometric slope of the microstructure as shown in Figure 4-4. At the bottom right of Figure 4-4, is shown the geometric relationship between the layer thickness, the geometric slope of the object and the lateral voxel distance. As a result, a suitable layer thickness (Δt_s) depending on the shape angle (θ_s) can be identified as:

$$\Delta t_s = d_l \cdot \tan \theta_s = v_a (1 - \alpha) \tan \theta_s, \theta_s < \tan^{-1} \frac{v_b}{v_a (1 - \alpha)}, \quad (4-3)$$

where θ_s is the angle between either the tangent plane or the plane associated to a face of a polyhedron of the manufactured object and the slicing plane, and v_b is the longitudinal size of a voxel. Although the maximum layer thickness is bounded by v_b , a smaller value is often used to obtain more compact structures for practical purposes. So, the suitable layer thickness can be re-identified to:

$$\Delta t_s = \begin{cases} v_a(1-\alpha)\tan\theta_s, & \text{if } \theta_s \neq 90^\circ \text{ and } \Delta t_s < \Delta t_{\max} \\ \Delta t_{\max} & , \text{otherwise} \end{cases} \quad (4-4)$$

where Δt_{\max} is the maximum layer thickness specified by the user. The Eq. 4-4 is considered as the layer thickness criterion which can guarantee a sealed shell created with a CSM approach.

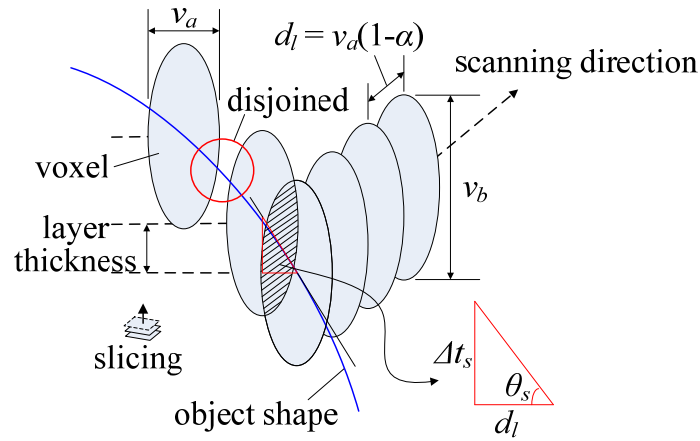


Figure 4-4 Schematic diagram of voxel overlap ratio and layer thickness.

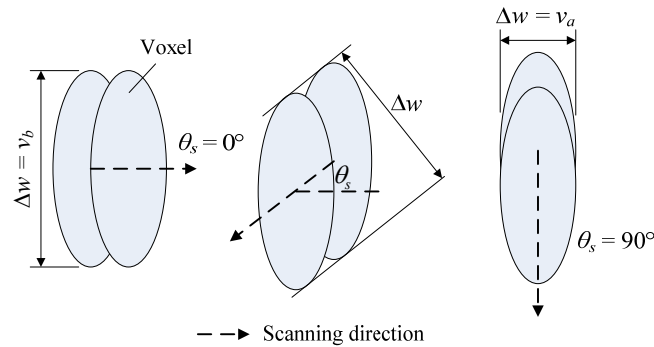


Figure 4-5 Schematic diagram of wall thickness or wire section.

In addition, a voxel owns two spatial resolutions, when manufacturing a surface or a wire, the wall thickness or section is variable within v_a to v_b depending on the relative positions of two adjacent voxels, as shown in Figure 4-5. Evaluating the value of a wall

thickness can help us predicting some dimensions as well as a critical location of a target microstructure. Assuming the thickness of a voxel envelope is given by the wall thickness (Δw), then it can be determined as:

$$\Delta w = \begin{cases} v_b, & \theta = 0^\circ \\ \sqrt{v_a^2 \tan^2 \theta_s + v_b^2} / \tan \theta_s, & 0^\circ < \theta < 90^\circ, \\ v_a, & \theta = 90^\circ \end{cases} \quad (4-5)$$

and is a complement to the non-manifold model of a microstructure to give a first estimate of the dimensions of the real object. Adjusting manufacturing parameters to dimensional constraints is still empirical at present since the current issues are surface and part quality. Dimensions would be also useful in the design of microstructures but there is not yet any specific study about the mechanical behavior of such components, hence planning effective dimensions of a microstructure, though a critical issue, is currently approached empirically and part of future developments.

Since the suitable layer thickness can be formulated as a function of the overlap ratio, the surface roughness of the microstructure can be indicated by the level of voxel overlapping. It means that if microstructures are manufactured with an identical overlap ratio, their surface roughness should be identical.

4.4 Two-dimensional slicing process for non-manifold model

The CSM, which only polymerizes the outer contours of an object instead of filling up its whole volume, is considered as the most efficient way to fabricate 3D objects regarding the manufacturing time needed to produce these objects. Nevertheless, to ensure a sufficient stiffness of the microstructure, at least a fully sealed shell must be built to keep the un-polymerized molecules inside the shells where volume sub-domains need to be produced. This constraint raises the following issues:

- Ultra-thin layers needed to represent the nearly planar areas

Such layer may cause the following problems:

1. low processing efficiency, i.e. relatively slow process,
2. un-fabricated areas due to a layer distance smaller than the resolution of the piezoelectric stage,
3. over polymerized reaction and structure deformation due to too much energy during exposure of the nearby areas.

- Un-sliced areas generating cavities

They are produced in the following situations:

1. when a surface area is parallel to the current slicing plane, its contours will be obtained by the slicing method but the area located inside will remain unprocessed, thus generating cavities,
2. when the slicing plane doesn't intersect some small critical surfaces, the corresponding geometrical features will be lost and undesired cavities will be the result of that configuration.

The TPP process can easily polymerize 3D wires using the 3D capabilities of the manufacturing equipments, so certainly it can deposit the object shape not only in one direction like some special LM processes including direct-metal deposition process [Singh & Dutta 01] and laser chemical vapor deposition [Park & Rosen 03]. These processes significantly differ from stereolithography that can use only one dot (voxel) per layer to produce wires orthogonal to the slicing plane. With TPP technology, microstructures can be produced through another process that can be regarded as an extension of the layer-by-layer method. Taking advantage of this exclusive property owned by TPP manufacturing equipment set up, a new slicing algorithm, based on a two-dimensional slicing method has been developed for the TPP micro-fabrication process. Considering a non-manifold polyhedral model possibly composed of three kinds of sub-domains, two treatments have been set up and are described as follows:

- Slicing surface and volume sub-domains

A critical slicing angle (θ_c) is specified by the user according to the shape of the microstructure and used to compare the shape angle (θ_s) of each triangular face to θ_c to generate two sub-domains. One is the major body domain ($\theta_s \geq \theta_c$), and the other one is the minor 'nearly planar' domain ($\theta_s < \theta_c$). The former is sliced by a set of planes whose normals are parallel to the laser beam direction. This procedure is called primary slicing phase and produces the body contour data. The latter is sliced along another direction which is perpendicular to the previous slicing planes. This procedure is called secondary slicing phase and produces relief hatching data to cover the entire surface domain, thus avoiding missing areas and taking advantage of the 3D kinematic capabilities of the TPP equipment. Here, the whole slicing process incorporating these two phases is denominated: Two-dimensional Slicing Method (TSM).

- Slicing wire sub-domains

Unlike the volume or surface sub-domains, the wires, which can be contained in the shape of non-manifold objects, are handled with a specific treatment. The slicing process is not applied and advantage is taken of the 3D capability of the TPP manufacturing equipment to produce real 3D paths. Therefore, the tessellation of wires is directly used to manufacture them. This procedure is called wire direct-writing process.

With surface and volume sub-domains, the critical slicing angle is a significant parameter. Based on the shape of the object, the laser power, and the feature of the available equipment, an acceptable minimum layer thickness (Δt_{min}) can be chosen by the user. Then, according to the layer thickness criterion (Eq. 4-4), a minimum critical slicing angle (θ_{cmin}) is obtained as:

$$\theta_{cmin} = \tan^{-1} \frac{\Delta t_{min}}{v_a (1 - \alpha)}. \quad (4-6)$$

In our tests, if the object has either a complex shape or many ‘nearly planar’ areas, the critical slicing angle can be chosen within 30~45 degrees. When considering regular shapes, the critical slicing angle can be defined by their local geometry in the neighborhood of the slicing plane.

The benefits of sorting the triangular faces of a polyhedron into two sub-domains are:

- Without ‘nearly planar’ surfaces, a larger layer thickness can be used to slice the major body domain, thus improving the manufacturing process efficiency.
- Collecting all the ‘nearly planar’ surfaces and then slicing them altogether avoids missing critical surfaces during the slicing process. Furthermore, these areas can be produced by another trajectory generation process, hence guaranteeing a manufacturing process covering the entire surface of the object.

Figure 4-6 shows the process flow of the two-dimensional slicing process. For example, the oscillator mentioned at section 3.1 is composed of two volume sub-domains: (a) the support and (c) the hammer, and a wire sub-domain (b) the spring. Based on the classification of sub-domains, different treatments need to be applied. For example, the spring belongs to the wire category, so wire direct-writing process is directly applied the wire direct-writing process to produce the corresponding polywire. As for the support and the hammer, they require a critical slicing angle to separate them into two face groups. Then, two slicing processes are applied sequentially to produce the body contours and relief hatching data, respectively. After applying all these

processes, the polywire, body contour data, and relief hatching data are merged together to produce the final slicing data.

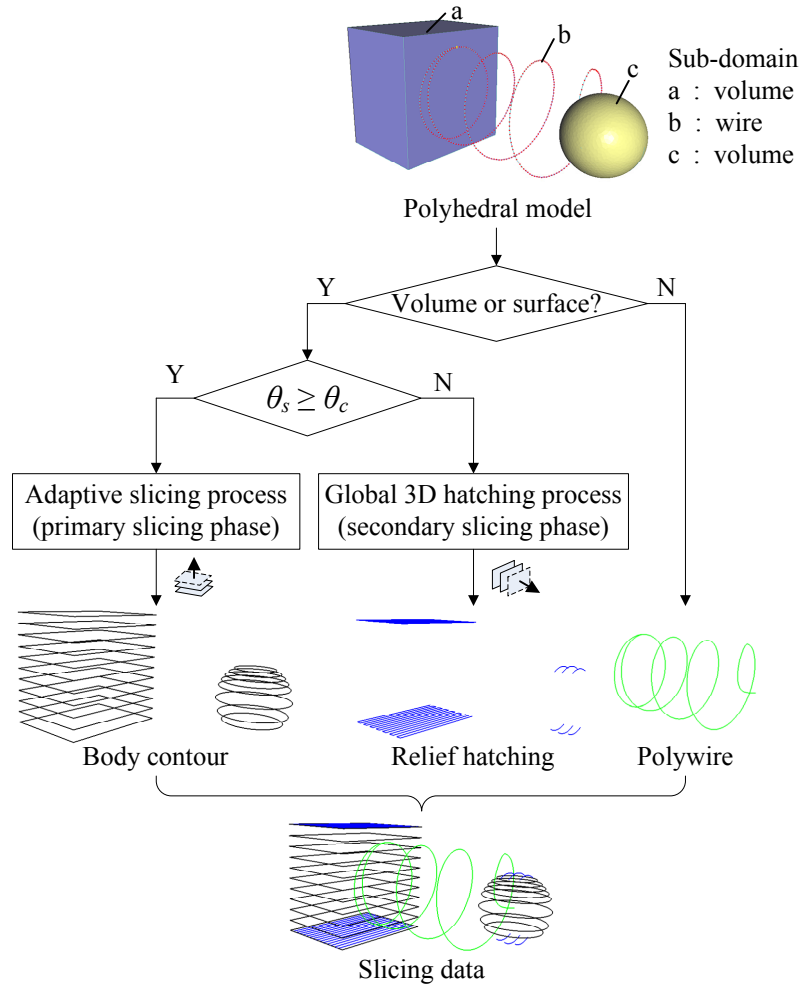


Figure 4-6 Process flow of the two-dimensional slicing process.

4.4.1 Adaptive slicing process (primary slicing phase)

In general, most of stereolithography technologies use a LM method to fabricate an object through a sequential accumulation of layers having equal thicknesses. However, either the staircase effect becomes significant when the system generates an object using thick slices or the fabrication time can become too slow if thin slices are used. According to the shape characteristics of the CAD model of the object, an Adaptive Slicing Process (ASP) can slice the CAD model into contours using variable thicknesses within an acceptable thickness range. This technique is regarded as an efficient strategy to decrease the fabrication time without drastically reducing the model accuracy.

From a manufacture point of view, the TPP micro-fabrication process can properly use an adaptive slicing process to increase the fabrication efficiency. However, at the

difference of stereolithography technologies, the staircase effect acts as a minor factor when an adaptive slicing process is applied to a TPP micro-fabrication process. Instead, keeping all voxels overlapping is the most significant constraint because it is essential for using CSM and increasing the robustness of the fabrication process with TPP.

As mentioned before, only triangular faces whose angles are greater than critical slicing angle are processed during the primary slicing phase. Without interfering with the ‘nearly planar’ areas or the small critical features, an ASP suited for CSM has been developed to improve the slicing process.

This method can predict and adjust dynamically the next layer thickness according to the geometric information in the current layer. The main idea is that when slicing the microstructure at a specific layer, the minimum shape slope can be obtained after scanning the intersection contour of the microstructure. With the addition of the lateral voxel size (v_a) and the overlap ratio (α), a predictive layer thickness between the current layer and the next one can be obtained with the layer thickness criterion. To prevent producing the separation of layers, the algorithm must ensure that there is no other small slope obtained between two layers. So, a refinement process adjusting the layer thickness is applied to find the optimal value.

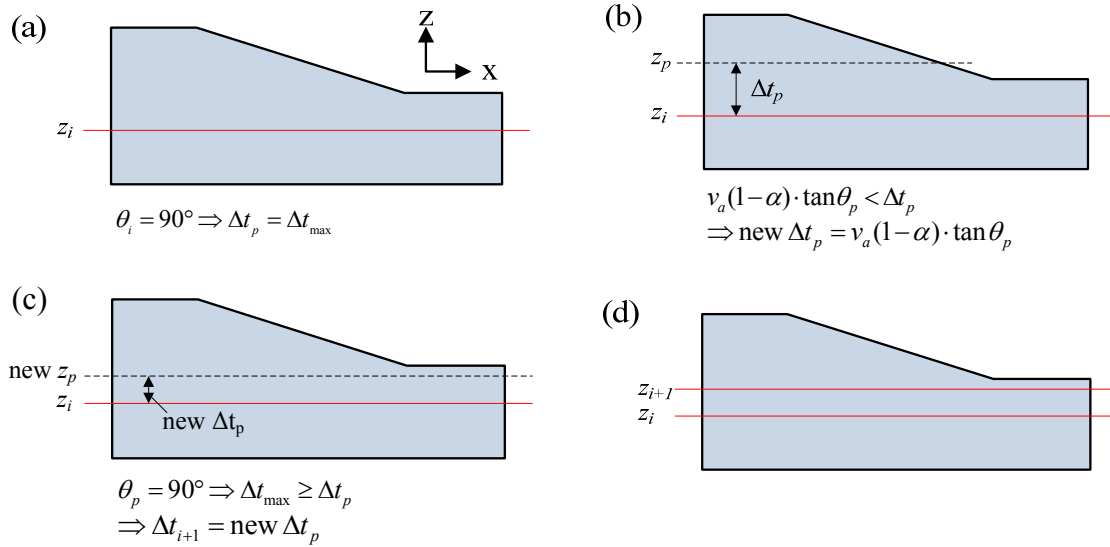


Figure 4-7 A schematic diagram of adaptive slicing process.

In what follows, an example is used to describe how the adaptive slicing process predicts and refines the layer thickness. Figure 4-7(a) shows the side view of a block with a slope. In this example, the slicing direction is along the z axis. In the first step, the minimum shape angle (θ_i) is 90 degrees after comparing all faces intersecting the slicing plane at z_i . So, in accordance to the layer thickness criterion (Eq. 4-4), the first predictive layer thickness (Δt_p) is Δt_{\max} . However, when pre-slicing at the altitude

$(z_i + \Delta t_p)$, the minimum shape angle in that layer (θ_p) is smaller than 90 degrees. Indeed, the suitable layer thickness at that layer should be $v_a(1-\alpha) \cdot \tan \theta_p$ and hence, it is also smaller than Δt_{max} . It means that some object shape features may be ignored between the slicing planes z_i and $(z_i + \Delta t_p)$. For this reason, reduce the layer thickness, and re-predict a new layer thickness $v_a(1-\alpha) \cdot \tan \theta_p$ as shown in Figure 4-7(b). When pre-slicing again at plane $z_i + \Delta t_p$ shown in Figure 4-7(c), the minimum shape angle at that layer (θ_p) is 90 degrees, the same as θ_i . It means that the object shape does not change between the slices at plane z_i and $(z_i + \Delta t_p)$. Therefore, this thickness Δt_p is an optimal value. Figure 4-7(d) shows that the next slicing plane z_{i+1} has been determined.

Assuming that the slicing plane is parallel to the x - y plane and the z coordinate of the microstructure is bounded by (z_{min}, z_{max}) , then the flowchart of the proposed ASP is described in Figure 4-8.

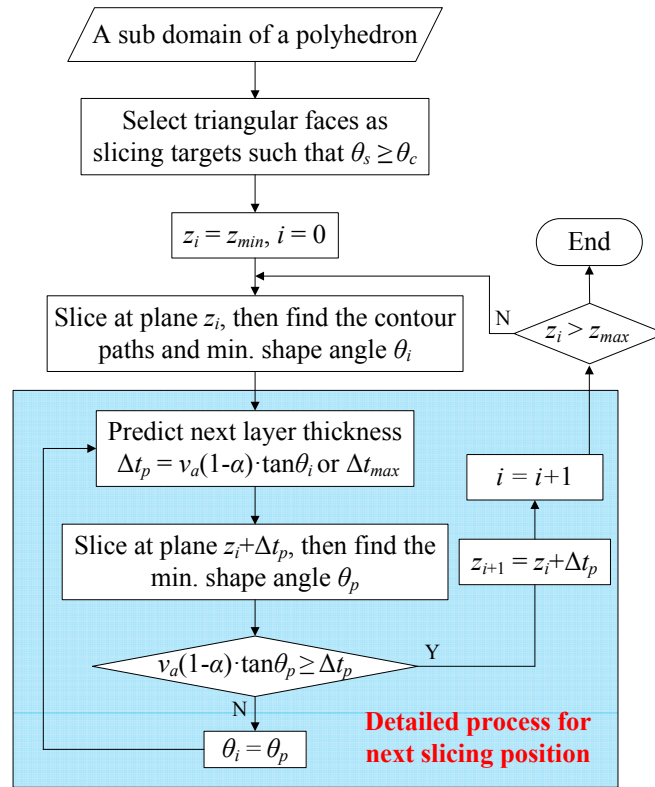


Figure 4-8 Flowchart of the proposed adaptive slicing process.

4.4.2 Global 3D hatching process (secondary slicing phase)

In TPP micro-fabrication, in order to obtain the best polymerization result, the laser light needs to avoid having the focusing light flux spot going through the polymerized resin (see section 1.8.5).

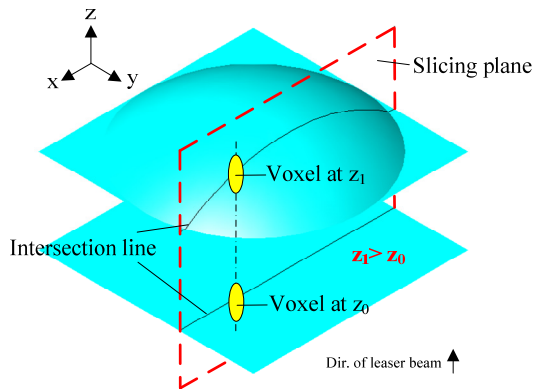
Because the laser beam trajectories of a layer in general SSM (i.e. the slicing

process with uniform layer thickness, see section 1.3.1) or ASP are purely 2D paths, the focal distance doesn't change in each layer. So, neither the SSM nor the ASP needs to consider laser ray constraint. However, TSM is a real 3D manufacturing method, and the focus spot of the laser beam changes its height in accordance to the height change of the parallel planes. For this reason, a mechanism is needed to avoid the focused spot going through the polymerized resin.

In TSM, all triangular faces of a polyhedral model are separated into two categories of sub-domains using a critical slicing angle. The faces belonging to each sub-domain may be sparsely distributed over the object surface, but this does not affect the slicing result with the primary slicing phase. Whatever the faces distribution, all the intersection lines will be at the same focal height because the normal of the slicing plane and the laser light are collinear. At the opposite, the contour lines obtained during the secondary slicing phase may have different focal heights due to the slicing plane whose normal is perpendicular to direction of the laser beam.

As shown in Figure 4-9(a), two distinct intersection paths are obtained by adopting a global slicing strategy at one slicing layer. When the laser light passes through one x - y position, it needs to produce two voxels at different focal heights (z_0 and z_1 , and $z_1 > z_0$). The variation of focal height is very large and raises difficulties when planning the order of laser beam trajectories during the real manufacturing process.

(a) Global slicing



(b) Adjacency-face group slicing

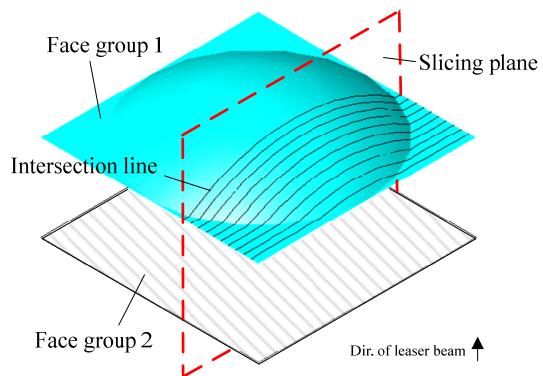


Figure 4-9 Comparison of slicing strategies devoted to the secondary slicing phase.

Therefore, the triangular faces lying in the secondary slicing phase are not subjected to the global slicing strategy anymore, rather the adjacency-face group slicing strategy into account. Figure 4-9(b) shows the concept of the adjacency-face group slicing strategy is applied to this face group. The triangular faces are separated again into several smaller sub-domains such that the faces contained into each of them are connected to each other. Then, each small sub-domain is sliced by a set of planes to

produce raster lines with a similar focal height. Following the concept of voxel overlap ratio again, the interval between raster lines is $v_a(1-\alpha)$ during this slicing phase, so that the layer thickness in the primary slicing phase is surely kept above $v_a(1-\alpha)\tan\theta_c$ ($\theta_c \neq 90^\circ$). The raster lines thus obtained can be considered as layer data. Differing from the primary slicing phase, this layer contains the 3D data resulting from the intersection computation, and the line inside is similar to the relief hatching layers, so this layer can be also called a relief hatching layer.

The benefit of relating all raster lines which have similar focus height to a same layer is that this focal distance can be used to compare it with other layers and determine more easily the fabricating order of laser beam trajectories during the path planning process. The details of this process are discussed in section 4.6. Figure 4-10 shows the flowchart of secondary slicing process.

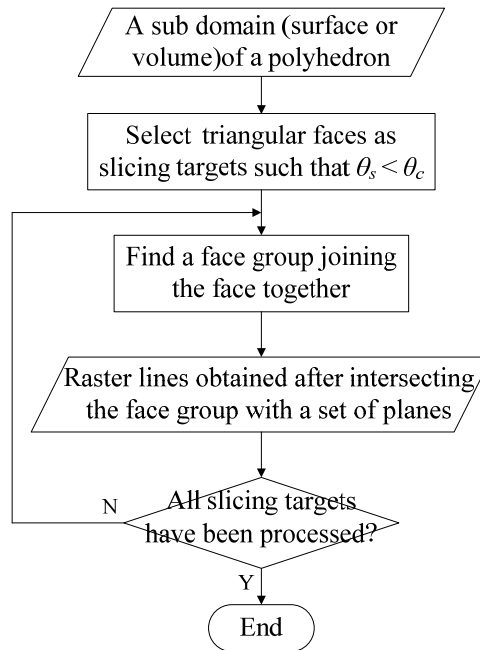


Figure 4-10 Flowchart of the global 3D hatching process.

4.4.3 Wire direct-writing process

As another extension to the standard LM process, the configuration of non-manifold objects (HLT_Component) containing wires (HLT_Wires) is handled with a specific treatment for these sub-domains. Indeed, the slicing process is not applied and advantage is taken of the 3D capability of the TPP manufacturing equipment to produce real 3D paths. Therefore, the tessellation of wires, i.e. polywires (see section 3.3.2), is directly used to manufacture them. Figure 4-11(a) shows a schematic diagram of wire direct-writing process. With this concept, arbitrary 3D wires, e.g. a spiral shown in

Figure 4-11(b), can be fabricated efficiently.

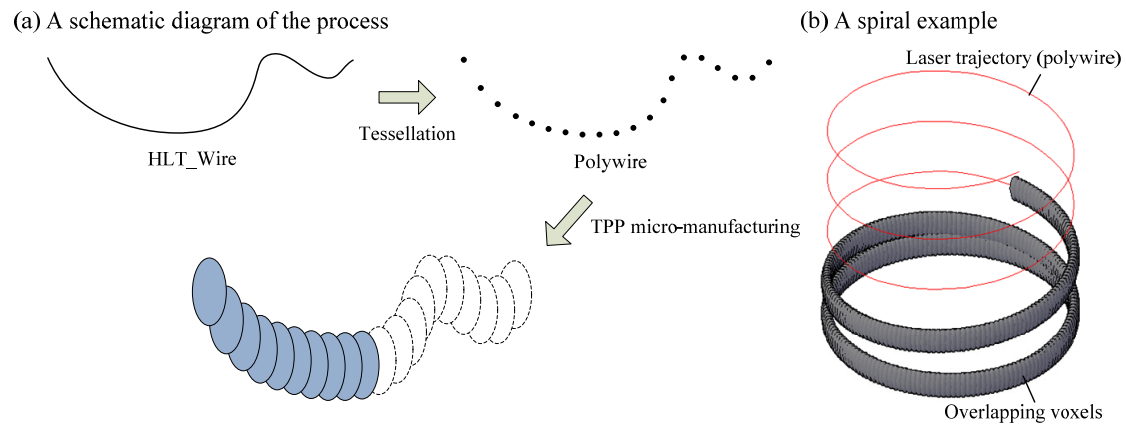


Figure 4-11 The wire direct-writing process.

4.5 Operators for enhancing the microstructure stiffness

Normally, using the CSM to fabricate a 3D object effectively increases the processing efficiency. However, it is accompanied by the critical issues about the micro-structure strength. The essential process which creates a fully sealed shell whenever needed where a non-manifold model contains either closed shells or cells, has been treated by the TSM discussed in section 4.4. This section presents two complementary ways to prevent a micro-structure collapse and stiffen its critical regions.

4.5.1 Welding sub-domains

If a non-manifold microstructure is fabricated, areas defined by curves and open surfaces have only a single row of voxels to connect them to other sub-domains of the microstructure, and the structure strength may not be stiff enough to resist its own weight. In order to process all the thin and small features, surface and wire welding processes have been developed to strengthen the microstructure. The principal concept of this process is either to create a sub-domain stiffening the micro-structure along its edges shared by three faces at least or to create a cone at a point joining wires to other sub-domains. Based on the geometric shape of welded locations, welding sub-domains can be categorized into two types:

- welding at adjacent surface sub-domains,
- and welding at a connection between a wire and any other type of sub-domain.

Since topological and geometrical relations between the polyhedral model and the

B-Rep NURBS CAD model input have been established during the tessellation process, the welds can be created easily and quickly because non-manifold connection configurations can be identified easily. Indeed, the overall shape representation used in the model processing environment is a mixed shape representation incorporating simultaneously a conformable polyhedron representation, a B-Rep NURBS model and the links between themselves through polyedges, partitions, and polywires explained in section 3.3.2.

Figure 4-12 illustrates a general configuration of surface welding at a connection between adjacent surface sub-domains. This process is separated into two steps:

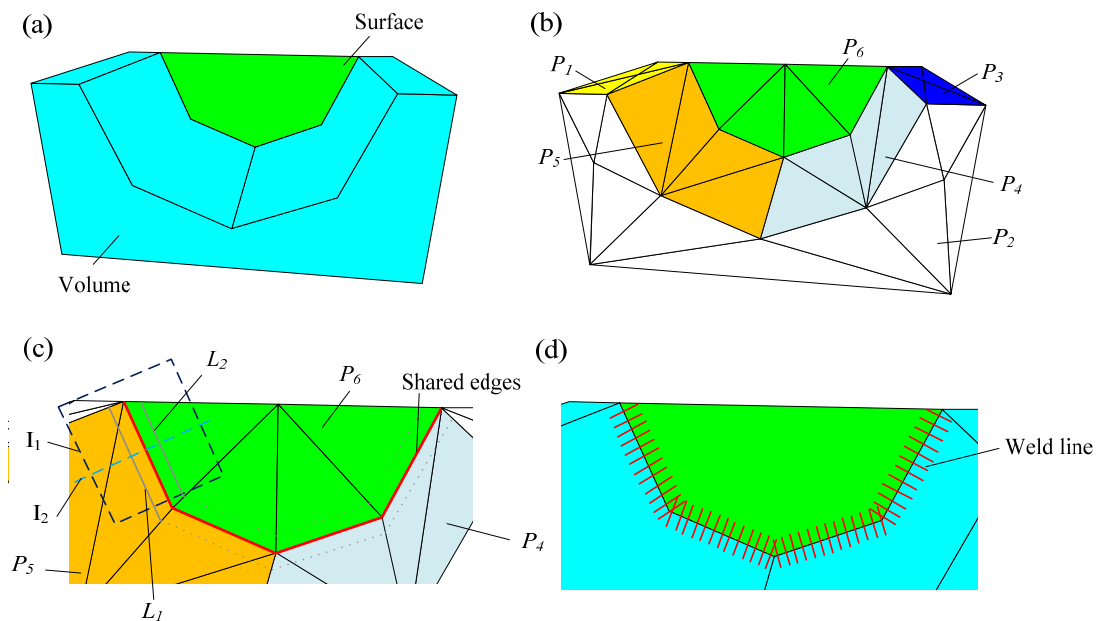


Figure 4-12 Surface welding at a connection between adjacent surface sub-domains.

1. User selection of the polyhedral edges needed to be processed:

Figure 4-12(a) is a polyhedron with two sub-domains: a volume (the block with a U-slot) and a surface. After tessellation, 10 partitions are obtained. Figure 4-12(b) shows partitions $P_1 \sim P_{10}$, ($P_7 \sim P_{10}$ don't show up) and their polyhedron faces. The target is to generate the welds between the surface and the U-slot. First, select two partition groups (one is P_4 , P_5 , and the other is P_6). Via their corresponding B-Rep faces, the adjacent B-Rep edges between two partition groups are identified. Through these B-Rep edges, their corresponding polyedges are used to find the polyhedral edges that need to be processed.

2. Apply two intersection operators to create a weld line:

Each polyhedral edge obtained from Step 1 can find two shared faces to generate a welding feature. In Figure 4-12(c), two intersection lines (L_1 and L_2)

are computed by intersecting a plane (I_1) whose normal is the average normal of the shared faces. The distance between the polyhedral edge and the intersection plane is the lateral voxel distance. Then, a second plane (I_2) perpendicular to the shared edge is used to intersect these two intersection lines L_1 and L_2 and a weld line is created by connecting the intersection points lying in I_2 and located between L_1 and L_2 . Figure 4-12(d) shows the result after finishing the welding process.

Regarding the process of point welding at a wire connected to other sub-domains of a microstructure, the welding feature is easier to create than surface welding ones. Firstly, the end of the candidate wire to be welded is identified as the reference vertex. Then, all polyhedron edges shared by the same reference vertex characterizing the non-manifold configuration are found. At each of these edges, we can compute the point whose distance from the reference vertex is the lateral voxel distance. Finally, the weld lines are obtained by connecting these points sequentially around the reference vertex, as shown in Figure 4-13.

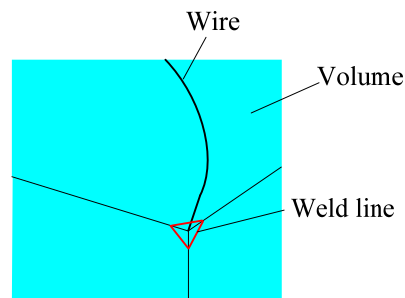


Figure 4-13 Point welding at a wire connected to other sub-domains.

4.5.2 Double contours

Most of the microstructure collapses occur in volume sub-domains of the polyhedral model. To avoid possible shape distortions, the microstructure is placed under an ultraviolet light to solidify after washing out the unexposed resin part with a solvent. However, a microstructure with high aspect ratio or large shape features may collapse before irradiating under the ultraviolet light.

Since the laser beam trajectories representing the volume sub-domains are always closed paths, the double contour method [Yang et al. 07] proposed by Yang et al. to increase the wall thickness is considered as an effective way to prevent the collapse of a microstructure. Therefore, to let our research concentrates on a global process flow, a simple offset path algorithm has been developed. The corresponding algorithm shows how to generate offset paths from a 2D closed path without checking self-intersecting

configurations. It is a preliminary and rough result but sufficient for only offsetting contours with very small values from original paths. Other researches concerning the generation of offset paths from a closed path can be found in [Park 05] and the references cited there.

To obtain a correct offset path, the original path must satisfy the following hypotheses:

1. The closed path contains data points $\{\mathbf{p}_i, i = 0, \dots, n\}$ and its orientation is counterclockwise,
2. The definition of segments $\{\mathbf{s}_i, i = 0, \dots, n\}$ in this path are

$$\mathbf{s}_i = \begin{cases} \mathbf{p}_{i+1} - \mathbf{p}_i, & i = 0, \dots, n-1 \\ \mathbf{p}_n - \mathbf{p}_0, & i = n \end{cases}, \quad (4-7)$$

3. Each two adjacent segments must not be collinear, i.e.

$$\{|\mathbf{s}_i \cdot \mathbf{s}_{i+1}| > 0, i = 0, \dots, n-1\},$$

4. The offset distance needs to be sufficiently small to ensure no self-intersecting situation.

Using Figure 4-14 as an example demonstrates the process of creating an offset path derived from a closed CCW path. The successive steps are listed as follows:

1. Identify the offset direction

Assume $\{\mathbf{n}_i, i = 0, \dots, n\}$ is the vector perpendicular to $\{\mathbf{s}_i, i = 0, \dots, n\}$. If $\{\mathbf{s}_i \times \mathbf{n}_i > 0, i = 0, \dots, n\}$, then the offset direction is internal. Otherwise, if $\{\mathbf{s}_i \times \mathbf{n}_i < 0, i = 0, \dots, n\}$, then the offset direction is external, as shown in Figure 4-14(a),

2. Generate the offset lines, and find the intersection points

Use the $\{\mathbf{s}_i, i = 0, \dots, n\}$ as the directions of the new lines. Toward each \mathbf{n}_i , offset a point with distance (d), and draw each new line. Use intersection algorithm (see section 1.8.1) to find all intersection points $\{\mathbf{p}'_i, i = 0, \dots, n\}$, as shown in Figure 4-14(b).

3. Create the offset path

Connect all $\{\mathbf{p}'_i, i = 0, \dots, n\}$, and the offset path is obtained, as shown in

Figure 4-14(c).

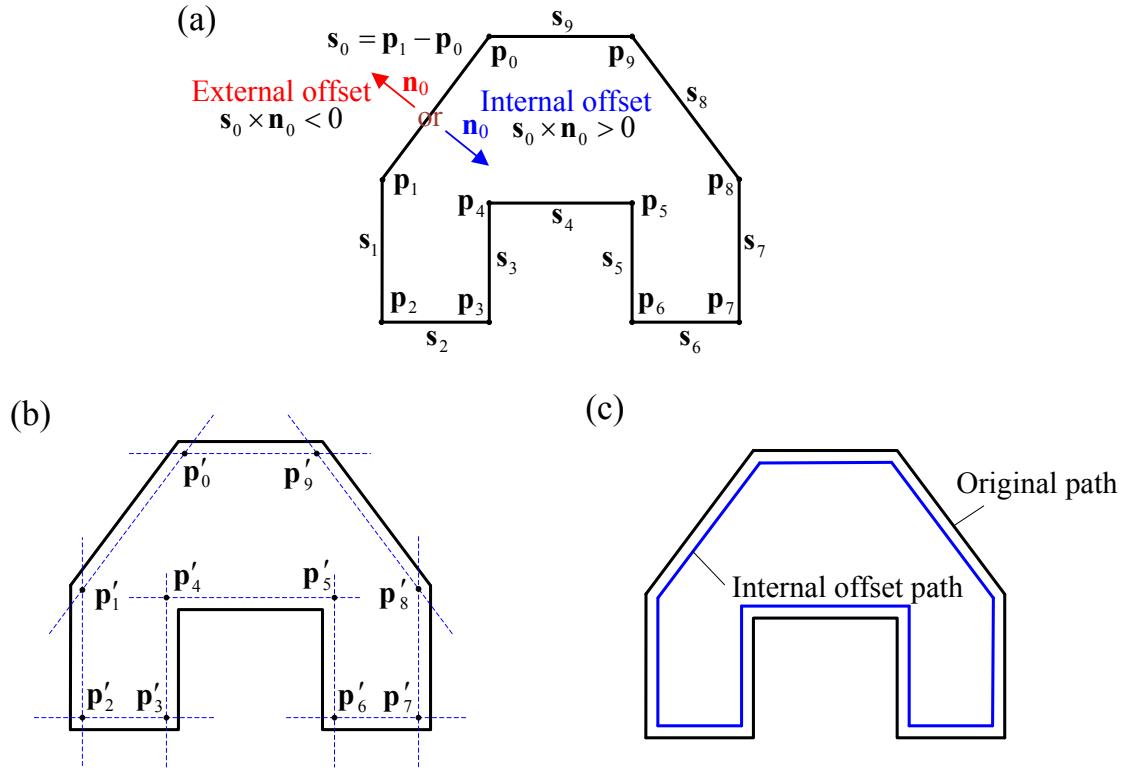


Figure 4-14 A schematic diagram of offset path derived from a closed CCW path.

4.6 Trajectory path planning

Because the refraction of polymerized region in the resin may differ from un-polymerized one, the scanning trajectories of the laser beam need to avoid as much as possible going through the polymerized region. Besides, to minimize the movement of the laser beam and the switching times of the shutter, an optimization of the trajectory planning process is needed. This section presents this procedure in detail.

4.6.1 Focal distance criterion to characterize laser beam trajectories

In TPP micro-fabrication, it is necessary to avoid the point at the focal spot of the laser beam passing through the polymerized region because it may change the intensity of the laser light and perturb the size of a voxel. This constraint has been discussed in section 1.8.5. For the above reason, some treatments such as the adjacency-face group slicing strategy in the global 3D hatching process has been taken into account in section 4.4.2. In addition, after obtaining all the laser beam trajectories which may come from body contours, relief hatchings, polywires, weld lines, or offset paths, a path sorting procedure need be performed to get the optimal fabricating order of the laser beam

trajectories.

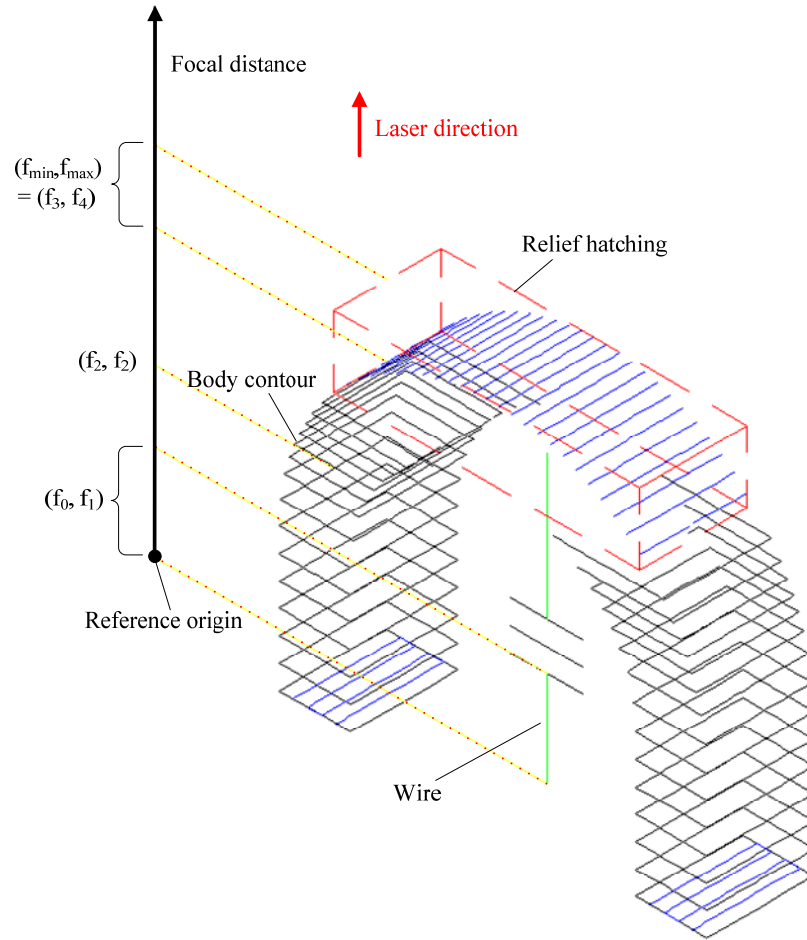


Figure 4-15 A schematic diagram of focal distance.

To sort these trajectories, a focal distance is introduced. Each laser beam trajectory can project itself onto the laser light direction and obtain its corresponding focal distance, as shown in Figure 4-15. Some laser beam trajectories are not represented to clarify the figure. To generate a convenient representation, the minimum focal distance is set to the reference origin of the micro-product. Besides, the focal interval is defined as (F_{min}, F_{max}) and used to characterize the focal domain of a set of trajectories. F_{min} and F_{max} represent the minimum and maximum focal distances of the trajectory(ies), respectively. If $F_{min} = F_{max}$, it means that the trajectory(ies) is/are 2D path(s). In this work, except the body contour data which must be 2D closed paths to define volume domains, the other types of laser beam trajectories may be either 2D or 3D open paths.

Based on the concept of focal distance, all the laser beam trajectories can be sorted to improve the fabrication order. Besides, to gain more processing efficiency, the minimum stage movement and minimum times for switching the shutter are also considered as sorting constraints for the trajectories. The whole sorting algorithm is

briefly introduced in Figure 4-16. It should be noticed that presently this sorting algorithm is mainly based on the concept of focal distance and the sorting efficiency is not addressed yet. Besides, all sorted laser beam trajectories must contain at least two 2D or 3D data points to be a valid trajectory.

Data: The list of laser beam trajectories $Lst-Ts$

Result: The list of sorted trajectories $Lst-SortedTs$

// Check the direction of 3D open paths

foreach laser beam trajectory T in $Lst-Ts$ **do**

if $T.type = OPEN_PATH$ and $T.f_{min} \neq T.f_{max}$ **then**

if the focal distance of $T.pts.head$ is far away to $T.f_{max}$ **then**

 reverse the direction of the trajectory T

end

end

end

// According to the maximum focal distance of each trajectory, sort laser beam trajectories from top to bottom

$Lst-InitSortedTs = \text{SortTrajectoryFromTopToBottom}(Ts)$

// Classify all 2D trajectories, i.e. $F_{max} = F_{min}$, having the same focal distance into the same group. A 3D trajectory defines a standalone group

$Lst-Lst-PGs = \text{ClassifyTrajectoryIntoPathGroup}(Lst-InitSortedTs)$

// Zigzag laser beam trajectories from top view of slicing plane

foreach $Lst-PG$ in $Lst-Lst-PGs$ **do**

$i = i + 1$

if number of trajectories in $Lst-PG > 1$ **then**

if $Odd(i)$ is true **then**

$Lst-PG = \text{SortTrajectoryFromLeftToRight}(Lst-PG)$

else

$Lst-PG = \text{SortTrajectoryFromRightToLeft}(Lst-PG)$

end

// Merge and rearrange 2D open paths while the minimum distance between extremities of adjacent paths is less than the lateral voxel distance

$Lst-PG = \text{Merge\&RearrangeTrajectory}(Lst-PG)$

end

foreach trajectory T in $Lst-PG$ **do**

 add T in $Lst-SortedTs$

end


```

end
// Rearrange closed paths
foreach trajectory  $T_i$  in Lst-SortedTs do
  if  $T_i \neq \text{Lst-SortedTs.tail}$  then
    set the next trajectory  $T_j$ 
    if  $T_j.type = CLOSED\_PATH$  then
       $SPt = \text{FindNodeWithMinimumDistance}(T_i.pts.tail, T_j)$ 
      rearrange  $T_j$  to let  $SPt$  as  $T_j.pts.head$ 
    end
  end
end

```

Figure 4-16 The sorting algorithm of laser beam trajectories in TPP micro-fabrication.

4.6.2 Voxel exposure position

After determining the fabricating order of laser beam trajectories, the next step is to determine the voxel exposure positions using a subdivision process to produce these trajectories. To keep the consistency of the voxel overlap ratio in a laser beam trajectory (see Eq. 4-1), the voxel lateral distance between two adjacent voxel exposure positions must be equal. In other words, all laser beam trajectories need to be subdivided with an identical subdivision distance $v_a(1-\alpha)$.

The sources of laser beam trajectory can be either a 2D path obtained from adaptive slicing or double contours processes or a 3D path obtained from secondary slicing, welding or wire direct-writing processes. There is one thing needed to highlight. What is called 2D paths means that these paths are laid on planes whose normal vectors are parallel to the laser beam direction. To make sure the distance is constant between two adjacent voxels having the same lateral distance, 3D laser beam trajectories must be projected on those planes first. Then, these 2D projected trajectories are subdivided to obtain the 2D voxel exposure positions and are mapped back to their original 3D trajectories to get their final 3D positions. There are two kinds of subdivision methods and they are described as follows:

1. Equidistant subdivision method

Since a laser beam trajectory needed to apply a subdivision process must be a 2D path, whether it is projected on a slicing plane or not, the simplest subdivision principle uses the concept of linear interpolation. In the proposed approach, it is called equidistant subdivision method.

This method directly generates the voxel exposure positions using a uniform subdivision distance applied to the laser beam trajectories, as shown in Figure 4-17. The detailed algorithm is presented in Figure 4-18.

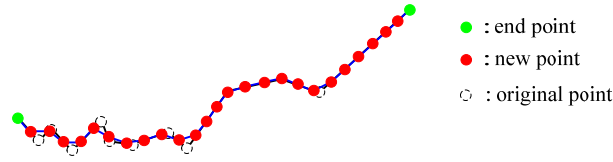


Figure 4-17: Equidistant subdivision method of a laser beam path.

Data: The laser beam trajectory T , lateral voxel distance d_l ,
normal of a slicing plane N

Result: The list of voxel exposure positions $Lst-Pts$

```

if  $T.type = CLOSED\_PATH$  then
    add  $T.pts.head$  in  $T.pts$ 
end
 $d = 0$ 
for  $i = 1$  to  $T.pts.count-1$ 
     $Vec = T.pts(i) - T.pts(i-1)$ 
     $d_f = Distance(Vec)$ 
     $\theta = GetAngleBetweenTwoVector(Vec, N) - \pi/2$ 
     $d_p = d_f * \cos\theta$ 
    while  $d < d_p$ 
         $Pt = T.pts(i-1) + Vec * d/d_p$ 
        add  $Pt$  in  $Lst-Pts$ 
         $d = d + d_l$ 
    end
     $d = d - d_p$ 
end
add  $T.pts.tail$  in  $Lst-Pts$ 

```

Figure 4-18 The equidistant subdivision algorithm.

2. Feature subdivision method

Although the equidistant subdivision method is quite simple, it cannot guarantee the correct shape of a micro-product fabricated with the subdivided trajectories. Figure 4-19 uses a 2D contour line to demonstrate this issue. Figure 4-19(a) depicts the voxel

exposure positions obtained by the equidistant subdivision method. When the length of a segment in a trajectory is not exactly a multiple of the subdivision distance, the boundary (feature points) of a trajectory may not be completely described, thus producing shape defects. In this thesis, a point obtained from the intersection of a slicing plane and a boundary curve of CAD model faces where there is a tangent plane discontinuity is called a feature point.

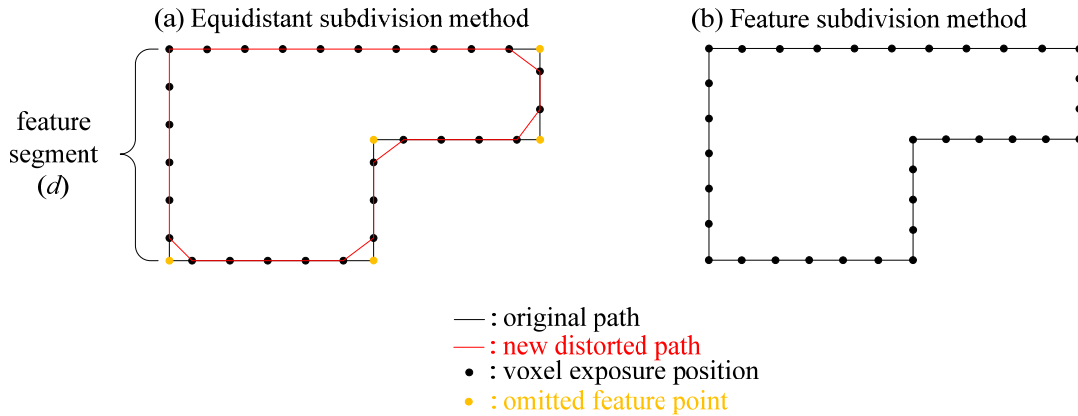


Figure 4-19 The path comparison of possible subdivided trajectory results.

The concept of the polyedge in the mixed shape representation (mentioned in section 3.3.2) is used again to develop the feature subdivision method and to solve the above issue. Because a polyedge is a tessellated result of a boundary curve (HLT-Edge) of a face (HLT-Face), an intersection point obtained from a slicing plane and a polyedge must be a feature point. This characteristic eases defining the feature points in an intersection contour line and subdividing the contour line based on these points to ensure the local critical shapes of a micro-product have been fabricated correctly. However, to obtain the polyedge information from a polyhedral model, the premise is that this polyhedral model must be produced through our proposed tessellation process (see in section 3.6) developed based on the mixed shape representation. In other words, polyhedral models obtained from different ways such as RE techniques are not suitable for this feature subdivision method.

A contour line is a set of 2D intersection points obtained from polyhedral faces. Depending on the tessellation parameters, i.e. deflection, edge length, angle, the same B-Rep NURBS face may be tessellated into different numbers of polyhedron faces. Different contour lines characterized by the number of points and the distance between two adjacent points may be obtained with different tessellation parameters based on the same slicing plane.

However, in our proposed tessellation process, the boundary curves (HLT_Edges) of a B-Rep NURBS face are always tessellated and linked to polyedges. No matter how

we change the tessellation parameters, the feature points will exist in the intersection lines, i.e. the above boundary curves, after applying the slicing process. More specifically, the intersection points, obtained from intersecting the polyedges and the slicing plane, are the feature points defined above. With this concept, it is easier to extract the feature points during the slicing process. If a polyhedron edge intersects with a slicing plane and this edge is belong to one of polyedges (the discretized representation of HLT_Edges), the intersection point is a feature point.

In the feature subdivision process, the feature points included in a contour line must be voxel exposure positions, so that the geometric features can be preserved as shown in Figure 4-19(b). To solve the situations where the distance between two feature points, i.e. a feature segment, is not a multiple of the lateral voxel distance, the real lateral voxel distances vary in all feature segments of a laser beam trajectory. To conform to the voxel overlapping criterion (see section 4.3), the voxel overlap ratio in each feature segment of a laser beam trajectory must be greater or equal to the default value set by the user. Therefore, the real voxel distance (d_{rl}) in each feature segment can be defined by:

$$d_{rl} = \begin{cases} \min \left[\frac{d}{\text{int}(d/d_l)}, \frac{d}{\text{int}(d/d_l)+1} \right] & , d \geq d_l \\ d & , d < d_l \end{cases} \quad (4-8)$$

where d_l , and d are the lateral voxel distance and the length of a feature segment, respectively. Since $d_{rl} \leq d_l$, it can ensure that the voxel overlap ratio will fit in with our expectations, i.e. the actual overlap ratio is greater or equal to the user specified one. The detailed algorithm is represented in Figure 4-20.

Data: The laser beam trajectory T , lateral voxel distance d_l , normal of slicing plane N

Result: The list of voxel exposed positions $Lst-Pts$

if $T.type = CLOSED_PATH$ **then**

 add $T.pts.head$ in $T.pts$

end

for $i = 1$ to $T.pts.count-1$

$Vec = T.pts(i) - T.pts(i-1)$

$d_f = \text{Distance}(Vec)$

$\theta = \text{GetAngleBetweenTwoVector}(Vec, N) - \pi/2$

$d_p = d_f * \cos\theta$

$d_{rl} = (d_p < d_l) ? d_p : \min[d_p/\text{int}(d_p/d_l), d_p/(\text{int}(d_p/d_l)+1)]$

```

for  $j = 0$  to  $\text{int}(d_p/d_{rl})-1$ 
     $Pt = T.pts(i-1) + Vec * j/\text{int}(d_p/d_{rl})$ 
    add  $Pt$  in  $Lst-Pts$ 
end
end
add  $T.pts.tail$  in  $Lst-Pts$ 

```

Figure 4-20 The feature subdivision algorithm.

The final result of the simulation process for TPP micro-manufacturing is obtained after all laser beam trajectories have been subjected to the subdivision process. Then, the manufacturing system (discussed in section 5.1) uses these laser beam trajectories to fabricate the microstructure through the control of the stage movement up to the right voxel positions and of the shutter to expose appropriately the resin under the laser beam.

4.6.3 Fabrication Time

In section 1.8.2, we know that applying different slicing strategies on a micro-product model will cause different processing efficiencies. In this thesis, the comparison of processing efficiencies according to different slicing algorithms subjected to a range of user-specified fabrication parameters is simplified into the comparison of fabrication times.

After obtaining all the voxel exposed positions, the preliminary fabrication time can be estimated and roughly separated into four items:

- Voxel exposure time:

This item represents the expected exposure time of all voxels,

- Shutter delay time:

A shutter is used to control the amount of laser light exposing the resin. When generating a laser beam trajectory during the TPP micro-fabrication process, the shutter must be opened and closed at the start and end points of a trajectory, respectively. From the mechanism point of view, the time between the transmission of a signal to the shutter until the shutter actually moves is named as shutter delay time. The time would be different depending on the technology (either mechanical or electric) and configurations of shutters,

- Stage moving time:

This item represents the overhead time which the stage spends to move across specified un-polymerized areas,

- System delay time:

Because of the configuration of a TPP micro-manufacturing system (details are discussed in section 5.1) is a little complex, it is difficult to set up a real-time control between software and hardware interfaces. So, the time the manufacturing system spends on transmission through these interfaces is named as system delay time. This item is a significant factor because it can influence the actual voxel exposure time.

Since system delay time is depending on the manufacturing equipments, it is difficult to state a generic quantification. So, it should be estimated on a case by case basis and used to calibrate the actual voxel exposure time. This practice is demonstrated in section 5.2. The following equations define the actual voxel exposure time based on the above hypotheses.

Firstly, the fabrication time (T) can be defined as:

$$T = n_v \cdot t_{de} + 2n_t \cdot t_s + \frac{d_t}{v_p} + t_{sp}, \quad (4-9)$$

where t_{de} , n_v , n_t , t_s , d_t , v_p , t_{sp} are the default exposure time per voxel, the number of voxels, the number of laser beam trajectories, the delay time of shutter switching, the total distance which the stage moves across the desired un-polymerized areas, the moving speed of the stage and system delay time, respectively. Assuming $n_v \gg n_t$ and $v_p \gg 0$, then the fabrication time can be reduced:

$$T = n_v \cdot t_{de} + t_{sp}. \quad (4-10)$$

If t_{sp} is greater than 0, it means that the actual voxel exposure time will be extended and the voxel size will be larger than expected one. Too crowded voxels may cause over polymerization and damage the microstructure. If we know the value of system delay time, we can calibrate the voxel exposure time during the fabricating process to avoid this situation. Rearranging Eq. 4-10 and dividing by number of voxels, the extended exposure time per voxel (t_{ee}) caused by the system delay time can be identified as:

$$t_{ee} = \frac{T - n_v \cdot t_{de}}{n_v} . \quad (4-11)$$

Since the magnitude of t_{ee} influences the exact exposure time per voxel, t_{ee} can be considered as a significant manufacturing parameter and must be evaluated before manufacturing a microstructure using the TPP process. Then, the actual exposure time per voxel (t_{re}) is:

$$t_{re} = t_{de} + t_{ee} . \quad (4-12)$$

4.7 The slicing data structure

The organization and content of the slicing data structure is described in this section. This data structure has two purposes:

- To store the data generated by the two-dimensional slicing method, the weld lines, and the double contour paths mentioned in sections 4.4, and 4.5, respectively.
- To build up a relationship between the slicing data, the polyhedron data structures and the tessellation ones.

The entities in slice data structure use list data structures to build their association. As such, their elements are ordered according to a linear sequence. Compared to arrays, lists perform generally better in inserting, extracting and moving elements at any position within the container, and therefore also in algorithms that make intensive use of these, like sorting algorithms [C++ Resources]. The main drawback of lists is that they lack direct access to their elements. They also require some extra memory to keep the binding information associated to each element, which may be an important factor for large lists of small-sized elements.

With the current object representation, the cardinality of entities can vary into a large extent. For example, it can be as small as tens of triangular faces or laser beam trajectories and as large as millions ones. Therefore, to increase the efficiency of data processing (element inserting, moving, memory usage, etc.), the lists appeared as more suited than arrays for our research.

As shown in Figure 4-21, the slicing data structure contains 6 entities: SLICE, SECTION, WIRE, WELD, PATH, and SLICE_POINT. Each entity, its attributes and their corresponding lists are described as follows:

larger than the acceptable layer thickness set during the primary slicing phase, then this next layer thickness will be reassigned to this value,

- Critical slicing angle: this value is specified by the user in accordance to the shape of the microstructure and it is used to compare the shape angle of each triangular face in a polyhedral model. Other details are given at section 4.4.
- Focal distances: they define the focal domain of the whole slice. Other details are given at section 4.6.

A SLICE includes 5 lists:

- A list of S_MAILLAGEP (sub-domains of the polyhedral model): it is used to connect sliced sub-domains (surfaces and volumes) of the polyhedral model,
- A list of SECTION,
- A list of WIRE,
- A list of WELD,
- A list of SCANPATH: after obtaining the simulation results (see section 4.6), all the sorted and subdivided laser beam trajectories are stored in this list.

To go a step further demonstrating how the SLICE data structure builds associations and store laser beam trajectories produced by our proposed treatments, several slice data structures obtained from a manufacturing model are illustrated from Figure 4-22 to Figure 4-26. Figure 4-22(a) shows a typical manufacturing model containing three different types of sub-domains: a volume (M_1), an open surface (M_2), and a wire (M_3). After applying the TSM and welding processes, the laser beam trajectories are shown in Figure 4-22(b). These trajectories are stored in an instance of SLICE entity, as shown in Figure 4-22(c).

2. SECTION: used to store the contour data produced by the slicing process. A SECTION is approximately equivalent to a layer in standard layered manufacturing method. However, a SECTION does not only contain the 2D closed paths, but also the 3D open paths such as the relief hatching patterns. A SECTION includes 3 attributes:

- Type: the proposed slicing process produces two kinds of slicing data through two slicing phases. In order to characterize them clearly, the SECTION contains the primary and secondary slicing data defined as CONTOUR_SECTION and HATCHING_SECTION, respectively,
- Reference point: it indicates a point lying on the slicing plane,

- Focal distance: it indicates the focal distances of the whole section data.

A SECTION only includes a PATH list. Laser beam trajectories belonging to the SECTION are stored in this list.

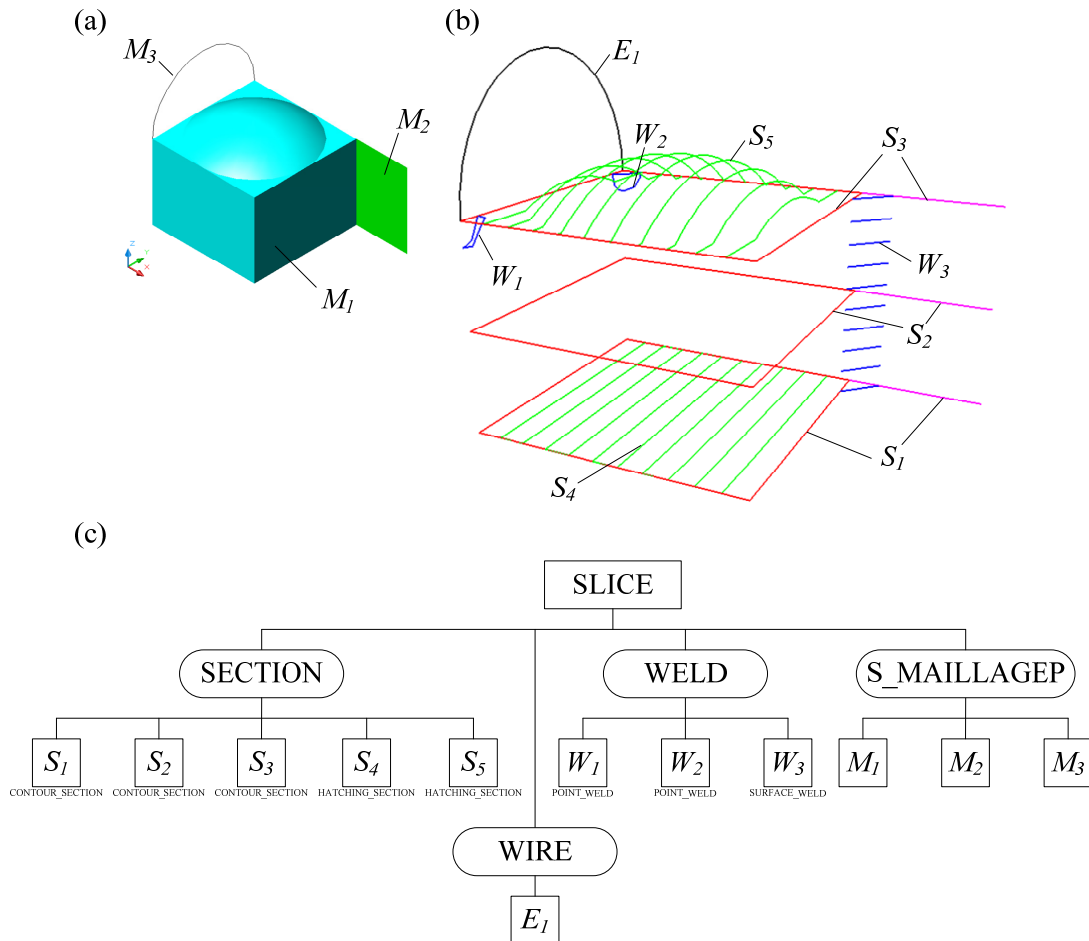


Figure 4-22 A typical instance of SLICE entity.

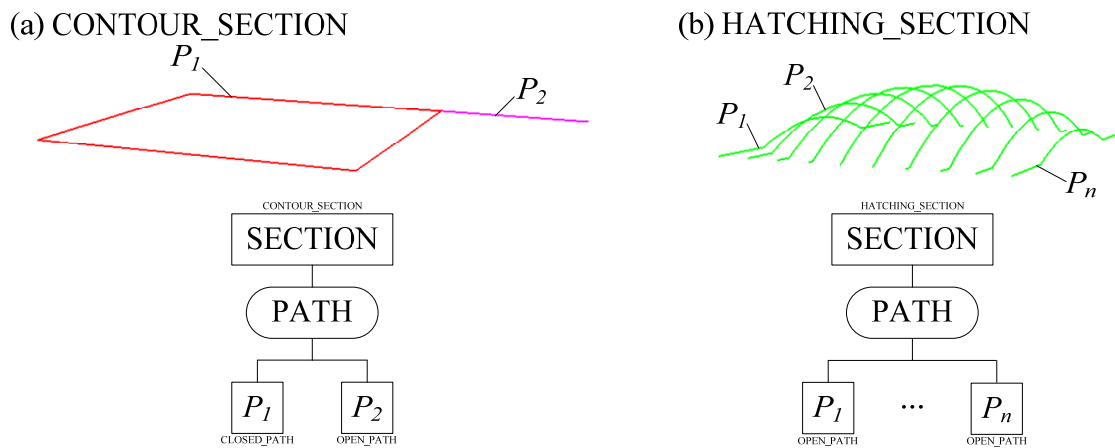


Figure 4-23 Two typical instances of SECTION entity.

Figure 4-23 shows two instances (S_2 and S_5) of the SECTION entity in Figure 4-22 (b). In Figure 4-23(a), S_2 is of type CONTOUR_SECTION. It is obtained from slicing the manufacturing model (see Figure 4-22(a)) during a primary slicing phase with a TSM process and is composed of two 2D paths (P_1 and P_2). As for Figure 4-23(b), S_5 is of type HATCHING_SECTION. It is obtained from slicing the model during the secondary slicing phase and is composed of n 3D open paths ($P_1 \sim P_n$).

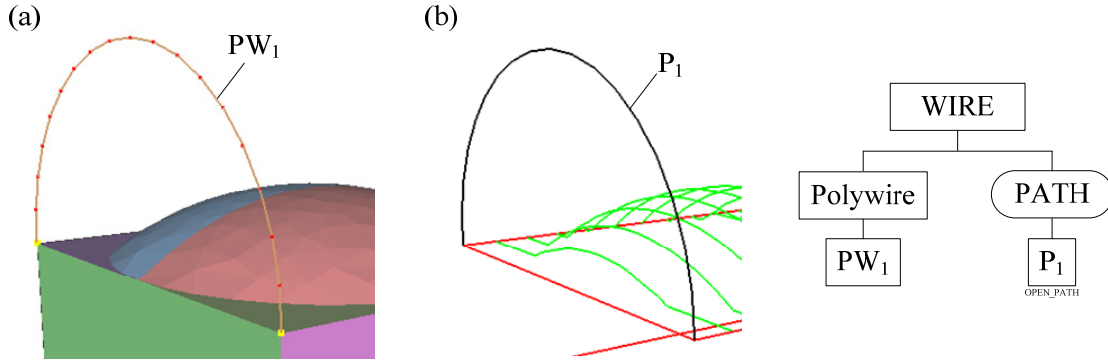


Figure 4-24 A typical instance of WIRE entity.

3. WIRE: it stores the data produced by the wire tessellation process. A WIRE includes 2 attributes:

- Polywire: this attribute makes an association with a HLT-Wire entity,
- Focal distances: it indicates the focal interval of the whole wire data,

A WIRE only includes a PATH list. Laser beam trajectories belonging to the WIRE are stored in this list.

Figure 4-24 shows an instance (E_I) of WIRE entity in Figure 4-22(b). After the tessellation process, the wire sub-domain (W_3) becomes to the polywire (PW_I) as shown in Figure 4-24(a). Since the component of PW_I is already an open path, it can be directly mapped to an instance (P_I) of PATH entity. The data structure of E_I is indicated at the right of Figure 4-24(b). The attribute ‘Polywire’ is used to create an association with the corresponding tessellated polyhedral model.

4. WELD: stores weld lines produced by the proposed welding process. A WELD includes 3 attributes:

- Type: the proposed welding process has two kinds of welding data. In order to recognize them clearly, the WELD contains the surface and point welding data defined as SURFACE_WELD and POINT_WELD, respectively,
- Node: if the weld type is POINT_WELD, this attribute is used to connect the

weld to the corresponding point of a wire,

- Focal distances: it indicates the focal interval of the whole weld data.

A WELD includes 2 lists:

- A list of partition groups: if the weld type is SURFACE_WELD, two partition groups must be specified to identify the common polyedges,
- A list of PATH: Weld lines belonging to the WELD are stored in this list.

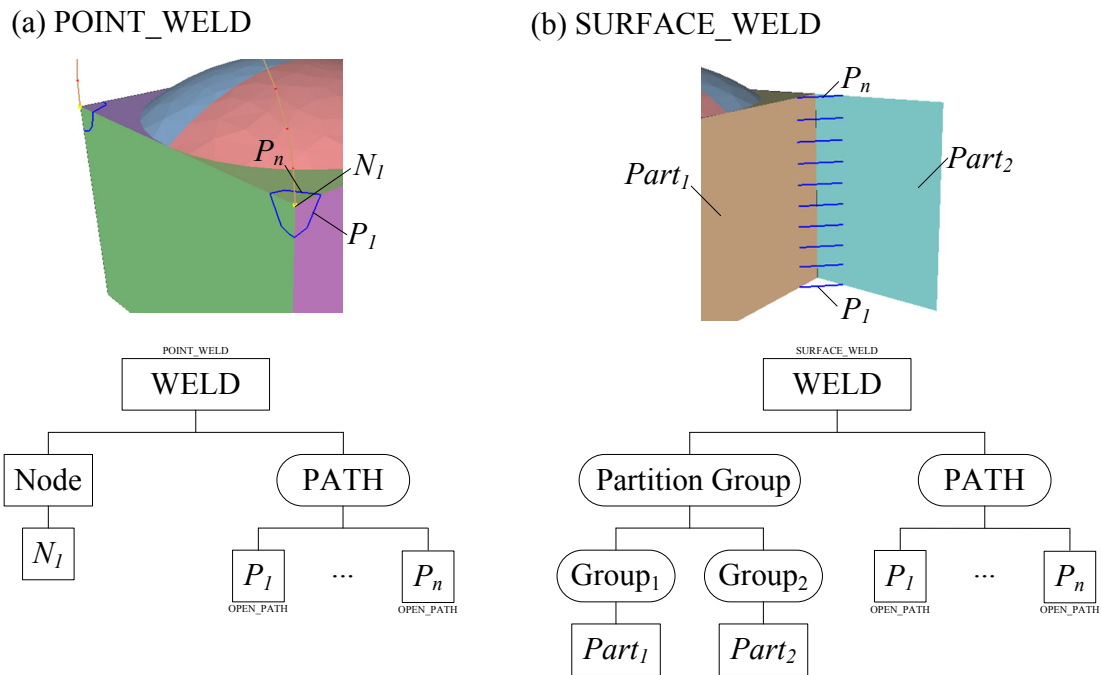


Figure 4-25 Two typical instances of a WELD entity.

Figure 4-25 shows two instances (W_1 and W_3) of WELD entity in Figure 4-22(b). In Figure 4-25(a), W_1 is of type POINT_WELD and it uses n open paths ($P_1 \sim P_n$) around the weld point (N_1), i.e. one extremity point of E_1 , to produce the corresponding laser beam trajectories. In Figure 4-25(b), W_3 is of type SURFACE_WELD and it uses n open paths ($P_1 \sim P_n$) along the intersection line of two partition groups ($Part_1$ and $Part_2$) to produce the corresponding laser beam trajectories.

5. PATH: it is the core entity to represent a laser beam trajectory such as a body contour, a relief hatching pattern, a weld line, etc. A PATH includes 2 attributes:

- Type: In order to distinguish clearly two configurations, a PATH is either an open or a closed trajectory characterized by an OPEN_PATH or a CLOSED_PATH status, respectively,

- Focal distance: it indicates the focal interval of the whole path data.

A PATH only includes a SLICE_POINT list. Data points belonging to the PATH are stored in this list.

Figure 4-26 shows two instances (P_1 and P_2) of PATH entities of Figure 4-23(a).

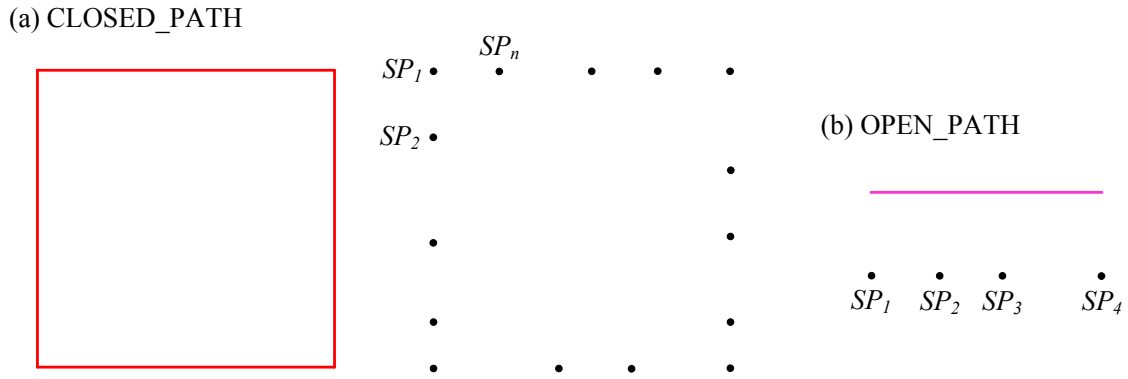


Figure 4-26 Two typical instances of PATH entity.

6. SLICE_POINT: it is the lowest level entity of the slice entity. A SLICE_POINT includes 2 attributes:

- Node: it contains the coordinates of a data point,
- Edge: if a data point is derived from the intersection with a polyhedral edge, this attribute is used to point to this polyhedral edge, i.e. it characterizes a feature point.

4.8 Conclusion

This chapter represents the simulation processing techniques set up to produce the essential laser beam trajectories required to manufacture a micro-product model.

The basic open or closed paths intersecting the polyhedral model representing the product are introduced first. In accordance with the characteristics of TPP, a voxel overlap ratio is introduced and used to define the layer thickness criterion which can guarantee the generation of a sealed shell created by CSM. In addition, a two-dimensional slicing method (TSM) suited for CSM is also developed. This overall process greatly increases the fabrication efficiency compared to SSM, and even ASP. Due to the use of the CSM to fabricate a 3D object, the structure strength of the object may not be sufficient. Therefore, two operators for enhancing the structure stiffness have been developed. Besides, the scanning path planning strategy is also taken into account to avoid some laser focusing problem. As a result, at the end of this chapter, a

slicing data structure and a scheduling process have been proposed to store and handle the slicing data.

Micro-products fabricated by TPP

Several micro-products fabricated with the proposed approach are presented in this chapter. These micro-products are divided into three categories: simple shapes, complex shapes, and non-manifold functional microstructures, and each categories discusses several specific issues such as non-manifold objects, processing efficiency, stiffening strategies for the volume sub domains or the connection between different sub-domains. At the beginning of this chapter, the TPP fabrication system and the correction of voxel exposure time are also introduced.

5.1 The micro-fabrication set-up

The TPP fabrication system layout developed by the SPECTRO laboratory is shown in Figure 5-1. A laser is used as the exposure source. Due to the weak sensitivity of commercial photopolymers, the NIR femto-second pulsed laser is often used to provide a light spot of high intensity. However, it is not only very expensive but also it may damage the material, so that only a small intensity window can be employed for safe fabrication [Martineau et al. 02].

In this thesis, we use the commercial resin (Photomer 3015 from Henkel) with 3% of highly sensitive additive two-photon sensitizer. The photo-initiator molecule is Benzidine, N, N'-bis(p-methoxyphenyl)-N, N'-diphenyl-(8CI) and its chemical synthesis is presented in Figure 5-2. The optical properties of the photo-initiator molecule are the following ones [Martineau et al. 02]:

- It presents a linear absorption with a maximum at 349 nm, and no absorption for wavelengths above 400 nm,
- The broad TPA absorption band is in the visible ranges (500 and 650 nm) due to a moderate conjugated charge transfer system.

Since this photo-initiator can efficiently initiate the polymerization in the visible range, a low cost frequency doubled Nd:YAG micro-laser providing low light intensity

is acceptable for our research [Wang et al. 02]. This laser and other major equipments as well as their specifications are summarized in Table 5-1. The laser beam is tightly focused with an objective lens (Numerical Aperture (NA) 1.25, immersion oil used for refractive index matching) into the volume of the resin, which is dropped on a microscope slide and mounted on a 3D piezoelectric stage. Although the resolution of the 3D stage is only 1 nm, the space resolution of the manufacturing equipments is restricted by the resolution of Digital/Analog output board which is 14 bits for the voltage range $-10\text{V} \sim +10\text{V}$. The travel range of the 3D stage is $100\text{ }\mu\text{m}$, so the exact resolution is 20 nm. The polymerized path can be produced by freely moving the 3D stage in each direction within a $100\text{ }\mu\text{m}$ range. The attenuator is inserted into the beam path to adjust the light intensity. A command driver is embedded into SIMPOLY software developed by our laboratory G-SCOP to process the laser beam trajectories to the format of manufacturing equipment. It can control the shutter on/off and the movement of the 3D stage. SIMPOLY also includes the tessellation and all simulation functions such as slicing and trajectory planning for the TPP micro-fabrication. The 3D microstructures are fabricated from up to bottom with the bottom of the microstructure attached to the stage. Besides, a camera located behind a dichroic mirror is used for online monitoring of the TPP micro-manufacturing process.

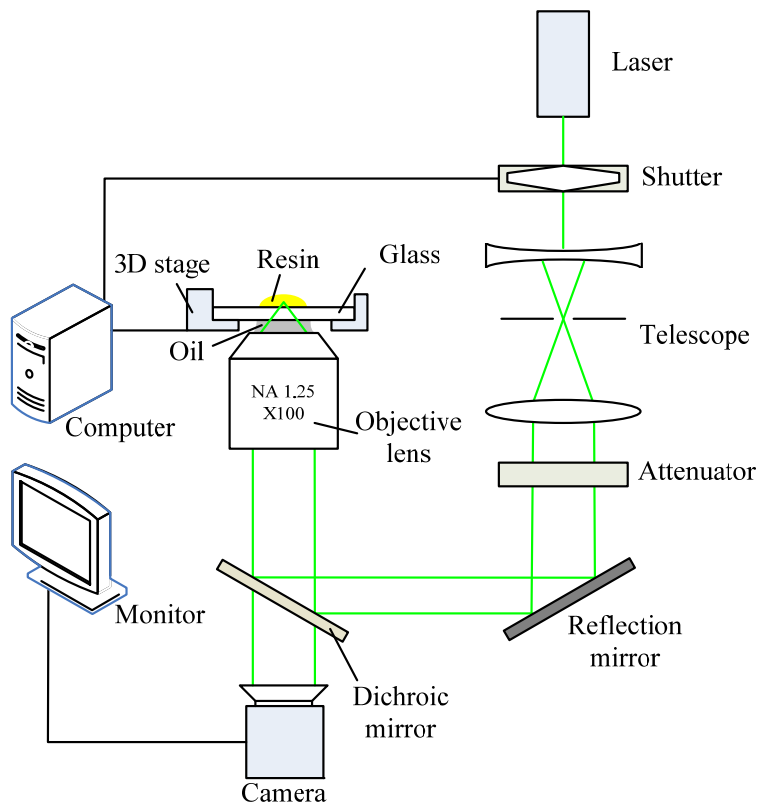
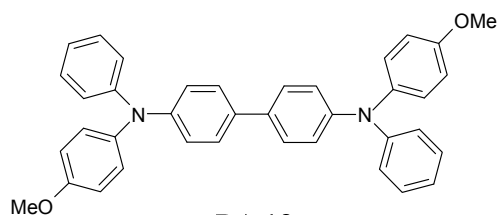


Figure 5-1 Schematic diagram of the TPP micro-fabrication system.



RA 12

Benzidine, N, N'-bis(p-methoxyphenyl)-N, N'-diphenyl-(8Cl)

Figure 5-2 Chemical structures of the photo-initiator: *RA 12*.

Table 5-1 The major manufacturing equipments and their main characteristics.

Item	Specifications
Microscope & objective lens	Zeiss Axiovert 2000 Zeiss A-plan 100x, NA=1.25 oil-immersed
Laser	Frequency doubled Nd:YAG micro-laser (532 nm) Repetition rate: 6.5 kHz Maximum pulse energy: 4 μ J Pulse duration: 0.5 ns
Shutter	Nm Laser LS2000 Switching speed: 400 ms Delay after command: 1.5 ms
3D piezoelectric stage	PI P-611.3S Travel range: 100 \times 100 \times 100 μ m Resolution: 1 nm
Digital/Analog Output Board	ICP DAS PIO-DA8 Analog output resolution: 14 bits Voltage output range: -10V \sim +10V Absolute accuracy: 0.01% FSR
Camera	Prosilica EC1280 Sensor Type: CMOS Sensor Resolution: 1280 \times 1024 pixels Full resolution frame rate: 24 fps

5.2 The correction of voxel exposure time

As discussed in section 4.6, it is difficult to reach the real time manufacture based on the data transferred from the host PC to the manufacturing equipment because of delays taking place during the data processing. Except for the time spent in the software

processing the input model, data processing refers to control signals passing to equipments until equipments really respond and it is this transmission that faces delays. Moreover, if a fabrication system is controlled by closed loop, it needs more time to wait feedback from equipments. Since a basic polymerized path in TPP micro-fabrication is made by contiguously exposing resin under a laser light, the time lag will cause a voxel to be exposed too much, hence producing an unexpected voxel size.

In this research, we assume that all the equipments of the fabrication system are highly reliable so that the system can be controlled by an open loop structure to reduce the system delay time. In other words, after a control signal is passed on to equipment (possibly with some delay time), the system will carry on with the next action. As a result, the system delay time issues can be simplified to an issue about message transmissions and another one related to processing operations in the software part of the manufacturing system.

To estimate the system delay time, two reference objects: a cube and a hemisphere (see Figure 5-3(a) and Figure 5-3(c)) were fabricated ten times for each of them. Figure 5-3(b) and (d) depict the slicing data of the cube and hemisphere, and they contain 9,219 and 5,438 voxel exposed positions, respectively. Table 5-2 shows the fabrication time (T) and the extended exposure time per voxel (t_{ee}) corresponding to the cube in Figure 5-3(a) fabricated with 10 ms of default exposure time per voxel (t_{de}). The t_{ee} evaluated with Eq.4-11 can be used to correct the exposure time per voxel. Referring to Eq.4-12, the actual exposure time per voxel (t_{re}) can be hypothesized to t_{de} plus t_{ee} .

Table 5-2 The actual fabrication times (with 10 ms of default voxel exposure time) for the cube and its corresponding extended exposure time per voxel.

No	1	2	3	4	5	6	7	8	9	10
T (s)	165.1	158.5	161.5	166.3	159.0	159.2	158.3	159.4	159.5	158.9
t_{ee} (ms/voxel)	5.9	5.2	5.5	6.0	5.2	5.2	5.1	5.2	5.3	5.2

From Table 5-2, we can observe that the variation of T across the various tests is rather small (the average time is 160.6 s and the standard deviation 2.85s). So, the average value of the actual fabrication time can be used to assign the T parameter in Eq.4-11. To evaluate the behavior of the relation between default and extended voxel exposure times, each reference model was fabricated ten times with a range of default voxel exposure times. The corresponding extended voxel exposure time are plotted in Figure 5-3(e). Although the relation is nonlinear, the t_{ee} (s) of the cube and of the hemisphere are similar with respect to the variation of t_{de} . As a result, fabricating

different shapes and obtaining similar extended exposure times suggest that it is possible to use these results to correct and evaluate the prescribed exposure time when we want to manufacture other micro-products.

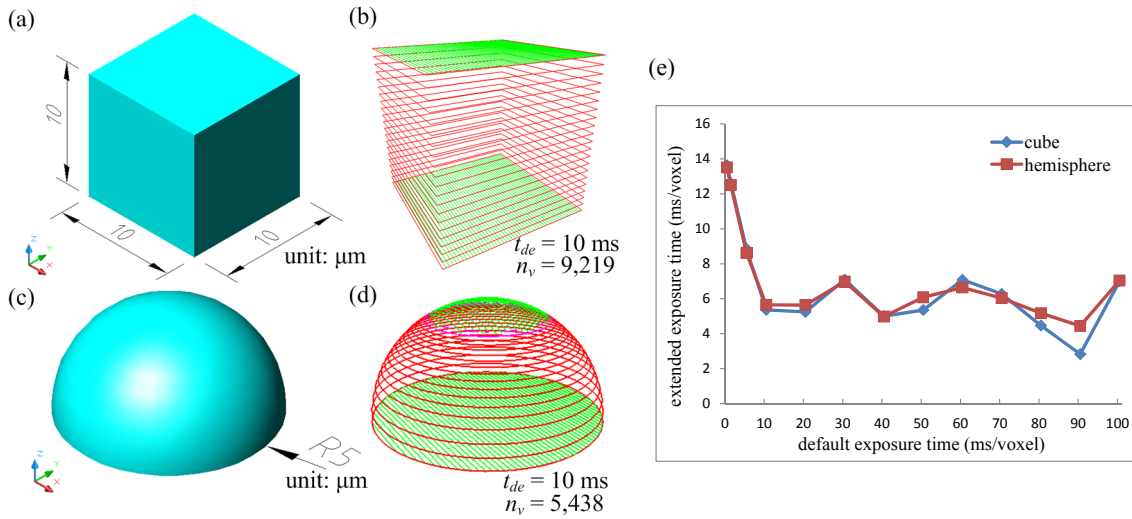


Figure 5-3 Fabrication of reference models for finding the extended exposure time per voxel.

5.3 The overall processing flow for the TPP micro-fabrication

Figure 5-4 shows the process flow of the proposed approach for the TPP micro-fabrication process. From the PV point of view, here, two upstream PVs, RE and design office, are included in proposed approach. Their vehicular data are called RE model and CAD model here. In Figure 5-4, except for the flows represented with black arrows where both models can be processed, the blue-dot and red flows are only processed by RE and CAD models, respectively. The overall procedure is decomposed into two steps according to their functions from the PV point of view and discussed as follows:

1. Reference model (manufacturing model) preparation (see block A in Figure 5-4):

The purpose is to produce a manufacturing model which conforms to the requirements of TPP micro-fabrication (discussed in chapter 3). According to the input source from upstream PVs, one of the following process flows is applied:

- Model preparation with input from RE:

If a shape of an existing object is needed for fabrication, a RE technique can be used to capture its 3D shape data. After data pre-processing and 3D mesh generation, a faceted model is created and exported through a STL file format. Then, this STL file is read by SIMPOLY and is converted to a polyhedron entity

(manufacturing model) directly. However, the HLT is not involved in this case, so the two specific processes: OBCD and welding sub-domain process cannot be executed because both of them use the concept of mixed representation. Indeed, these two processes aren't needed because they are suitable for non-manifold models and the RE model is of manifold type most of the time.

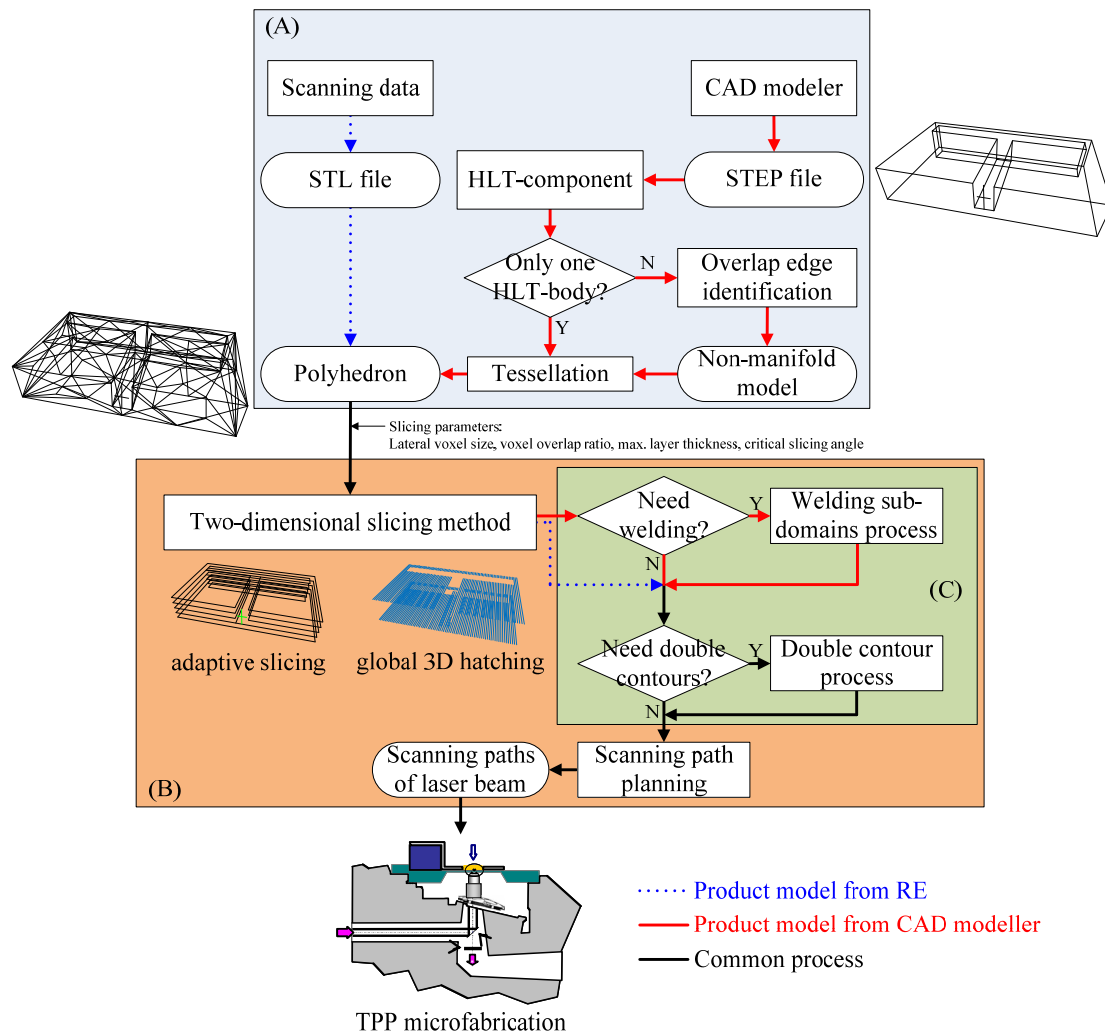


Figure 5-4 The process flow of the proposed approach for the TPP micro-fabrication process.

- Model preparation with input from the design office:

To fabricate a specific functional micro-product, a designer can use a commercial CAD modeler to design his, resp. her, digital model and export it through a STEP file format. Then, this STEP file is read by SIMPOLY, and converted into a mixed representation incorporating the HLT data. If the CAD model is composed of several disconnected shape elements, then the OBCD process is firstly carried out to identify all overlapping boundary curves. Finally,

a conformable polyhedron (manufacturing model) is produced after applying the proposed tessellation process,

2. Simulation of the manufacturing process (see block B in Figure 5-4)

The purpose is to produce laser beam trajectories from a manufacturing model. The simulation process (detailed in chapter 4) includes two main processes and two optional procedures. The trajectories of a manufacturing model are obtained and arranged by the TSM and trajectory path planning processes. If the user considers that the structure is too weak, the specific operations: weld sub-domains and double contour processes (see block C in Figure 5-4) can be chosen to increase the stiffness locally by reinforcing the connections between two sub-domains or increasing the wall thickness of the micro-product, respectively.

After obtaining the laser beam trajectories of a manufacturing model, a micro-product is fabricated with the experimental equipments mentioned at section 5.1 through the driver linking SIMPOLY to this equipment.

5.4 Objects with simple shapes

In previous discussions, comparing SSM and ASP with TSM, TSM cannot only fabricate completely all the necessary surfaces of an object, but it also increases the processing efficiency. As a result, different slicing algorithms such as SSM, ASP, and TSM are used to fabricate simple shapes and investigate their influence over processing efficiency.

As a first example, a micro-stair with two steps and a small slope (10 degrees) is considered. Its CAD model is created with Autodesk Mechanical DeskTop 2007 (MDT), and converted to a STEP file, as shown in Figure 5-5(a). Figure 5-5(b) shows the polyhedral model tessellated from the STEP file in SIMPOLY software. To highlight the effect of TSM, the micro-stair is processed with two different approaches to generate laser beam trajectories. One uses SSM and, of course, checking the resulting slicing data, two fully flat steps become cavities (see left of Figure 5-5(c)). The other one uses TSM whose slicing data is composed of contours and hatching data (see left and centre of Figure 5-5(d)). The actual exposure time of each voxel is 20 ms with a laser power of 5 μ W. Under these manufacturing conditions, the lateral size of a voxel sets around 360 nm. With a voxel overlap ratio of 0.45, the layer thickness of the micro-stair made by SSM is 35 nm. Even though it took 20 minutes to complete, two steps are still not filled up resulting in an unacceptable shape, as shown at right of Figure 5-5(c). With an identical voxel overlap ratio, the micro-stair made by TSM took only 7 minutes to manufacture all the digital model surfaces, as shown at right of Figure

5-5(d). As a result, using TSM can greatly reduce (here 80%) the processing time. The critical slicing angle is 10 degrees, and based on the layer thickness criterion, the layer thickness should be the same as for SSM but the slope of the micro-stair is produced during the secondary slicing phase of TSM, so a larger layer thickness can be used. In this case the layer thickness and the hatching distance are the identical: $0.2\ \mu\text{m}$.

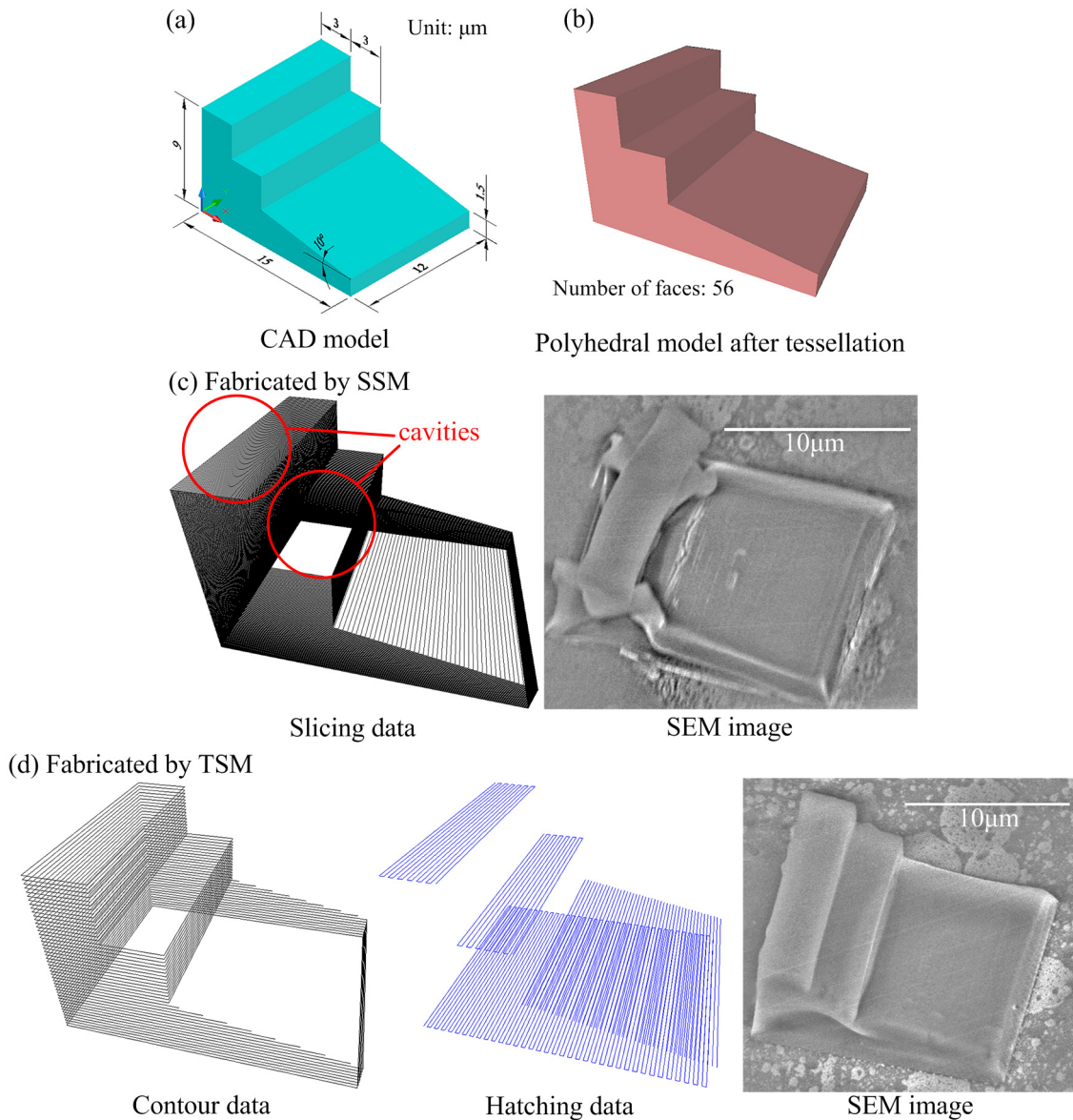


Figure 5-5 The micro-stair fabricated with SSM and TSM.

A second test case is the micro-hemisphere. Its CAD model is also created by MDT and converted to a STEP file, as shown in Figure 5-6(a). Figure 5-6(b) shows the polyhedral model tessellated from the STEP file input in SIMPOLY. Since the hemisphere is an axially symmetric shape, it can be used to observe the transition configurations between contour and hatching trajectories of the laser beam by setting different critical slicing angles. The manufacturing conditions are the same those for the

micro-stairs. Figure 5-6(c) and (d) show the slicing data and SEM images of hemispheres with critical slicing angles of 30 and 45 degrees. Obviously, the transition configurations between primary and secondary trajectories of the laser beam are blended very well due to the positioning accuracy of the piezoelectric stage.

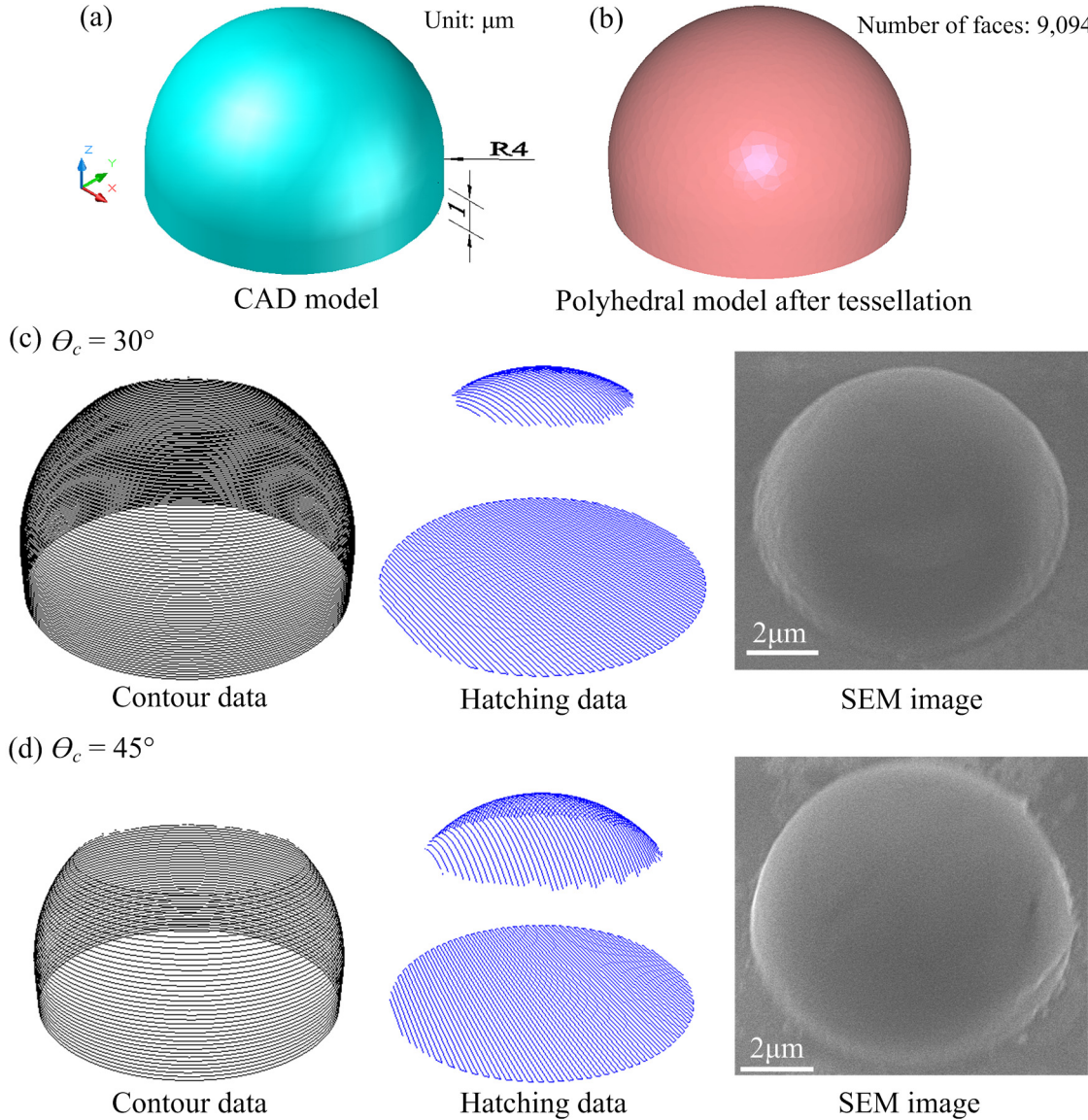


Figure 5-6 Micro-hemispheres fabricated by TSM with different critical slicing angles.

In addition, Figure 5-7 shows a comparison of the simulation of the model processing efficiency for this simple shape (micro-hemisphere) with different fabrication parameters. The simulation conditions are the later voxel size of 360 nm, a voxel overlap ratio of 0.45, an actual expose time of 20 ms, and a maximum layer thickness of 0.2 μm . In Figure 5-7(a), the proposed TSM (critical slicing angle of 30 degrees) is the most efficient fabrication strategy. It reduces by 86% and 21% the fabrication time compared to SSM and ASP, respectively. Figure 5-7(b) shows the

fabrication times of the micro-hemispheres fabricated by TSM only but with different critical slicing angles. When increasing the critical slicing angle, the corresponded fabricating time gradually decreases. Because relief hatchings are used to fabricate some areas whose shape angle are smaller than the critical slicing angle, then larger layer thicknesses can be used to fabricate the remaining areas. In this case however, if the critical slicing angle is greater than 45 degrees, the layer thickness will be bounded by the maximum layer thickness in order to generate more compact structures with a higher stiffness. For example, if the critical slicing angle is set to 50 degrees, then the suitable layer thickness would be $0.36 \mu\text{m} \times (1 - 0.45) \times \tan 50^\circ = 0.236 \mu\text{m}$ which is greater than the maximum layer thickness ($0.2 \mu\text{m}$). Based on the layer thickness criterion, the effective layer thickness is set to $0.2 \mu\text{m}$. Therefore, the fabrication time of hemispheres, whose critical slicing angles are greater than 45 degrees, tend to be similar.

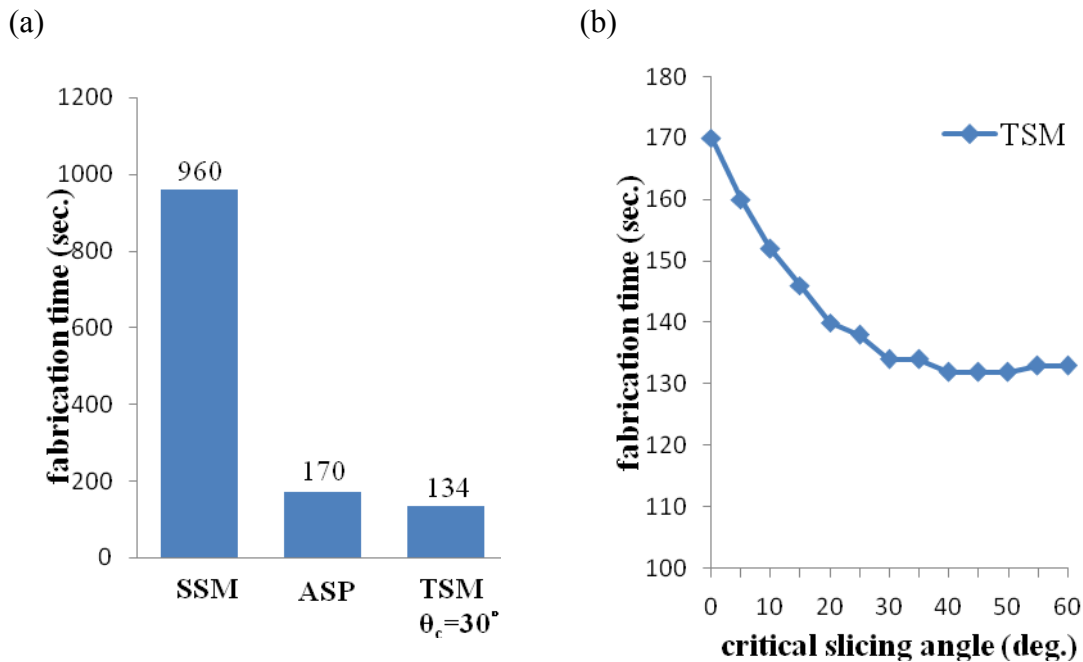


Figure 5-7 The processing efficiency comparisons for a simple shape (micro-hemisphere).

5.5 Objects with complex shapes

To further demonstrate the ability of TSM, a more complex 3D microstructure (micro-dragon) has been produced. The original polyhedral model of the dragon contained 871,414 polygons and is obtained from the Stanford Computer Graphics Laboratory, as shown in Figure 5-8(a). Then, SIMPOLY is used to simplify the model to 16,620 polygons and scale down to 1:5000 ($41 \times 18 \times 29 \mu\text{m}^3$) [Véron & Léon 98], as shown in Figure 5-8(b).

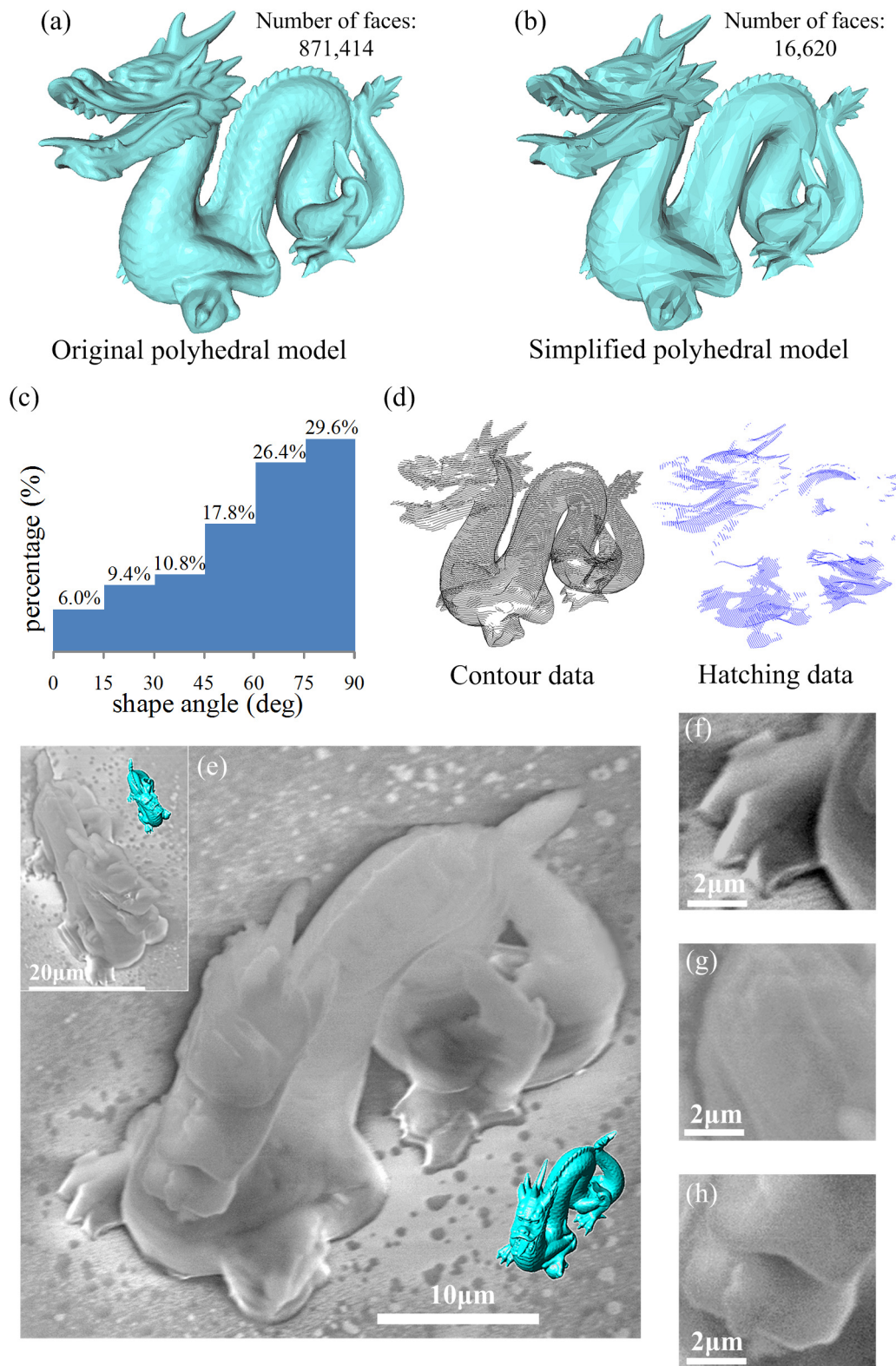


Figure 5-8 The micro-dragon fabricated by TSM.

After investigating the triangular faces of the polyhedral model, we found that there are many ‘nearly flat’ regions in the dragon model (Figure 5-8(c)). Therefore, a large critical slicing angle (45 degrees) is specified to reduce the processing time. This means that there is 26.2% of the area of the dragon that are addressed as relief hatching

trajectories for the fabrication. Besides, the voxel overlap ratio is set to 0.45 and the layer thickness and hatching distance are set to 0.25 μm . The micro-dragon is fabricated with a laser power of 13 μW and actual exposure time of 20 ms/voxel. Under these fabricating conditions, the lateral size of a voxel reaches 460 nm as observed from a SEM image.

To obtain the contour and hatching data showed in Figure 5-8(d), it took 4.68 minutes (characteristics of the computer: CPU: Intel Core Duo T7200 2.0GHz, Memory: DDRII 667MHz RAM 2GB). Figure 5-8(e) shows the SEM images of the micro-dragon obtained by TSM. It took 19 minutes to fabricate it. The inset is the same object with a different view angle. The nearly flat regions are distributed over the dragon's paw, back and mouth. Figure 5-8(f)-(h) show these neighborhoods and the transition areas of the laser trajectories produced by two different slicing directions. Here, there is no cavity but a smooth surface. If we only use SSM to manufacture a micro-dragon with the same surface roughness as in Figure 5-8(e), we estimate that it would take 12.66 hours to fabricate and the layer thickness needed would be 5 nm, which largely exceeds the resolution of our manufacturing equipments.

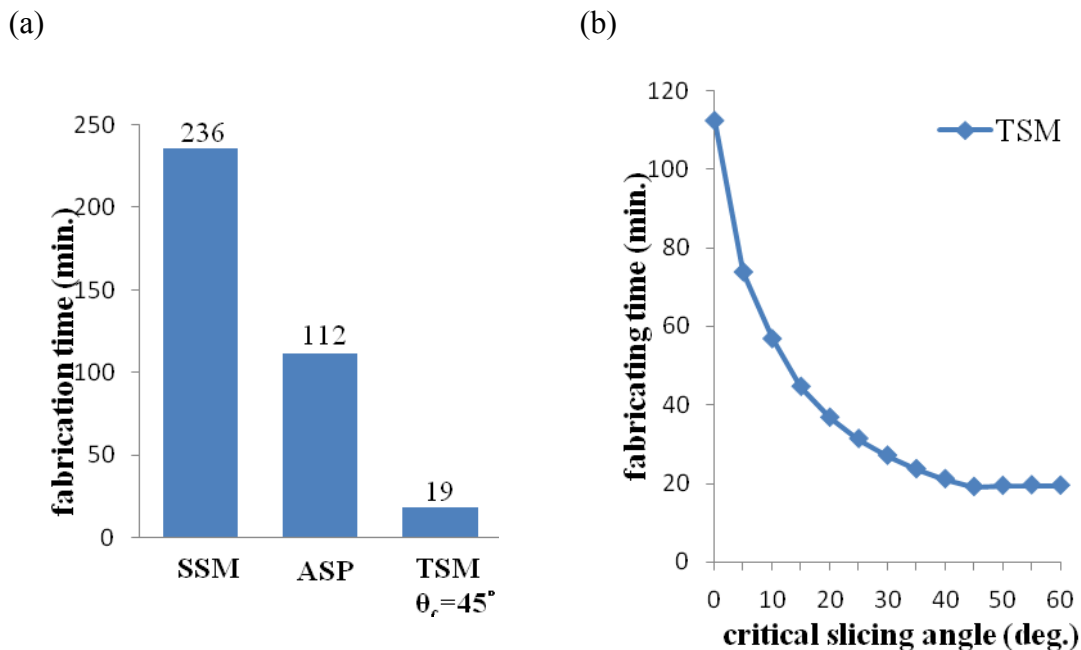


Figure 5-9 Processing efficiency comparisons for a complex shaped object (micro-dragon).

Figure 5-9 is similar to Figure 5-7. It shows the comparisons of the simulation processing efficiencies for complex-shaped objects (micro-dragon) according to different fabrication modes and parameters. The simulation conditions are similar to the above manufacturing ones, except the maximum layer thickness which is set to 25 μm .

Again, in Figure 5-9(a), the dragon fabricated by TSM with a critical slicing angle of 45 degrees characterizes the most efficient manufacturing process and reduces by 92% and 83% the fabrication time of SSM and ASP, respectively. It deserves to be mentioned that the difference between TSM and ASP is greater than for the simple shape shown in Figure 5-6(a). This is because the micro-dragon contains many ‘nearly flat’ and irregular regions and small layer thicknesses will be chosen to avoid the layer separation in ASP. In this case, TSM indeed shows its potential of reducing fabrication time. Figure 5-9(b) shows the fabrication times of the micro-dragon fabricated by TSM with different critical slicing angles. When increasing the critical slicing angle, the corresponding fabrication time also gradually decreases as in Figure 5-9(b).

Table 5-3 Comparison between micro-bull and micro-dragon

	Micro-bull*	Micro-dragon
Exposure source	Ti:Sapphire laser (150 fs pulsewidth)	Nd:YAG laser (0.5 ns pulsewidth)
Lateral size of a voxel	150 nm	460 nm
Size	around $15 \times 8 \times 8 \mu\text{m}^3$	$41 \times 18 \times 29 \mu\text{m}^3$
Exposure time	1 ms (no correction)	20 ms
Laser thickness	50 nm	250 nm
Voxel overlap ratio	0.67	0.45
Slicing method	CSM	TSM
Number of voxels	100,000	59,940
Fabricating time	13 minutes	19 minutes

*: refer to [Kawata et al. 01, Tanaka et al. 02, Sun et al. 03a]

Table 5-3 gives a brief comparison between the benchmark example micro-bull (see Figure 1-28(d)) [Kawata et al. 01, Tanaka et al. 02, Sun et al. 03a] and our micro-dragon. Although the micro-bull and micro-dragon are made with different types of lasers (femto-second and nano-second pulsed lasers, respectively) and the object sizes are also different, there is still some observations that can be interpreted here.

Since the voxel overlap ratio used for the micro-bull is higher than our micro-dragon, the surface roughness is certainly better than that of the micro-dragon. 6 hours would be necessary if the micro-dragon is fabricated with the same fabricating conditions as the micro-bull. However, a long processing time would face external perturbations, such as vibrations, and challenge the stability of the laser power output and of experiment equipments. Details are explained in section 1.8.3. Besides, it's also difficult to fabricate larger objects with high quality surface roughness due to the gravity.

Indeed, the unfinished parts ‘flies’ in the resin during process mentioned in section 1.8.5, but it may shift its original position due to the rheology of the resin subjected to gravity over a long process time. Therefore, a larger voxel size is chosen in this case. Considering the voxel size as a manufacturing parameter during the manufacturing process is one way to solve this issue, and can be the target of future research.

5.6 Objects as non-manifold functional microstructures

Microstructures incorporating kinematic functions or like functions, such as membranes, can be produced with the TPP process. Their digital models are represented as non-manifold models. This section shows what we need to process non-manifold models during the TPP micro-fabrication preparation process.

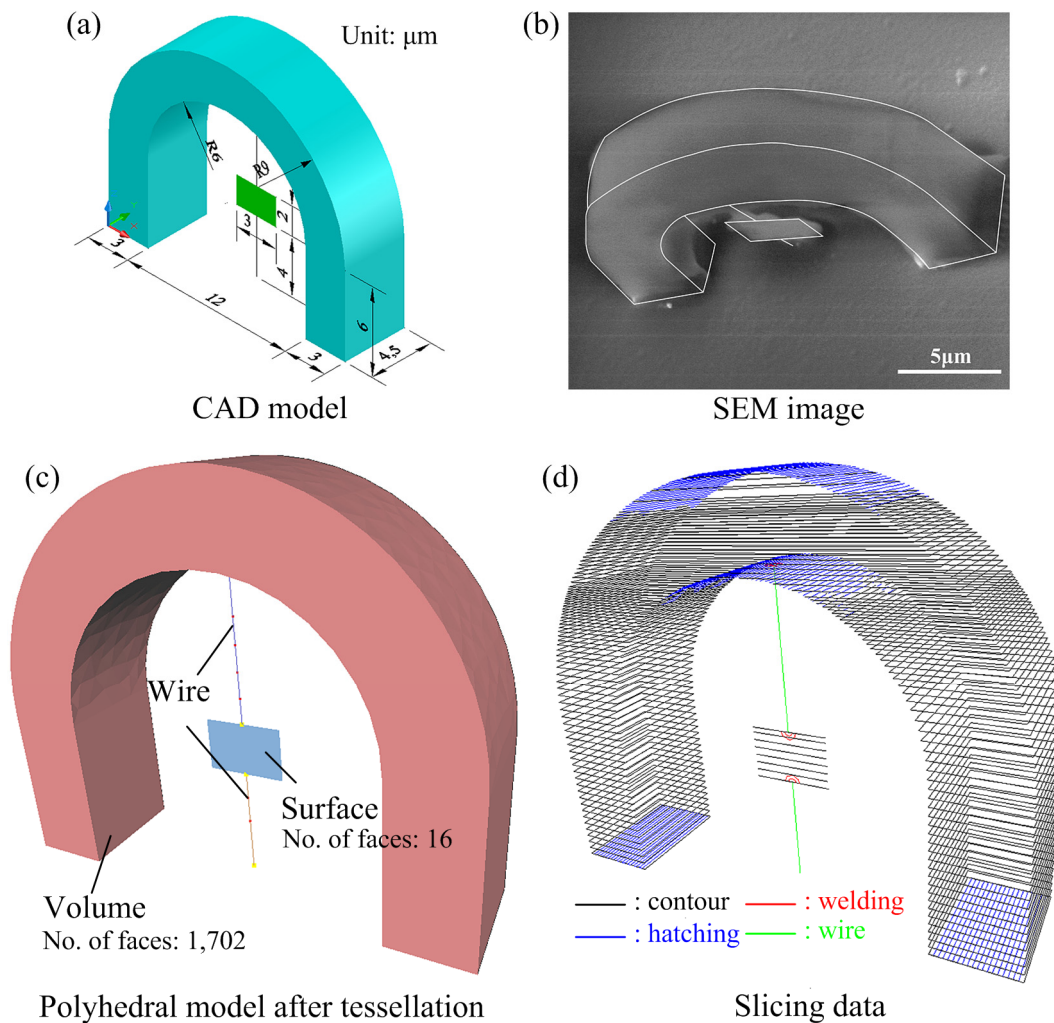


Figure 5-10 The non-manifold microstructure incorporating a volume (arch), an open surface (plane), and two wires.

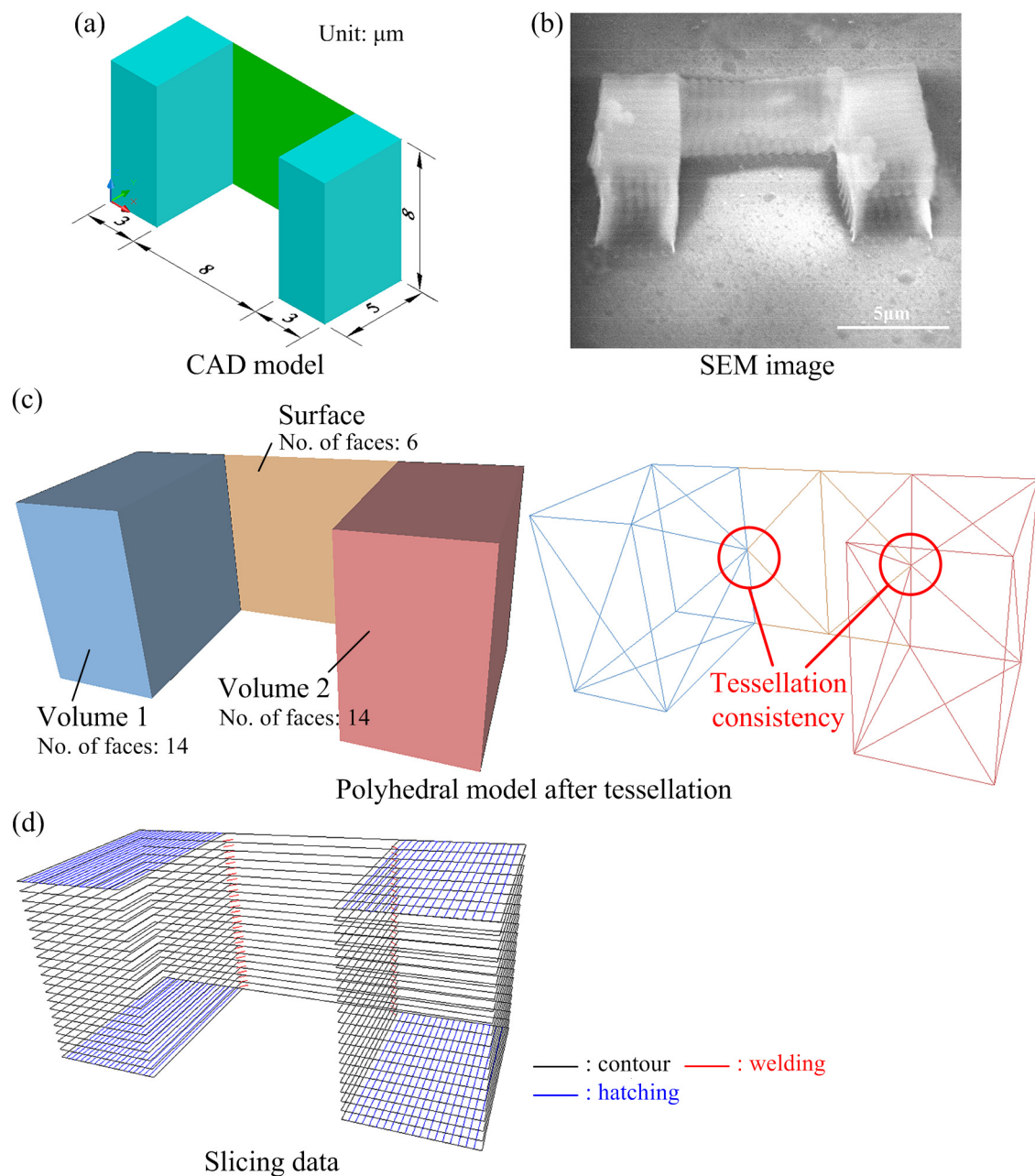


Figure 5-11 A non-manifold microstructure incorporating two volumes (blocks) and an open surface (membrane).

Figure 5-10(a) depicts the CAD model of a microstructure corresponding to an assembly configuration incorporating kinematic functions. This model is the manufacturing model containing the laser beam trajectories and the wires form deformable joints enabling relative movements of rotation between the plate and the gantry. Figure 5-10(b) depicts the SEM image of the microstructure produced with the TPP manufacturing equipment. It must be noticed that this ‘compound’ element include wires, surface and volume sub domains in a single object. After importing the CAD model as a STEP file into SIMPOLY, either the IMS or OBCD process is carried out to produce a non-manifold model. Then, the polyhedron resulting from the tessellation

process of the non-manifold model previously obtained is shown on Figure 5-10(c). Figure 5-10(d) illustrates the results obtained from the TSM and welding processes with SIMPOLY software.

Figure 5-11(a) shows the picture of a microstructure representing a single component that is represented as non-manifold model because it incorporates a membrane like function to bind two distant parallelepiped volumes. Such configurations are often found in micro-fluidic sensors. Figure 5-11(b) is a SEM image of the micro-manufactured component. Similarly to Figure 5-10(c), at the left of Figure 5-11(c) is represented the tessellated result obtained from the non-manifold model of Figure 5-11(a), and at right is illustrated the consistency of the tessellation result with the proposed tessellation process. The laser beam trajectories obtained from TSM and welding processes are presented in Figure 5-11(d). It should be noticed that Figure 5-11(d) contains welding micro-manufacturing features to stiffen the link between the membrane-like sub-domain and the volume ones. These welds form a blending area between these two sub-domains.

The first results (see Figure 5-10(b) and Figure 5-11(b)) show that both geometries are correctly produced, despite some shape discrepancies due to the stabilization of the process (fine tuning of the laser beam) which reflects the adjustments that were needed during the first tests whereas the shape quality has been improved for the micro-dragon that has been produced later. One can note that all elements are present (wires, membranes, ...) with good connections between each others, illustrating the efficiency of the whole model processing.

5.7 Conclusion

A CAD/CAM system for TPP micro-fabrication is implemented by synthesizing the research results coming from previous chapters. The system layout has been introduced at the beginning of the chapter. The time-lag issue caused by data transmissions and processing operations through the software part of the fabrication system has been subjected to a preliminary analysis and a simple correction process has been proposed. The processing flow of the TPP fabricating system stringed up the significant contributions of this study and it described completely the development process of a micro-product manufacture.

Three fabrication examples, two objects with simple shapes and one with a complex shape, have been set up to prove that the fabrication efficiency of proposed TSM process is better than SSM and ASP. Finally, two objects as non-manifold functional microstructures have been fabricated. The results fabricated by the laser

beam trajectories obtained from their conformable non-manifold polyhedral models are used to demonstrate that our proposed method can fully exploits the characteristics of TPP micro-fabrication equipment: manufacturing smallest possible shape features.

Conclusions and perspectives

6.1 Conclusions

At the beginning of this thesis, analyses and discussions have been presented about the principle and the present stage of TPP micro-fabrication to current un-solved critical issues for the development of the TPP micro-manufacturing process. Then, a product model acquisition, a preparation and a simulation processes for the TPP micro-manufacturing process have been proposed, thus defining a concept of product view for TPP micro-fabrication. The overall research has been accomplished at NTU and jointly at INPG and UJF. Taking into account the process requirements, the following objectives have been achieved:

- Color product model acquisition from a reverse engineering process:

With the aid of a programmable control of the laser beam power of a scanning device, an adaptive scanning line capturing process has been developed to obtain an object's shape without damaging its intrinsic color. An automated process of texture map generation and of orientation between a CAD model and a texture space have been developed to automate the mapping between a CAD model and its intrinsic color data. Finally, an integrated scanning system has been developed to verify the proposed approach. Except for creating a color CAD model quickly, the color mapping information extracted from our approach can also be used to fabricate colored components in RP industry,

- Non-manifold product model preparation for micro-fabrication:

Considering CAD modelers and data exchange standards does not provide an efficient way to handle the non-manifold representation that has been demonstrated as necessary to produce a wide diversity of micro-products, an IMS and OBCD processes have been developed to assist a user in building non-manifold models from topological and geometrical point of views,

- Conformable polyhedral model as an outcome of the non-manifold models' tessellation :

A tessellation process using the concept of mixed shape representation and *OverlapEdge* has been developed to keep the topological relationships between an original B-Rep NURBS model and a tessellated polyhedron. In a tessellated polyhedron, polyedges and partitions are linked to boundary curves and faces in a B-Rep model, and polywires are linked to wire-frame sub domains. With these connections, not only conformable non-manifold polyhedrons can be produced, but also high level operations can be carried out, such as the welding process of sub-domains developed in this thesis,

- Increasing the manufacturing efficiency:

A TSM slicing process differing from the traditional slicing process, which has only one slicing direction, has been developed. To increase the TPP manufacturing efficiency, it uses an additional slicing direction perpendicular to the reference one to fabricate nearly plane areas. In our micro-dragon example, it can save 92% and 83% fabrication time compared to SSM, and ASP, respectively,

- Optimization of scanning path planning:

The optical properties between polymerized and un-polymerized parts of the resin may be different and influence the manufacturing result. Therefore, a concept of focal distance has been used to sort the fabrication sequences of laser beam trajectories to reduce the effect of these transformations of optical properties,

- Enhancing strategies to improve microstructures' stiffness:

A welding process for sub-domains and a double contour trajectory process have been developed to enhance the connections between different sub-domains and increase the wall thicknesses of volume sub-domains, respectively,

- Illustrative examples of the proposed approach:

Several fabrication examples have been made with the proposed TPP micro-fabrication process. They are used to confirm that all the desired shapes and functions were fabricated and all the approaches mentioned above have successfully achieved their objectives.

6.2 Perspectives

This thesis has been developed a synthesized approach to solve mostly main critical issues encountered during the development process of TPP micro-manufacturing.

Micro-products contained different shapes (1D, 2D, 3D, or their combinations) and configurations (whether single component or assembly) can be fabricated by following our proposed approach. However, this proposed approach is still related to the early stage of TPP process development, and further manufacturing schemes may appear to be able to address more precisely manufacturing and functional requirements for microstructures. The considered perspectives which can extend our research are as follows:

- The quantitative evaluation of orientation mapping needs be explored to improve the quality of texture mapping. Filtering the color gray level value from the proposed 3D color model also needs be implemented to complete this work,
- The detailed fabrication parameters and characteristics of the TTP system need be investigated to improve the fabrication accuracy and performance,
- From the manufacturing point of view, the laser beam energy interacting with the polymerized part needs more investigations and analyses with respect to the path planning trajectories,
- Further works may include the microstructure partitioning capabilities to enhance algorithms involved in the microstructure model processing. Such partitioning capabilities will help structure the trajectory scheduling,
- Consider the voxel size as a manufacturing parameter during manufacturing process, so according the shape and function of a micro-product, varied wall thicknesses can be assigned (i.e. thin wall thickness represents the detail features and thick one represents the main body).

Bibliography

- [Agoston 05] Agoston, M. K., 2005, *Computer Graphics and Geometric Modelling: Implementation and Algorithms*, Springer, United States.
- [Albamont & Goshtasby 03] Albamont, J., and Goshtasby, A., 2003, "A Range Scanner with a Virtual Laser", *Image and Vision Computing*, **21**, pp.271-284.
- [Armstrong 94] Armstrong, C. G., 1994, "Modelling Requirements for Finite-Element Analysis", *Computer-Aided Design*, **26**(7), pp.573-578.
- [Austin et al. 04] Austin, M. D., Ge, H., Wu, W., Li, M., Yu, Z., Wasserman, D., Lyon, S. A., and Chou, S.Y., 2004, "Fabrication of 5 nm Linewidth and 14 nm Pitch Features by Nanoimprint Lithography", *Applied Physics Letters*, **84**(26), pp.5299-5301.
- [Bosson-Ehoomann et al. 06] Bosson-Ehoomann, J., Mihut, A., Tosa, N., Astilean, S., Pierre, M., Rambaud, C., Vurth, L., Baldeck, P., and Stephan, O., 2006, "Two-photon Fabrication of Metallic Nanowires for Plasmonics", *Nonlinear Optics, Quantum Optics*, **35**(1-3).
- [Buss 03] Buss, S. R., 2003, *3-D Computer Graphics: a Mathematical Introduction with OpenGL*, Cambridge University Press, United Kingdom.
- [Bustillo et al. 98] Bustillo J. M., Howe, R. T., and Muller, R. S., 1998, "Surface Micromachining for Microelectromechanical Systems", *Proceedings of the IEEE*, **86**(8), pp.1552-1574.
- [Byun & Lee 06] Byun, H. S., and Lee, K. H., 2006, "Determination of Optimal Build Direction in Rapid Prototyping with Variable Slicing", *International Journal of Advanced Manufacturing Technology*, **28**, pp.307-313.
- [C++ Resources] C++ Resources Network, <http://www.cplusplus.com/reference/stl/list/>.
- [Carey & Greenberg 85] Carey, R. J., and Greenberg, D. P., 1985, "Textures for Realistic Image Synthesis", *Computers and Graphics*, **9**(2), pp.125-138.

- [CGAL] CGAL, Computational Geometry Algorithms Library, <http://www.cgal.org/>.
- [Clark et al. 97] Clark, J., Trucco, E., and Wolff, L. B., 1997, "Using Light Polarization in Laser Scanning", *Image and Version Computing*, **15**, pp.107-117.
- [Cunningham et al. 06] Cunningham, L. P., Veilleux, M. P., and Campagnola, P. J., 2006, "Freeform Multiphoton Excited Microfabrication for Biological Applications Using A Rapid Prototyping CAD-based Approach", *Optics Express*, **14**(19), pp.8613-8621.
- [Dimov et al. 06] Dimov, S. S., Matthews, C. W., Glanfield, A., and Dorrington, P., 2006, "A Roadmapping Study in Multi-material Micro Manufacture", *Conference on Multi-material Micro Manufacture, Proceedings, Elsevier*, xi;xxv, Grenoble, France.
- [Divliansky et al. 05] Divliansky, I. B., Weaver, G., Petrovich, M., Jabbour, T., Seigneur, H. P., Parnell-Lampen, C., Thompson, A., Belfield, K. D., and Kuebler, S. M., 2005, "CAD-integrated System for Automated Multi-photon Three-dimensional Micro- and Nano-fabrication", *Progress in Biomedical Optics and Imaging – Proceedings of SPIE*, **5720**, pp.196-203.
- [Duan et al. 04] Duan, X.-M., Sun, H.-B., Kaneko, K., and Kawata, S., 2004, "Two-photon Polymerization of Metal Ions Doped Acrylate Monomers and Oligomers for Three-dimensional Structure Fabrication", *Thin Solid Films*, **453**(54), pp.518-521.
- [Dutta et al. 01] Dutta, D., Prinz, F. B., Rosen, D., and Weiss, L., 2001, "Layered Manufacturing: Current Status and Future Trends", *Journal of Computing and Information Science in Engineering*, **1**(1), pp.60-71.
- [French & Sarro 98] French, P. J., and Sarro, P. M., 1998, "Surface Versus Bulk Micromachining: the Contest for Suitable Applications", *Journal of Micromechanics and Microengineering*, **8**, pp.45-53.
- [Gonzalez & Woods 92] Gonzalez, R. C., and Woods, R. E., 1992, *Digital Image Processing*, pp.484-486.
- [Guo et al. 06] Guo, R., Xiao, S., Zhai, X., Li, J., Xia, A., and Huang, W., 2006, "Micro Lens Fabrication by Means of Femtosecond Two Photon Photopolymerization", *Optical Express*, **14**(2), pp.810-816.
- [Hamri 06] Hamri, O., 2006, "Method, Models and Tools for Finite Element Model Preparation Integrated into a Product Development Process", Ph.D. thesis, Institut

National Polythchnique de Grenoble, France.

- [Hamri et al. 06] Hamri, O., Léon, J.-C., Giannini, F., Falcidieno, B., Poulat, A., Fine, L., 2006, "Interfacing Product Views Through a Mixed Shape Representation. Part 1: Data Structure and Operators", *Proceedings of Virtual Concept 2006*, Playa Del Carmen, Mexico.
- [Haske et al. 07] Haske, W., Chen, V. W., Hales, J. M., Dong, W., Barlow, S., Marder, S. R., and Perry, J. W., 2007, "65 nm Feature Sizes Using Visible Wavelength 3-D multiphoton lithography", *Optical Express*, **15**(6), pp.3426-3436.
- [Heckbert 86] Heckbert, P. S., 1986, "Survey of Texture Mapping," *IEEE Computer Graphics and Applications*, pp.56-67.
- [Huang & Menq 01] Huang, J., and Menq, C. H., 2001, "Automatic Data Segmentation for Geometric Feature Extraction from Unorganized 3-D Coordinate Points", *IEEE Transaction on Robotics and Automation*, **17**(3), pp.268-279.
- [Huang & Tai 00] Huang, M. C., and Tai, C. C., 2000, "The Pre-processing of Data Points for Curve Fitting in Reverse Engineering", *International Journal of Advanced Manufacturing Technology*, **16**(9), pp.635-642.
- [Ikuta & Hirowatari 93] Ikuta, K., and Hirowatari, K., 1993, "Real Three Dimensional Microfabrication Using Stereo Lithography and Metal Molding", *Proceedings of IEEE MEMS'93*, pp.42-47.
- [Jain et al. 06] Jain, A., Vadav, V., Mittal, A., and Gupta, S., 2006, "Probabilistic Approach to Modeling of 3D Objects Using Silhouettes", *Journal of Computing and Information Science in Engineering*, **6**(4), pp.381-389.
- [Jia et al. 07] Jia, B., Serbin, J., Kim, H., Lee, B., Li, J., and Gu, M., 2007, "Use of Two-photon Polymerization for Continuous Gray-level Encoding of Diffractive Optical Elements", *Applied Physics Letters*, **90**, 073503.
- [Kaneko et al. 03] Kaneko, K., Sun, H.-B., Duan, X.-M., and Kawata, S., 2003, "Two-photon Photoreduction of Metallic Nanoparticle Gratings in A Polymer Matrix", *Applied Physics Letters*, **83**(7), pp.1426-1428.
- [Kato et al. 05] Kato, J.-I., Takeyasu, N., Adachi, Y., Sun, H.-B., and Kawata, S., 2005, "Multiple-spot Parallel Processing for Laser Micronanofabrication", *Apply Physics Letters*, **86**, 044102.
- [Kawata et al. 01] Kawata, S., Sun, H.-B., Tanaka, T., and Takada, K., 2001, "Finer Features for Functional Microdevices", *Nature*, **412**, pp.697-698.

- [Knoll et al. 06] Knoll, A., Dürig, U., Züger, O., and Güntherodt, H.-J., 2006, "Micron-sized Mechanical Oscillators Created by 3D Two-photon Polymerization: Towards a Mechanical Logic Device", *Microelectronic Engineering*, **83**, pp.1261-1264.
- Kovacs, G. T. A., Maluf, N. I., and Petersen, K. E., 1998, "Bulk Micromachining of Silicon", *Proceedings of the IEEE*, **86**(8), pp.1536-1551.
- [Kullarni & Dutta 96] Kullarni, P., and Dutta, D., 1996, "An Accurate Slicing Procedure for Layered Manufacturing", *Computer-Aided Design*, **28**(9), pp.683-697.
- [Kumar & Dutta 97] Kumar, V., and Dutta, D., 1997, "An Assessment of Data Formats for Layered Manufacturing", *Advances in Engineering Software*, **28**, pp.151-164.
- [Lee et al. 06] Lee, K.-S., Yang, D.-Y., Park, S. H., and Kim, R. H., 2006, "Recent Developments in the Use of Two-photon Polymerization in Precise 2D and 3D Microfabrications", *Polymers for Advanced Technologies*, **17**, pp.72-82.
- [Li et al. 02] Li, X., Choi, H., and Yang, Y., 2002, "Micro Rapid Prototyping System for Micro Components", *Thin Solid Films*, **420-421**, pp.515-523.
- [Lim et al. 05] Lim, T. W., Park, S. H., and Yang, D.-Y., 2005, "Contour Offset Algorithm for Precise Patterning in Two-photon Polymerization", *Microelectronic Engineering*, **77**, pp.382-388.
- [Lin et al. 04] Lin, C.-L., Wang, I., Mouriau, M., Casalegno, R., Andraud, C., and Baldeck, P. L., 2004, "Two-photon Induced Polymerization of Photo-driven Microsensors", *Nonlinear Optical Transmission and Multiphoton Processes in Organics II*, *Proceedings of SPIE*, **5516**, pp.52-62.
- [Lin et al. 06] Lin, C.-L., Wang, I., Dollet, B., and Baldeck, P. L., 2006, "Velocimetry Microsensors Driven by Linearly Polarized Optical Tweezers", *Optics Letters*, **31**(3), pp.329-331.
- [Loffredo] Loffredo, D. "Fundamentals of STEP Implementation", STEP Tools Inc., New York, United States.
- [Luis Pérez et al. 01] Luis Pérez, C. J., Vivamcos Calvet, J., and Sebastián Pérez, M. A., 2001, "Geometric Roughness Analysis in Solid Free-form Manufacturing Processes", *Journal of Materials Processing Technology*, **119**, pp.52-57.
- [Luo & Tzou 04] Luo, R. C., and Tzou, J. H., 2004, "Implementation of a New Adaptive Slicing Algorithm for the Rapid Prototyping manufacturing System", *IEEE/ASME*

- Transactions on Mechatronics, **9**(3), pp.593-600.
- [Mäntylä 88] Mäntylä, M., An Introduction to Solid Modeling, 1988, Computer Science Press, United States.
- [Martineau et al. 02] Martineau, C., Anémian, R., Andraud, C., Wang, I., Bouriau, M., Baldeck, P. L., 2002, "Efficient Initiators for Two-photon Induced Polymerization in The Visible Range", Chemical Physics Letters, **362**, pp.291-295.
- [Maruo et al. 98] Maruo, S., and Kawata, S., 1998, "Two-photon-absorbed Near-infrared Photopolymerization for Three-dimensional Microfabrication", Journal of Microelectromechanical Systems, **7**(4), pp.411-415.
- [Maruo et al. 03a] Maruo, S., Ikuta, K., and Korogi, H., 2003, "Force-controllable, Optically Driven Micromachines Fabricated by Single-step Two-photon Microstereolithography", Journal of Microelectromechanical Systems, **12**(5), pp.533-539.
- [Maruo et al. 03b] Maruo, S., Ikuta, K., and Korogi, H., 2003, "Submicron Manipulation Tools Driven by Light in a Liquid", Applied Physics Letters, **82**(1), pp.133-135.
- [Maruo & Inoue 06] Maruo, S., and Inoue, H., 2006, "Optically Driven Micropump Produced by Three-dimensional Two-photon Microfabrication", Applied Physics Letters, **89**, 144101.
- [Maruo & Inoue 07] Maruo, S., and Inoue, H., 2007, "Optically Driven Viscous Micropump Using a Rotating Microdisk", Applied Physics Letters, **90**, 084101.
- [Niem 94] Niem, W., 1994, "Robust and Fast Modelling of 3D Natural Objects from Multiple Views", SPIE Proceedings: Image and Video Processing II, **2182**, pp.288-397.
- [Niem & Broszio 95] Niem, W., and Broszio, H., 1995, "Mapping Texture from Multiple Camera Views onto 3D-object Models for Computer Animation", Proceedings of the International Workshop on Stereoscopic and Three Dimensional Imaging, Santorini, Greece, pp.99-105.
- [Niem 99] Niem, W., 1999, "Automatic Reconstruction of 3D Objects Using a Mobile Camera," Image and Vision Computing, **17**, pp.125-134.
- [Ovsianikov et al. 07] Ovsianikov, A., Doraiswamy, A., Narayan, R., and Chichkov, B. N., 2007, "Two-photon Polymerization for Fabrication of Biomedical Devices", Microfluidics, BioMEMS, and Medical Microsystems V, Proceedings of SPIE,

6465, 646500.

- [Pandey et al. 03] Pandey, P. M., Reddy, N. V., and Dhande, S. G., 2003, "Improvement of Surface Finish by Staircase Machining in Fused Deposition Modeling", *Journal of Materials Processing Technology*, **132**, pp.323-331.
- [Park & Rosen 03] Park, J.-H., and Rosen, D. W., 2003, "Generation of Process Plans for Laser Chemical Vapor Deposition", *Proceedings ASME Computers and Information in Engineering Conference*, DETC2003/CIE-48187, Sep. 2-6, Chicago.
- [Park 05] Park, S. C., 2005, "Hollowing Objects with Uniform Wall Thickness", *Computer-Aided Design*, **37**, pp.451-460.
- [Park et al. 05] Park, S. H., Lee, S. H., Yang, D.-Y., Kong, H. J., and Lee, K.-S., 2005, "Subregional Slicing Method to Increase Three-dimensional Nanofabrication Efficiency in Two-photon Polymerization", *Applied Physics Letters*, **87**, 154108.
- [Park et al. 07] Park, S.-H., Jeong, J.-H., Choi, D.-G., Kim, K.-D., Altun, A. O., Lee, E.-S., Yang, D.-Y., and Lee, K.-S., 2007, "Adaptive Bonding Technique for Precise Assembly of Three-dimensional Microstructures", *Applied Physics Letters*, **90**, 233109.
- [Patil et al. 00] Patil, L., Dutta, D., Bhatt, A. D., Jurens, K., Lyons, K., Pratt, M. J., and Sriram, R. D., "Representation of Heterogeneous Objects in ISO 10303 (STEP)", 2000, *ASME International Mechanical Engineering Congress and Exposition*, Orlando, Florida.
- [Pitts et al. 00] Pitts, J. D., Campagnola, P. J., Epling, G. A., and Goodman S. L., 2000, "Submicron Multiphoton Free-Form Fabrication of Proteins and Polymers: Studies of Reaction Efficiencies and Applications in Sustained Release", *Macromolecules*, **33**, pp.1514-1523.
- [Qian & Dutta 98] Qian, X., and Dutta, D., "An Architecture for Interoperability of Layered Manufacturing Data", 1998, *Proceedings, ASME Design Engineering Technical Conferences*, Atlanta, Georgia.
- [Requicha 99] Requicha, A. A.G., 1999, *Geometric Modeling: a First Course*.
- [Rossignac & Requicha 99] Rossignac, J., and Requicha, A., 1999, *Solid Modeling*, Webster, J. editor, *Encyclopedia of Electrical and Electronics Engineering*, John Wiley.
- [Ruppert 95] Ruppert, J., 1995, "A Delaunay Refinement Algorithm for Quality

- 2Dimensional Mesh Generation”, *Journal of Algorithms*, pp.548-585.
- [Sabourin et al. 96] Sabourin, E., Houser, S. A., and Bøhn, J. H., 1996, “Adaptive Slicing Using Stepwise Uniform Refinement”, *Rapid Prototyping Journal*, **2**(4), pp.20-26.
- [SCRA 06] SCRA, 2006, *STEP Application Handbook, Version 3*, North Charleston, United States.
- [Shewchuk 96] Shewchuk, J. R., 1996, “Triangle: Engineering a 2D Quality Mesh Generator and Delaunay Triangulator”, *First Workshop on Applied Computational Geometry*, (Philadelphia, Pennsylvania), ACM, pp.124-133.
- [Singh & Dutta 01] Singh, P., and Dutta, D., 2001, “Multi-direction Slicing for Layered Manufacturing”, *Journal of Computing and Information Science in Engineering*, **1**, pp.129-142.
- [Stellacci et al. 02] Stellacci, F., Bauer, C. A., Meyer-Friedrichsen, T., Wensellers, W., Alain, V., Kuebler, S. M., Pond, S. J. K., Zhang, Y., Marder, S. R., and Perry, J. W., 2002, “Laser and Electron-beam Induced Growth of Nanoparticles for 2D and 3D Metal Patterning”, *Advanced Materials*, **14**(3), pp.194-198.
- [Straub et al. 04] Straub, M., Nguyen, L. H., Fazlic, A., and Gu, M., 2004, “Complex-shaped Three-dimensional Microstructures and Photonic Crystals Generated in a Polysiloxane Polymer by Two-photon Microstereolithography”, *Optical Materials*, **27**, pp.359-364.
- [Sun et al. 00] Sun, H.-B., Kawakami, T., Xu, Y., Ye, J.-Y., Matuso, S., Misawa, H., Miwa, M., and Kaneko, R., 2000, “Real Three-dimensional Microstructures Fabricated by Photopolymerization of Resins Through Two-photon Absorption”, *Optics Letters*, **25**(15), pp.1110-1112.
- [Sun et al. 01] Sun, H.-B., Takada, K., and Kawata, S., 2001, “Elastic Force Analysis of Functional Polymer Submicron Oscillators”, *Applied Physics Letters*, **79**(19), pp.3173-3175.
- [Sun et al. 03a] Sun, H.-B., and Kawata, S., 2003, “Two-photon Laser Precision Microfabrication and Its Applications to Micro-nano Devices and Systems”, *Journal of Lightwave Technology*, **21**(3), pp.624-633.
- [Sun et al. 03b] Sun, H.-B., Takada, K., Kim, M.-S., Lee, K.-S., and Kawata, S., 2003, “Scaling Laws of Voxels in Two-photon Photopolymerization Nanofabrication”, *Applied Physics Letters*, **83**, pp.1104-1106.

- [Sun et al. 03c] Sun, H.-B., Maeda, M., Takada, K., Chon, J. W. M., Gu, M., and Kawata, S., “Experimental Investigation of Single Voxels for Laser Nanofabrication via Two-photon Photopolymerization”, 2003, *Applied Physics Letters*, **83**, pp.819-821.
- [Sun et al. 04] Sun, H.-B., Suwa, T., Takada, K., Zaccaria, R. P., Kim, M.-S., Lee, K.-S., Kawata, S., 2004, “Shape Precompensation in Two-photon Laser Nanowriting of Photonic Lattices”, *Applied Physics Letters*, **85**(17), pp.3708-3710.
- [Sunday a] Sunday, D., http://geometryalgorithms.com/Archive/algorithm_0104/algorithm_0104.htm.
- [Sunday b] Sunday, D., http://geometryalgorithms.com/Archive/algorithm_0104/algorithm_0104B.htm.
- [Tanaka et al. 02] Tanaka, T., Sun, H.-B., and Kawata, S., 2002, “Rapid Sub-diffraction-limit Laser Micro/Nanoprocessing in a Threshold Material System”, *Applied Physics Letters*, **80**(2), pp.312-314.
- [Takada et al. 05] Takada, K., Sun, H.-B., and Kawata, S., 2005, “Improved Spatial Resolution and Surface Roughness in Photopolymerization-based Laser Nanowriting”, *Applied Physics Letters*, **86**, 071122.
- [Takada et al. 06] Takada, K., Sun, H.-B., and Kawata, S., 2006, “The Study on Spatial Resolution in Two-photon Induced Polymerization”, *Micromachining Technology for Micro-Optics and Nano-Optics IV*, *Proceedings of SPIE*, **6110**, 61100A.
- [Thian et al. 06] Thian, S. C. H., Tang, Y., Fuh, J. Y. H., Wong, Y. S., Lu, L., and Loh, H. T., 2006, “Micro-rapid-prototyping via Multi-layered Photo-lithography”, *International Journal of Advanced Manufacturing Technology*, **29**, pp.1026-1032.
- [Tosa et al. 06] Tosa, N., Bosson, J., Pierre, M., Rambaud, C., Bouriau, M., Vitrant, G., Stéphan, O., Astilean, S., and Baldeck, P. L., 2006, “Optical Properties of Metallic Nanostructures Fabricated by Two-photon Induced Photoreduction”, *Proceedings of SPIE*, **6195**, 619501.
- [Várady et al. 97] Várady, T., Martin, R. R., and Cox, J., 1997, “Reverse Engineering of Geometric Models – an Introduction”, *Computer-Aided Design*, **29**(4), pp.255-268.
- [Várady & Benkő 00] Várady, T., and Benkő, P., 2000, “Reverse Engineering B-rep models from Multiple Point”, *Proceedings of Geometric Modeling and Processing*, *IEEE, Hong Kong*, pp.3-12.

- [Véron & Léon 98] Véron, P., and Léon, J.-C., 1998, "Shape Preserving Polyhedral Simplification with Bounded Error", *Computers & Graphics*, **22**(5), pp.565-585.
- [Volino & Magnenat Thalmann 98] Volino, P., and Magnenat Thalmann, N., 1998, "The SPHERIGON: a simple polygon patch for smoothing quickly your polygonal meshes", *Proceeding of Computer Animation 98*, pp.72-78.
- [Wang et al. 02] Wang, I., Bouriau, M., Baldeck, P. L., Martineau, C., and Andraud, C., 2002, "Three-dimensional Microfabrication by Two-photon-initiated Polymerization with A Low-cost Microlaser", *Optics Letters*, **27**(15), pp.1348-1350.
- [Woo et al. 02] Woo, H., Kang, E., Wang, S., and Lee, K. H., 2002, "A New Segmentation Method for Point Cloud Data", *International Journal of Machine Tools & Manufacture*, **42**(2), pp.167-178.
- [Wu et al. 06] Wu, S., Serbin, J., and Gu, M., 2006, "Two-photon Polymerization for Three-dimensional Micro-fabrication", *Journal of Photochemistry and Photobiology A: Chemistry*, **181**, pp.1-11.
- [Xing et al. 07] Xing, J.-F., Dong, X.-Z., Chen, W.-Q., Duan, X.-M., Takeyasu, N., Tanaka, T., and Kawata, S., 2007, "Improving Spatial Resolution of Two-photon Microfabrication by Using Photoinitiator with High Initiating Efficiency", *Applied Physics Letters*, **90**, 131106.
- [Xu et al. 02] Xu, Z. Q., Ye, S. H., and Fan, G. Z., "Color 3D Reverse Engineering", 2002, *Journal of Materials Processing Technology*, **129**, pp.495-499.
- [Yau et al. 00] Yau, H.-T., Chen, C.-Y., and Wilhelm, R. G., 2000, "Registration and Integration of Multiple Laser Scanned Data for Reverse Engineering of Complex 3D Models", *International Journal of Production Research*, **38**(2), pp.269-285.
- [Yang et al. 07] Yang, D.-Y., Park, S. H., Lim, T. W., Kong, H.-J., Yi, S. W., Yang, H. K., and Lee, K.-S., 2007, "Ultraprecise Microreproduction of a Three-dimensional Artistic Sculpture by Multipath Scanning Method in Two-photon Photopolymerization", *Applied Physics Letters*, **90**, 079903.
- [Z Corporation] Z Corporation, <http://www.zcorp.com/>.
- [Zhang et al. 99] Zhang, X., Jiang, X. N., and Sun, C., 1999, "Micro-stereolithography of Polymeric and Ceramic Microstructures", *Sensors and Actuators*, **77**, pp.149-156.
- [Zhang et al. 02] Zhang, L.-C., Han, M., and Huang, S.-H., 2002, "An Effective

Error-tolerance Slicing Algorithm for STL Files”, *International Journal of Advanced Manufacturing Technology*, **20**, pp.363-367.

Appendix A

Basic intersection algorithms

This appendix introduces the basic principles of intersection algorithms such as the intersection between 3D lines/segments [Sunday b], the intersection of a plane and a 3D segment [Sunday b], and the intersection of a triangle and a plane.

1. Intersection of 3D lines/segments

To compute intersections between lines or segments in 3D, the use of a parametric equation representation is well established, and a line defined by two distinct points \mathbf{p}_0 and \mathbf{p}_1 can be written as:

$$\mathbf{p}(s) = \mathbf{p}_0 + s(\mathbf{p}_1 - \mathbf{p}_0) = \mathbf{p}_0 + s\mathbf{u} \quad (\text{A-1})$$

where s is a real number and $\mathbf{u} = \mathbf{p}_1 - \mathbf{p}_0$ is a line direction vector (see Figure A-1). Using linear interpolation $\mathbf{p}(0) = \mathbf{p}_0$, and $\mathbf{p}(1) = \mathbf{p}_1$, and when $0 \leq s \leq 1$, $\mathbf{p}(s)$ is a point on the finite segment between \mathbf{p}_0 and \mathbf{p}_1 . Furthermore, if $s < 0$ then $\mathbf{p}(s)$ is outside the segment on the \mathbf{p}_0 side and if $s > 1$ then $\mathbf{p}(s)$ is outside the segment on the \mathbf{p}_1 side.

To find whether two lines intersect or not, the primary treatment needed is to check whether the line/segments are parallel or not. Let two lines be given by equations: $\mathbf{p}(s) = \mathbf{p}_0 + s(\mathbf{p}_1 - \mathbf{p}_0) = \mathbf{p}_0 + s\mathbf{u}$ and $\mathbf{q}(t) = \mathbf{q}_0 + t(\mathbf{q}_1 - \mathbf{q}_0) = \mathbf{q}_0 + t\mathbf{v}$, either or both of them can be regarded as a finite segment or a ray. Therefore, these lines are parallel if and only if their directions are collinear, namely $\mathbf{n}_u \cdot \mathbf{v} = 0$ where \mathbf{n}_u is a vector being perpendicular to \mathbf{u} . It is considered here that the numerical processing of such a configuration is not an issue that is addressed specifically. Computational geometry libraries available to strengthen the treatment of such configurations are now available with capabilities to handle exact arithmetic and diagnose many numerical singularities [CGAL] but where not incorporated to concentrate on the manufacturing preparation issues.

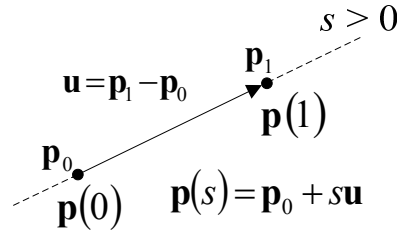


Figure A-1 The parametric equation of a line.

- **Lines/segments are parallel**

When the above condition is true, the two lines are either coincident or do not intersect at all. Coincidence can be checked by testing if a point on one line, such as \mathbf{p}_0 , also lies on the other line $\mathbf{q}(t)$. That is, there exists a t_0 such that $\mathbf{p}_0 = \mathbf{q}(t_0) = \mathbf{q}_0 + t_0 \mathbf{v}$. If these conditions hold, either two infinite lines or one infinite line and one finite segment are coincident. However, if both lines are finite segments, then they may or may not overlap. In this case, it is necessary to solve for t_0 and t_1 such that $\mathbf{p}_0 = \mathbf{q}(t_0)$ and $\mathbf{p}_1 = \mathbf{q}(t_1)$. If the segment intervals $[t_0, t_1]$ and $[0, 1]$ are disjoint, then there is no intersection. Otherwise, the intervals of intersection can be $[r_0, r_1] = [t_0, t_1] \cap [0, 1]$. Then the intersection segment is $\mathbf{q}(r_0)\mathbf{q}(r_1) = \mathbf{p}_0\mathbf{p}_1 \cap \mathbf{q}_0\mathbf{q}_1$.

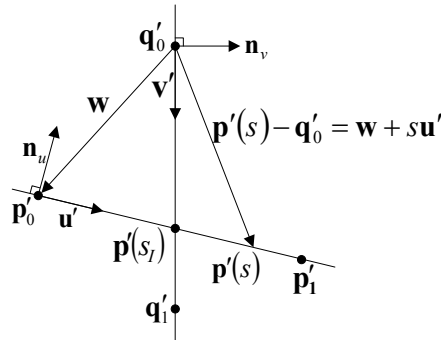


Figure A-2 The intersection of projection lines.

- **Lines/segments are not parallel**

When the two 3D lines/segments are not parallel, they may intersect at a unique point, and if they do intersect, their linear projections onto a 2D plane will also intersect. Figure A-2 shows the linear projections of line $\mathbf{p}(s)$ and $\mathbf{q}(t)$ onto a 2D plane where \mathbf{p}'_0 , \mathbf{p}'_1 , \mathbf{q}'_0 , and \mathbf{q}'_1 are the projection points of \mathbf{p}_0 , \mathbf{p}_1 , \mathbf{q}_0 , and \mathbf{q}_1 ; \mathbf{u}' and \mathbf{v}' are the projection vectors of \mathbf{u} and \mathbf{v} ; $\mathbf{p}'(s)$ is projection line of $\mathbf{p}(s)$, and \mathbf{n}_u and \mathbf{n}_v are the vectors perpendicular to \mathbf{u}' and

\mathbf{v}' , respectively. Assuming that there exist a 2D intersection point \mathbf{i} , at $\mathbf{p}'(s_I)$ and $\mathbf{q}'(t_I)$, then $\mathbf{p}(s)$ and $\mathbf{q}(t)$ intersect if $\mathbf{p}'(s_I) = \mathbf{q}'(t_I)$.

To determine s_I , the vector equality $\mathbf{p}'(s) - \mathbf{q}'_0 = \mathbf{w} + s\mathbf{u}'$ where $\mathbf{w} = \mathbf{p}'_0 - \mathbf{q}'_0$ is used. At the intersection point, the vector $\mathbf{p}'(s) - \mathbf{q}'_0$ is perpendicular to \mathbf{n}_v , so $\mathbf{n}_v \cdot (\mathbf{w} + s_I\mathbf{u}) = 0$. Solving this equation, the result is:

$$s_I = \frac{-\mathbf{n}_v \cdot \mathbf{w}}{\mathbf{n}_v \cdot \mathbf{u}}. \quad (\text{A-2})$$

Similarly, solving for $\mathbf{q}(t_I)$, the result is:

$$t_I = \frac{\mathbf{n}_u \cdot \mathbf{w}}{\mathbf{n}_u \cdot \mathbf{v}}. \quad (\text{A-3})$$

The denominators of Eq. A-2 and A-3 vanish only when the lines are parallel, i.e. $\mathbf{n}_v \cdot \mathbf{u} = 0$ or $\mathbf{n}_u \cdot \mathbf{v} = 0$. If one of the two lines is either a finite segment or a ray, then the intersection point is inside the segment only when $0 \leq s_I \leq 1$ (or $s_I \geq 0$ for a ray). If both lines are segments, then both solution parameters, s_I and t_I , must lie in the $[0, 1]$ interval for the segments to intersect.

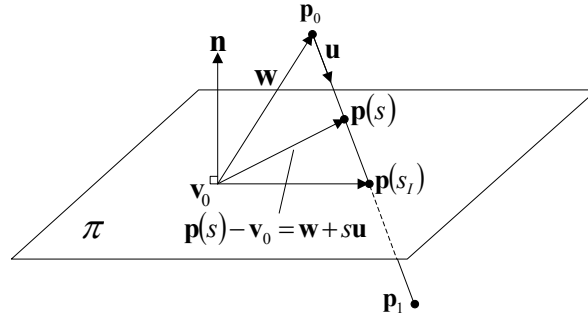


Figure A-3 Intersection of a 3D segment and a plane.

2. Intersection of a plane and a 3D segment

In Figure A-3, let a 3D segment $\mathbf{p}_0\mathbf{p}_1$ be given by the parametric equation: $\mathbf{p}(s) = \mathbf{p}_0 + s(\mathbf{p}_1 - \mathbf{p}_0) = \mathbf{p}_0 + s\mathbf{u}$, where $0 \leq s \leq 1$, and \mathbf{u} is the line direction vector of the segment $\mathbf{p}_0\mathbf{p}_1$. A plane π is also given by the point \mathbf{v}_0 lying on it and its normal vector \mathbf{n} . If the segment $\mathbf{p}_0\mathbf{p}_1$ isn't parallel to plane π ($\mathbf{n} \cdot \mathbf{u} \neq 0$), then the segment $\mathbf{p}_0\mathbf{p}_1$ and the plane π intersect at a unique point $\mathbf{p}(s_I)$. At this intersection point, the vector $\mathbf{p}(s) - \mathbf{v}_0 = \mathbf{w} + s\mathbf{u}$, where $\mathbf{w} = \mathbf{p}_0 - \mathbf{v}_0$, is perpendicular to \mathbf{n} . This is equivalent to the dot product condition: $\mathbf{n} \cdot (\mathbf{w} + s\mathbf{u}) = 0$. Solving it, the result is:

$$s_I = \frac{-\mathbf{n} \cdot \mathbf{w}}{\mathbf{n} \cdot \mathbf{u}} = \frac{\mathbf{n} \cdot (\mathbf{v}_0 - \mathbf{p}_0)}{\mathbf{n} \cdot (\mathbf{p}_1 - \mathbf{p}_0)}. \quad (\text{A-4})$$

If there is an intersection between the segment $\mathbf{p}_0\mathbf{p}_1$ and plane π , then $0 \leq s_I \leq 1$. Other singular configurations are not described here to focus only on the key features needed for micro-product processing.

3. Intersection of a triangle and a plane

Consider a triangle T with vertices \mathbf{p}_0 , \mathbf{p}_1 , and \mathbf{p}_2 lying in a plane π' and a plane π passing through the point \mathbf{v}_0 with the normal vector \mathbf{n} . Unless they are parallel, the two planes π' and π intersect in a line L , and when the triangle T intersects the plane π , it will be a segment contained in the line L , as shown in Figure A-4. When the triangle T doesn't intersect the plane π , all three of its vertices lie on the same side of the plane π . Otherwise, when the triangle T does intersect the plane π , at least one point of triangle T must be on one side of the plane π or exactly on the plane π . So, the intersection algorithm between a plane and a 3D segment mentioned before can be used to find the intersection point(s). A simple test using the signed distance from the point to the plane is useful to find on which side of a plane a point is. This test is described below [Sunday a].

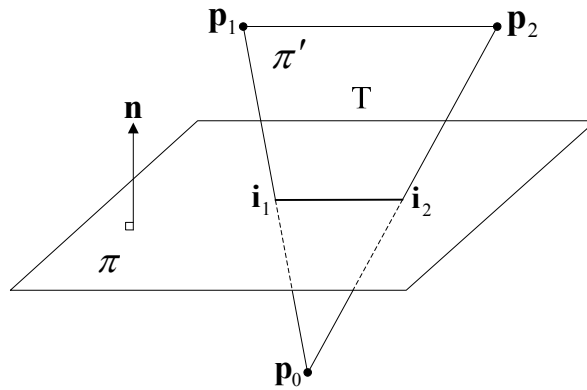


Figure A-4 Intersection of a triangle and a plane.

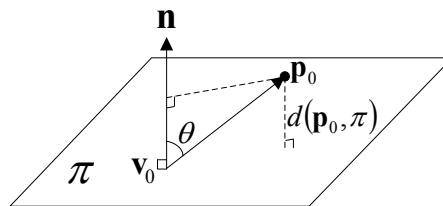


Figure A-5 Distance of a point to a plane.

Assume a point \mathbf{v}_0 lies on plane π whose normal vector is \mathbf{n} , the distance from an arbitrary 3D point \mathbf{p}_0 to the plane π can be computed by using the dot product to get the projection of the vector $(\mathbf{p}_0 - \mathbf{v}_0)$ onto \mathbf{n} as shown in the Figure A-5. The resulting distance is given as follows:

$$d(\mathbf{p}_0, \pi) = |\mathbf{p}_0 - \mathbf{v}_0| \cos \theta = \frac{\mathbf{n} \cdot (\mathbf{p}_0 - \mathbf{v}_0)}{|\mathbf{n}|}. \quad (\text{A-5})$$

This formula gives a signed distance which is positive on one side of the plane and negative on the other one. Therefore, the sign of $d(\mathbf{p}_0, \pi)$ can be used to simply test which side of the plane a point is on. For example, $\mathbf{p}_0\mathbf{p}_1$ is one of the edges of triangle T in Figure A-4, and it intersects the plane π only when the two points are on opposite sides of that plane ; that is $d(\mathbf{p}_0, \pi) \cdot d(\mathbf{p}_1, \pi) < 0$. Conversely, when $d(\mathbf{p}_0, \pi) \cdot d(\mathbf{p}_1, \pi) > 0$, there is no intersection between the segment and π . Also, if $d(\mathbf{p}_0, \pi) \cdot d(\mathbf{p}_1, \pi) = 0$, then either one or both points lie on plane π . When both are on plane π , the whole edge $\mathbf{p}_0\mathbf{p}_1$ lies in this plane.

VITA

Name: Chao-Yaug LIAO

Date of birth: December 4, 1975

Place of birth: Kaohsiung County, Taiwan

Address: No.173, Zhongzheng Rd., Dashe Shiang,
Kaohsiung County, Taiwan

Phone: +886-7-351-1465

Email: d89522030@ntu.edu.tw



Academic background:

- 1997 B.S., Department of Mechanical Engineering, National Cheng Kung University, Tainan, Taiwan
- 2000 M.S., Department of Mechanical Engineering, National Taiwan University, Taipei, Taiwan
- 2008 Ph.D., Mécanique et Energétique, Université Joseph Fourier, Grenoble, France
- 2008 Ph.D., Department of Mechanical Engineering, National Taiwan University, Taipei, Taiwan